

FORM FINDING AND ANALYSIS OF EXTENSIBLE MEMBRANES ATTACHED TO 2-D
AND 3-D FRAMES INTENDED FOR MICRO AIR VEHICLES VIA EXPERIMENTALLY
VALIDATED FINITE ELEMENT METHODS

By

YAAKOV JACK ABUDARAM

A DISSERTATION PRESENTED TO THE GRADUATE SCHOOL
OF THE UNIVERSITY OF FLORIDA IN PARTIAL FULFILLMENT
OF THE REQUIREMENTS FOR THE DEGREE OF
DOCTOR OF PHILOSOPHY

UNIVERSITY OF FLORIDA

2013

© 2013 Yaakov Jack Abudaram

To my mother, who has given me her unconditional love, and has shown me the way to
success

ACKNOWLEDGMENTS

First and foremost I would like to thank my advisor, Dr. Ifju, not only for providing the funds for my research, but also for making himself available to give me the path to the most innovative and practical solutions I needed for challenging problems. Dr. Ifju is as intelligent as he is compassionate, and this virtue makes him an exceptional being. I am proud to have worked with him more than anyone else.

The research I was involved in was a portion of a much larger project under the leadership of Dr. Hubner. I owe my deepest gratitude to him for his immense amount of contribution in writing and publishing my first journal paper.

Thanks go to Dr. Ukeiley, Dr. Mohseni, and Dr. Mecholsky for accepting to be in my committee. Their invaluable inputs strengthen this thesis, thereby yielding further journal publications.

I am grateful to my colleagues, Bradley LeCroix, Sean Rohde, Jason Cantrell, Jason Rue, and Kelvin Chang for their help in the analysis of my data, creation of profound ideas, and editing my papers.

I have learned the fundamental concepts of flexible wings from Dr. Stanford in 2009. I published and presented my first conference paper with his help, and he has been a major influence on my research to this day. I would like to thank him for replying to every email I sent him promptly, diligently, and patiently.

It is quoted that every successful man has a woman behind him. I am fortunate enough to have three beautiful women to help me propel in my life: the first lady is my mother, Ojeni, who has always been compassionate, understanding, and supportive of me. The second wonder is my sister, Rifka, who always listens and tries to solve any kind of problem I may have. I am also thankful to her for her immense help in my

computer aided design (CAD) drawings; her expertise in mechanical engineering and design made this work to be completed much sooner than it would have been. Finally, my lifelong love, Dr. Leah Portnow always has the proper cure for my challenges: when I am perplexed, she is encouraging; when I am overwhelmed, she helps me take a break with a warm tea, and when I need help in editing my papers, she always makes herself available to correct my errors carefully and conscientiously.

TABLE OF CONTENTS

	<u>page</u>
ACKNOWLEDGMENTS.....	4
LIST OF TABLES.....	9
LIST OF FIGURES.....	10
ABSTRACT.....	21
INTRODUCTION.....	23
Micro Air Vehicle Design.....	23
Wing Flexibility.....	23
Perimeter and Batten Reinforced Wings.....	24
Aerodynamics.....	25
Effects of Low Aspect Ratio Wings and Reynolds Number.....	25
Shape and Flow Measurements.....	27
Tensioning and Membrane Attachment Techniques.....	28
Importance of Pre-tension.....	28
Form Finding Methods.....	31
DEVELOPING FABRICATION METHODS VIA THERMAL EXPANSION FOR PRE- TENSIONING MAV WINGS AND TEST ARTICLES.....	37
2-Dimensional (2-D) Cases.....	37
Pre-tensioning Method via Thermal Expansion.....	37
Preparation of Test Articles.....	38
Silicone rubber membrane preparation.....	38
2-D specimen preparation.....	39
Heating element.....	39
Composite Frames.....	40
3-Dimensional (3-D) Cases.....	40
Silicone Rubber Application on 3-D Frames.....	40
Silicone Rubber Application on 3-D Wings.....	42
Visual Image Correlation System.....	42
Properties of Silicone Rubber Membrane.....	43
NUMERICAL MODELING AND EXPERIMENTAL VALIDATION FOR THERMAL EXPANSION FABRICATION METHOD.....	51
Pre-tensioning Results for 2-D Frames.....	51
Experimental Validation.....	51
Open Cell.....	52
Numerical Analysis for Open Cell.....	54

VIC Results for Single and Multiple Cell Configurations	55
Closed Cell	56
Pre-tensioning Results for 3-D Frames	58
Numerical Analysis	58
Experimental Validation	59
Specimen-A	59
Specimen-B	61
Specimen-C	61
Specimen-D	62
Specimen-E	63
Pre-tensioning Results for Perimeter Reinforced Wings	64
Silicone Rubber Membrane Relaxation Test Results	66
COMPUTER SIMULATIONS FOR THERMALLY EXPANDING AND ADHERING SILICONE RUBBER MEMBRANES	92
Curved Membrane Nomenclature	92
Simulations for Closed Cell Circular Frames	95
Effect of Membrane Strain at Attachment for Closed Cells	95
Effect of Aspect Ratio for Closed Cells	96
Effect of Depth Ratio for Closed Cells	97
Simulations for Open Cell Circular Frames	98
Effect of Membrane Strain at Attachment for Open Cells	99
Effect of Aspect Ratio for Open Cells	100
Effect of Depth Ratio for Open Cells	102
Simulations for Doubly Curved Frames	103
Effect of Membrane Strain at Attachment for Doubly Curved Frames	103
Effect of Aspect Ratio for Doubly Curved Frames	104
Effect of Depth Ratio for Doubly Curved Frames	105
Effect of Asymmetry for Double Curved Frames	106
Displacement, Stress, and Strain Gradients of Selected Cases	109
Comparison of Double Curved Symmetrical and Unsymmetrical Cases	109
Displacement Gradients on a Double Curved Frame with 100% Depth Ratio	111
MANUFACTURING METHODS OF CO-CURING MEMBRANE AND WING SKELETONS	150
Fabrication of 2-D Specimens via Co-cure Method	151
Fabrication of Wings and Pre-tensioning via Co-cure Method	152
Corona Treatment	152
Fabrication of Width Tapered Double Cantilever Beam	153
Complete Experimental Arrangements	154
RESULTS AND DISCUSSION OF CO-CURE METHOD	160
Membrane Pre-tensioning on 2-D Specimens via Co-cure Method	160
Membrane Pre-tensioning on MAV Wings via Co-cure Method	161

Width Tapered Cantilever Beam (WTCB) Test for Corona Treatment.....	163
CONCLUSIONS AND FUTURE WORK.....	170
Conclusions	170
Future Work	171
RESULTS FROM FIVE 2-D CO-CURED SPECIMENS	173
LIST OF REFERENCES	181
BIOGRAPHICAL SKETCH.....	190

LIST OF TABLES

<u>Table</u>		<u>page</u>
2-1	Properties of silicone rubber membrane	44
3-1	The dimensions and pre-strains of the two sets of membrane wings	56
4-1	Local aspect ratios with respect to initial and final inflection points.	107
6-1	Average forces (N) recorded on all specimens.....	163

LIST OF FIGURES

<u>Figure</u>		<u>page</u>
1-1	Two different types of airplanes that are fabricated in Micro Air Vehicle Laboratory at the University of Florida.....	36
2-1	Method to measure pre-tension on membranes using VIC system	45
2-2	Application of primer for the preparation of frames.....	45
2-3	Complete experimental setup.	46
2-4	Dimensions of open and closed cell membrane/carbon-fiber assembly.	46
2-5	Application of silicone rubber on a 3D frame.	47
2-6	Six disparate curved specimens adhered to speckled silicone rubber membrane at appropriate temperatures.	48
2-7	Doubly curved carbon fiber mold and frame lay-up.	49
2-8	Cured doubly curved carbon fiber mold and frame when membrane is attached.....	49
2-9	Silicone membrane laid to allow uniform expansion on the MAV wing mold.	50
3-1	Strain vs temperature plot for silicone rubber and ULE Glass.	67
3-2	Normal strain in x-direction when attached at 140°C for the open cell model.....	67
3-3	Normal strain in y-direction when attached at 140°C for the open cell model....	68
3-4	Shearing Strain when attached at 140°C for the open cell model.	68
3-5	Strain versus experimental steps plot when attached at 140°C for open cell model.....	69
3-6	Stress plots in x-and y-direction along with shearing stress at room temperature for open cell when attached at 140°C.....	69
3-7	Abaqus mesh density created for the numerical analysis of planar cases.....	70
3-8	Numerical simulation and experimental results comparison for strains in x- and y-directions when the membrane is attached at 140°C.	70
3-9	Membrane wing models of one, two and three cells (left to right) with targeted pre-strains of 1%, 2% and 4% (bottom to top).	71

3-10	VIC result for 4% pre-strained 1-cell configuration attached at 210°C.....	71
3-11	VIC result for 4% pre-strained 2-cell configuration attached at 210°C.....	72
3-12	VIC result for 4% pre-strained 3-cell configuration attached at 210°C.....	72
3-13	Strain versus experimental steps plot when attached at 180°C for closed cell model.....	73
3-14	Stress plots in x-and y-direction along with shearing stress at room temperature for closed cell when attached at 180°C.	73
3-15	Abaqus mesh created for the numerical analysis of 3-D specimens.	74
3-16	Abaqus mesh density created for the numerical analysis of MAV wings.	74
3-17	Normalized out-of-plane displacements for the 15-layer curved closed cell; R=63.5mm when attached at 100°C.....	75
3-18	Data from 10 specimens for normalized transverse displacements along the chordwise direction compared to numerical results.	75
3-19	Data from 10 specimens for normalized transverse displacements along the spanwise direction compared to numerical results.	76
3-20	Strains in y-direction for the 15-layer curved closed cell; R=63.5mm when attached at 100°C.....	76
3-21	Data from 10 specimens for spanwise strains compared to numerical results along the chordwise direction.	77
3-22	Data from 10 specimens for spanwise strains compared to numerical results along the spanwise direction.	77
3-23	Strains in x-direction for the 15-layer curved closed cell; R=63.5mm when attached at 100°C.....	78
3-24	Data from 10 specimens for chordwise strains compared to numerical results along the chordwise direction.	78
3-25	Data from 10 specimens for chordwise strains compared to numerical results along the spanwise direction.	79
3-26	VIC results for strains in x-and y-directions for the 2-layer curved closed cell; R=63.5mm when attached at 100°C.....	79
3-27	Normalized out-of-plane displacements for the 15-layer curved closed cell; R=127mm when attached at 140°C.....	80

3-28	Strains in y-direction for the 15-layer curved closed cell; R=127mm when attached at 140°C.....	81
3-29	Strains in y-direction for the 15-layer curved closed cell; R=127mm when attached at 140°C.....	82
3-30	Normalized out-of-plane displacements for the 15-layer doubly curved closed cell; R ₁ =R ₂ =63.5mm when attached at 140°C.....	83
3-31	Strains in y-direction for the 15-layer doubly curved closed cell; R ₁ =R ₂ =63.5mm when attached at 140°C.	84
3-32	Strains in x-direction for the 15-layer doubly curved closed cell; R ₁ =R ₂ =63.5mm when attached at 140°C.	85
3-33	Normalized out-of-plane displacements for the 15-layer curved open cell; R=63.5mm when attached at 100°C.....	86
3-34	Strains in y-direction for the 15-layer curved open cell; R=63.5mm when attached at 100°C.....	87
3-35	Strains in x-direction for the 15-layer curved open cell; R=63.5mm when attached at 100°C.....	88
3-36	Normalized out-of-plane displacements for perimeter reinforced wing.	89
3-37	Spanwise strains for perimeter reinforced wing.	89
3-38	Chordwise strains for perimeter reinforced wing.....	90
3-39	Numerical spanwise stresses for perimeter reinforced wing.....	90
3-40	Numerical chordwise stresses for perimeter reinforced wing.	91
3-41	Normal and shear strains before and after wing tunnel experiments.....	91
4-1	Curved membrane nomenclature.	112
4-2	Two alternate perspectives to approach the varying depth ratio problem.....	112
4-3	Normalized maximum out-of-plane displacements versus temperature for various depth ratios when a silicone membrane is attached on a closed curved frame with an AR of 0.5.	113
4-4	Spanwise strains at the maximum out-of-plane displacement locations versus membrane strain at attachment for various depth ratios when a silicone membrane is attached on a closed curved frame with an AR of 0.5.....	113

4-5	Chordwise strains at the maximum out-of-plane displacement locations versus membrane strain at attachment for various depth ratios when a silicone membrane is attached on a closed curved frame with an AR of 0.5.	114
4-6	Spanwise stresses (kPa) at the maximum out-of-plane displacement locations versus membrane strain at attachment for various depth ratios when a silicone membrane is attached on a closed curved frame.....	114
4-7	Chordwise stresses (kPa) at the maximum out-of-plane displacement locations versus membrane strain at attachment for various depth ratios when a silicone membrane is attached on a closed curved frame.....	115
4-8	Normalized maximum out-of-plane displacements for various aspect ratios and depth ratios for a silicone membrane attached on a closed curved frame at 100°C (1.7% membrane strain).	115
4-9	Spanwise strains at the maximum out-of-plane displacement locations versus aspect ratio for various depth ratios when a silicone membrane is attached on a closed curved frame at 100°C (1.7% membrane strain).	116
4-10	Chordwise strains at the maximum out-of-plane displacement locations versus aspect ratio for various depth ratios when a silicone membrane is attached on a closed curved frame at 100°C (1.7% membrane strain).	116
4-11	Spanwise stresses (kPa) at the maximum out-of-plane displacement locations versus aspect ratio for various depth ratios when a silicone membrane is attached on a closed curved frame at 100°C).....	117
4-12	Chordwise stresses (kPa) at the maximum out-of-plane displacement locations versus aspect ratio for various depth ratios when a silicone membrane is attached on a closed curved frame at 100°C.....	117
4-13	Normalized maximum out-of-plane displacements versus depth ratio for various aspect ratios when a silicone membrane is attached on a closed curved frame at 100°C (1.7% membrane strain).	118
4-14	Spanwise strains at the maximum out-of-plane displacement locations versus depth ratio for various aspect ratios when a silicone membrane is attached on a closed curved frame at 100°C (1.7% membrane strain).	118
4-15	Chordwise strains at the maximum out-of-plane displacement locations versus depth ratio for various aspect ratios when a silicone membrane is attached on a closed curved frame at 100°C (1.7% membrane strain).	119
4-16	Spanwise stresses (kPa) at the maximum out-of-plane displacement locations versus depth ratio for various aspect ratios when a silicone membrane attached on a closed curved frame at 100°C.....	119

4-17	Chordwise stresses (kPa) at the maximum out-of-plane displacement locations versus depth ratio for various aspect ratios when a silicone membrane attached on a closed curved frame at 100°C.....	120
4-18	Determining the location of maximum out-of-plane displacement.	120
4-19	Normalized maximum out-of-plane displacements versus temperature for various depth ratios when a silicone membrane is attached on an open curved frame with an AR of 0.5.	121
4-20	Location of the maximum out-of-plane displacements versus membrane strain at attachment for various depth ratios when a silicone membrane is attached on an open curved frame with an AR of 0.5.....	121
4-21	Spanwise strains at the maximum out-of-plane displacement locations versus membrane strain at attachment for various depth ratios when a silicone membrane is attached on an open curved frame with an AR of 0.5.	122
4-22	Chordwise strains at the maximum out-of-plane displacement locations versus membrane strain at attachment for various depth ratios when a silicone membrane is attached on an open curved frame with an AR of 0.5. ...	122
4-23	Spanwise stresses (kPa) at the maximum out-of-plane displacement locations versus membrane strain at attachment for various depth ratios when a silicone membrane is attached on an open curved frame.....	123
4-24	Chordwise stresses (kPa) at the maximum out-of-plane displacement locations versus membrane strain at attachment for various depth ratios when a silicone membrane is attached on an open curved frame.	123
4-25	Normalized maximum out-of-plane displacements versus aspect ratio for various depth ratios when a silicone membrane is attached on an open curved frame at 100°C (1.7% membrane strain).	124
4-26	Location of the maximum out-of-plane displacements versus AR for various depth ratios when a silicone membrane is attached on an open curved frame at 100°C (1.7% membrane strain).	124
4-27	Spanwise strains at the maximum out-of-plane displacement locations versus AR for various depth ratios when a silicone membrane is attached on an open curved frame at 100°C (1.7% membrane strain).	125
4-28	Chordwise strains at the maximum out-of-plane displacement locations versus AR for various depth ratios when a silicone membrane is attached on an open curved frame at 100°C (1.7% membrane strain).	125

4-29	Spanwise stresses (kPa) at the maximum out-of-plane displacement locations versus AR for various depth ratios when a silicone membrane is attached on an open curved frame at 100°C (1.7% membrane strain).....	126
4-30	Chordwise stresses (kPa) at the maximum out-of-plane displacement locations versus AR for various depth ratios when a silicone membrane is attached on an open curved frame at 100°C (1.7% membrane strain).....	126
4-31	Normalized maximum out-of-plane displacements versus depth ratio for various aspect ratios when a silicone membrane is attached on an open curved frame at 100°C (1.7% membrane strain).	127
4-32	Location of the maximum out-of-plane displacements versus DR for various aspect ratios when a silicone membrane is attached on an open curved frame at 100°C (1.7% membrane strain).	127
4-33	Spanwise strains at the maximum out-of-plane displacement locations versus depth ratio for various aspect ratios when a silicone membrane is attached on an open curved frame at 100°C (1.7% membrane strain).	128
4-34	Chordwise strains at the maximum out-of-plane displacement locations versus depth ratio for various aspect ratios when a silicone membrane is attached on an open curved frame at 100°C (1.7% membrane strain).....	128
4-35	Spanwise stresses (kPa) at the maximum out-of-plane displacement locations versus depth ratio for various aspect ratios when a silicone membrane is attached on an open curved frame at 100°C	129
4-36	Chordwise stresses (kPa) at the maximum out-of-plane displacement locations versus depth ratio for various aspect ratios when a silicone membrane is attached on an open curved frame at 100°C.	129
4-37	The two extreme displacement locations of a membrane on a doubly curved frame.	130
4-38	Normalized maximum out-of-plane displacements versus membrane strain at attachment for various depth ratios when a silicone membrane is attached on a closed double curved frame with an AR of 0.5.	130
4-39	Location of the maximum out-of-plane displacements versus membrane strain at attachment for various depth ratios when a silicone membrane is attached on a closed double curved frame with an AR of 0.5.....	131
4-40	Spanwise strains at the maximum out-of-plane displacement locations versus membrane strain at attachment for various depth ratios when a silicone membrane is attached on a closed double curved frame with an AR of 0.5.	131

4-41	Chordwise strains at the maximum out-of-plane displacement locations versus membrane strain at attachment for various depth ratios when a silicone membrane is attached on a closed double curved frame.	132
4-42	Spanwise stresses (kPa) at the maximum out-of-plane displacement locations versus membrane strain at attachment for various depth ratios when a silicone membrane is attached on a closed double curved frame	132
4-43	Chordwise stresses (kPa) at the maximum out-of-plane displacement locations versus membrane strain at attachment for various depth ratios when a silicone membrane is attached on a closed double curved frame	133
4-44	Normalized maximum out-of-plane displacements for various aspect ratios and depth ratios for a silicone membrane attached on a double curved frame at 100°C (1.7% membrane strain).	133
4-45	Location of the maximum out-of-plane displacements versus AR for various depth ratios when a silicone membrane is attached on a doubly curved frame at 100°C (1.7% membrane strain).	134
4-46	Spanwise strains at the maximum out-of-plane displacement locations versus AR for various depth ratios when a silicone membrane is attached on an open curved frame at 100°C (1.7% membrane strain).	134
4-47	Spanwise strains at the maximum out-of-plane displacement locations versus AR for various depth ratios when a silicone membrane is attached on an open curved frame at 100°C (1.7% membrane strain).	135
4-48	Spanwise strains at the maximum out-of-plane displacement locations versus AR for various depth ratios when a silicone membrane is attached on an open curved frame at 100°C (1.7% membrane strain).	135
4-49	Spanwise strains at the maximum out-of-plane displacement locations versus AR for various depth ratios when a silicone membrane is attached on an open curved frame at 100°C (1.7% membrane strain).	136
4-50	Normalized maximum out-of-plane displacements versus depth ratio for various aspect ratios when a silicone membrane is attached on a closed doubly curved frame at 100°C (1.7% membrane strain).....	136
4-51	Location of the maximum out-of-plane displacements versus DR for various aspect ratios when a silicone membrane is attached on a closed doubly curved frame at 100°C (1.7% membrane strain).	137
4-52	Spanwise strains at the maximum out-of-plane displacement locations versus depth ratio for various aspect ratios when a silicone membrane is attached on a closed doubly curved frame at 100°C (1.7% membrane strain).....	137

4-53	Chordwise strains at the maximum out-of-plane displacement locations versus depth ratio for various aspect ratios when a silicone membrane is attached on a closed doubly curved frame at 100°C (1.7% membrane strain).	138
4-54	Spanwise stresses (kPa) at the maximum out-of-plane displacement locations versus depth ratio for various aspect ratios when a silicone membrane is attached on a closed doubly curved frame at 100°C.....	138
4-55	Chordwise stresses (kPa) at the maximum out-of-plane displacement locations versus depth ratio for various aspect ratios when a silicone membrane is attached on a closed doubly curved frame at 100°C	139
4-56	Schematic for the locations of asymmetry (side view).	139
4-57	Effect of inflection point on AR_{local} of each curve.	140
4-58	Normalized maximum out-of-plane displacements versus inflection point for a combination of ARs and DRs when a silicone membrane is attached on a doubly curved frame at 100°C (1.7% membrane strain).....	140
4-59	Normalized minimum out-of-plane displacements versus inflection point for a combination of ARs and DRs when a silicone membrane is attached on a doubly curved frame at 100°C (1.7% membrane strain).....	141
4-60	Location of the maximum out-of-plane displacements along the chord length versus inflection point for a combination of ARs and DRs when a silicone membrane is attached on a doubly curved frame at 100°C.....	141
4-61	Location of the minimum out-of-plane displacements along the chord length versus inflection point for a combination of ARs and DRs when a silicone membrane is attached on a doubly curved frame at 100°C.....	142
4-62	Spanwise strains at the maximum out-of-plane displacement locations versus inflection point for a combination of ARs and DRs when a silicone membrane is attached on a doubly curved frame at 100°C (1.7% membrane strain).....	142
4-63	Spanwise strains at the minimum out-of-plane displacement locations versus inflection point for a combination of ARs and DRs when a silicone membrane is attached on a doubly curved frame at 100°C (1.7% membrane strain).....	143
4-64	Chordwise strains at the maximum out-of-plane displacement locations versus inflection point for a combination of ARs and DRs when a silicone membrane is attached on a doubly curved frame at 100°C.....	143
4-65	Chordwise strains at the minimum out-of-plane displacement locations versus inflection point for a combination of ARs and DRs when a silicone membrane is attached on a doubly curved frame at 100°C.....	144

4-66	Spanwise stress (kPa) at the maximum out-of-plane displacement locations versus inflection point for a combination of ARs and DRs when a silicone membrane is attached on a doubly curved frame at 100°C.....	144
4-67	Spanwise stress (kPa) at the minimum out-of-plane displacement locations versus inflection point for a combination of ARs and DRs when a silicone membrane is attached on a doubly curved frame at 100°C.....	145
4-68	Chordwise stress (kPa) at the maximum out-of-plane displacement locations versus inflection point for a combination of ARs and DRs when a silicone membrane is attached on a doubly curved frame at 100°C.....	145
4-69	Chordwise stress (kPa) at the minimum out-of-plane displacement locations versus inflection point for a combination of ARs and DRs when a silicone membrane is attached on a doubly curved frame at 100°C.....	146
4-70	Normalized out-of-plane displacement gradients for three frames that have various inflection points with AR=0.5, DR=0.8, and attached at 100°C	146
4-71	Spanwise strain gradients for three frames that have various inflection points with AR=0.5, DR=0.8, and attached at 100°C.	147
4-72	Chordwise strain gradients for three frames that have various inflection points with AR=0.5, DR=0.8, and attached at 100°C.....	147
4-73	Spanwise stress gradients for three frames that have various inflection points with AR=0.5, DR=0.8, and attached at 100°C.	148
4-74	Chordwise stress gradients for three frames that have various inflection points with AR=0.5, DR=0.8, and attached at 100°C.....	148
4-75	Normalized out-of-plane displacement gradient for a membrane attached on a double curved frame with AR=0.5, DR=1.0, and attached at 100°C.....	149
5-1	An actual perimeter reinforced MAV fabricated via co-cure method with a combination of clear silicone rubber membrane and carbon-fiber skeleton, and a batten reinforced latex rubber MAV one year after manufacturing.	156
5-2	Specimen parts (silicone rubber film and carbon fiber frame) dimensions to be co-cured.....	156
5-3	Experimental steps involved in the construction and analysis of the MAV wings.	157
5-4	Preparation of tapered double cantilever beam.....	157
5-5	Experimental setup for the analysis of the WTDCB specimens B) Analysis of the deformed silicone membrane.	158

5-6	Experimental setup for the analysis of the deformed silicone membrane.	159
6-1	Developed pre-strains on 2-D specimens in x-direction with co-cure method. .	165
6-2	Developed pre-strains on 2-D specimens in y-direction with co-cure method. .	165
6-3	Developed shear pre-strains on 2-D specimens with co-cure method.....	166
6-4	Out-of-plane displacements on the membrane for the three samples of perimeter reinforced wings.	166
6-5	Pre-strain gradients in x-direction shown for the three samples of perimeter reinforced wings.	167
6-6	Pre-strain gradients in y-direction shown for the three samples of perimeter reinforced wings.	167
6-7	Shearing strain gradients for the three samples of perimeter reinforced wings.	168
6-8	WTDCB tests for corona treated and untreated silicone on bidirectional carbon fiber.....	168
6-9	WTDCB tests for corona treated and untreated silicone on unidirectional carbon fiber.....	169
A-1	Normal strains in x-direction for specimen 1 at each step.	173
A-2	Normal strains in y-direction for specimen 1 at each step.	173
A-3	Shearing strains for specimen 1 at each step.....	174
A-4	Normal strains in x-direction for specimen 2 at each step.	174
A-5	Normal strains in y-direction for specimen 2 at each step.	175
A-6	Shearing strains for specimen 2 at each step.....	175
A-7	Normal strains in x-direction for specimen 3 at each step.	176
A-8	Normal strains in y-direction for specimen 3 at each step.	176
A-9	Shearing strains for specimen 3 at each step.....	177
A-10	Normal strains in x-direction for specimen 4 at each step.	177
A-11	Normal strains in y-direction for specimen 4 at each step.	178
A-12	Shearing strains for specimen 4 at each step.....	178

A-13	Normal strains in x-direction for specimen 5 at each step.	179
A-14	Normal strains in y-direction for specimen 5 at each step.	179
A-15	Shearing strains in for specimen 5 at each step.	180

Abstract of Dissertation Presented to the Graduate School
of the University of Florida in Partial Fulfillment of the
Requirements for the Degree of Doctor of Philosophy

FORM FINDING AND ANALYSIS OF EXTENSIBLE MEMBRANES ATTACHED TO 2-D
AND 3-D FRAMES INTENDED FOR MICRO AIR VEHICLES VIA EXPERIMENTALLY
VALIDATED FINITE ELEMENT ANALYSIS

By

Yaakov Jack Abudaram

December 2013

Chair: Peter Ifju
Major: Aerospace Engineering

This work is concerned with a new method to apply consistent and known pre-tension to silicone rubber membranes intended for micro air vehicles as well as an understanding in the science of developed pre-tension in membranes constrained by 2-D and 3-D frames and structures. Pre-tension has a marked effect on the static and dynamic response of membrane wings and controls the overall deflections, as such control and measurement of the membrane pre-tension is important. Two different 2-D frame geometries were fabricated to evaluate the technique. For open-cell frames, the pretension was not uniform, whereas it was for closed-cell frames. Results show developed full-field stress and strain fields as a function of membrane attachment temperature and frame geometry along with experimental iterations to prove repeatability. The membranes can be stretched to a specific pretension according to the temperature at which it adheres to frames.

Strain fields in membranes attached to 3-D frames at various temperatures are modeled through FEA utilizing Abaqus to be able to predict the developed membrane deformations, stresses, and strains. Rigid frames with various curvatures are built via

appropriate molds and then adhered to silicone rubber membranes and elevated to various temperatures to achieve different pre-strains for experimental validation. Additional experiments are conducted for more complex frame geometries involving both convex and concave topologies embedded within frames. Results are then compared with the Abaqus outputs to validate the accuracy of the FEA model.

Highly compliant wings have been used for MAV platforms, where the wing structure is determined by some combination of carbon fiber composites and a membrane skin, adhered in between the layers of composite material. Another new technique of attaching membranes firmly on wing structures is introduced, which involves the application of a technology known as corona treatment coupled with another method of tensioning silicone membranes on any given frame geometry. Corona treatment provided a means of increasing adhesion of silicone on carbon fiber through the use of a high-frequency high-voltage air plasma discharge. The silicone membrane is co-cured with carbon fiber under vacuum pressure at an elevated temperature. After cool down, the membrane is tensioned.

CHAPTER 1 INTRODUCTION

Micro Air Vehicle Design

Micro air vehicles, or “MAVs”, are defined as an aircraft with a maximum size of 15cm and are capable operating at speeds of 25mph or less [1]. Despite their size, MAVs are expected to be able to carry a payload of 20 grams for 20-60 minutes [2]. The idea is a design of a small, reliable, and an inexpensive vehicle that can survey a remote area that is not easily accessible with ground transportation [3]. For example, a MAV may be placed under a missile and jettisoned right before the missile reaches the targeted area to send images of the damage to the base. A variety of wings may be envisioned for these vehicles, such as fixed, rotary, and flapping while this work is concerned with the fixed type [4]. Design, configuration, fabrication, and successful flight tests of fixed wings have been accomplished by a number of research groups, such as Ifju et al. [5], Mohseni et al. [6], Ailinger et al. [7], Wu et al. [8], and Grasmeyer et al. [9].

Wing Flexibility

Flexible membrane concept is utilized in hang gliders [10, 11], sails, kites, and various MAV configurations mimicking different species of birds, insects, and bats [12, 13, 14]. The reason behind being inspired by the natural fliers is to overcome the unsteady aerodynamics due to flying at low Reynolds numbers, which in turn causes transition, separation, reattachment, and fluid-structure interaction [15]. For example, Mastramico and Hubner [16] have shown that scalloping the trailing edge of a wing, which is a configuration that is commonly seen in a bat’s wing, removes the excessive membrane vibration and reduces the drag coefficient significantly in comparison to the

lift coefficient [17]. Shyy et al. [18] has proven that flexible wings perform better in comparison to their rigid counterparts. Shyy et al. [19] also documents several aerodynamic qualities unique to MAV flight citing the favorable scaling characteristics, including the low inertia and reduced stall speeds, the low Reynolds numbers that promote boundary layer separation, the transitional flows to turbulent regimes and the low lift to drag ratios. In addition, Song and Breuer have experimentally investigated the dynamics of compliant wing membrane as related to mammalian flight [20].

Perimeter and Batten Reinforced Wings

The controllability and range of operation of micro air vehicles (MAVs) can be greatly diminished in the presence of unsteady, gusty conditions [21]. Even indoor flight (envisioned for small flapping vehicles) can suffer from similar problems, due to air vents and ducting. While several complex, active mechanisms have been envisioned to maintain smooth level flight in unsteady conditions, energy budgets onboard MAVs are limited [22] and simple passive mechanisms may suffice. Extremely compliant wings have been used for MAV platforms to assist in aircraft controllability [23], where the wing structure is predicated by some combination of carbon fiber composites to form a wing skeleton, and a membrane skin (latex rubber) attached to the carbon fiber skeleton. The wing topology (placement of carbon fiber) can potentially be tailored to obtain the desired change in aerodynamic performance through passive shape adaptation [24].

Load alleviation is a potential benefit (through unsteady gust alleviation, delayed stall, decreased lift slopes, minimized drag, etc.), and may be obtained with flexible wing designs particular with an unattached trailing edge [4]. Figure 1-1A shows a MAV wing utilizing this concept. The trailing edge deflects upward due to aerodynamic loading,

resulting in a nose-down geometric twist of the flexible wing section. This adaptive washout decreases wing loading. For example, as the vehicle flies into a head on wind gust, the effective airspeed increases. Because of the wing's flexibility and design, the larger dynamic pressure causes the wing to twist downward and decrease the generated lift, which results in a near-constant lift history through the gust [25].

An alternative membrane wing design concept, called a perimeter reinforced wing (Figure 1-1B), is utilized for load augmentation. During flight, at various angles of attack and depending on flight speed, the membrane flexes upward increasing the camber, or aerodynamic twisting of the wing, causing an increase in lift and a more negative pitching moment slope. For either design, if more flexibility is desired the number of battens or the batten stiffness may be reduced or the modulus of elasticity or thickness of the membrane may be reduced. This may result in excessive membrane vibration [26].

Aerodynamics

Effects of Low Aspect Ratio Wings and Reynolds Number

Such a relationship between dynamic pressure and elastic wing compliance may not always be so straightforward. Increasing the flight speed accentuates the positive deflection of the trailing edge described above for load alleviation, but alters the Reynolds number as well. The range of tested flight speeds (5 to 15 m/s) equates to fairly low chord-based Reynolds numbers between $3.3 \cdot 10^4$ and 10^5 . The flow structures present throughout this range of Reynolds numbers should show substantial variations, and thus aerodynamic performance will as well. As reviewed by Carmichael [27]: for Reynolds numbers below $5 \cdot 10^4$, the laminar separated flow may not have time to reattach to the surface. Above $5 \cdot 10^4$, the flow may reattach, forming a long separation

bubble over the wing [28]. Minimizing the size of the separation bubble is of obvious interest since it reduces lift and increases drag by changing the pressure distribution, shape of the airfoil and the effective thickness, which is opposite of what is intended for the ideal design of an airplane [29, 30]. For increased Reynolds numbers, the size of the bubble decreases, generally resulting in a decrease in form drag [31]. Reynolds numbers for typical fixed wing micro air vehicles are between 10^4 and 10^5 , a span that sees extremely complex and mutable flow fields develop over a wing [32]: flow separation [33], transition, and reattachment [34], periodic vortex shedding [35], swirling, and pairing [36], and strong interactions with three-dimensional tip vortices [37] have all been reported. The length of transition was proposed to be modeled by Roberts [38], Davis et al. [39], and Volino et al. [40] on the boundary layer edge, while Mayle [41], Roberts et al. [42], and Praisner et al. [43] were able to predict the transitional length by creating models that utilized the local Reynolds number based on the momentum thickness. The underlying physics, as discussed by Young and Horton [44], depend on many factors including Reynolds number and wing shape, the latter of which is not pre-determined for an elastic membrane wing.

Though many suitable aeroelastic computational tools exist [4] for membrane micro air vehicle wings, they cannot always be expected to faithfully reproduce the complex physics described above, particularly in post-stall regimes. Experimental wind tunnel testing can provide an initial link between wing structure, Reynolds number, and load alleviation, which can in turn be used to tune the aeroelastic models for a detailed exploration of the design space. Existing literature on wind tunnel testing of membrane wings generally discuss up to three facets of the underlying physics: load

measurements (lift, drag, etc.), shape measurements (displacements and strains of the elastic membrane under aerodynamic loading), and flow measurements.

Stanford et al. [24] used numerical methods and experimental validation to optimize flexible wing topology and showed that a flexible wing can be designed such that it out performs a rigid counterpart no matter what the objective (lift, lift/drag, longitudinal stability, gust rejection, delayed stall, etc.). Therefore, when done correctly, a flexible wing is better than a rigid counterpart.

Shape and Flow Measurements

Shape measurements for membrane wings are typically non-contact optical methods, as strain gages and load cells are too intrusive. Song et al. [45] use stereo photogrammetry for displacement measurements of a membrane sheet stretched between two rigid posts, with a reported resolution between 35 and 40 μm . Data is available at discrete markers placed along the wing. Projection moiré interferometry requires no such marker placement (a fringe pattern is projected onto the wing surface), and the resulting data set is full-field. However, displacement resolutions reported by Fleming et al. [46] for micro air vehicle work are relatively poor (250 μm), the dual-camera system must be rotated during the α -sweep, and only out-of-plane data is available, making strain calculations (if needed) impossible. Stanford et al. [4] utilized a visual image correlation system for membrane wings, which is a full-field speckle-based technique with a displacement resolution of 10 μm . This method is utilized in the current work as well, and will be described below. Wu et al. [47] has extended the image correlation method for high speed deformation measurements of flapping membrane wings.

Experimental flow measurements for membrane wings include recent work with particle image velocimetry (PIV) by Hu et al. [48] and Rojratsirikul et al. [49] concerning an aspect ratio-5 membrane wing. The former is able to show that trailing edge washout can keep the flow attached to the flexible surface up to 14° angle of attack, while a rigid wing under similar conditions shows a very large separation bubble. The latter find that mean membrane shape is insensitive to angle of attack, though time-averaged flow is not, through the development of flow separation and vortex shedding. The authors are also able to show a strong time-dependent correlation between membrane vibration and the height of the shear layer [49]. A similar wing is studied by Mastramico and Hubner [16] to correlate the elastic membrane structure with the velocity deficits within the wake.

Tensioning and Membrane Attachment Techniques

Importance of Pre-tension

Membrane pre-tension also plays a major role in the static and dynamic response of membrane wings and affects the overall time-averaged deflections as well as vibration frequencies and modes [50]. Too low pre-tension may result in aerodynamic inefficiency (lower lift and higher drag) due to excessive membrane deformation and lifting; too high pre-tension will approach the performance of the rigid model. Additionally, long-term time-dependent properties and membrane durability will eventually play a role. This is a considerable drawback of latex membranes which degrade more readily when handled or when they come in contact with liquid (e.g. water, oil, or alcohol) compared to silicon rubber membranes. Immediately after manufacturing, latex starts to lose tension and degrades rapidly. Silicone rubber also

shows signs of relaxation after long trials of experiments (Figure 3-41); however, in comparison to latex loss of maximum 0.5% strain is insignificant.

The full-field measurement and the repeatable application of the membrane pre-tension is important to be able to effectively assess the benefits of membrane wings and incorporate into computational and experimental optimization and design investigations. Initial methods used to apply pre-tension when fabricating MAV wings were rudimentary: the membrane was stretched over a foam pad, pinned on the perimeter and then adhered to the composite skeleton/frame. An approximation of the overall pre-tension was calculated based on the initial membrane stretch prior to adhesion to the frame. Depending on the boundaries of the frame (fully enclosed, open at one end, etc), the membrane would relax in one or more directions, resulting in a non-uniform stress field. Additionally, the process did not lend itself to good repeatability. Johnston et al. [51] took steps to improve the process by stretching the membrane over a pre-designed pedestal prior to adhesion to the frame. The global pre-strain was determined by measuring the distance between two burnished marks (one mark for the latex at zero tension and another mark after pre-tensioning) on the plates, in which the quoted accuracy was 0.2% strain.

Work by Rojratsirikul et al. [52, 53] found that membrane vibration is caused by the separated flows to interact with the membrane to produce unsteadiness. In another study, he realized a combination of chordwise and spanwise vibrational modes were a result of tip vortices and vortex shedding [54]. He further elaborated his research by changing the pre-tension of the membrane and concluded that increase in tension,

which caused an excess length, increased the vibrational frequency, and the vibrations were delayed at higher angles of attacks for airfoils with excess length [55].

Gordnier et al. [56] computationally investigated the flexible airfoils through combining a sixth order Navier-Stokes solver with a nonlinear membrane structural model to explain that the unsteady response of flexible membrane is an effect of angle of attack, membrane pretension, and Reynolds number. Increasing the membrane tension caused a lower camber on the wing, which resulted in an increasingly unsteady flow that reduced the frequency for vortex shedding.

Rojratsirikul et al. [55] has studied the oscillations on a pure membrane airfoil by altering the amount of strain on latex, in which the membrane is restricted at both the leading edge and the trailing edge, but not constrained on the sides. Hubner et al. [17] investigated the vibrational frequencies at the trailing edge of various wing models mimicking batten reinforced wings.

Amory Timpe [57] investigated three 5-cell wings, each cell with 80cmX80cm dimensions and wings with 1.3%, 2.8%, and 4.2% strains. He reported a change in vibrational frequency with the increase of an angle of attack and increase of strain. Change in vibrational frequency on a membrane wing can be explained through the analogy of a guitar string frequency, which is predicted by length (L), harmonics (n), tension (T), and density (μ). Until the stall angle is reached, as the AOA of the wing is increased, the pressure under the membrane also increases causing an increase in camber, increase in strain in both spanwise and chordwise directions, and a decrease in thickness, which all contribute to a higher vibrational frequency. All of these parameters can be found in the vibrating string equation although the proportions may not be the

same for a MAV wing. A shift is observed with an increasing pre-strain on a wing, similar to a higher pitch sound in the thinner strings of a guitar. Conversely, an increase in air speed for a given AOA should not change the oscillations; however, the amplitude of the wave should increase. Similarly, plucking a string with a higher force would cause an increase in volume, but the note/frequency would not change. All the aforementioned parameters are expected to have a more significant role in a perimeter reinforced wing as the loads are higher toward the camber in oppose to trailing edge.

Stanford et al. [24] developed a numerical model to simulate the fluid structure interaction of flexible wings as mentioned at the end of the Aerodynamics section of this chapter. In that work he also included membrane pre-tension and investigated the sensitivity of various performance measures as a function of membrane pre-tension. However, the pre-tension was employed as a uniform (or constant) value over the wing area. This assumption or simplification will be validated in this work. If the distribution of pre-tension is not constant, this study will serve as a guide to establish the appropriate pre-tension distribution in elastomer membrane wings.

Form Finding Methods

The preliminary method of form finding was derived from the “soap bubble analogy,” which is defined as a physical model to a mathematical problem of minimal surfaces [58] that has a mean curvature of zero. This idea was formulated in “elasticity theory” by Sophie Germain [59]. Nevertheless, the idea of “soap film” is not widely accepted by many researchers since the idealism of minimal surfaces is applicable to only specific cases [60]. Lewis described form finding in relation to numerical modeling as “finding a shape that approximates the state of the full static equilibrium.”

Veenendaal et al. [61] categorized and explained the three methods of form finding in

detail: stiffness matrix method (a fundamental technique that utilizes the elastic and geometric stiffness matrices), geometric stiffness method, and dynamic equilibrium method. Very similar categorizations were made by several other research groups such as Bletzinger [62], Barnes [63], and Schek [64] as mentioned by Veenendaal. He then compared the various form finding techniques to investigate the key differences and similarities. One of the oldest form finding techniques, the grid method, was presented by Siev and Eidelman [65] in 1964, and the research was further extended for 3D structures by Haug and Powell in 1972 [66].

Schek [64] is the inventor of the “force density method,” which was implemented by many other researchers (Basso and Del Grosso [67], Grundig, Singer, and Strobel [68], Pauletti and Pimenta [69], Zhang and Ohsaki [70], and Van Mele and Block [71]) to find various solutions to form finding. This idea was based on the force-length ratios through a large mesh created over the surface of the structure. Maurin and Motro [72] and Sanchez et al. [73] improvised this method by adding multiple steps with force adjustments.

Membrane structures are required to be pre-tensioned, as it cannot be under compressive loadings. This means the initial pre-strain is determined according to the mission for which the structure is set. For example, a batten reinforced wing seen on Figure 1-1A may have been requested to have a 2% spanwise strain at the trailing edge region by an aerodynamicist, as this condition is claimed to be optimum for wind washout and reduced drag due to less vibration at the trailing edge. Haber and Abel [74] stated that flexural stresses do not occur in membrane structures to overcome unbalanced forces, which must be canceled out with pre-strain gradients throughout the

membrane topology. The authors proposed various techniques to solve the initial equilibrium problem: generalized least squares stress determination methods, assumed geometric stiffness method, iterative smoothing method, nonlinear displacement analysis approach with slip, and a combined approach. Argyris, Angelopoulos, and Bichat [75] discussed a computational method to predict the displacements and stresses in roof structures. Linkwitz [76] devised a direct formulation method between elastically stretched bars and nodes utilizing Schek's force density method. Buchholdt et al. [77] exemplified the membrane and cable net analogy for an initial configuration in equilibrium. Two research groups, Knudson and Scordelis [78], and Ohyama and Kawamata [79] developed a method utilizing the least squares technique to compute the forces in cable nets. Maurin and Motro [80] showed that the cable net method lacks the ability to calculate the shear stresses of membranes and suggested a simpler and more effective tool, the surface density method [81]. Barnes et al. [82] defined another form finding method for pre-strained membrane roof structures through the simultaneous vector method and the kinetic damping process. The author classified prestressed membrane applications into radial membranes and geodesic patterning (meshing the shortest distance between two points on a given curved surface) to further elaborate cases with complicated topologies. A novel method of geodesic patterning was discussed by Tan [83] in 1999, who formulated a physical approach by altering the mathematical model Argyris [75] proposed, which resulted in a computationally more effective technique for final membrane topology.

In 1999, Bletzinger and Ramm [62] stated that traditional methods of linearization cause singular solutions; therefore, the authors presented a modern non-linear finite

element technique involving “differential geometry, continuum mechanics, and numerical continuation” for form finding applied to membrane and cable elements. Ten years later Bletzinger, Firi, Linhard, and Wuchner [84] advanced this method to show applications on textile membranes supported with cables, pre-stressed cable nets, and even “bat wing” formed structures. Finally in 2005, Wuchner and Bletzinger [85] presented a projection method for “the form finding of anisotropic pre-stressed membrane structures”.

Deformations in cable, hypar, spatial nets were calculated by Lewis [86] using non-linear methods (linear load-displacement relationship and equation of dynamic equilibrium); however, results did not converge for saddle nets. Later, Lewis [87] solved the problem through a combination of three methods: soap film analogy, force density method, and dynamic relaxation.

All works cited related to form finding methods is applicable to inextensible membranes and the majority of the papers are not experimentally validated. This work will focus on silicone rubber film, which is extensible and wrinkle effects [88] are negligible. The membranes are thermally expanded in two and three dimensions and applied to appropriate frames. Corresponding numerical models are generated for form finding through the Abaqus software, and finite element results are validated with the experimental data extracted from the visual image correlation system. Also, in this research, the two deficiencies of membrane wings (poor durability of latex membrane material and the inability to control the consistency of membrane pre-tension) are addressed. First, silicone rubber is used to replace latex rubber as the elastomer membrane material. Silicone rubber is significantly more durable and retains its

elasticity for a longer duration than latex rubber. The disadvantage is that most adhesives do not adhere well to silicone rubber. This dissertation will provide a solution to this problem. Second, a new technique to apply a consistent and a spatially known pre-tension to membrane MAVs and test articles is developed. The technique heats the membrane prior to the attachment to the frame or skeleton, enabling thermal expansion to stretch the membrane relative to room temperature. The membranes are pretreated with a randomized speckle pattern to enable digital image correlation assessment of the resulting strain field once or as the frame/membrane assembly cools. The research will detail the technique and discuss the full-field pre-strain results on two different frame geometries.

In addition a co-cure method is introduced in Chapter 5 and Chapter 6; which involves the fabrication of 2-D and 3-D raw carbon fiber geometries cured together with the silicone rubber film under vacuum pressure in a conventional oven. Only experimental results are reported for this method as the science behind the membrane displacements and strains after co-curing are not entirely understood.



A



B

Figure 1-1. Two different types of airplanes that are fabricated in Micro Air Vehicle Laboratory at the University of Florida A) Batten Reinforced B) Perimeter Reinforced

CHAPTER 2 DEVELOPING FABRICATION METHODS VIA THERMAL EXPANSION FOR PRE- TENSIONING MAV WINGS AND TEST ARTICLES

Since ample evidence exists that a flexible wing combining a carbon fiber skeleton and a compliant elastomer membrane can be designed that is superior to a rigid counterpart, there is motivation to produce robust versions. Current latex rubber versions fall short in terms of durability, therefore, this section will cover methods to fabricate wings and test articles using silicone rubber, which is vastly superior in terms of environmental durability. A step-by-step procedure was applied to planar, single camber, and dual camber test articles. Visual Image Correlation (VIC) was used to measure the pre-tensions as a result of attaching the silicone rubber. As such, a random speckling pattern was applied to test articles, required by the VIC.

2-Dimensional (2-D) Cases

2-D cases were analyzed first to simplify the problem, which involved two types of frames with open and closed sections. The silicone rubber film was both thermally and mechanically stretched about twenty times to negate the effects of hysteresis, which is discussed in detail in Chapter 3.

Pre-tensioning Method via Thermal Expansion

The general procedural steps used to apply a pre-tensioned membrane to the frame of interest, in this case silicone rubber to a carbon fiber frame, are listed below and schematically shown in Figure 2-1.

- Step 1: Apply a speckle pattern to the membrane. This is further discussed in the “preparation of test articles” section. Then acquire an image of the speckled membrane at room temperature as the initial field reference.
- Step 2: Heat the membrane on a heating surface. For this investigation, a 5 mm thick aluminum plate was placed on a commercial hot-plate to effectively diffuse heat from the hot-plate coils into a uniform field. Temperature and uniformity was

measured with a hand-held infrared thermometer that had a resolution of $\pm 1.5^{\circ}\text{C}$ over the free surface of the hot plate.

- Step 3: Attach the heated membrane to the frame using silicone adhesive.
- Step 4: Acquire images of the membrane as it cools to room temperature at desired intervals. The analysis of the images led to a temperature-strain calibration curve.
- Step 5: Acquire images of the membrane after it cools to room temperature.
- Step 6: Cut membrane overhangs and acquire another picture at room temperature.
- Step 7: Optional (performed for technique evaluation): cut the membrane from the frame and acquire an image to assess any effects of hysteresis.

Images were acquired from two cameras, forming an image pair. Each pair was analyzed with Visual Image Correlation software (VIC). While the resulting displacement field was composed of both the elastic deformation of the membrane and the inherent rigid body motions during the attachment of the frame on the membrane, cutting the membrane overhang regions as well as cutting the membrane from the frame on the final step, the computed strain field was unaffected by these motions.

Preparation of Test Articles

Analysis of the method laid out in Figure 2-1 required a prepared silicone rubber film to be adhered on a 2-D frame on a temperature controlled surface.

Silicone rubber membrane preparation

A random speckle pattern was applied on the black silicone rubber film via flat white spray paint in a similar fashion as Stanford et al. [5]. The paint on the membrane does not significantly change the elongation properties of the material. The silicone membrane is then repeatedly (approximately 10 times) heated up to $\sim 200^{\circ}\text{C}$ and cooled down to $\sim 0^{\circ}\text{C}$ to eliminate any effects of hysteresis.

2-D specimen preparation

Because silicone rubber adhesive does not robustly adhere on any surface by nature (except for silicon rubber), a silicon adhesive primer (identified as SS4155 01P by GE Silicones) was applied to the carbon fiber frame surface at room temperature. Application of the silicone primer was through filter paper providing an even distribution of the primer. After waiting for the solvent in the primer to evaporate (approximately 30 minutes), the two parts of raw silicone (Dragon Skin – Shore 20A) were mixed in a separate cup to attach the membrane on the frames immediately at the desired elevated temperature shown in Step 3. The pot life of the silicone mixture is reported as 15 minutes at room temperature. At higher temperatures (150°C-200°C) the raw silicone cures within a second and the cure time increases as the attachment temperature decreases; therefore, for lower temperatures the frame/membrane assembly was pressed together for longer durations to ensure the raw mixture was fully cured before cooling. Images were acquired with increments of 20°C during the cooling process.

Heating element

To heat the silicone membrane uniformly, a commercially available hot-plate was combined with an aluminum plate manufactured to fit inside the hot-plate. The aluminum plate was spray coated with a flat black paint to increase the surface emissivity for the infrared thermometer. To capture the amount of expansion and contraction of the membrane, two VIC cameras are positioned above the specimen and remained stationary throughout the experiments, each at a different viewing angle. Before taking each image, the temperature of the membrane was measured with an infrared thermometer that had a sensitivity of $\pm 1^\circ\text{C}$ between 10°C to 30°C and outside that range a sensitivity of $\pm 1.5^\circ\text{C}$.

Composite Frames

For the development of the silicone rubber attachment procedure two frames were fabricated out of ten layers of prepreg plain-weave carbon-fiber/epoxy. The dimensions of the open and closed cells are shown in Figure 2-4.

3-Dimensional (3-D) Cases

This section will discuss the preparation of various 3-D structures: five idealized frames were manufactured to validate the numerical method, and five perimeter reinforced wings were fabricated to test the accuracy of the Finite Element Model for a more complicated scenario.

Silicone Rubber Application on 3-D Frames

Various shapes of 3 dimensional specimens were prepared out of plain-weave pre-preg carbon-fiber/epoxy to experimentally validate the numerical results. Initially a 5mm thick and 63.5mm radius aluminum cylindrical block was used as a mold to construct a closed frame composed of 15 layers of carbon fiber to ensure proper rigidity. The raw carbon fiber was cured on the mold in an oven at 135°C for two hours. Finally, the curved carbon fiber plate window was cut according to the dimensions shown in Figure 2-5. The experimental steps to apply the silicone rubber film on the frame were similar to the procedure explained for 2D frames with some exceptions:

- Step 1: Apply a speckle pattern to the membrane. Then acquire an image of the speckled membrane placed on the aluminum cylinder at room temperature as the initial field reference.
- Step 2: Heat the membrane on the heated surface. For this investigation, a 5mm thick aluminum cylindrical block was placed in a commercial convection oven to provide uniform heat distribution on the cylinder. Temperature and uniformity was measured with a hand-held infrared thermometer that has an accuracy of $\pm 1.5^{\circ}\text{C}$ over the free surface of the aluminum cylinder.
- Step 3: Attach the curved frame to the heated membrane using silicone adhesive.

- Step 4: Acquire images of the membrane after the attachment and at room temperature.

All frame windows shown in Figure 2-6, except for the wing, had 50mm width by 100mm curved length dimensions. A 15 layer closed cell (Figure 2-6B) was fabricated to investigate the effect of frame stiffness and the change in membrane deformations and strains in comparison to its rigid counterpart (Figure 2-6A). The third frame (Figure 2-6C) was constructed by doubling the radius to validate the numerical model for an altered curvature.

Analysis of the double curved frame (Figure 2-6D) required the fabrication of a double curved mold to allow the membrane uniformly expand in three dimensions. 15 layers of carbon fiber were laid on and curved in between the two identical aluminum cylinders shown in Figure 2-7. The raw carbon fiber was cured in the oven for two hours at 135 °C under vacuum pressure. A similar procedure was repeated to construct the frame out of the carbon fiber mold and the frame window was cut with a dremel tool according to the aforementioned dimensions (50mm width by 100mm curved length) to compute the deformations and strains in the membrane (assembly shown in Figure 2-8) and compare the results to the numerical model.

Another configuration of a 15 layer carbon fiber frame with an open end (Figure 2-6E) was constructed to mimic a batten reinforced wing and validate the Abaqus results with the open curved experimental model. The excess membrane from the open end was cut after the silicone rubber was adhered to the open cell. This frame was not speckled because Specimen-A was already proven to be rigid enough to withstand the forces applied by the silicone rubber film.

Silicone Rubber Application on 3-D Wings

For the fabrication of the actual MAV wing, only the wing (125 mm wingspan, 104 mm root chord, and aspect ratio of 1.2) of the MAV seen in Figure 2-6F was considered for a more complex scenario that involves camber and reflex. The camber at the root was 6.8%, the reflex at the root was -1.4%, and 9 deg of positive geometric twist (nose up) was built into the wingtip. Silicone rubber membrane was heated to uniformly expand on the mold surface (Figure 2-9) in the oven up to approximately 120°C and allowed to cool down to 100°C to attach the wing frame and acquire images by the VIC system for the analysis.

Visual Image Correlation System

All deformations were measured with visual image correlation. The underlying principle is to calculate the displacement field of a test specimen by tracking the deformation of a random speckling pattern applied to the surface[89]. Two pre-calibrated cameras digitally acquire this pattern before and after loading, using stereo-triangulation techniques. The VIC system then determines a region in the image of the deformed specimen that maximizes a normalized cross-correlation function corresponding to a small subset of the reference image. The reference image is acquired when no load is applied to the structure. The image space is iteratively swept by the parameters of the cross-correlation function to transform the coordinates of the original reference frame to coordinates within the deformed image. As it is unlikely that the deformed coordinates will directly fall onto the sampling grid of the reference image, accurate grey-value interpolation schemes are implemented to achieve optimal sub-pixel accuracy without bias [90].

The twin cameras were connected with a PC via an IEEE 1394 firewire cable, and a unit was used to synchronize the camera triggers for instantaneous shots. A standard acquisition board installed in the computer performed digitalization of the images, and the image processing was performed by VIC3D-2007 software, provided by Correlated Solutions, Inc. Typical data results obtained from the VIC system consist of geometry of the surface in discrete coordinates (x, y, z) and the corresponding displacements (u, v, w). The VIC system places a grid point every N pixels, where N is user defined. A final post-processing option involves calculating the in-plane strains (ϵ_{xx} , ϵ_{yy} , and ϵ_{xy}). This is completed by mapping the displacement field onto an unstructured triangular mesh, and conducting the appropriate numerical differentiation for finite strain measurements. The strain resolution of the VIC system is estimated to be $300\mu\epsilon$, a relatively high value (compared to strain gages, for example) due to the fact that the data is obtained by appropriately differentiating the displacement fields. The VIC system was not expected to have the resolution to capture the accurate strain information in the frame; therefore, only the membrane deformation was taken into account for calculations.

Properties of Silicone Rubber Membrane

Elastic modulus and Poisson's ratio values were calculated experimentally utilizing the VIC system. Longitudinal strips of silicone membrane (12:1 aspect ratio) were weighted and the resulting deformations were measured. The value provided for the elastic modulus was calculated by means of a linear regression of the Eulerian stress and the resulting longitudinal strain. The thermal coefficient of expansion was computed in a similar manner by recording the temperatures with the infrared thermometer and strain values utilizing the VIC system. An ultra low expansion glass was also analyzed

to validate the experiments, which the results can be seen along with silicone rubber CTE analysis in Figure 3-1. The thickness of the silicone membrane was measured with digital calipers while the operating temperature range was provided by the manufacturer. All measure properties are shown in Table 2-1.

Table 2-1. Properties of silicone rubber membrane

Property	Value (Unit)
Elastic Modulus (E)	385 kPa
Poisson's Ratio	0.431
Thermal Expansion Coefficient(CTE)	$2.83 \times 10^{-4}/\text{C}$
Thickness	0.281 mm
Operating Temperature Range	-62.0°C – 218°C

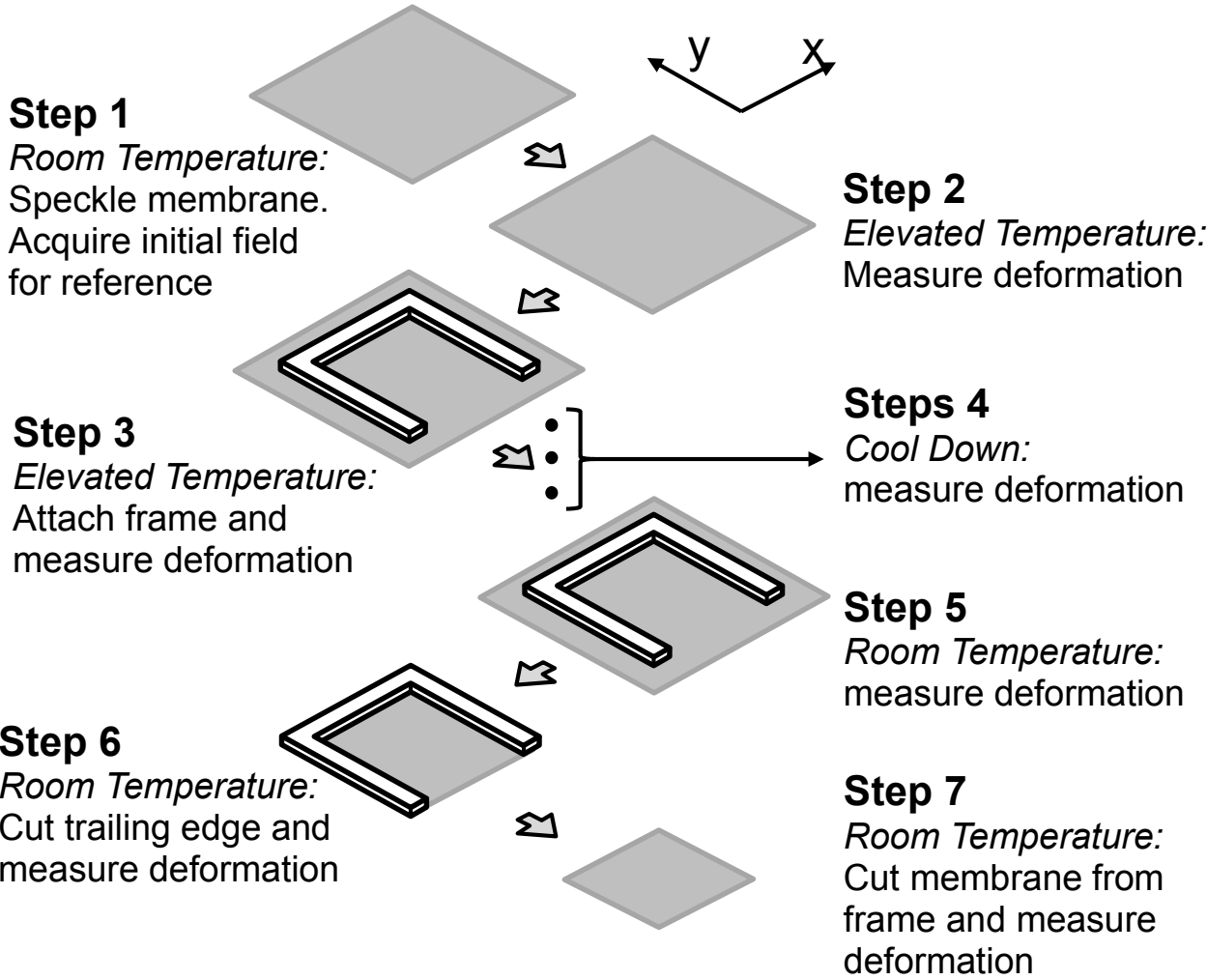


Figure 2-1. Method to measure pre-tension on membranes using VIC system

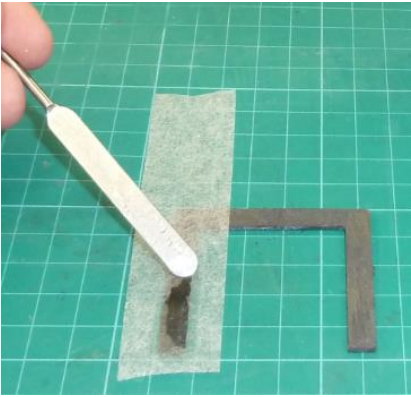


Figure 2-2. Application of primer for the preparation of frames.

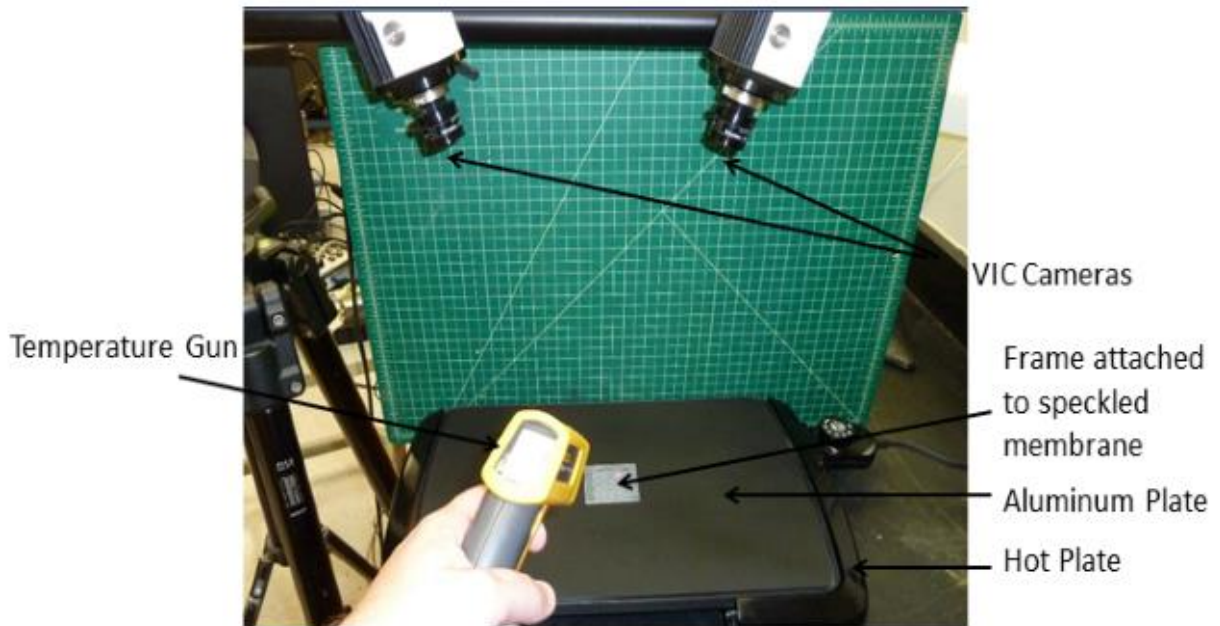


Figure 2-3. Complete experimental setup.

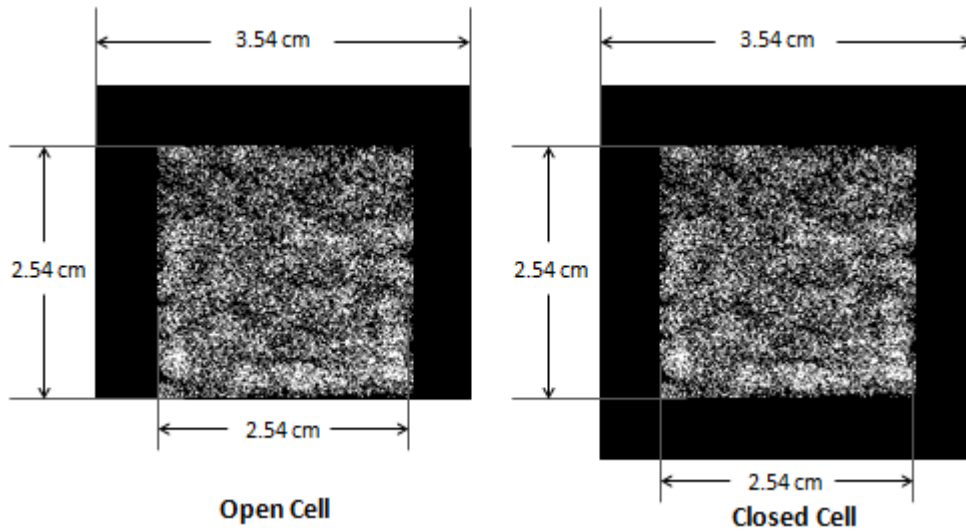


Figure 2-4. Dimensions of open and closed cell membrane/carbon-fiber assembly.

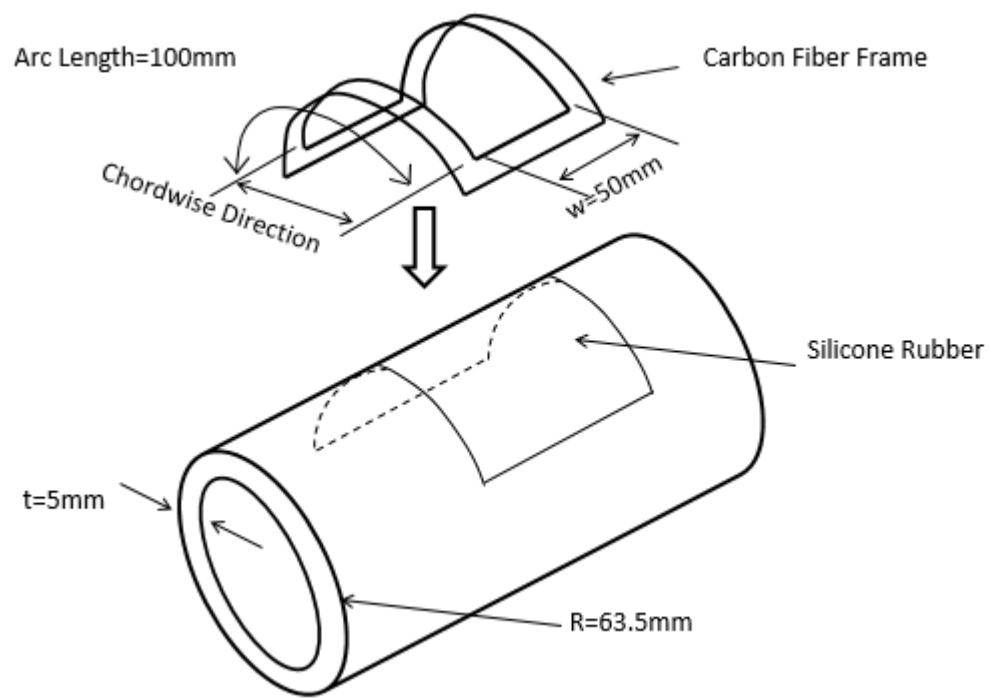


Figure 2-5. Application of silicone rubber on a 3D frame.

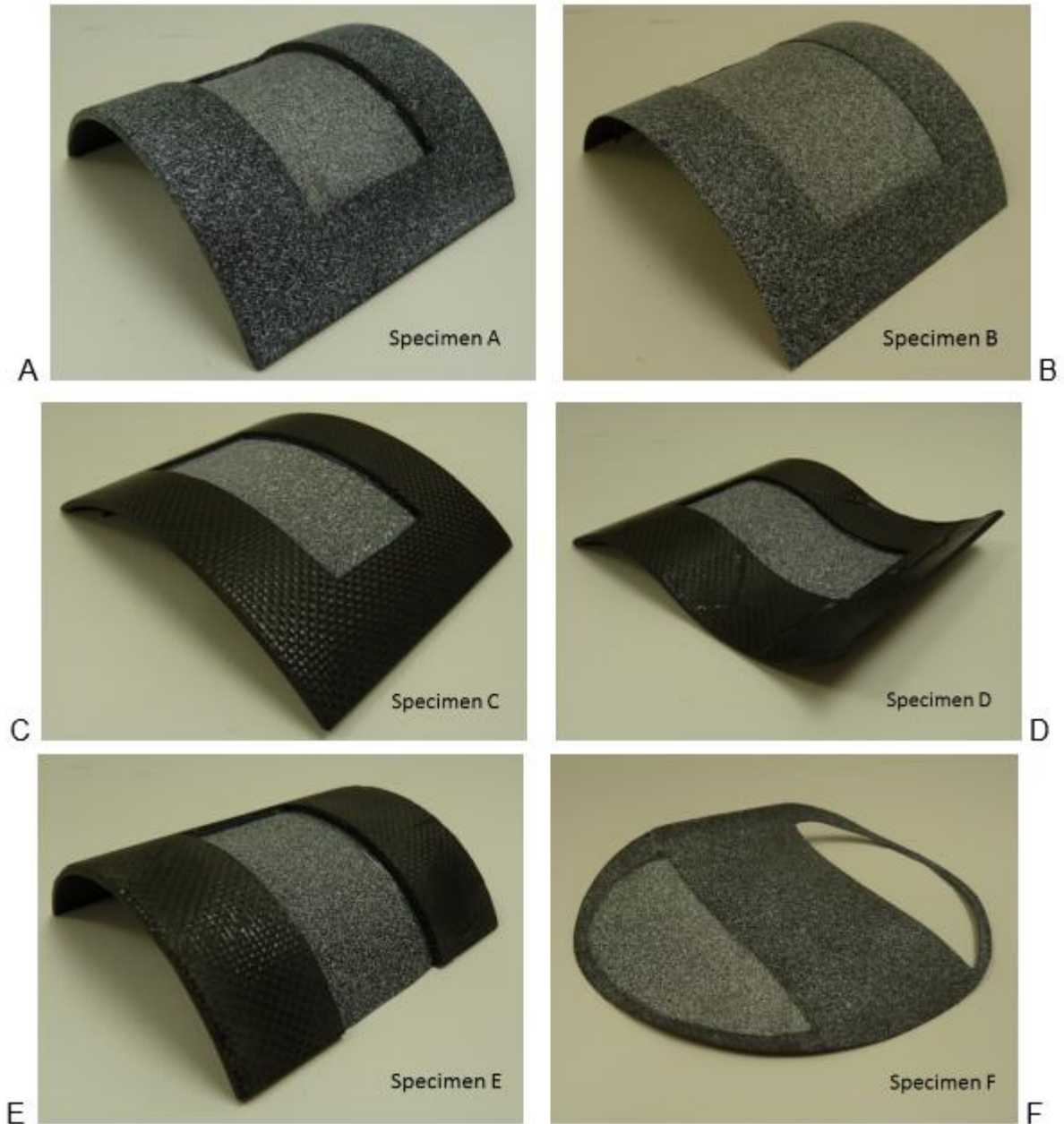


Figure 2-6. Six disparate curved specimens adhered to speckled silicone rubber membrane at appropriate temperatures A) Closed, R=63.5mm curved, 15 layer sample attached at 100 °C B) Closed, R=63.5mm curved, 2 layer sample attached at 100 °C C) Closed, R=127mm curved, 15 layer sample attached at 140 °C D) Closed, R=63.5mm doubly curved, 15 layer sample attached at 140 °C E) Open, R=63.5mm curved, 15 layer sample attached at 100 °C F) Perimeter reinforced 2 layer MAV wing sample attached at 100 °C.

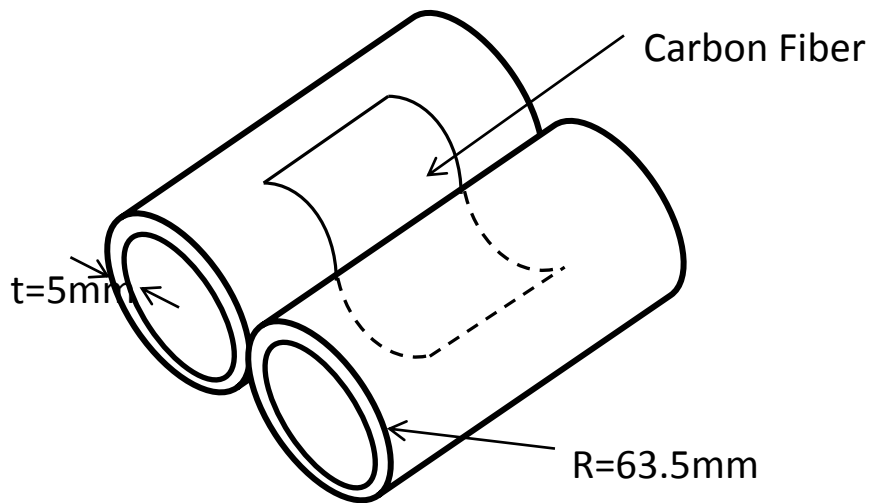


Figure 2-7. Doubly curved carbon fiber mold and frame lay-up.

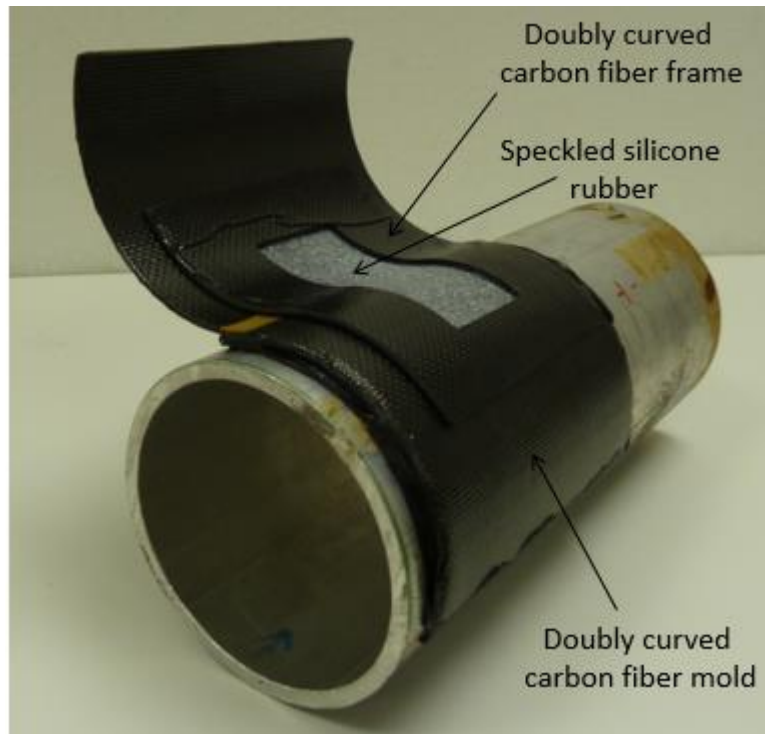


Figure 2-8. Cured doubly curved carbon fiber mold and frame when membrane is attached.



Figure 2-9. Silicone membrane laid to allow uniform expansion on the MAV wing mold.

CHAPTER 3
NUMERICAL MODELING AND EXPERIMENTAL VALIDATION FOR THERMAL
EXPANSION FABRICATION METHOD

Pre-tensioning Results for 2-D Frames

Experimental Validation

Two experiments were conducted to validate the experimental techniques that were employed in this work. Possible sources of error were the index of refraction change at the air between the hot plate and VIC cameras as well as non-uniformity of the temperature at the hot plate.

Images from a sample of black silicone rubber with a white speckling pattern were acquired via VIC system to plot the strain results against various temperatures from approximately 40°C to 200°C. The slope of the line was calculated to be $2.82 \cdot 10^{-4}/^{\circ}\text{C}$, which matches the handbook value of silicone rubber to the third significant figure (Figure 3-1). The standard deviation bars shown in the figure were from five consecutive experiments for each material. The infrared thermometer had a sensitivity of $\pm 1^{\circ}\text{C}$ between 10°C to 30°C and outside that range a sensitivity of $\pm 1.5^{\circ}\text{C}$, in which a 1.5°C of inaccurate reading would cause approximately 400 $\mu\epsilon$ error in the strain data. The VIC system's resolution was estimated to be 200 $\mu\epsilon$, and the non-uniform temperature distribution across the membrane caused $\pm 350\mu\epsilon$ variation. As reported in Figure 3-1 the standard deviation among five experiments increases with higher attachment temperatures, where the highest value was reported to be 250 $\mu\epsilon$ at 200°C, also indicating that the highest error was contributed by the infrared thermometer.

A second experiment involved the use of a 13cm by 13cm and 1.3cm thick Corning Co. ultra low expansion (ULE) glass. The glass was first painted black and then a random white speckling pattern was applied for tracking any potential deformations.

ULE glass was heated up to 160°C on the top speckled surface, which is the maximum temperature that can be achieved utilizing the hot plate. Figure 3-1 shows the data recorded along with zero slope value for the ULE glass specimen.

Open Cell

Strain results are given for a membrane attached at 140°C to an open cell with the inner dimensions of 2.5cm by 2.5cm in Figure 3-2 to Figure 3-4. Strains were computed with the increments of 20°C for this particular experiment. The average strains on each step were calculated and plotted. A similar procedure was repeated for the attachment at 100°C and 180°C. The stresses for the 140°C experiment were plotted using the strain values in both directions along with the experimentally computed elastic modulus and Poisson's ratio values.

Only the normal strain in the y-direction is reported in Figure 3-3. Darker areas, where slightly higher strain magnitudes observed at 140°C free expansion state may be an effect of the membrane not touching the surface of the hotplate at every single point (Figure 3-2 and Figure 3-3). Similar data is presented in Figure 3-4 for the shearing strain when the silicone membrane is attached at 140°C. The variation between the shearing strain values becomes more significant as the membrane approaches room temperature. The symmetry with respect to y-axis (zero shearing strain exactly in the middle tracing a straight line and same oval shape with different signs on the left and right side) clearly shows uniform membrane attachment.

At the 140°C free expansion state, reported average strain values are similar in both directions as can be seen in Figure 3-13. When the frame is attached on the membrane, a similar average strain is computed. The adhesive on the frame cures in approximately 1 second when in contact at this temperature; thereby, not giving ample

time for the membrane to cool down during the curing process. There is, however, a slightly lower average strain (less than 0.01%) when the membrane is attached at 140°C in comparison to free expansion. This could be a result of a slight cool down during the 1 second period. As the temperature decreases, the trailing edge of the frame starts moving in the positive y-direction. Finally at room temperature, negative values of strain are observed, which is due to the Poisson's effect. The membrane deformation is symmetric with respect to y-axis, which shows that the silicone is uniformly attached on the frame.

The same procedure was repeated five times to determine the margin of error and repeatability of the experiments; standard deviation bars are drawn in Figure 3-13. At 140°C the average strains in the x-and y-directions for free thermal expansion are computed to be within three significant figures of each other, which, once again, prove the repeatability due to temperature uniformity on the silicone membrane. The slight difference in two directions after attachment may be caused by the raw silicone (adhering agent) flow when the frame is pressed down. Average strain values in the y-direction decrease linearly during the cool down process due to the open geometry of the frame, which is not constricted at one end. Strain values in x-direction follow a similar trend following a horizontal line as the membrane movement is restricted in the x-direction.

The stress gradients seen on Figure 3-9 for normal and shear were achieved using Hooke's law for isotropic elasticity utilizing the previously calculated values for elastic modulus and Poisson's ratio, along with the strains that were computed by the VIC system. A more uniform stress distribution is perceptible in the x-direction

compared to the y-direction as the frame is constrained by the two legs of the frame; however, because the loop is open in the y-direction, more variation in strain is observed. The center line of the shearing stress image has no shearing stress while two extreme values ($\sim\pm 5.5\text{Kpa}$) are seen symmetrically on both sides.

Numerical Analysis for Open Cell

Since the experiments are proven to be repeatable, a numerical analysis using the commercially available software, Abaqus, was performed to show strain predictions can be made to simulate various scenarios. Quadrilateral shell elements with reduced integration (S4R elements), are used assuming the membrane expands uniformly in every direction. The silicone rubber should not be heated above the operating temperature range (Table 1-1), which enables the membrane to be thermally expanded up to only 5%. Linear finite element analysis (FEA) is used since the membrane expansion is in the linear region as shown in the experimental validation section (Figure 3-1). Three edges of the membrane are constrained by applying “Encastre ($U_1=U_2=U_3=UR_1=UR_2=UR_3=0$)” boundary condition. The membrane part seeded appropriately to achieve the fine mesh grid shown in Figure 3-7. Initial temperature is set to 140°C and the final temperature is modified to 25°C from the predefined fields in the software.

One of the disadvantages of using the VIC system is that the software has difficulty interpreting the results toward the specified boundary. Therefore, the data at the boundary are omitted from the experimental results in Figure 3-8. FEA predicts high magnitudes of strain concentrations at the open edge corners; however, this effect is not captured with the VIC due to the aforementioned limitation of the method. Numerical

and experimental data in both directions are in good correspondence within the region experiments are validated.

One of the disadvantages of using the VIC system is that the software has difficulty interpreting the results toward the specified boundary. Therefore, the data at the boundary are omitted from the experimental results in Figure 3-8. FEA predicts high magnitudes of strain concentrations at the open edge corners; however, this effect is not captured with the VIC due to the aforementioned limitation of the method. Numerical and experimental data in both directions are in good correspondence within the region experiments are validated.

VIC Results for Single and Multiple Cell Configurations

In support of an experimental investigation [50], to understand the physics of membrane aeroelasticity a number of wind tunnel test articles were fabricated using the method previously developed. For the membrane wings, silicone rubber was adhered to the rigid 7075-T6 2.0 mm thick aluminum frame. The frame had a span of 15.24 cm and a chord of 7.62 mm thus the AR is 2. The batten width was 3.8mm for all the models. The membrane cell depth was 80% of wing chord length. The cell span was varied according to the number of cell on the frame. The membrane wings are shown in Figure 3-9. Dimensions are listed in Table 3-1.

Table 3-1 also shows the average targeted and actual pre-strains recorded for all types of wings. The magnitudes slightly varied from one wing to another. The possible sources of error can be given as the non-uniformity of temperature distribution across the plate, fast cool down process during the attachment of aluminum frame on the silicone rubber film, and inaccurate temperature readings.

Table 3-1. The dimensions and pre-strains of the two sets of membrane wings

	1 Cell	2 Cell	3 Cell
Wing Chord (mm)	76.2	76.2	76.2
Wing Span (mm)	152.4	152.4	152.4
Cell Chord (mm)	61.0	61.0	61.0
Cell Span (mm)	144.8	70.5	45.7
Average Targeted Spanwise Pre-Strains	1.0%, 2.0%, 4.0%	1.0%, 2.0%, 4.0%	1.0%, 2.0%, 4.0%
Average Actual Spanwise Pre-Strains for Set #1	1.1%, 1.9%, 4.0%	1.0%, 2.1%, 3.9%	1.0%, 2.0%, 3.9%
Average Actual Spanwise Pre-Strains for Set #2	1.1%, 2.1%, 3.8%	1.0%, 2.0%, 3.8%	1.0%, 2.0%, 3.9%

Three different pre-strain levels (1%, 2% and 4%) were prescribed to each different frame geometry (cell aspect ratio) via a thermal skin technique explained in detail in Chapter 2. The pre-strain levels represent a spatially-average spanwise strain. The membrane was scalloped such that 15.2 mm was removed from the trailing edge. Scalloping the trailing-edge is thought to improve aerodynamic efficiency by decreasing drag.

Results in Figure 3-10 – Figure 3-12 show that magnitude of average pre-strain developed in the spanwise direction are independent of the aspect ratio as long as the attached temperature remains constant. Frame geometries with 1-cell, 2-cell, and 3-cell were attached at 60 °C, 105 °C, and 210 °C to accomplish 1%, 2%, and 4% strains, respectively. A 2.54cmX2.54cm frame also required the same temperatures to achieve the same corresponding spanwise strains.

Closed Cell

Another frame was constructed out of carbon fiber with the same inner dimensions of 2.5cm by 2.5cm in the form of a perimeter reinforced cell to be adhered on the

silicone membrane at 180°C. Strains are fairly uniform in both directions (Figure 3-13); however, slightly greater strains in the x-direction were observed in comparison to y-direction, which could be due to the different flow of adherent agent as mentioned in the open cell case. Strain magnitudes do not change significantly in both directions as the closed cell assembly is cooled down to room temperature. The variation of strain in x-direction could be explained by the aforementioned Poisson's effect. Initially, for all experiments a large amount of hysteresis was observed when comparing step 1 (free membrane at room temperature before attachment at higher temperatures) and step 11 (free membrane cut out after the entire experimental process.) This effect of hysteresis (about 0.5% strain) was greatly diminished by cooling and heating the silicone about 20 times before conducting the experiments.

The same procedure was conducted by attaching the silicone at 100°C and 180°C and each additional experiment was repeated three times. Then the specimen was allowed to cool down to room temperature and the average strain values on the surface were plotted as seen in Figure 3-13. The lines follow an almost linear trend, which allows one to adjust the temperature to achieve any desired tension up to approximately an average of 17kPa in the spanwise direction for the given geometry (Figure 3-14). Approximately zero shear stress is reported on the surface of the silicone rubber membrane, which proves the uniformity of stress distribution once again. As the temperature lowers from 180°C to 150°C, a small percentage of relaxation (approximately 0.15% strain) is analyzed; however, this effect is diminished as the temperature decreases toward the room temperature.

Pre-tensioning Results for 3-D Frames

Numerical Analysis

As mentioned in Chapter 2, the membrane is attached to an excessively thick carbon fiber frame to circumvent the effects of frame deformation on the silicone rubber membrane. Therefore, the boundary conditions were set to “Encastre ($U_1=U_2=U_3=UR_1=UR_2=UR_3=0$)” assuming zero displacement and rotation in the nodes that lie on the perimeter. This boundary condition was removed at the free edge for the open loop model. For all closed models, including the wing, M3D4R elements were used for the silicone rubber region, which is defined as “a 4-node quadrilateral membrane, reduced integration, and hourglass control” by the Abaqus program. Although the membrane elements work very similar to the shell elements, slightly closer strain results (in the order of approximately 0.001) were achieved by using the quadrilateral 3-D membrane elements with reduced integration (M3D4R elements) for the silicone rubber, though results did not converge for the open curved model. Subsequently, an attempt to address this issue to a dummy tensile stress was added at the free edge, which caused numerical singularities for a range of magnitudes. Therefore, the membrane elements were replaced with quadrilateral S4R shell elements for the 3-D open cell model. Mesh density of single and doubly curved models are shown in Figure 3-15.

The wing was partitioned into two sections: quadrilateral shell elements with reduced integration (S4R elements) were used with a high elastic modulus for the frame because the experiments showed minute strain changes on the 2-layer wing frame (Figure 3-26); M3D4R elements were used for the silicone rubber section as shown in

Figure 3-16. Fine element mesh of the assembly was achieved by setting the approximate global size to “1.0” when seeding the part.

Usage of membrane elements in Abaqus required the non-linear geometry option to be turned on for the analysis, although the membrane was stretched only within the linear region. Material coefficients were calculated by inputting the experimental stress-strain values for a hyperelastic material within the program by setting the energy potential according to Mooney-Rivlin principal. Additionally, silicone rubber is assumed to be isotropic, uniformly expanding with temperature in all directions.

Experimental Validation

Disparate curved carbon fiber frame structures were attached on silicone rubber membranes as thoroughly explained in Chapter 2. The data was transported to MATLAB: out-of-plane displacements were normalized with respect to the chord length (w/c), and strains in x-and y-directions (ϵ_{xx} and ϵ_{yy}) were analyzed along the spanwise and chordwise lengths. Plot comparisons between the experimental and the numerical results are discussed below:

Specimen-A

Figure 3-17 shows the measured displacement fields at room temperature (25°C) when attached at 100°C for the closed curved frame with a radius of 63.5mm. This indicates that the membrane skin strain is 1.7% at the instant of frame attachment according to Figure 3-1. This result is confirmed experimentally by comparing the initial image (free silicone rubber at room temperature on aluminum cylinder) to the free membrane at 100°C. The standard deviation bars are estimated statistically from 10 repeated experiments. Individual data sets showing the normalized out-of-plane

displacements and strains are also reported in Figure 3-18 and Figure 3-19. The error is reported to be higher toward the extreme ends which may have been due to a combination of two reasons: VIC system has difficulty analyzing the data toward the selected boundary and the excess adhesive at the edges affects the deformations and strains on the border lines. Note that the amount of excess adhesive varies from one sample to another. VIC software analyzes the data starting from approximately 1mm-3mm away from the selected boundary; therefore, some of the experimental data at the edge locations is missing in the figures. The peak standard deviation value recorded for displacements is 0.07mm, which is expected since the VIC system's resolution error is estimated to be 0.05mm [90]. Out-of-plane displacements for numerical and experimental outputs show good correspondence in terms of trend and magnitude, although numerical results slightly overestimate the displacements toward the ends in the spanwise direction. Overall membrane curvature is concave in the spanwise direction and convex in the chordwise direction; however, out-of-plane displacement magnitudes remain positive (into the curvature) for either direction when the membrane is cooled down to room temperature.

The highest standard deviations for strains in x-and y-directions are estimated to be 1300 $\mu\epsilon$ and 880 $\mu\epsilon$ respectively (Figure 3-20 through Figure 3-25), which may be caused by human error involved during the experiments. Strains are extremely sensitive to the attached temperature ($\pm 5^\circ\text{C}$ causes strain differences in the order of $\pm 1200 \mu\epsilon$ in the numerical simulation) and steadiness is required to prevent wrinkling due to slightly shifting the frame at the instant of attachment. Nevertheless, numerical model predicts the trends very well while the absolute strain magnitudes are slightly overestimated by

approximately 800 $\mu\epsilon$ from the average experimental strain values. Large strain gradients are present in both models along the left and right edges for ϵ_{xx} ; however they are not entirely visible in the experimental results. Also, the low y-strain magnitudes at the corners are not completely seen on the experimental model because the VIC system experiences difficulties in estimating the values closer to the edges of the area of interest as outlined by Stanford et al. [91].

Specimen-B

Another frame identical to the dimensions of Specimen-A is manufactured with the exception of thickness (built with only 2-layers of carbon fiber) to investigate the effect of frame stiffness on membrane deformations and strains. The frame and the membrane skin were analyzed separately since the VIC software detected too much noise on the border of the two materials. This is likely due to frame thickness and/or slight adhesive overflow. The two images are then superimposed to output the data as shown in Figure 3-26. Results reported prove that the frame does not bend considerably to affect the membrane strains. Developed strains within the silicone rubber skin at room temperature in the x-and y-directions are similar to the ones shown in Figure 3-20 and Figure 3-23 showing that the two layer configuration was equivalent to a rigid frame.

Specimen-C

To further confirm the numerical predictions another solid carbon-fiber frame (Figure 2-6C) with a different curvature ($R=127\text{mm}$) attached at a higher temperature (140°C) is analyzed in a similar manner as shown in Figure 3-27 through Figure 3-29 . The experiment was repeated only 3 times, and the best fitting data set is reported in the figures with the same error bars that are carried over from the first curved

membrane analysis. Out-of-plane displacements are in agreement both in terms of trend and magnitude; however, once again, the trend line slightly deviates toward the leading and trailing edges in the chordwise direction. The maximum deviation is 0.08mm, which may have been affected by the excess adhesive and the fabrication procedure. Note that the peak displacement dropped in comparison to the results shown in Figure 3-17 due to the increase in curvature causing the membrane to follow a straighter path.

The silicone rubber film was stretched up to 2.85% uniformly when attached to the frame at 140°C. Strain values developed at room temperature in the y-direction range between 2.7% to 3.5%, and strains in x-direction vary throughout the membrane from 1.6% to 2.8%. Once again, the experiment validates the accuracy of the numerical model for strains in either direction.

Specimen-D

The out-of-plane displacement magnitude/gradient results for the doubly curved frame are symmetrical with respect to the chordwise line while they were equal and in opposite directions with respect to the spanwise line as shown in Figure 3-30. Experimental results in chordwise direction match well although a slight shift is observed after the midpoint in the plot. Numerical results predict a line, where zero displacements exist along the span in the middle, which is theoretically correct; however, this condition is not fully satisfied experimentally anywhere in between the upper and lower halves of the specimen. This may be due to some manufacturing errors in the frame and/or human errors explained for in Specimen-A during attachment. Nevertheless, both numerical and experimental plots in terms of out-of-plane displacement gradients show good correspondence.

The model is very successful in estimating the strains in y-direction that range from approximately 1.8% up to 3.6% (Figure 3-31). As expected, lower strain values (0.7% -2.8%) are observed in the chordwise direction, where concavity is prevalent (Figure 3-32). The membrane, naturally, tries to find the shortest path between its constrained ends and slacks along the curve. The shortest path is obviously a straight line; however, the strains x-direction also affect the magnitude in the y-direction due to Poisson's effect; therefore, keeping a convex path.

Specimen-E

To mimic an exaggerated cell in a batten reinforced wing shown in Figure 1-1B, an open end version of Specimen-A was created (Figure 2-6E). The membrane was allowed to thermally expand up to 100°C and attached to the frame. A shift of the peak out-of-plane displacement from the half chord position to 70% length toward the leading edge (the upper edge where the membrane is constrained) is clearly evident from Figure 3-33 while the magnitude of the peak value remains approximately the same when compared to Specimen-A results. The numerical model predicts negative values at the open end indicating the membrane curvature changes from concave to convex toward the trailing edge. This effect is not proven experimentally as the VIC system has difficulty analyzing the data at the open end. All erroneous values at the edges are removed from the experimental results shown in Figure 3-33 through Figure 3-35, since VIC software has difficulty measuring the data closer to the boundary. Out-of-plane displacements from the experimental output clearly validate the Abaqus simulations for the open loop configuration.

Strain data shown in Figure 3-34 and Figure 3-35 along the spanwise and chordwise directions pass through the peak location of out-of-plane displacements also.

The high strain values observed at the open corner of numerical model are not captured by the VIC system; however, the strain gradient toward the open corner in the experimental model indicates this prediction is mostly likely accurate. Chordwise experimental ϵ_{yy} values follow a slightly more negative slope in comparison to the numerical prediction, which estimates a constant 2.4% strain in the mid-section of membrane (Figure 3-34). Spanwise ϵ_{yy} values slightly increase toward the edges, but at various locations of the image this effect is muted.

Chordwise experimental ϵ_{xx} data agree with the numerical model up to 40% along the line, and after that point, VIC detects that the strain values keep increasing linearly up to the leading edge location. The spanwise strains in the x-direction are well predicted by the numerical model.

Pre-tensioning Results for Perimeter Reinforced Wings

Actual perimeter reinforced wings described in Chapter 2 are analyzed utilizing the previously used techniques for two complex real life scenarios, where the complexity comes from the wing topology: The membrane was allowed to freely expand over a hot surface prior to applying the frame. The results are then verified with numerical analysis.

As mentioned in the numerical analysis section, the carbon fiber frame was assumed to be rigid enough to withstand the tensile forces of the thin membrane. The frame was speckled to confirm that the deformations and strains are insignificant in comparison to the silicone membrane; however, VIC software had extreme difficulty calculating the strains in the thinner areas. This problem could have been overcome by

using higher resolution cameras or focusing the imaging sensors on the smaller portions of the wing, but the assumption produced well predicted results.

Out-of-plane displacements from the numerical analysis and the experimental data are in good correspondence (Figure 3-36). At the extreme locations an insignificant amount of deviation is observed as seen in some of the other 3-D specimens. Two extremes of maximum out-of-plane displacements are observed in the camber and reflex, in which the absolute values were observed to be 0.01 and 0.004 respectively. Displacement magnitude was much higher toward the leading edge since the camber of the wing was much higher than the reflex (camber=6.8% and reflex= -1.4%).

Both models agree that strains in y-direction within the membrane vary from 1.6% to 1.9%; however, in the experimental data the strain gradients are different at various locations (Figure 3-37.) The greatest source of experimental error is the inability of silicone rubber film forming into the shape of the mold topology, meaning the membrane might not have been contacting the mold surface at every point. Magnitude and gradient of chordwise strains (Figure 3-38) agree well although lower magnitudes of strains (in the order of 0.3%) are reported closer to the leading edge, which may be due to experimental errors contributed by the attachment temperature, aforementioned contact issue, and human error during attachment. As the numerical and experimental strain gradients are calculated to be very similar, only the non-linear finite element stress results are reported in Figure 3-39 and Figure 3-40. Membrane stresses in both directions vary between 17kPa and 21kPa while zero stresses are shown on the frame as this part of the assembly is assumed rigid in the calculations.

Silicone Rubber Membrane Relaxation Test Results

After preparing similar wings shown in the VIC Results for Single and Multiple Configuration Section, the specimens were subjected to extensive wind tunnel experiments (approximately 100 cycles) for two months. Figure 3-41 shows the relaxation of silicone rubber membrane in the mid-cell of a 5- celled wing after the experiments were conducted by Zhang Zheng [92]. A decrease of about 0.5% strain is observed in the x-direction as higher magnitudes of strain are developed in the restricted direction. However, the relaxation is not as significant for the y-direction and shear, and the amount of strain developed in these directions even before testing are relatively very low. When compared to latex rubber, these minor relaxation results show the value of the attachment techniques using silicone rubber membranes.

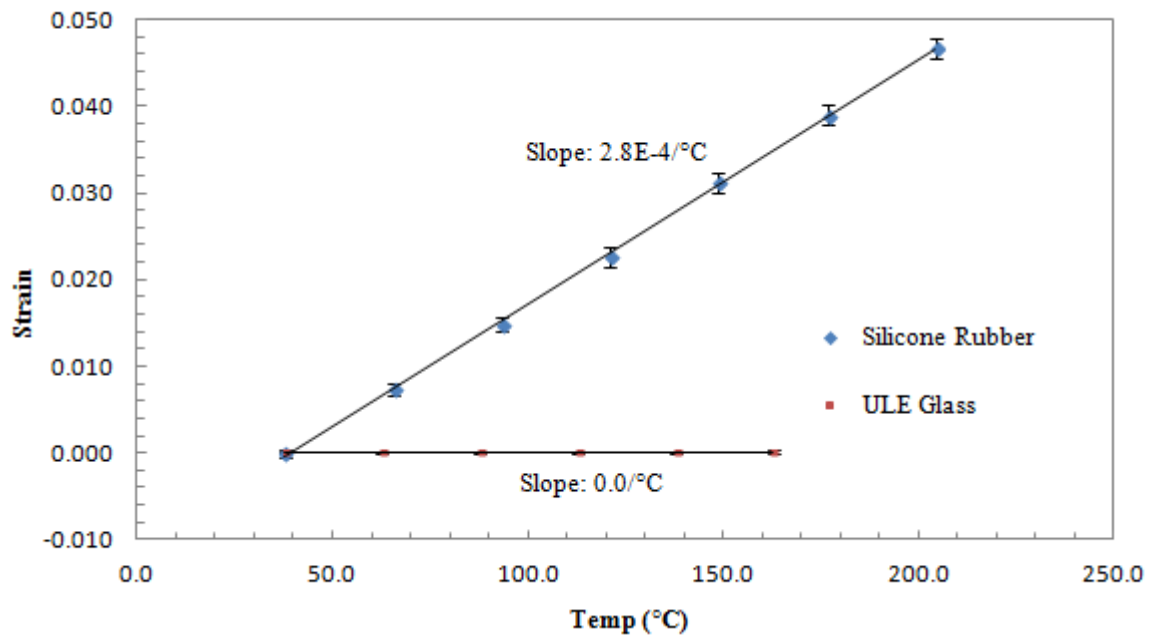


Figure 3-1. Strain vs. temperature plot for silicone rubber and ULE Glass.

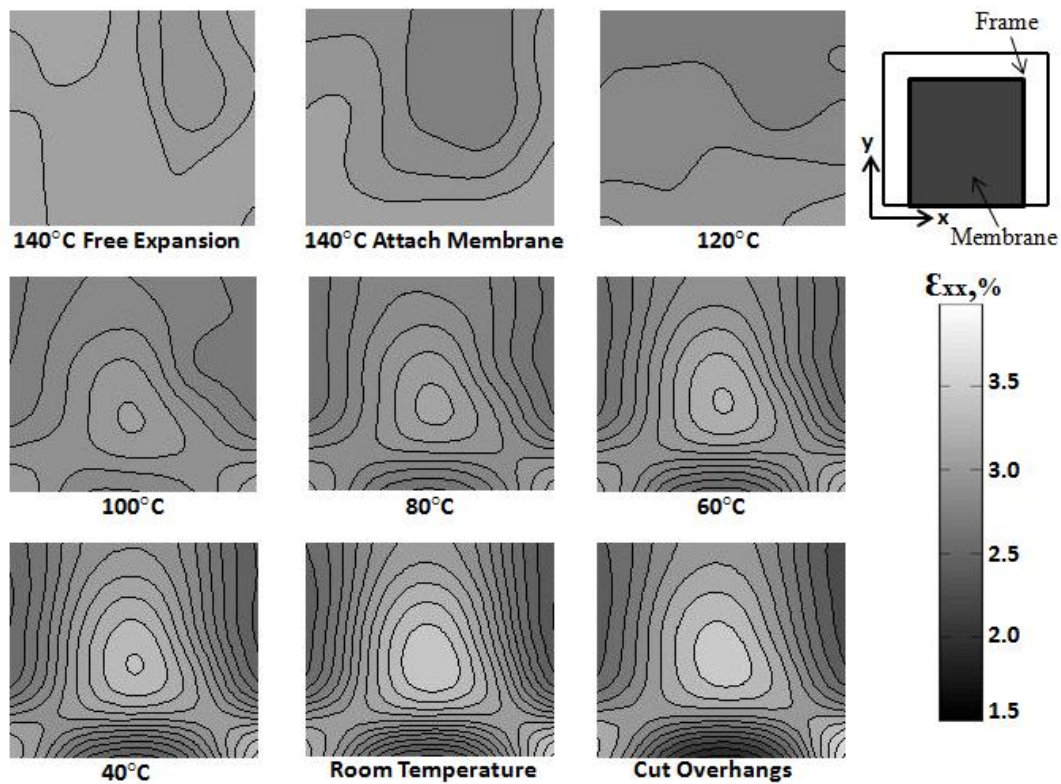


Figure 3-2. Normal strain in x-direction when attached at 140°C for the open cell model.

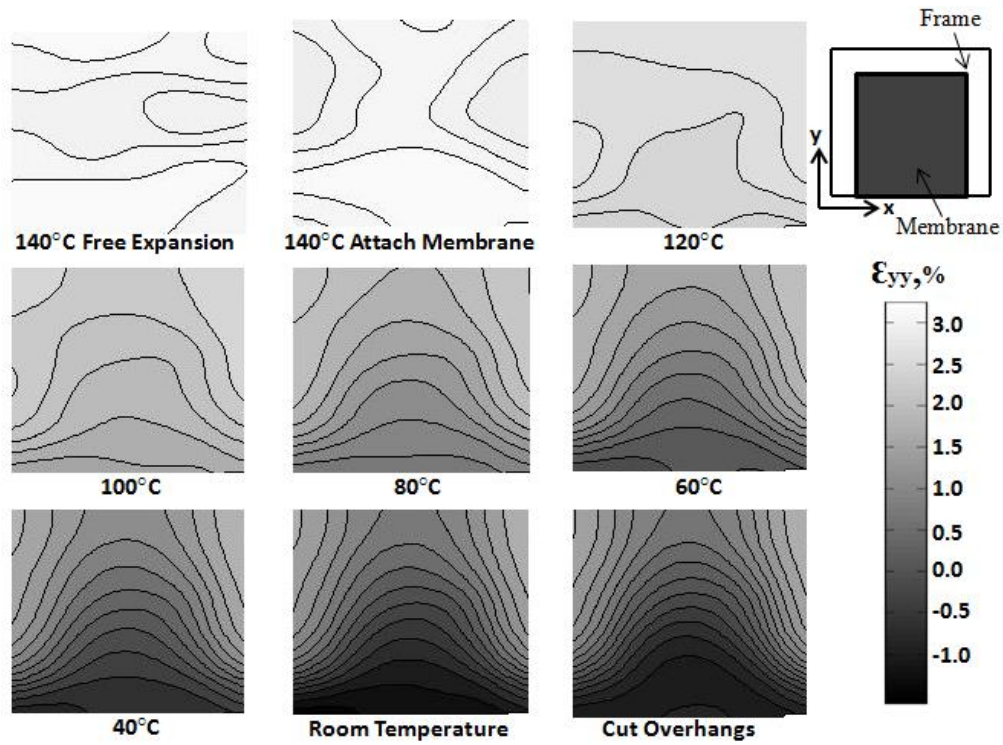


Figure 3-3. Normal strain in y-direction when attached at 140°C for the open cell model.

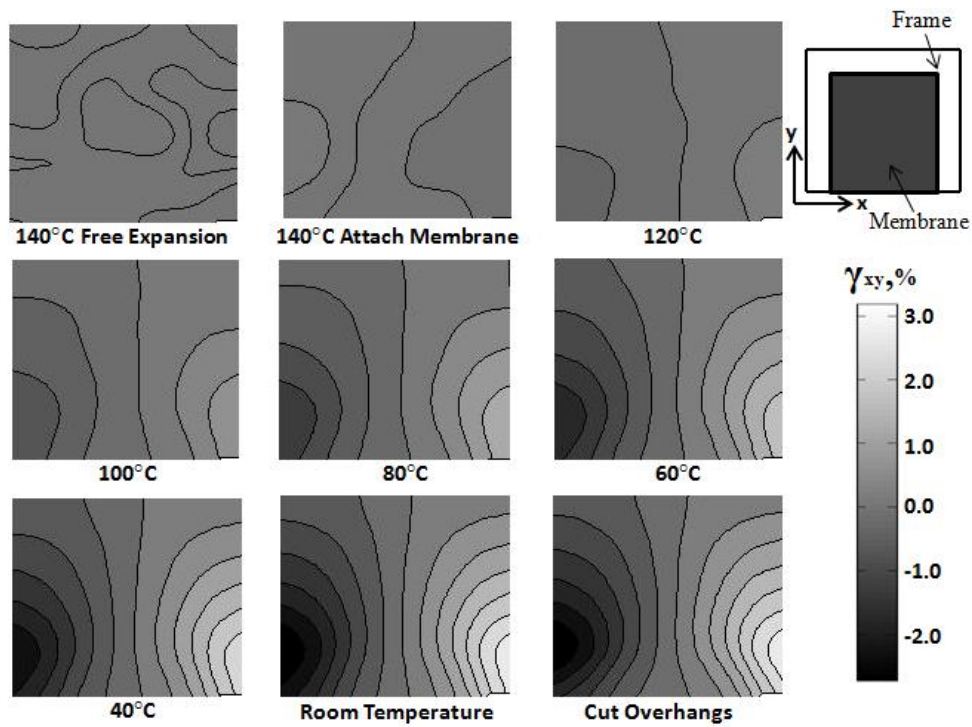


Figure 3-4. Shearing Strain when attached at 140°C for the open cell model.

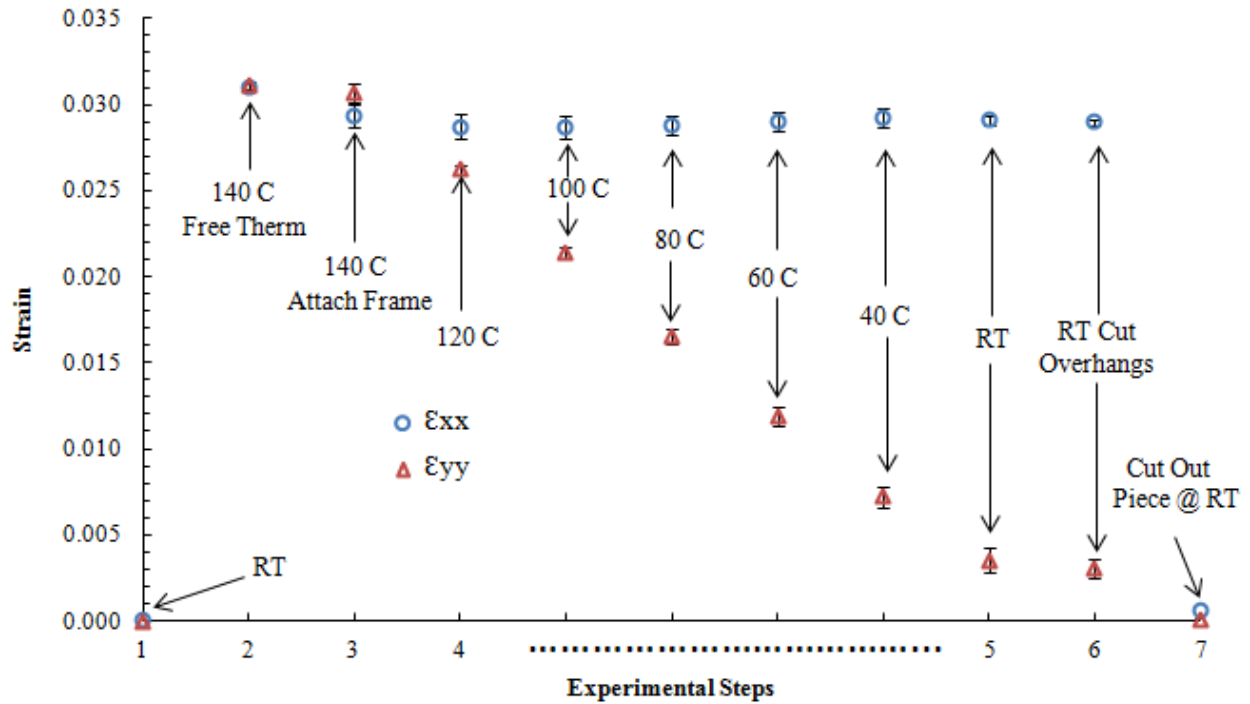


Figure 3-5. Strain versus experimental steps plot when attached at 140°C for open cell model.

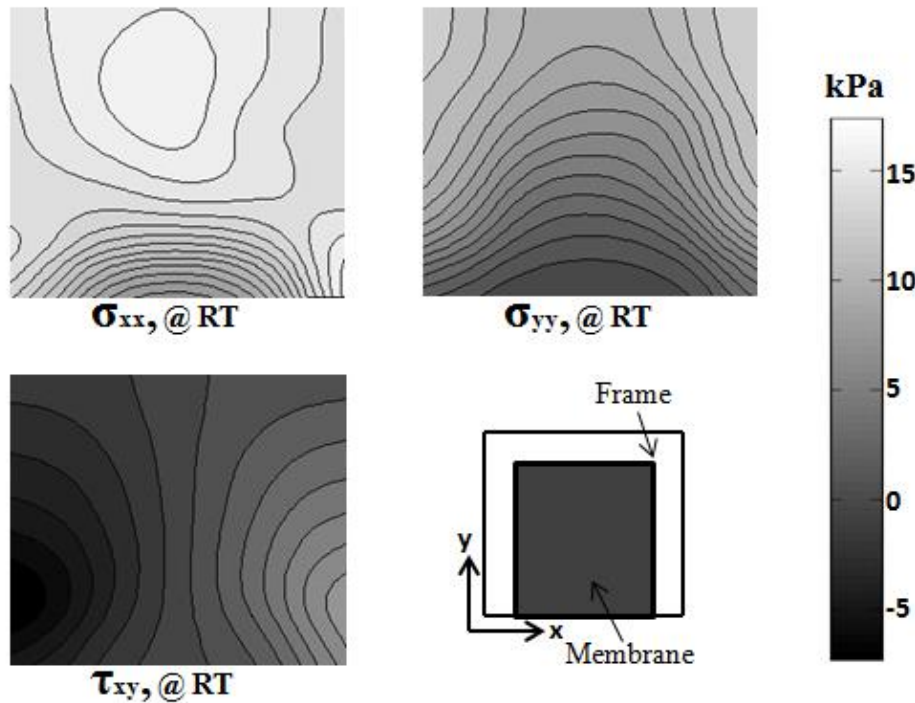


Figure 3-6. Stress plots in x-and y-direction along with shearing stress at room temperature for open cell when attached at 140°C.

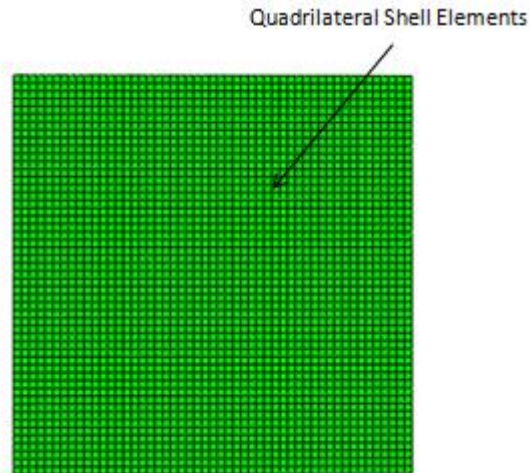


Figure 3-7. Abaqus mesh density created for the numerical analysis of planar cases.

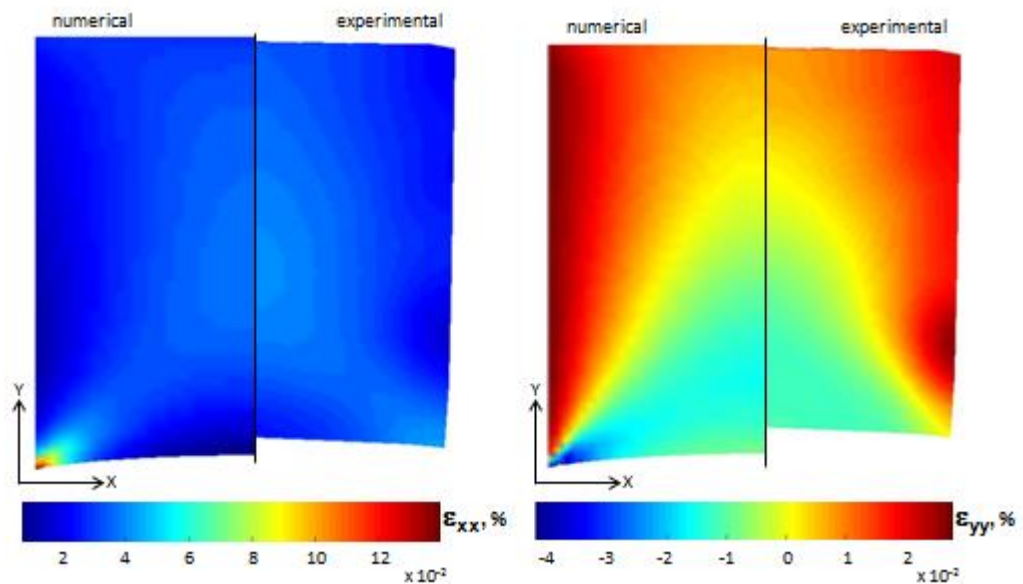


Figure 3-8. Numerical simulation and experimental results comparison for strains in x- and y-directions when the membrane is attached at 140°C.

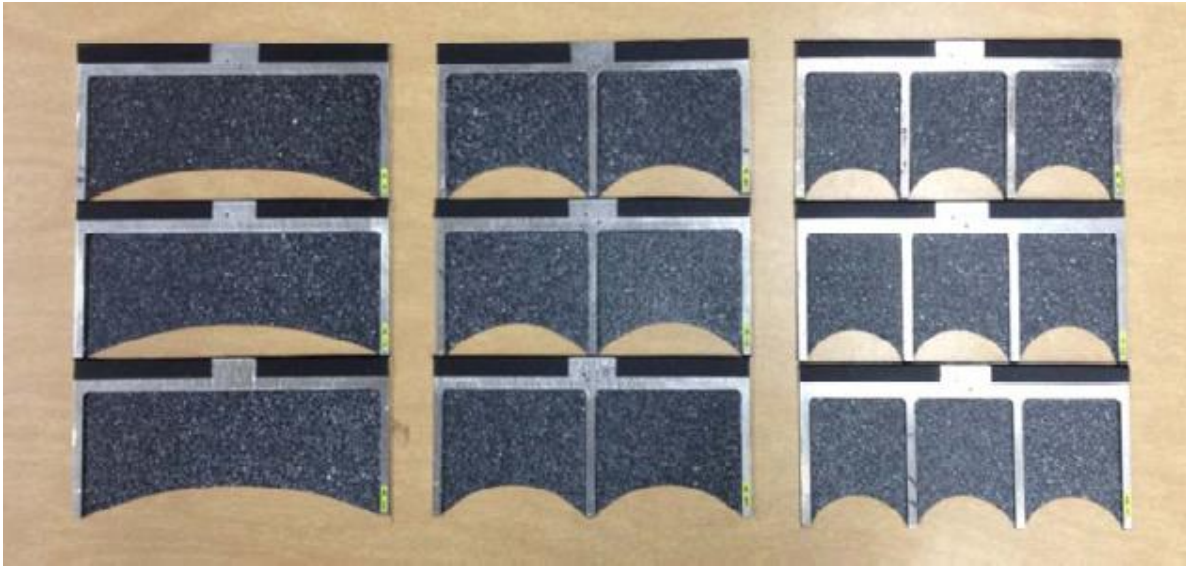


Figure 3-9. Membrane wing models of one, two and three cells (left to right) with targeted pre-strains of 1%, 2% and 4% (bottom to top).

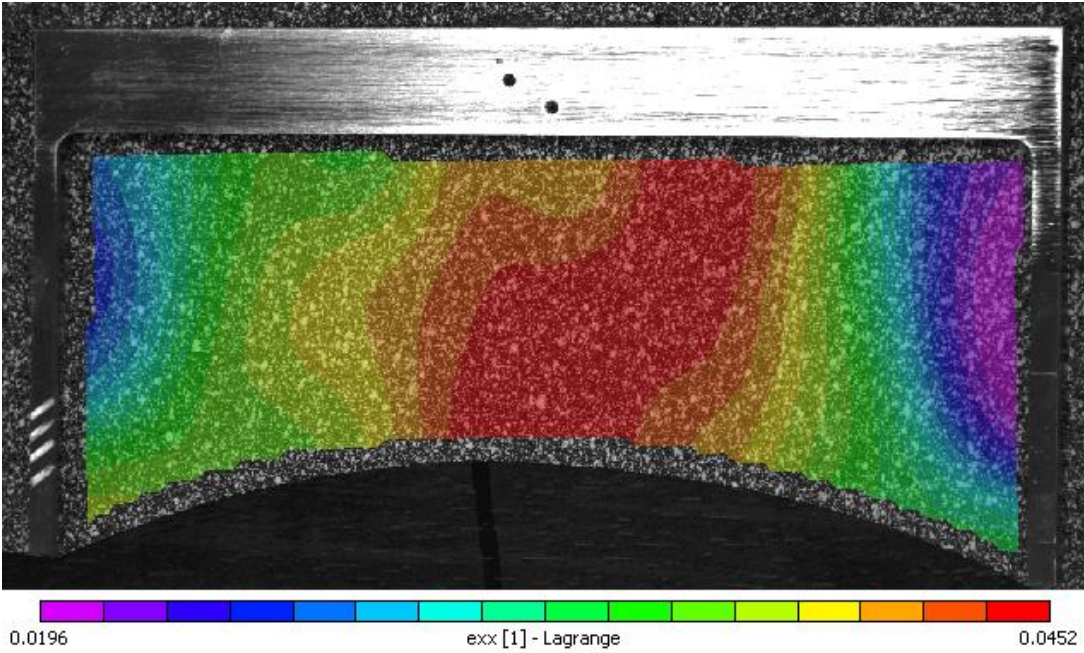


Figure 3-10. VIC result for 4% pre-strained 1-cell configuration attached at 210°C.

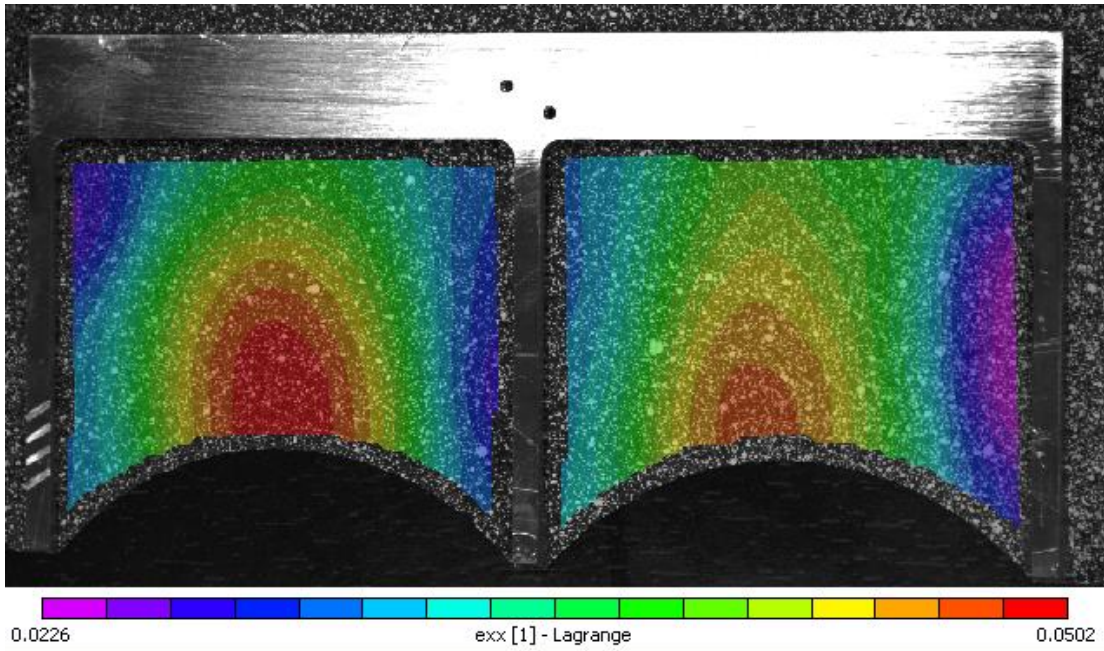


Figure 3-11. VIC result for 4% pre-strained 2-cell configuration attached at 210°C.

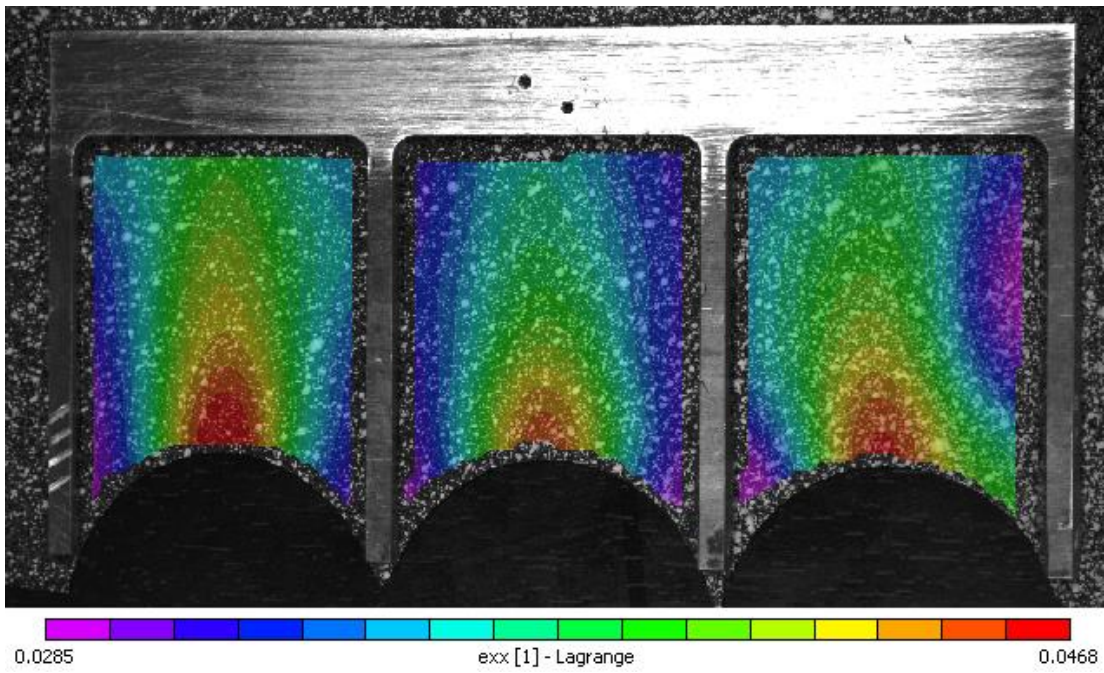


Figure 3-12. VIC result for 4% pre-strained 3-cell configuration attached at 210°C.

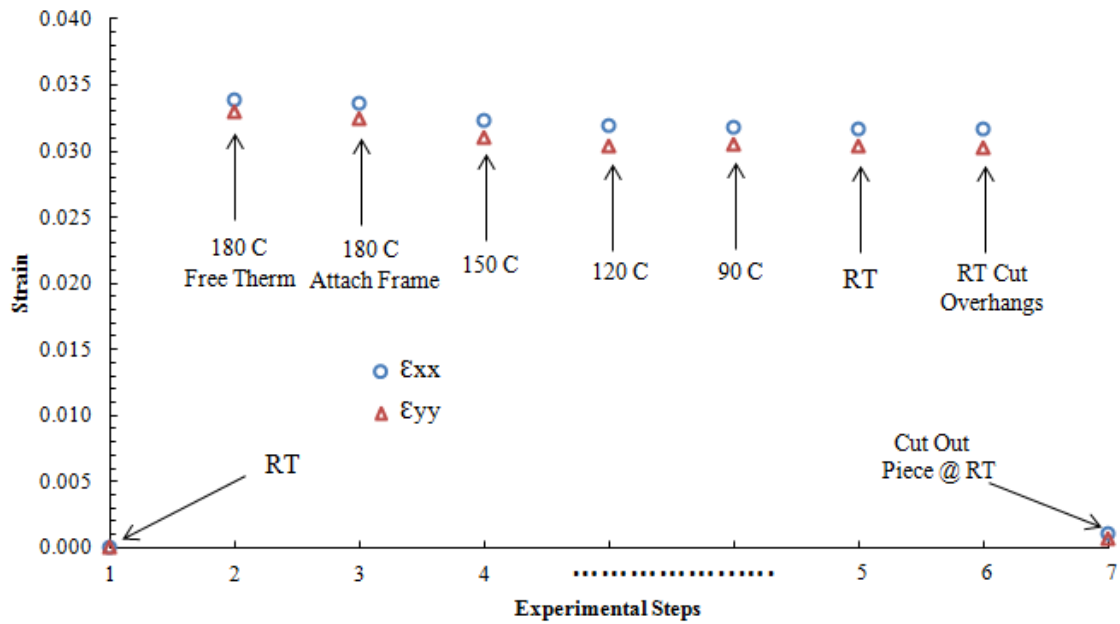


Figure 3-13. Strain versus experimental steps plot when attached at 180°C for closed cell model.

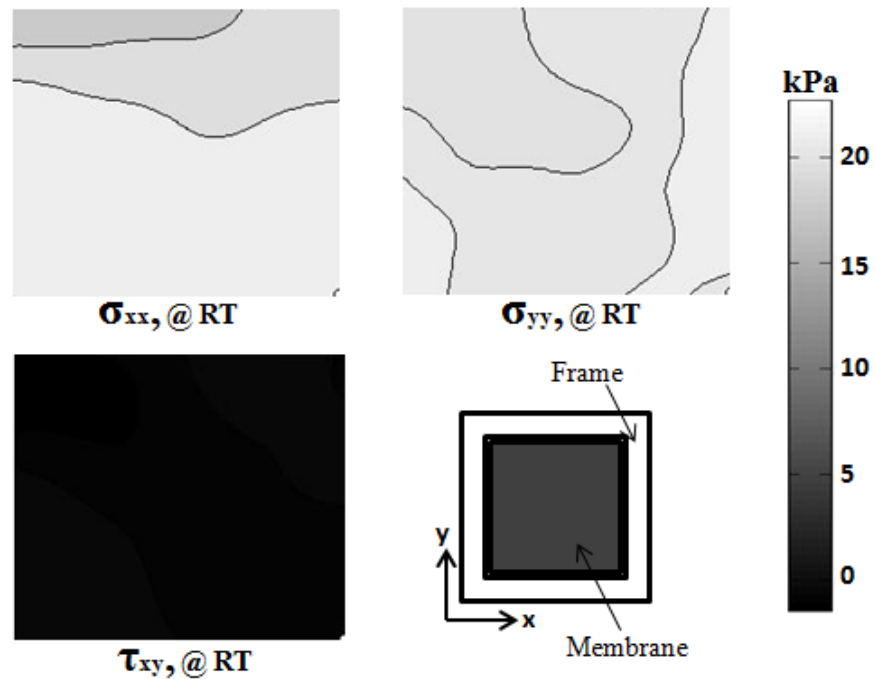


Figure 3-14. Stress plots in x-and y-direction along with shearing stress at room temperature for closed cell when attached at 180°C.

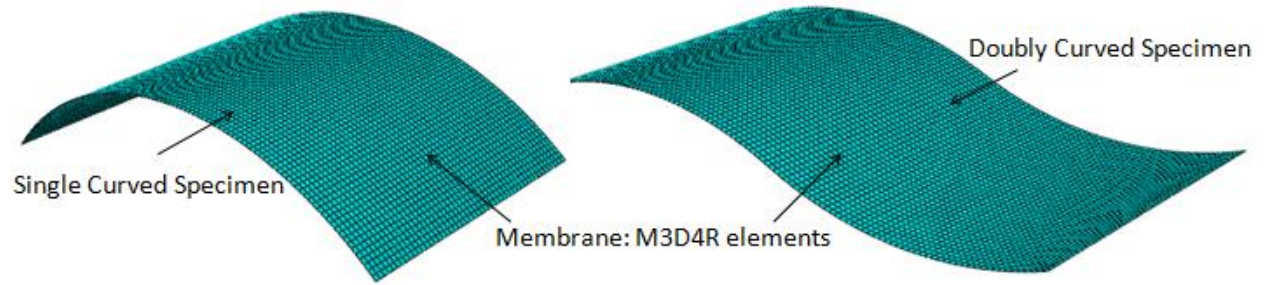


Figure 3-15. Abaqus mesh created for the numerical analysis of 3-D specimens.

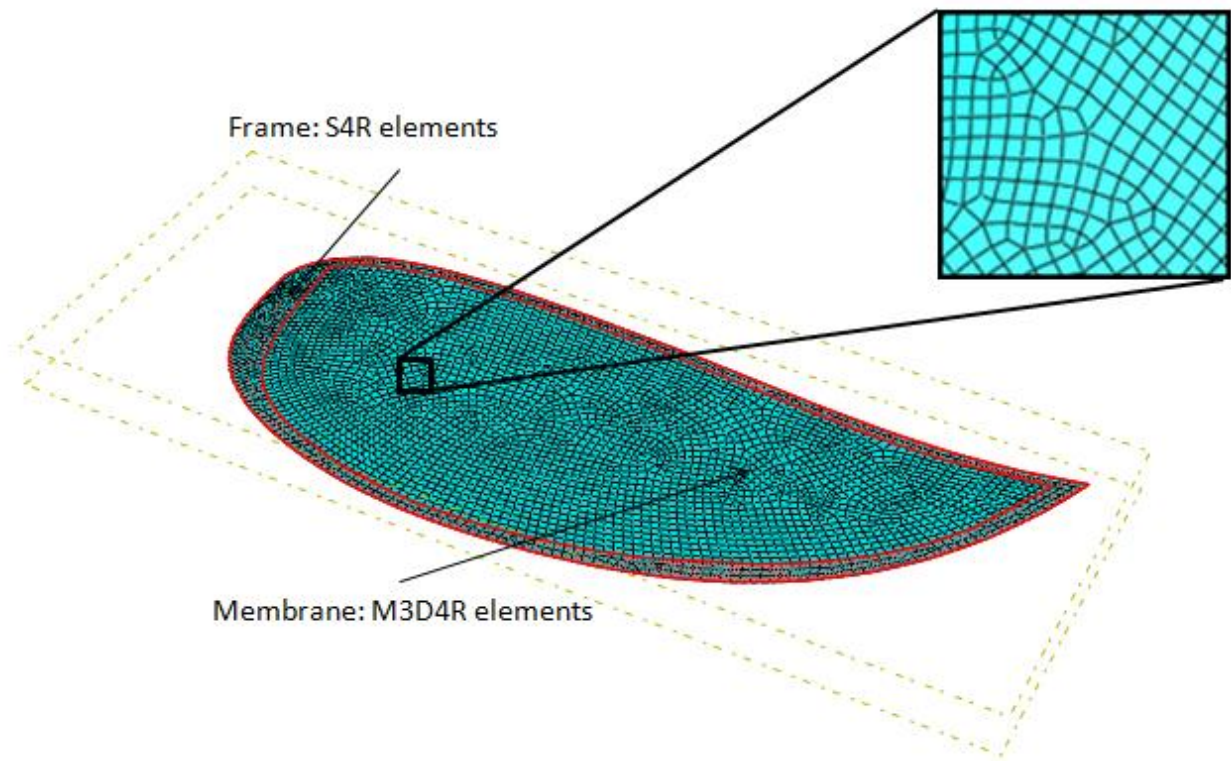


Figure 3-16. Abaqus mesh density created for the numerical analysis of MAV wings.

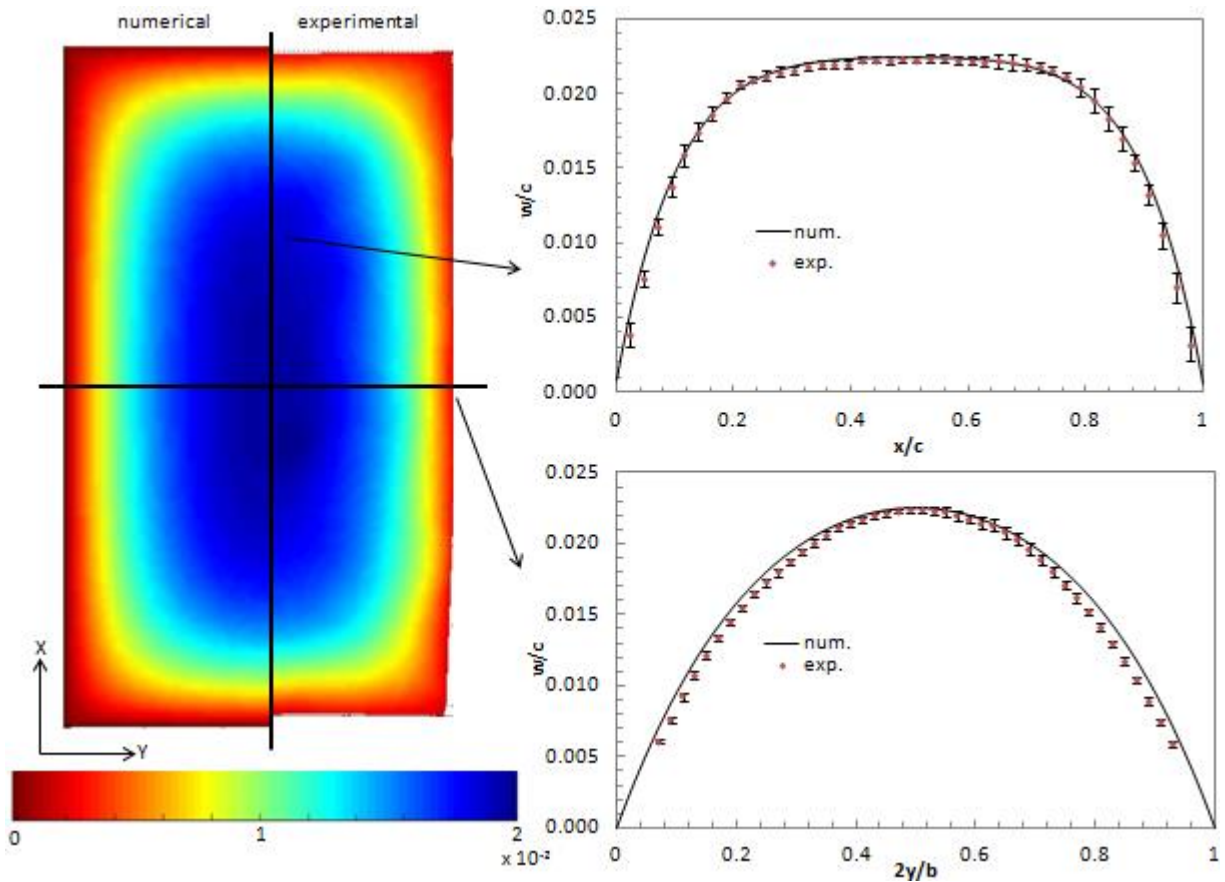


Figure 3-17. Normalized out-of-plane displacements for the 15-layer curved closed cell; $R=63.5\text{mm}$ when attached at 100°C .

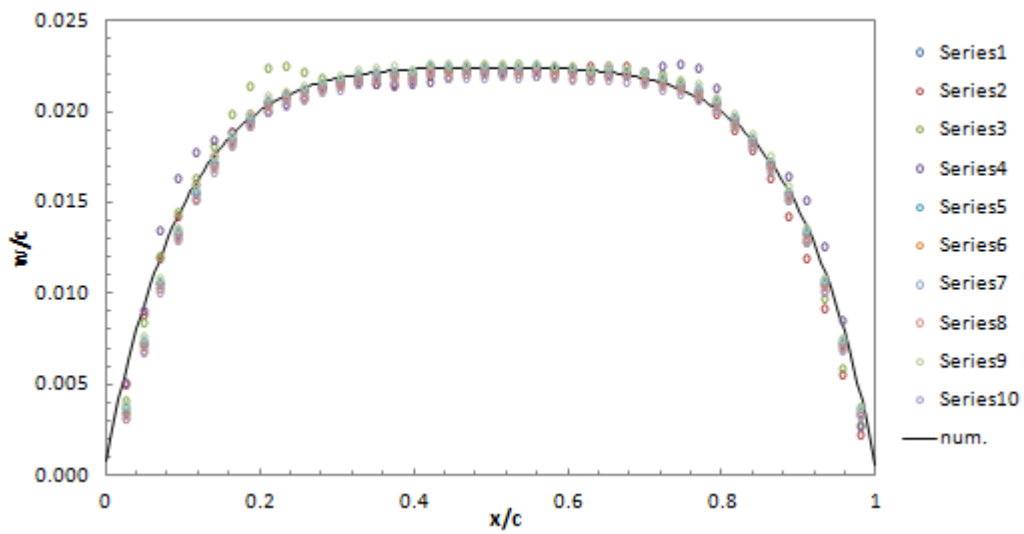


Figure 3-18. Data from 10 specimens for normalized transverse displacements along the chordwise direction compared to numerical results.

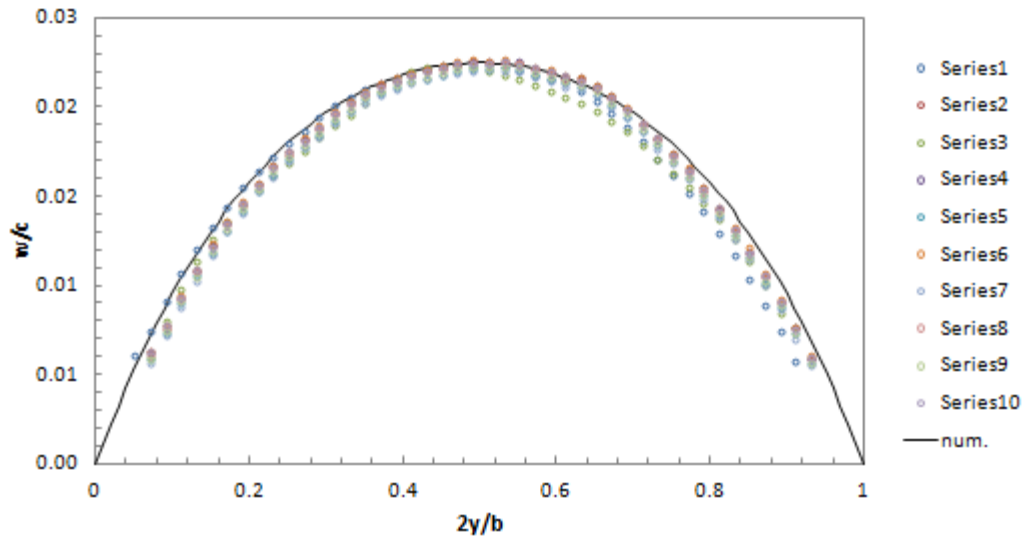


Figure 3-19. Data from 10 specimens for normalized transverse displacements along the spanwise direction compared to numerical results.

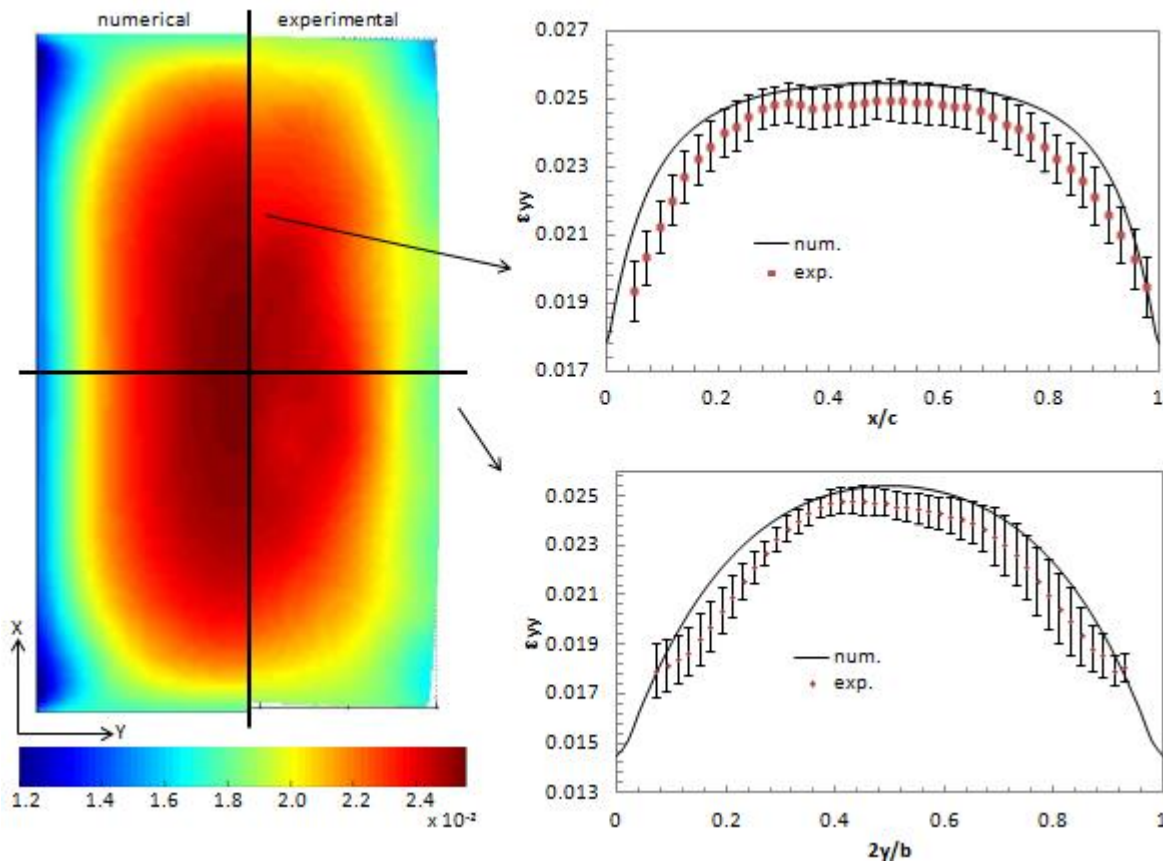


Figure 3-20. Strains in y-direction for the 15-layer curved closed cell; $R=63.5\text{mm}$ when attached at 100°C .

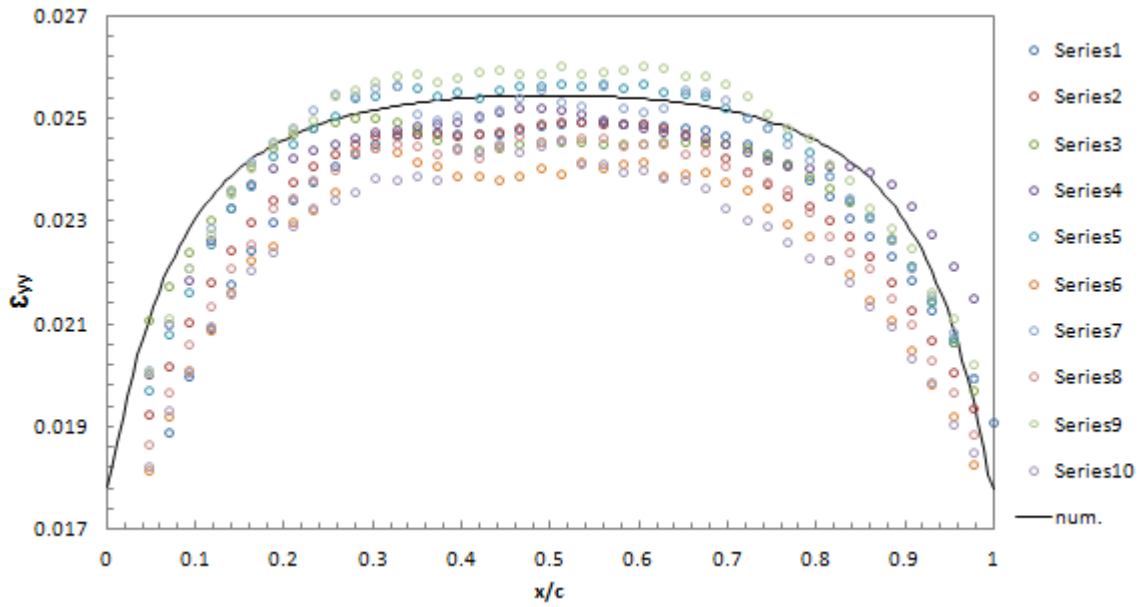


Figure 3-21. Data from 10 specimens for spanwise strains compared to numerical results along the chordwise direction.

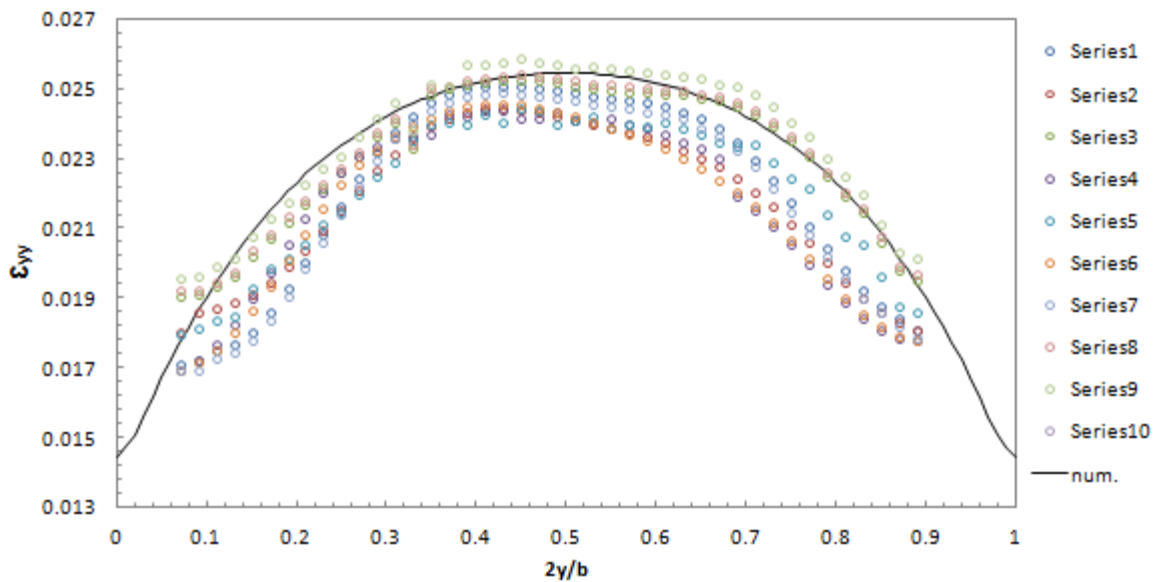


Figure 3-22. Data from 10 specimens for spanwise strains compared to numerical results along the spanwise direction.

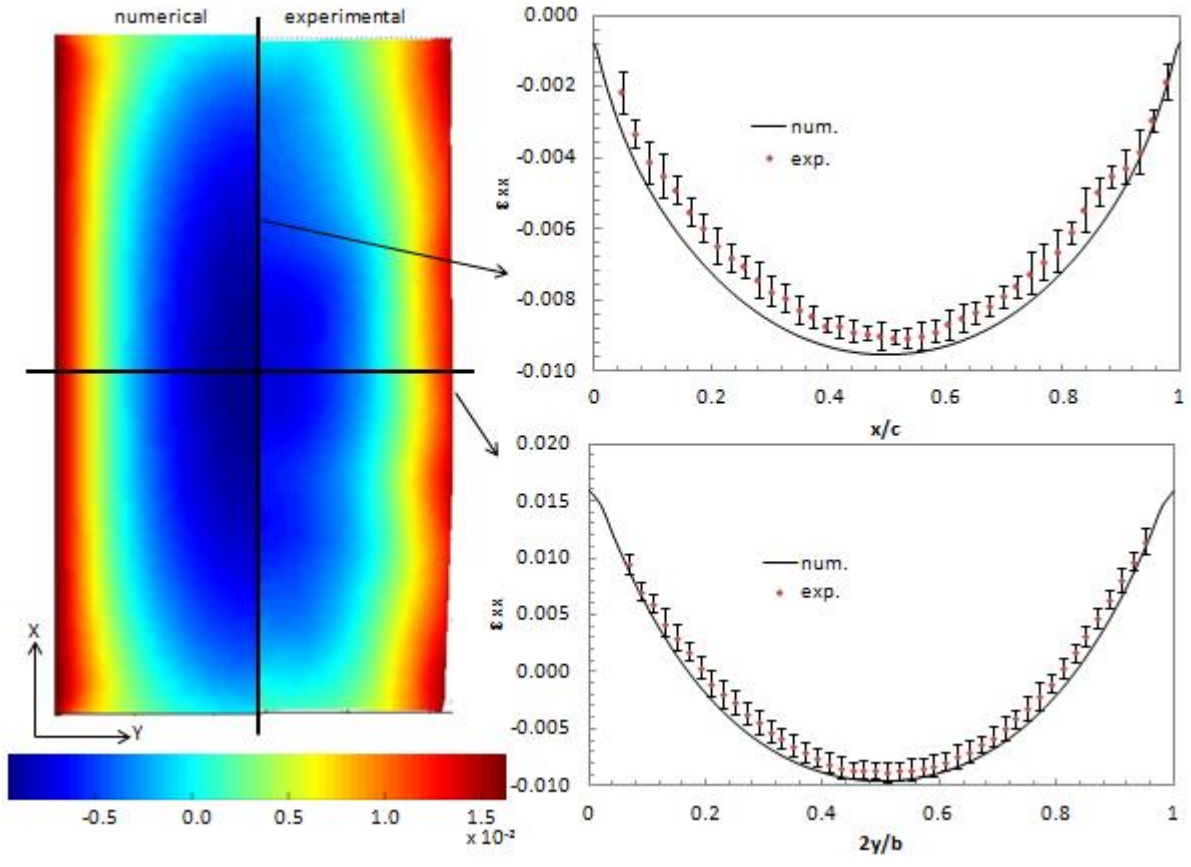


Figure 3-23. Strains in x-direction for the 15-layer curved closed cell; $R=63.5\text{mm}$ when attached at 100°C .

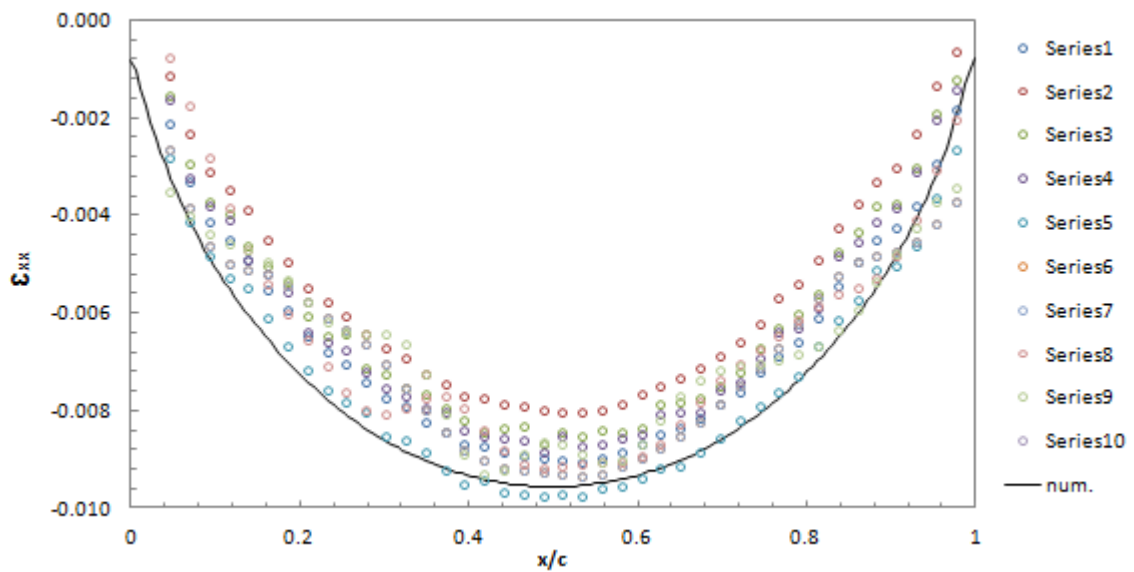


Figure 3-24. Data from 10 specimens for chordwise strains compared to numerical results along the chordwise direction.

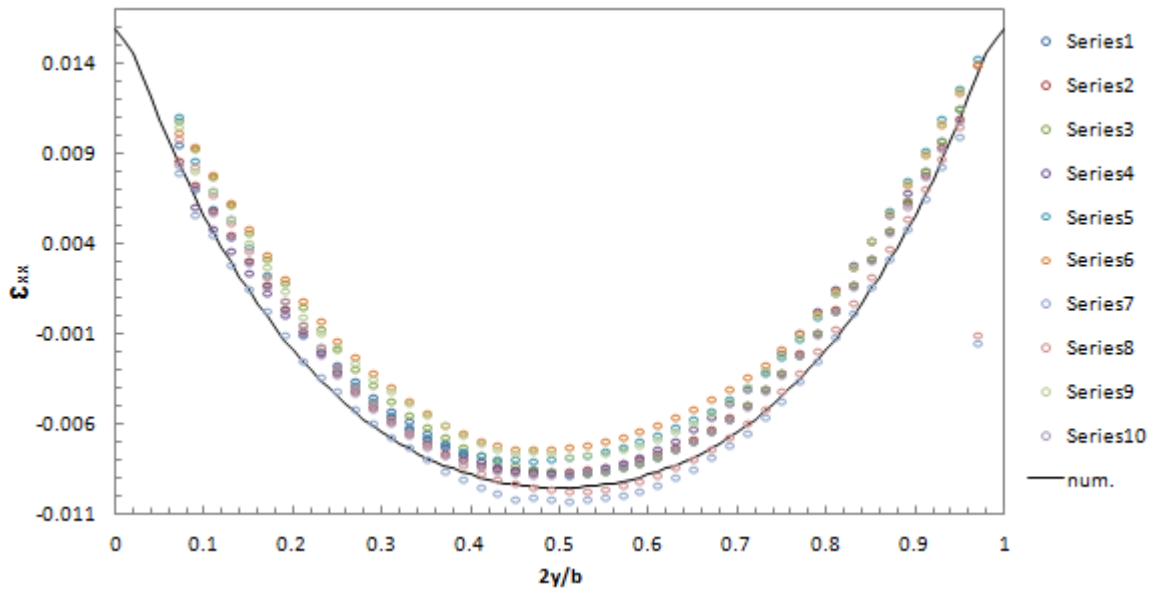


Figure 3-25. Data from 10 specimens for chordwise strains compared to numerical results along the spanwise direction.

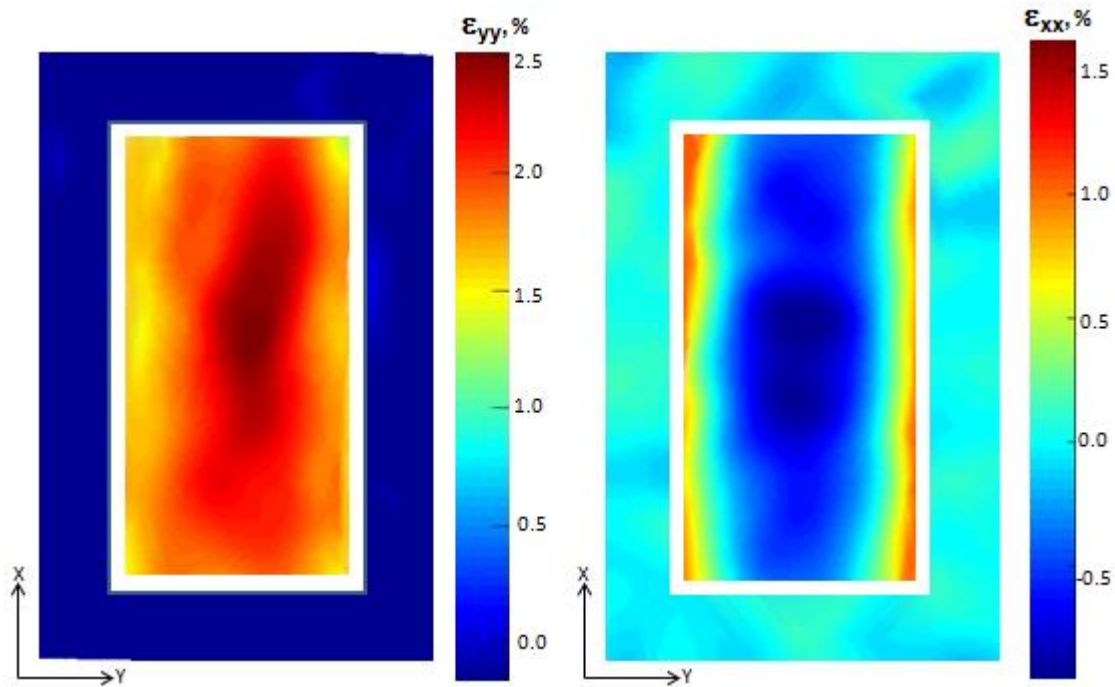


Figure 3-26. VIC results for strains in x-and y-directions for the 2-layer curved closed cell; R=63.5mm when attached at 100°C.

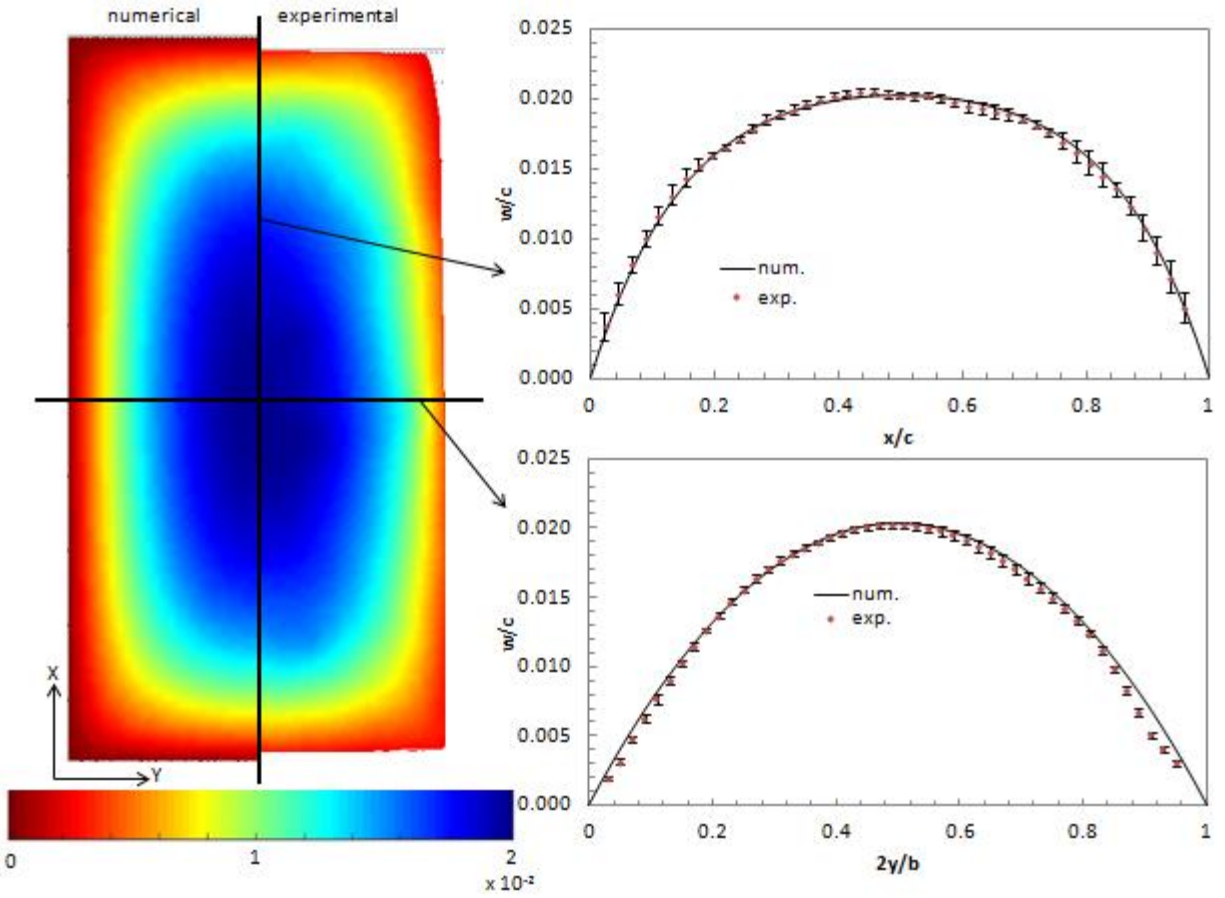


Figure 3-27. Normalized out-of-plane displacements for the 15-layer curved closed cell; $R=127\text{mm}$ when attached at 140°C .

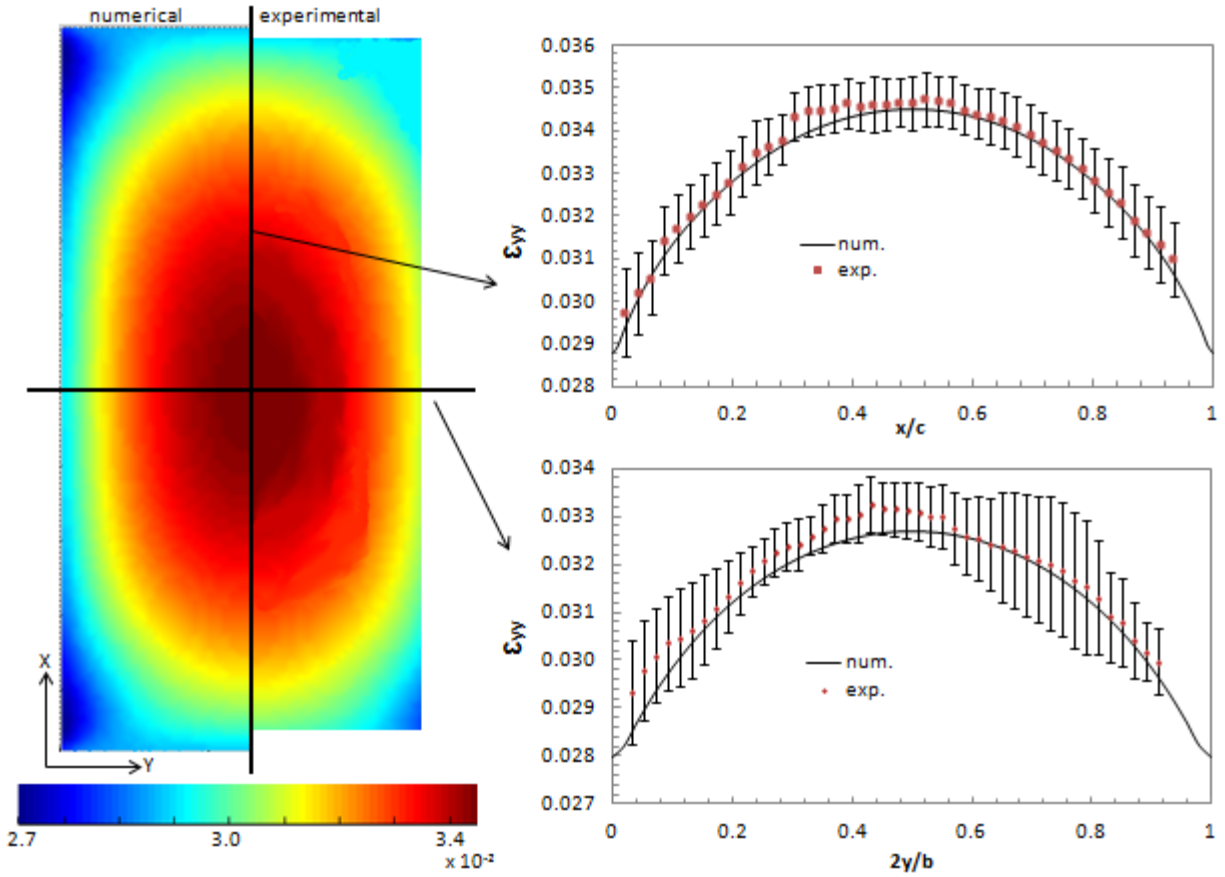


Figure 3-28. Strains in y-direction for the 15-layer curved closed cell; $R=127\text{mm}$ when attached at 140°C .

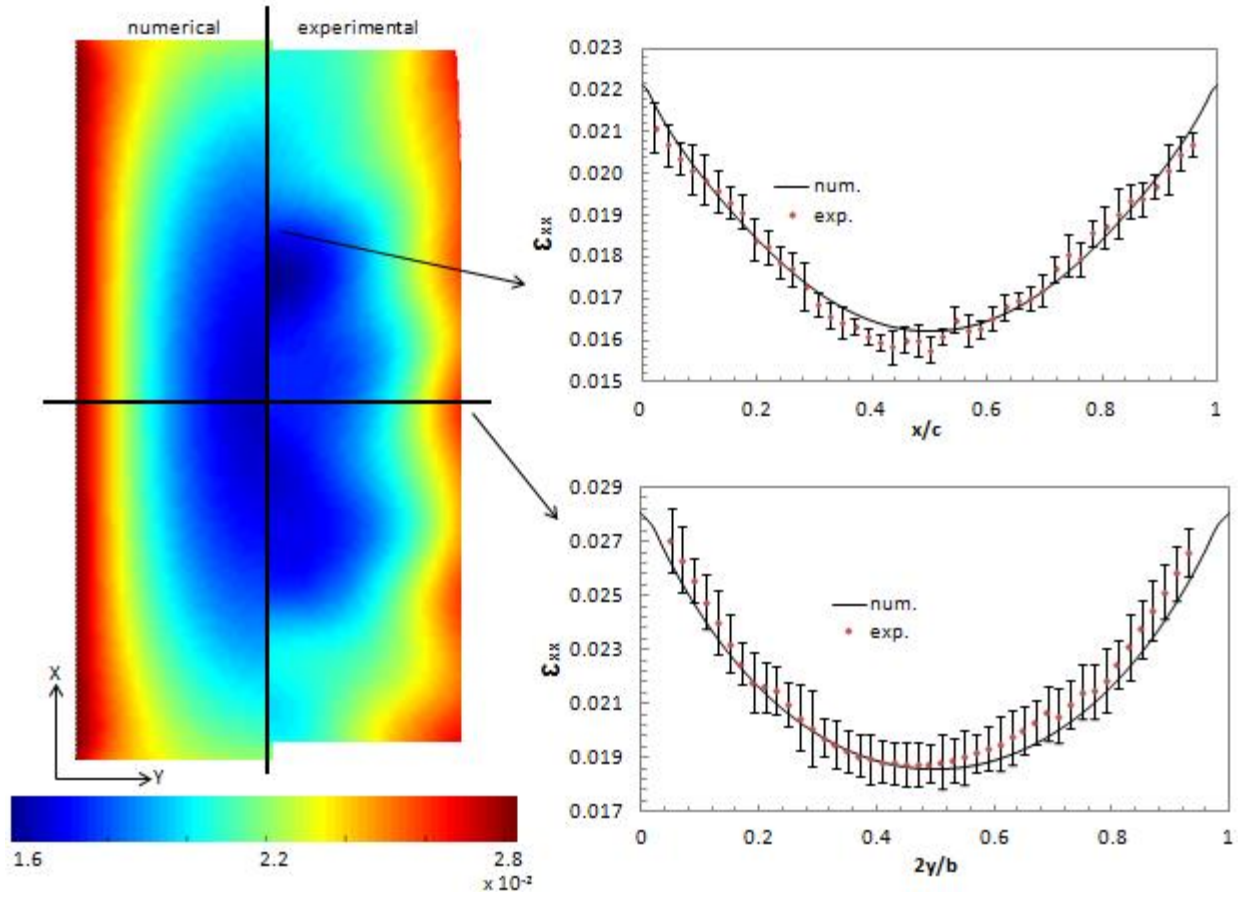


Figure 3-29. Strains in y-direction for the 15-layer curved closed cell; $R=127\text{mm}$ when attached at 140°C .

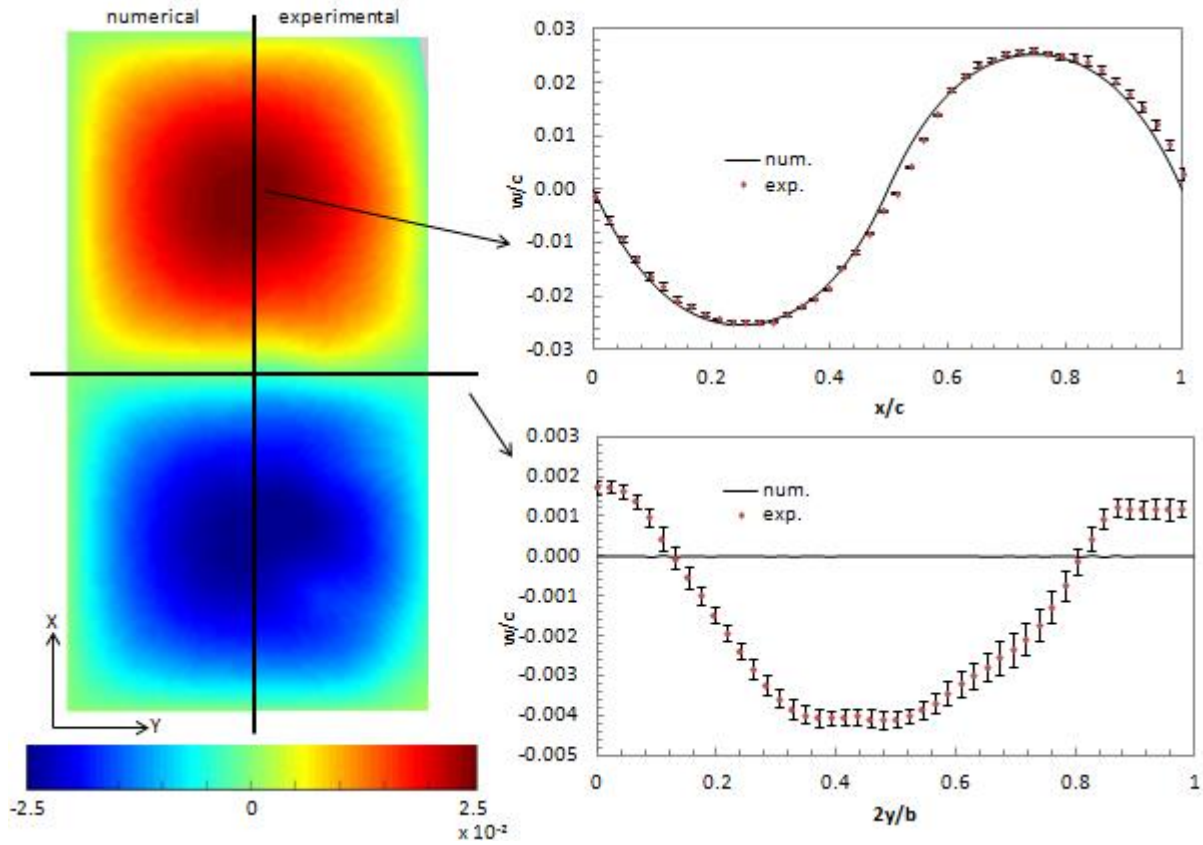


Figure 3-30. Normalized out-of-plane displacements for the 15-layer doubly curved closed cell; $R_1=R_2=63.5\text{mm}$ when attached at 140°C .

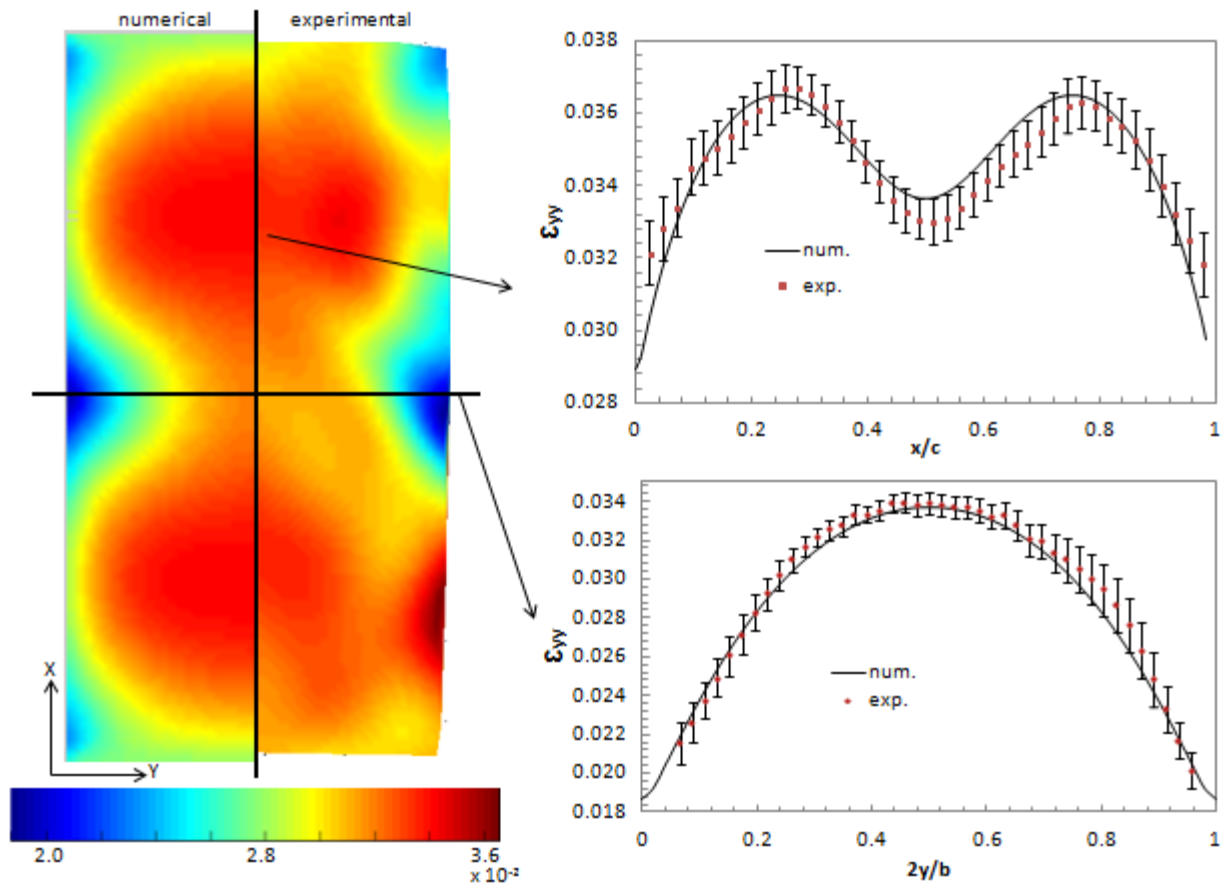


Figure 3-31. Strains in y-direction for the 15-layer doubly curved closed cell; $R_1=R_2=63.5\text{mm}$ when attached at 140°C .

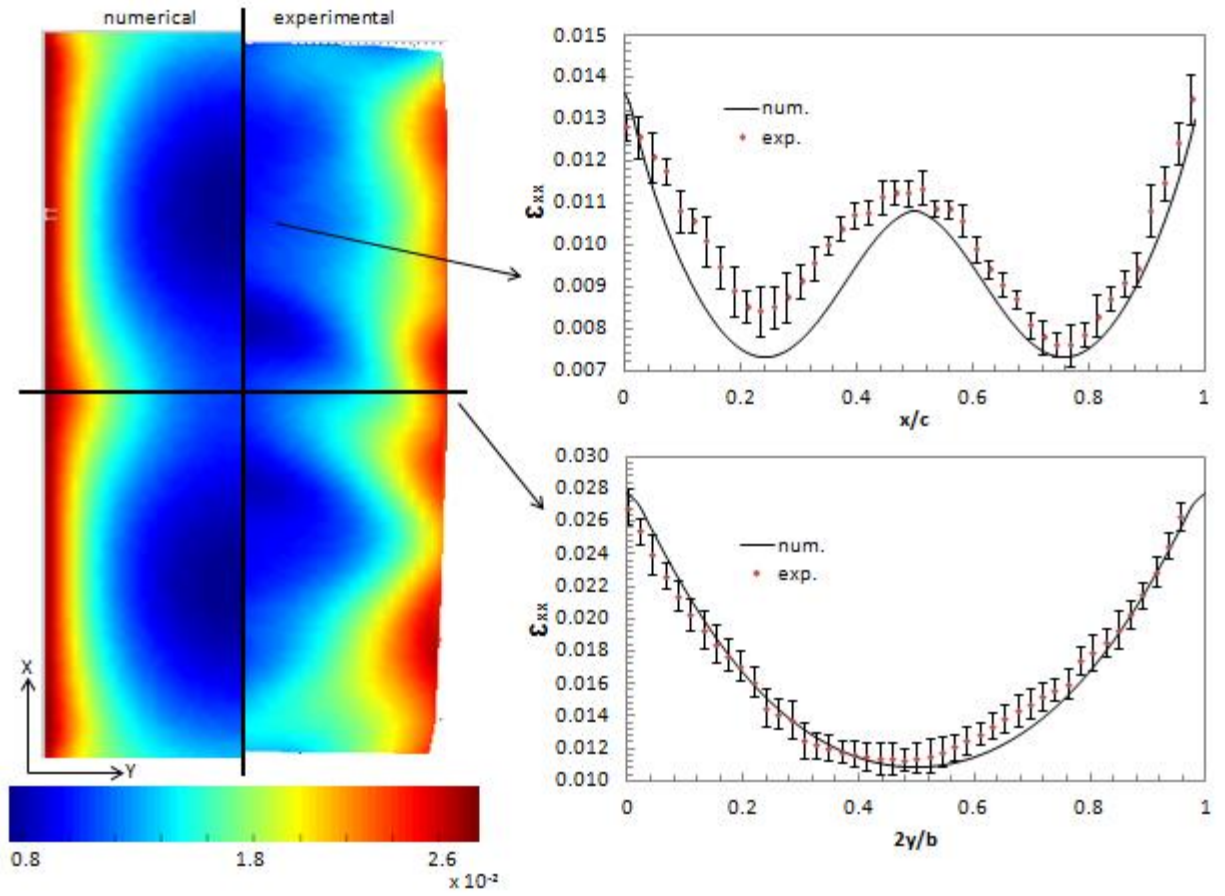


Figure 3-32. Strains in x-direction for the 15-layer doubly curved closed cell; $R_1=R_2=63.5\text{mm}$ when attached at 140°C .

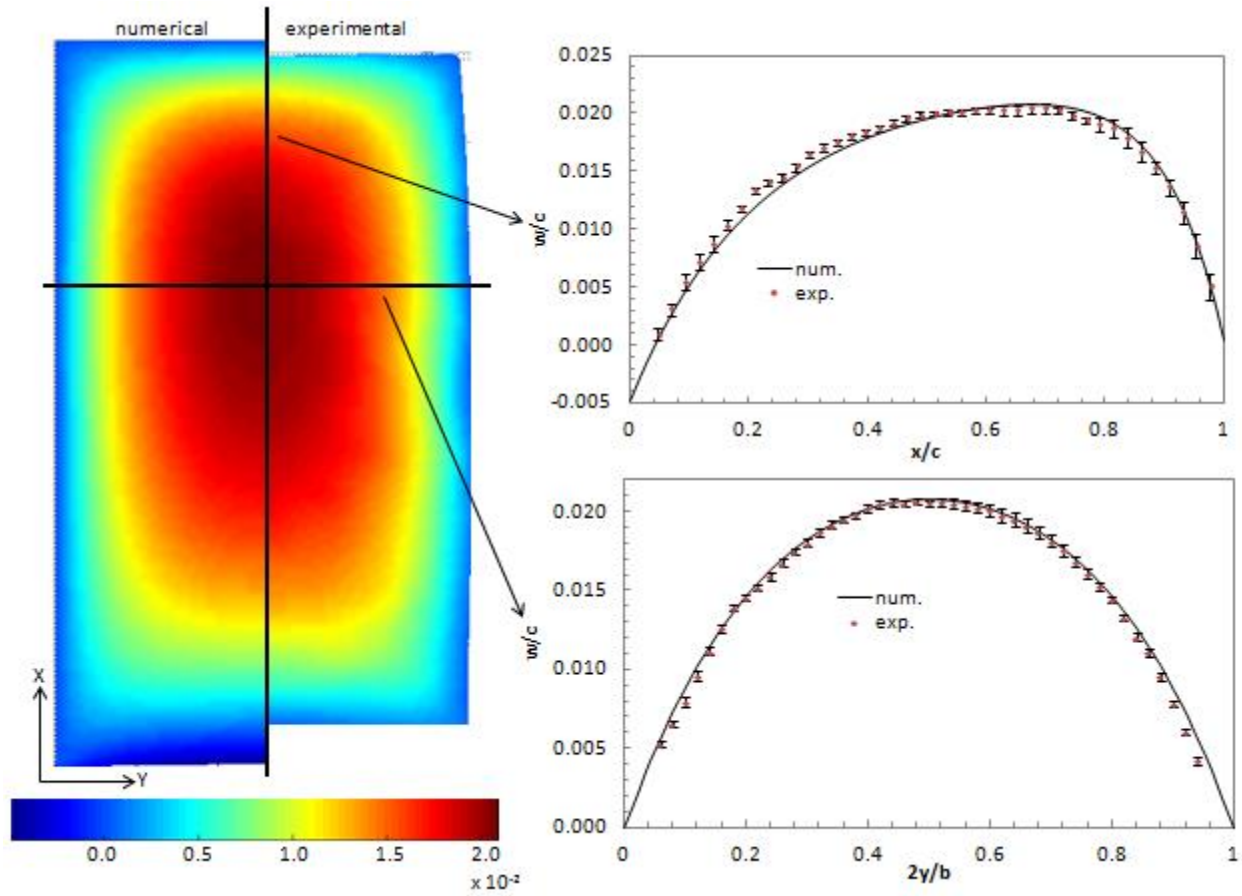


Figure 3-33. Normalized out-of-plane displacements for the 15-layer curved open cell; $R=63.5\text{mm}$ when attached at 100°C .

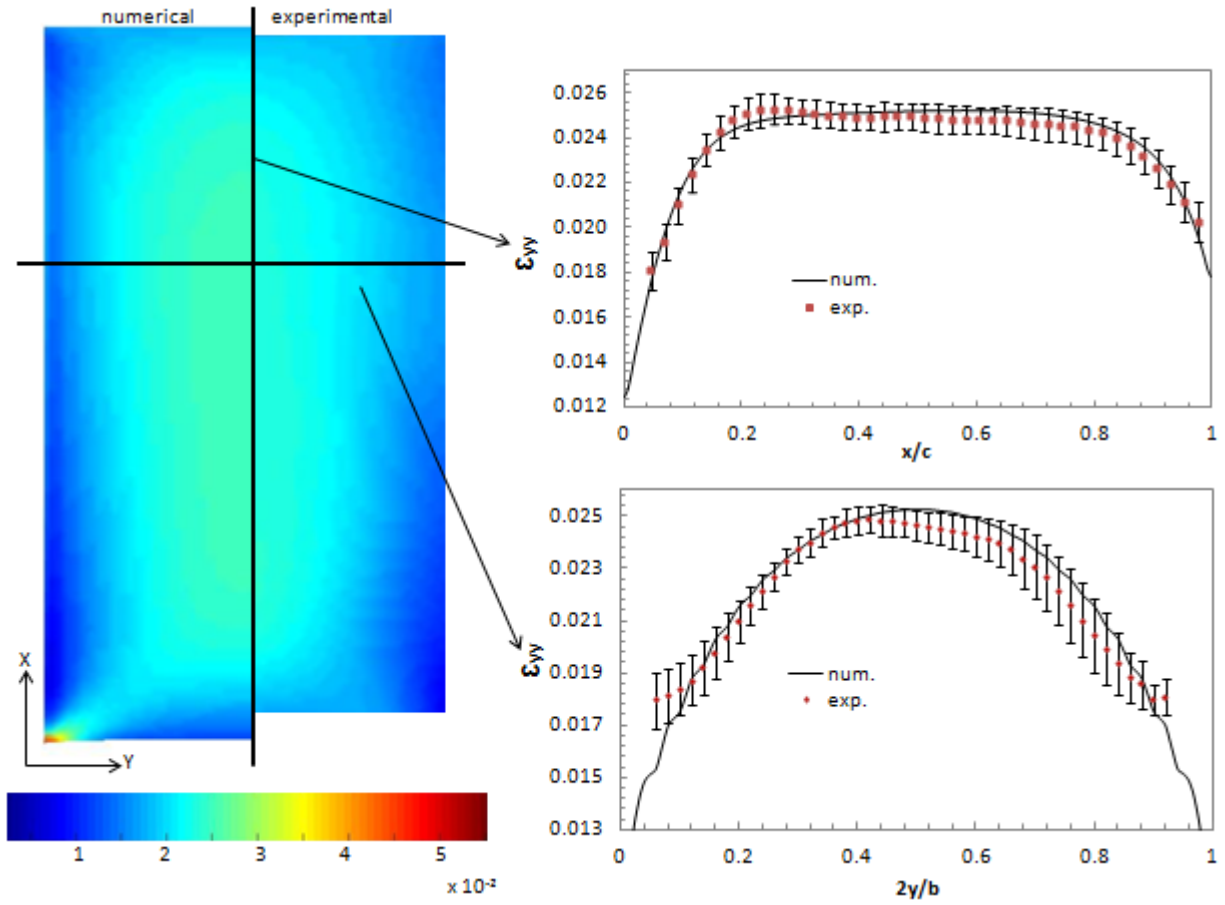


Figure 3-34. Strains in y-direction for the 15-layer curved open cell; R=63.5mm when attached at 100°C.

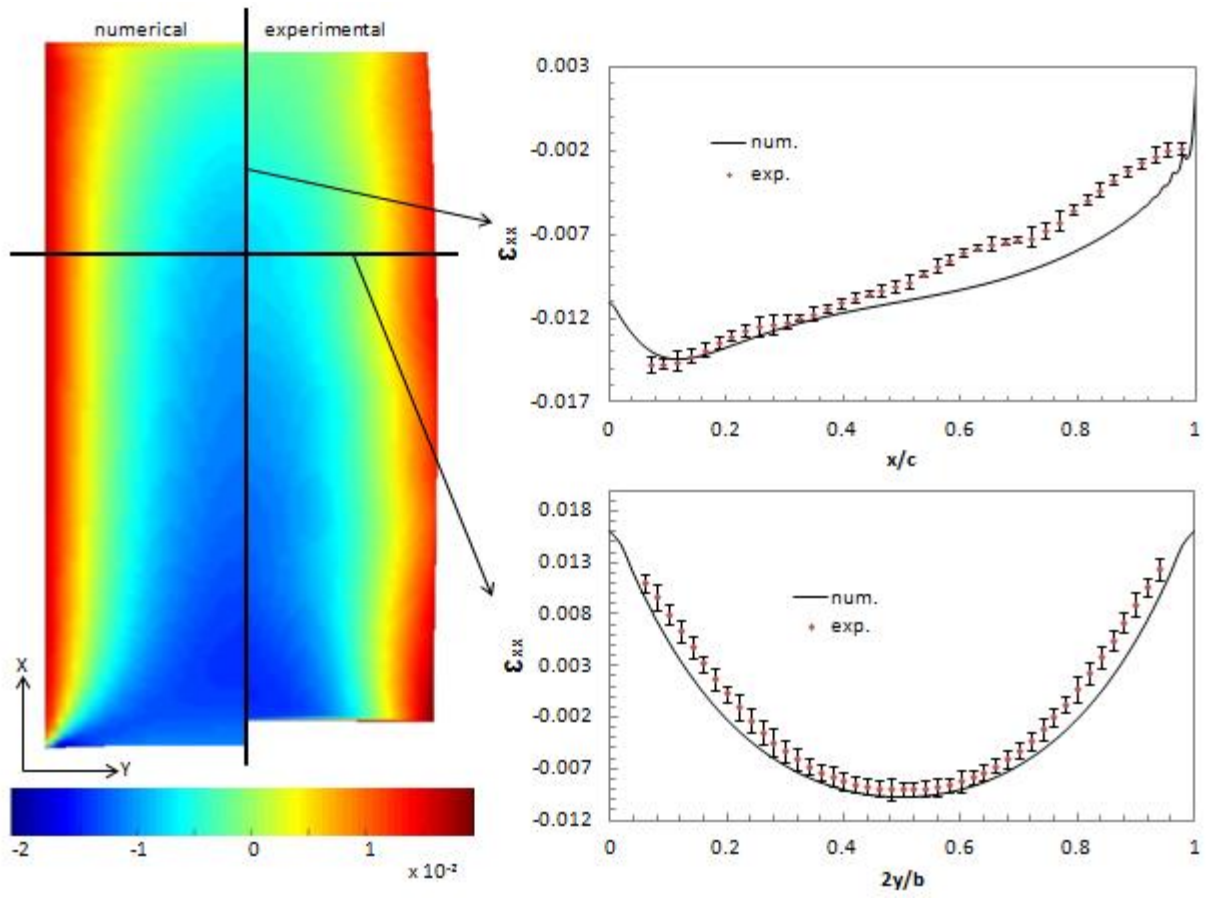


Figure 3-35. Strains in x-direction for the 15-layer curved open cell; $R=63.5\text{mm}$ when attached at 100°C .

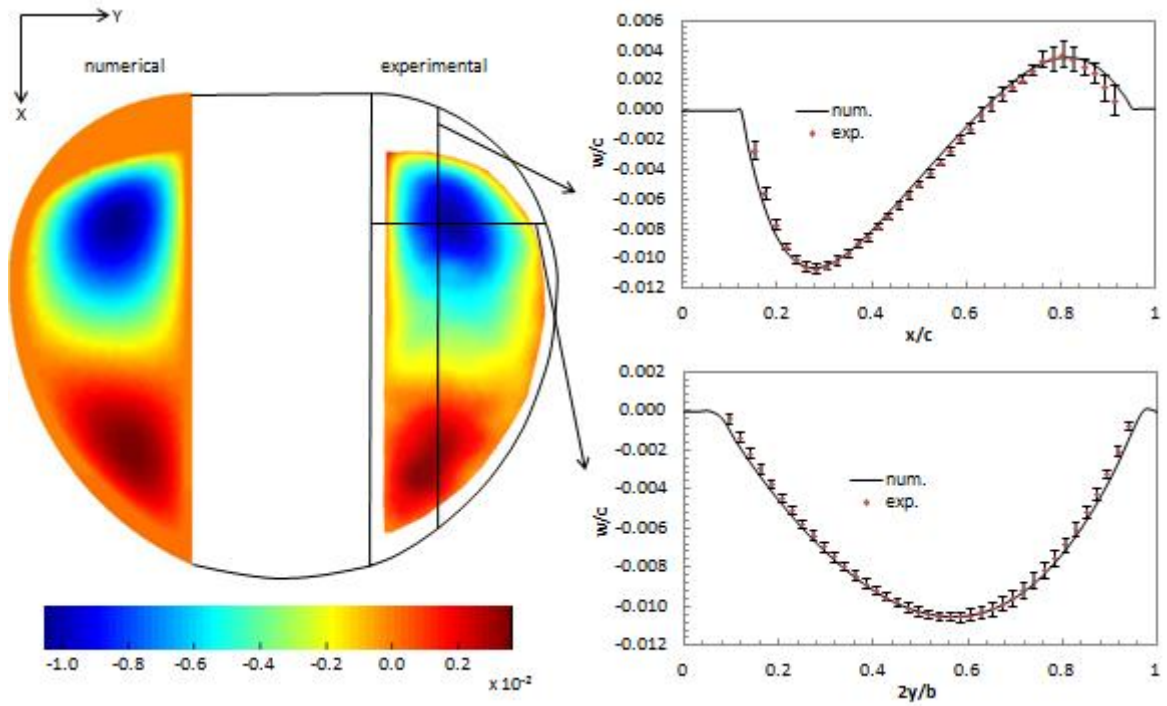


Figure 3-36. Normalized out-of-plane displacements for perimeter reinforced wing.

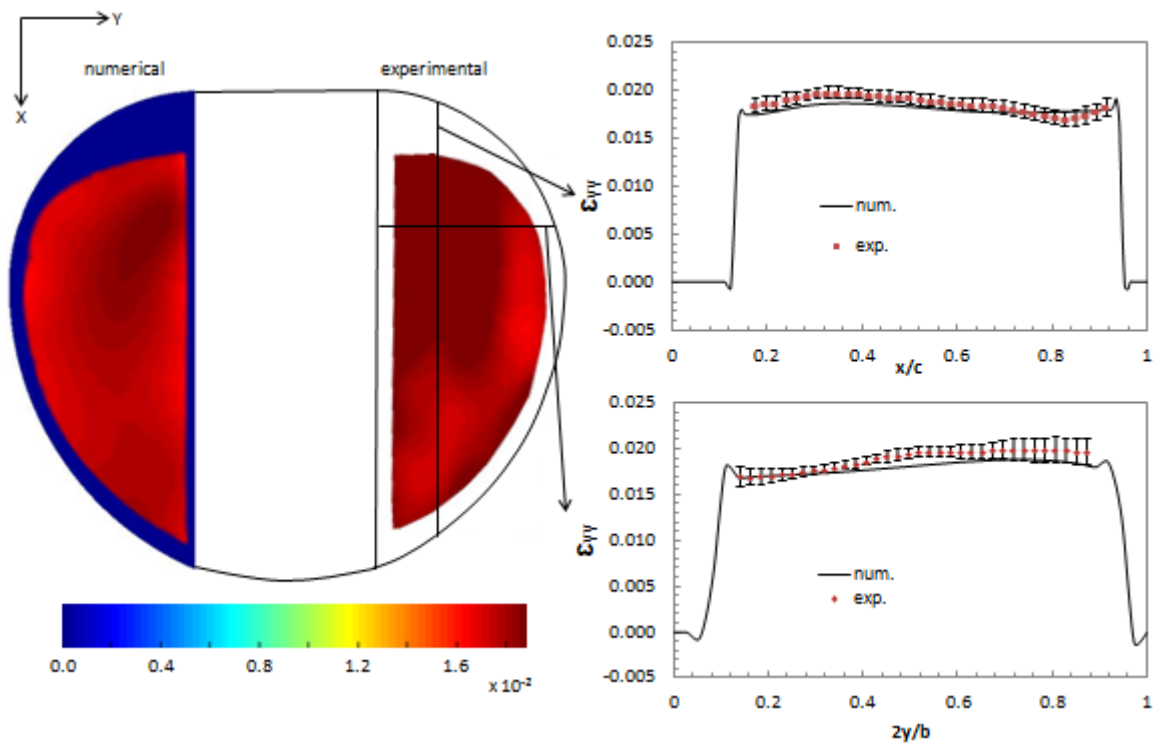


Figure 3-37. Spanwise strains for perimeter reinforced wing.

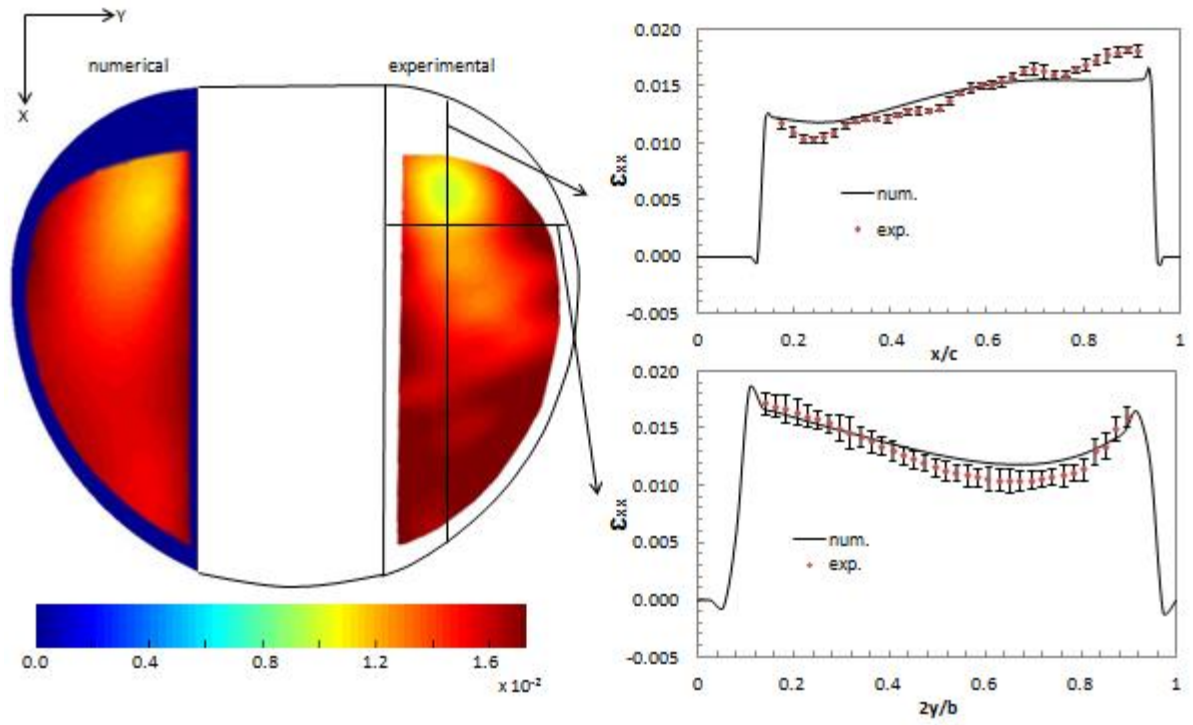


Figure 3-38. Chordwise strains for perimeter reinforced wing.

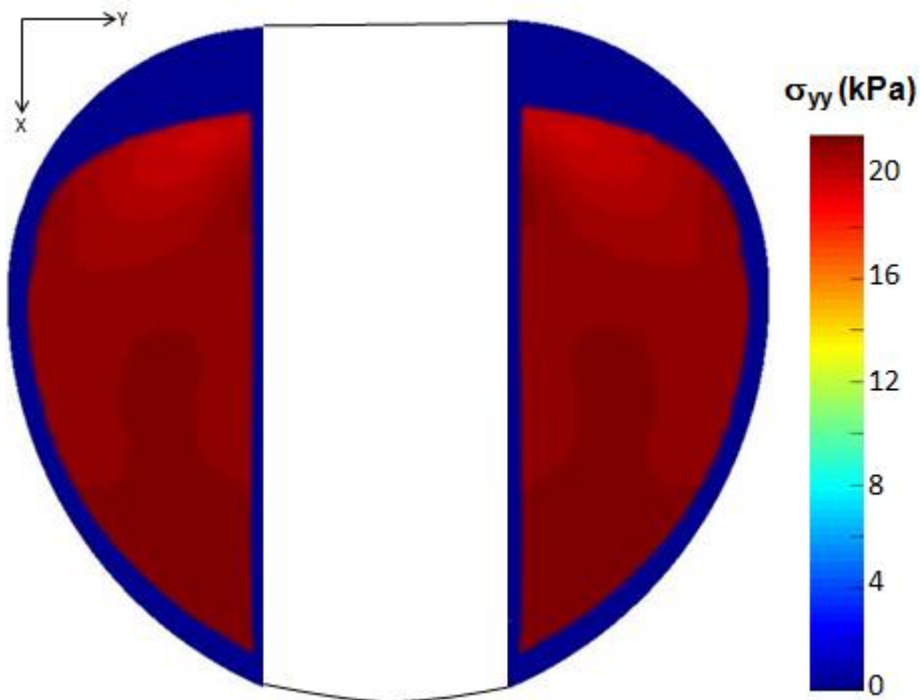


Figure 3-39. Numerical spanwise stresses for perimeter reinforced wing.

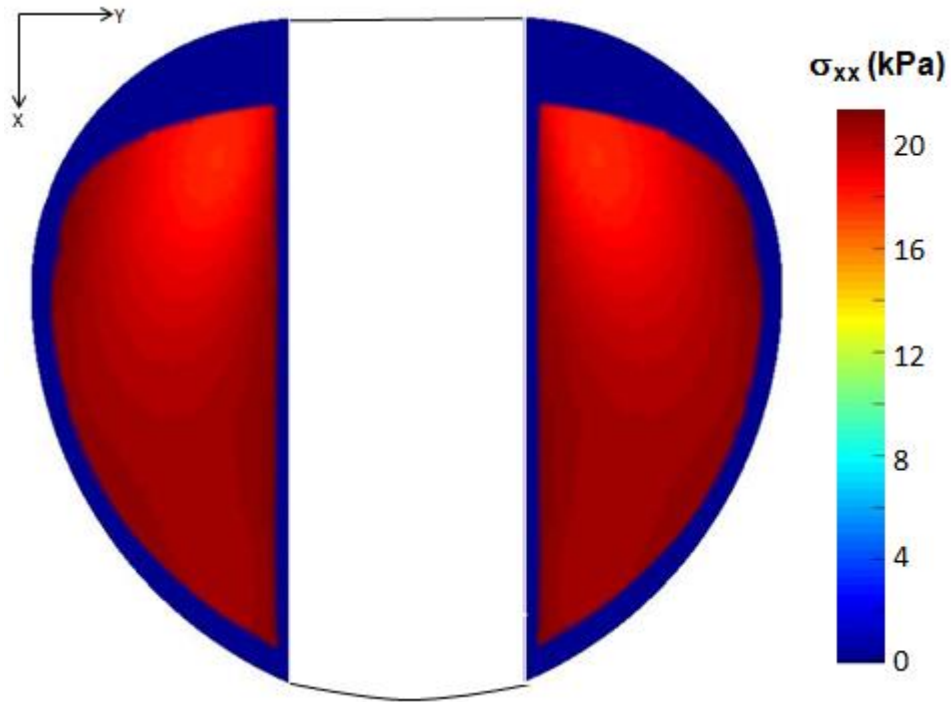


Figure 3-40. Numerical chordwise stresses for perimeter reinforced wing.

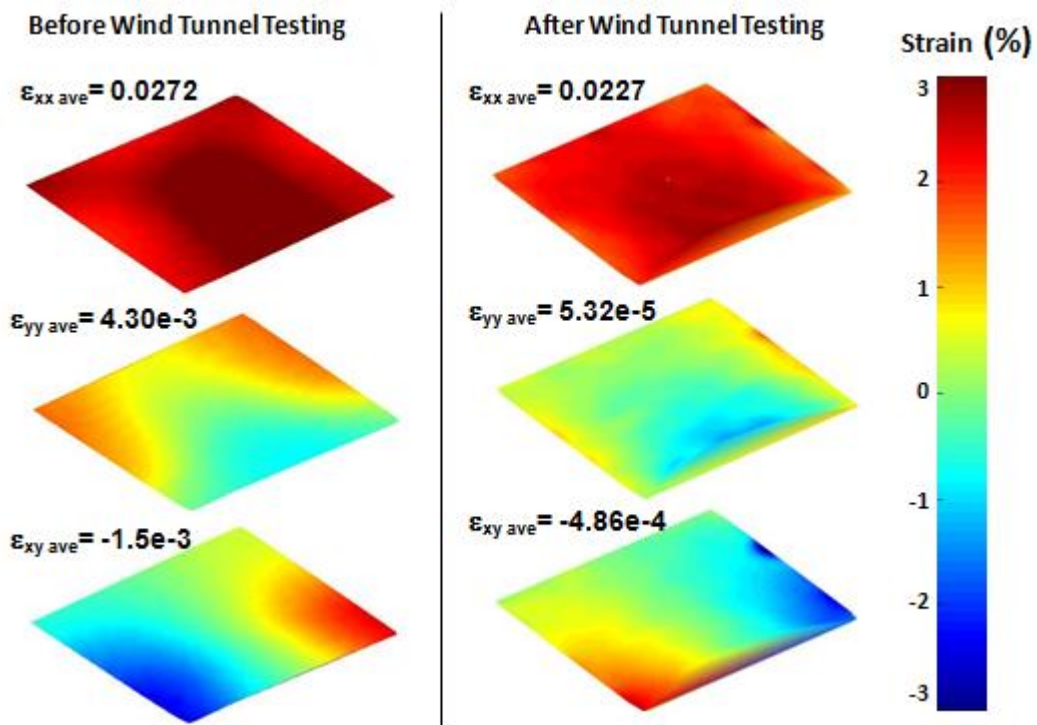


Figure 3-41. Normal and shear strains before and after wing tunnel experiments.

CHAPTER 4 COMPUTER SIMULATIONS FOR THERMALLY EXPANDING AND ADHERING SILICONE RUBBER MEMBRANES

Since the experimental pre-tensioning results agreed with the Abaqus predictions for 3-D frames as discussed in Chapter 3, numerous cases were simulated to understand the effects of temperature, chord length, and span on membrane deformations, strains, and stresses. Chapter 4 will first explain the detailed nomenclature of curved frames and then categorize various cases according to the different types of frames classified in the earlier chapters (closed curved cell, open curved cell, and doubly curved cell.) Simulation results will be explained in detail with the aid of figures.

Curved Membrane Nomenclature

- d = depth
- R = radius
- θ = chord angle
- b = span
- c = chord
- $\frac{d}{R}$ = depth ratio (DR)
- $\frac{b}{c}$ = aspect ratio (AR)

Is it possible to achieve the same normalized displacements from Figure 3-17, and the strains from Figure 3-20 and Figure 3-23 for varying values of curvatures? The answer is affirmative only if the proportion of the depth ratio, aspect ratio, and the membrane strain at attachment remain constant. Therefore, the problem can be nondimensionalized through the following equations derived from Figure 4-1:

$$d = R - R\cos\theta = R[1 - \cos(\theta)] \quad [4.1]$$

The depth ratio becomes

$$\frac{d}{R} = 1 - \cos(\theta), \quad [4.2]$$

and the chord length can be expressed as

$$c = 2R\sin(\theta). \quad [4.3]$$

This statement can be clarified with the following example:

Example: A circular carbon fiber frame with a 50 mm radius is chosen with a chord length of 70mm, and span of 35mm. The silicone rubber membrane is requested to be attached to that frame at 100°C. Specify the chord and span dimensions for a 700 mm radius frame so that the normalized displacement and strain gradients would be identical for both frames.

Solution: From [4.3] the angle, θ , can be determined to be plugged into [4.2] to find the depth ratio.

$$\theta = \arcsin\left(\frac{c}{2R}\right) = \arcsin\left(\frac{70}{2 \cdot 50}\right) = 0.775 \text{ rad.}$$

$$\frac{d}{R} = 1 - \cos(0.775) = 0.29$$

The aspect ratio can easily be calculated to be 0.5 from the span/chord ratio, so if the depth ratio of 0.29 and the aspect ratio 0.5 is applied on the frame with a radius of 700 mm, one can be assured that the normalized displacement and strain gradients will remain unchanged when the same type of silicone rubber membrane is attached at 100°C. The angle required for the depth ratio (29%) is already calculated, and can be inserted in [4.3] to find the chord length needed for the larger frame:

$$c = \sin(0.775) \cdot 2 \cdot 700 \text{ mm} = 980 \text{ mm} .$$

Finally, the corresponding span length can be calculated as 490mm from the given aspect ratio of 0.5.

Figures in this chapter will show the effect of membrane strain at attachment and aspect ratio for varying depth ratios, and the effect of depth ratio for varying aspect

ratios on normalized displacements, stresses, and strains. These figures can be approached from two perspectives to understand the change of depth ratio from one frame to another (Figure 4-2): viewpoint #1 suggests looking at a constant radius frame and decreasing the chord length with a decreasing depth ratio or vice versa. If the aspect ratio is kept constant, the span value is changed according to the instantaneous chord length. Viewpoint #2 is an alternate approach to visualize the problem, such that one may keep the chord length and span constant (to keep the AR constant), and increase the radius as the DR decreases or vice versa. For example, Figure 4-3 shows the effect of temperature with various DR values on the out-of-plane displacements. One may perceive the 100% depth ratio as a frame with a radius of 100mm, where the chord length is 200mm and span is 100mm as the AR is kept constant at 0.5. For the first approach, the frame size decreases as the DR decreases (smaller span for smaller chord lengths to keep $AR=0.5$), where at $DR=0\%$ the frame window becomes a point at the peak of the circle. However, for the second viewpoint, the chord length and span size remain constant, but the radius increases with a decreasing DR, where at $DR=0\%$, a 2-D frame with a 200mmX100mm opening is visualized. Both approaches are equally acceptable and function in a similar fashion.

Computer simulations are generated utilizing viewpoint #2 because the seed/mesh size would have had to be decreased significantly for lower depth ratio values as the surface area of the membrane decreases from $DR=100\%$ to 0% , where surface area becomes infinitesimally small. To change the parameters (radius, temperature, depth ratio, etc.) on the Abaqus program an intermediary script, "Python," was used to control the inputs via Matlab software. Several loops were created to run an array of specified

variables. After the FEA software was run, results were output back into Matlab to be processed (extracting maximum displacements, stresses, and strains at the maximum displacement locations), and then tabulated on an Excel sheet to be plotted.

Simulations for Closed Cell Circular Frames

Computer simulations on closed cell circular frames were performed to understand the membrane deformations on perimeter reinforced MAV wings with no reflex. Various cases with different membrane strain at attachments and geometries were run to see the effect on maximum normalized displacements and the stresses/strains at these locations. All of the maximum displacements were normalized to the chord length shown in Figure 4-1. As expected, since no out-of-plane displacements were analyzed on 2-D cases, the stresses and strains at the center of symmetry will be reported.

Effect of Membrane Strain at Attachment for Closed Cells

Effect of membrane strain at attachment is analyzed running 120 cases from 30°C to the maximum operating temperature of 220°C (recommended by the silicone membrane manufacturer as seen on Table 2-1 for a realistic simulation) for six different depth ratios. A typical MAV wing would have a depth ratio of 8% or less, though to understand the nature of the membrane, ratios up to 100% are investigated. The final geometric constraint, the aspect ratio, is chosen to be 0.5, and if different ARs are chosen, the magnitude of the membrane strain at attachment effect remains the same.

As expected, membrane strain at attachment does not impact the normalized displacements for DR=0%, which replicates a 2-dimensional wing/frame. When the depth ratio is increased slightly to 2%, a maximum displacement of approximately 0.01 is computed after the membrane strain at attachment of 50°C at the center of the membrane (due to the symmetry) as can be seen in Figure 4-3; however, this value

remains relatively the same up to 220°C. As the depth ratio is increased, the membrane strain at attachment becomes more prevalent, where the maximum normalized displacements increase linearly for higher temperatures.

Spanwise strains increase linearly for all depth ratios (Figure 4-4); however, the line is steeper as the depth ratio approaches 100% due to Poisson's effect on additional forces of a larger normalized geometry. Corresponding spanwise stresses also increase linearly with temperature, but the depth ratio does not have a notable effect on these stresses (Figure 4-6). For depth ratios of 2% and higher, analysis shows negative chordwise strains at the lower membrane strain at attachments (Figure 4-5), but the values start increasing linearly at higher temperatures. Nevertheless, this effect is entirely muted when the depth ratio is 100%. Stresses in this direction behave similar to the strains (Figure 4-7).

All the data clearly shows that as the camber of a MAV wing is increased for a certain membrane strain at attachment, higher out-of-plane displacements are expected. On the other hand, the membrane strain at attachment does not have a detrimental effect on out-of-plane displacements when looked at a wing with a given camber. For example, displacements do not vary significantly for membrane strains at attachment after 1.4% for a depth ratio of 8% (Figure 4-3), but the corresponding stresses and strains do. Therefore, the only way to control the displacements is to change the geometry and stresses/strains can be controlled by altering the membrane strain at attachment.

Effect of Aspect Ratio for Closed Cells

In this section effect of aspect ratio is under investigation; therefore, from the perspective of viewpoint #2 (Figure 4-2) the chord length and membrane strain at

attachment parameters are kept constant while the span is increased gradually until the span value becomes equal to double the chord length. As expected, for all 2-D cases zero out-of-plane displacements are measured (Figure 4-8). For 3-D cases, out-of-plane displacements peak at a w/c value and then plateau as the AR value is increased, in which this effect is more easily discernible for depth ratios of 13%, 25%, and 100%. Peak displacements are shifted from DR=100% to 13% and advanced from DR= 8% to 2% with respect to aspect ratio values. Displacement curves increase in magnitude for DRs from 0% to 8% while a decrease in magnitude is computed for DRs from 13% to 100%, where the decrease is certainly not gradual. The most dramatic effect is achieved by a depth ratio of 8% among the chosen values of DRs; however, another plot is discussed in the “Effect of Depth Ratio” section to better understand which DR would make the most impact on the out-of-plane displacements.

Initial spanwise strain slopes increase with respect to increasing values of depth ratios; nevertheless, peak strain magnitudes are shifted for DRs 0%-8%, and advanced for DRs 13%-100% (Figure 4-9). Spanwise strain magnitudes are gradually decreased after the peak for all depth ratios. Chordwise strains behave much more differently, such that the initial slopes decrease with respect to higher DR values and eventually plateau for larger magnitudes of aspect ratios (Figure 4-10). Spanwise and chordwise stress curves follow a similar path with decreasing initial slopes and eventually follow a zero slope line (Figure 4-11 and Figure 4-12).

Effect of Depth Ratio for Closed Cells

To understand the effect of depth ratio, AR was kept constant for each of the lines shown in Figure 4-13 while only the curvature was used as a variable. For various AR values, the computational results show that at the DR value of approximately 11% out-

of-plane displacements reach the peak magnitudes. This means if a batten reinforced MAV wing's percent camber is kept to a value close to 11%, membrane deformations will be very sensitive to aspect ratio as can be seen from Figure 4-8. As the aspect ratio is increased, the peak displacements gradually increase. Aspect ratios of 0.5 and 1.0 follow a similar path after a depth ratio of approximately 60%; however, a MAV wing would never have such aggressive camber.

Spanwise strain curves behave differently for each one of the aspect ratios (Figure 4-14): for $AR=0.1$ the strain is 17% at a very low depth ratio and increases with relatively small increments; for $AR=0.5$ the path starts with a steep straight line, flattens, and decreases with small increments; for $AR=1.0$ after the peak strain, the curve decreases more drastically; and finally for $AR=2.0$ the strain increase follows the same slope as the one seen for $AR=0.5$, however, peak value stops at a much lower value, drastically declines at $DR=25\%$, and then follows a zero slope path. Chordwise strain curve magnitudes decrease both in magnitude and initial slope with respect to decreasing values of aspect ratios (Figure 4-15). Stresses in both directions follow similar paths as the strains (Figure 4-16 and Figure 4-17). Spanwise stresses are significantly higher than the chordwise stresses, where for higher ARs the chordwise stresses approach zero stress magnitudes. Therefore, it may be possible to see wrinkles perpendicular to the leading edge for higher aspect ratios for extreme values of depth ratios.

Simulations for Open Cell Circular Frames

To investigate the membrane stains and deformations on batten reinforced MAV wings, where the trailing edge is not constrained, idealized simulations for open celled circular frames were run. A 2-D/3-D case comparison is possible for closed cells as the

maximum displacement location always occurs at the center of the membrane for the rectangular geometry. Simulations for 2-D cases are omitted in this section due to the asymmetric nature of the stress and strain gradients on the membrane (the maximum out-of-plane displacement location changes for 3-D cases, and all out-of-plane displacement are zero for 2-D cases). Therefore, the locations of the maximum normalized deformations are also reported as the open edge creates asymmetric gradients (Figure 3-33), i.e. with increasing membrane strains at attachment the maximum displacement location moves toward the center. The location is determined by dividing the distance of maximum out-of-plane displacement by the chord, in which the parameters can be seen in Figure 4-18. The constrained straight end is called the leading edge while the free end is named the trailing edge, alluding to a typical MAV wing nomenclature. The remainder of the parameters is identical to those shown in Figure 4-1.

Effect of Membrane Strain at Attachment for Open Cells

For the investigation of membrane strain at attachment on displacements and strains, the aspect ratio was set to 0.5 while the membrane strain at attachment was increased from 0.0% to 5%, similar to the procedure outlined in the previous section for closed cells. Out-of-plane displacements behave very similar to those shown in Figure 4-3; however, magnitudes are slightly lower as the trailing edge of the membrane is free (Figure 4-19). For the curved closed cells the maximum out-of-plane deformation location occurs in the middle (50%) due to symmetry, but in the open case the maximum out-of-plane displacement starts at a point closer to the leading edge and moves toward the center. The open case never reaches the 50% of the chord length (Figure 4-20), which may be due to the trailing edge spanwise strains increasing and

behaving more like a closed cell as the membrane strain at attachment is increased. At 100% depth ratio the behavior is the opposite, where the maximum out-of-plane displacement starts at the center and moves toward the leading edge with increasing membrane strain at attachments.

Spanwise strains follow an increasing linear trend and the slopes proportionally increase with increasing depth ratios (Figure 4-21). When the depth ratio is 100%, all strains analyzed in the chordwise direction were negative; however, this effect is muted as the depth ratio decreased (Figure 4-22). Corresponding stresses in both directions behave similar to the strains in terms of trend lines, and the plots clearly show increasing the membrane strain at attachment causes the membrane to be tighter in both directions (Figure 4-23 and Figure 4-24). Nevertheless, depth ratio does not seem to have a detrimental effect on spanwise stresses. When these stress results are compared to the closed cell results, almost no difference is observed in the spanwise direction as the membrane is constrained at both ends; however, a decrease of slope in the chordwise direction is easily seen when Figure 4-7 is compared with Figure 4-24 since the trailing edge of the membrane is allowed to be free.

Effect of Aspect Ratio for Open Cells

The open trailing edge has an immense effect on out-of-plane displacements in terms of AR since the magnitudes are halved when Figure 4-8 is compared to Figure 4-25. Once again the slopes increase up to DR=8% and decrease after DR=13%. To better tune which depth ratio would be the most sensitive to the aspect ratio Figure 4-31 is created, which is discussed in the next section. When spoken in terms of MAVs, increasing the batten spacing causes larger out-of-plane displacements for a given percent camber, and after a certain value of distance between the battens, the

displacements remain unaffected; however, strains in both directions change. For very low aspect ratios, the location of peak out-of-plane displacements occur at the center, behaving similar to a closed rectangular section while as the aspect ratio is increased, the peak location moves toward the leading edge for all cases. This effect was muted for some cases: at DR =8% this location stagnates after an AR of 0.3 and at DR =2% maximum out-of-plane displacement location moves slightly back toward the center and remains at approximately 44% of chord length.

Spanwise strain curve peaks shift and the initial slopes decrease with respect to AR as the depth ratio is decreased (Figure 4-27). All peaks reach approximately the same spanwise strain value of approximately 2.4%. The peak strain value fluctuated depending on the value of depth ratio in the closed cell simulations (Figure 4-9). For example, for DR=2% the peak spanwise strain was approximately 2.0% for a closed curved frame whereas the peak was higher (2.4%) for an open cell. This may be due to the interaction of the forces, where for the closed cell configuration the membrane was stretched more in the chordwise direction, and the corresponding spanwise strain was less because of Poisson's effect. In the open cell section the situation was the opposite (lower chordwise strain due to free membrane at the trailing edge); therefore, higher strain peaks are achieved for DR=2%. At the other extreme end, where DR=100% results for both open and closed configurations are almost identical. Also, similar chordwise strain results to those seen for the closed cell simulations are reported for the open cells, except for the DR=2% as mentioned earlier (Figure 4-28). Stresses in both directions at the peak out-of-plane displacement locations decrease as the aspect ratio

was increased; however, chordwise stresses drop more rapidly down to 0 kPa. This drop was shifted as the depth ratio was decreased from 100% to 2%.

Effect of Depth Ratio for Open Cells

When the normalized maximum displacement versus depth ratio results of closed cells (Figure 4-13) are juxtaposed with open cells (Figure 4-31), almost no difference was observed for ARs of 0.1 and 0.5, and increasing magnitudes of differences are obtained for ARs of 1.0 and 2.0. Figure 4-31 shows that the maximum displacements are unaffected by the unsupported membrane at the trailing edge when the span was kept relatively short with respect to the chord length. Even the peak w/c location stays at 50% when the AR was kept low; however, the location was changed drastically by the increased depth ratio (after approximately DR=25%) as the span was increased with respect to chord length (Figure 4-32).

Spanwise and chordwise strains also behave very similar to the plots shown for closed configurations at lower aspect ratios (0.1 and 0.5); however, strain curves in both directions behave differently at higher AR values (Figure 4-33 and Figure 4-34). All curves start with an initial slope, except for the AR=2.0 curve where only a decline with increasing values of depth ratio was calculated. Spanwise stresses at the maximum w/c increase with decreasing aspect ratios and follow a relatively linear-flat trend line (Figure 4-35). Zero chordwise stresses are shown for AR=2.0 on Figure 4-36, which means the membrane was slack regardless the depth ratio. Increased initial slopes and stresses are reported as the AR values are increased. The stress plots show that if the batten spacing of a MAV wing was increased, the membrane may be slack in the chordwise direction, which may be resolved by adding more battens in the middle or adjusting the tension by increasing the membrane strain at attachment.

Simulations for Doubly Curved Frames

Doubly curved frame simulations are intended to be idealized versions of MAV wings with a camber and reflex, which enables an understanding of membrane deformations upon attachment to wing frames. Similar types of analysis are also applied to closed doubly curved frames to inspect the effects of membrane strain at attachment, aspect ratio, and depth ratio. In addition, the geometry seen on Figure 4-37 was changed from symmetrical ($c_1=c_2$) to asymmetrical by varying the individual chord lengths and keeping the same radius (from the viewpoint #1 perspective) for each curve to understand the effect of asymmetry on various depth ratios.

When the symmetric geometry was preserved, only the positive normalized out-of-plane displacements with the corresponding stresses and strains are plotted, as the minimum extreme has the same magnitudes; however, both extremes are analyzed for asymmetric simulations. Note that membrane displacements are downward when the frame curvature was convex and upward when the curvature was concave as indicated in the figure. Determining the location of maximum out-of-plane displacement was accomplished similar to the open curved frames: a location of 25% would mean the center of the curve and 50% would be the mid-point of the entire chord length. For example, the w/c (+) location shown in above figure is approximately at 35%.

Effect of Membrane Strain at Attachment for Doubly Curved Frames

The initial slopes of higher DR curves are increased as the membrane strain at attachment was elevated, and the peak out-of-plane displacements are shifted as the depth ratio is increased, where at DR=100 the line is linearly increasing up to 220°C (Figure 4-38). Peak displacement location is stagnant in the middle of each curve for the DR=2% case regardless of the membrane strain at attachment since the simulation is

very close to a 2-D case (Figure 4-39). For lower membrane strains at attachment, the peak displacement location starts from closer to the center of the entire structure as the depth ratio is increased and approaches the middle of the curve with less aggressive declining slopes.

Since the membrane is constrained at both ends in the spanwise direction, strains behave very similar to those seen for both closed and open curved cases (Figure 4-40). However, many different forces are in control in the chordwise direction (forces due to depth ratio, aspect ratio, and additional forces from the neighboring curvature). All chordwise strains at DR=100 are negatively declining and with increasing depth ratios this effect is gradually muted with increasing slopes (Figure 4-41). As the value of the DR is increased, spanwise stress slopes significantly increase (Figure 4-42) relative to its closed and open single curved counterparts (Figure 4-6 and Figure 4-23). As expected, chordwise stress magnitudes are much lower and increase with greater depth ratios (Figure 4-43).

Effect of Aspect Ratio for Doubly Curved Frames

Effects of various ARs on out-of-plane displacements are very similar to the previous cases, where as the depth ratio is increased for DRs after 13%, curves start with lower initial slopes and peak at lower w/c values (Figure 4-44). For DR=2%, the normalized displacement values are almost identical to the open curved cell displacements shown in Figure 4-25 as these cases are very close to a 2-D case. However, as the depth ratio is increased, 3-D effects start to dominate and the curves behave slightly different, such as advanced or shifted peaks, different magnitudes, etc. The maximum displacement location starts behind the center of a single curve, moves toward the center as the AR is increased, and remains stagnant after an aspect ratio of

approximately 0.3 (Figure 4-45). For larger depth ratios the maximum w/c location never reaches the center of the curve.

Once again, spanwise strains at the maximum displacement location are similar to those shown for other configurations as the membrane is linearly constrained at both ends (Figure 4-46). The curves intersect at several locations indicating that obtaining the same spanwise strains is possible for the same AR and a different DR. Chordwise strains decrease with a linear slope and plateau, where the strains are shifted as the DR is decreased up until DR=2% (Figure 4-47). Strains for all ARs are positive at DR=2% as this case is very close to the 2-D cases, where only one out-of-plane displacement peak is observed. Spanwise stresses are approximately 21 kPa for ARs of 0.1 or less, and as the AR is increased initial slopes become more negative with higher depth ratios, where for higher DRs the curves follow a linear constant value of 13.5 kPa (Figure 4-48). Chordwise stress curves behave similar; however, for DRs of 13% and above zero stresses are present (Figure 4-49).

Effect of Depth Ratio for Doubly Curved Frames

Depth ratio does not have a significant effect on low aspect ratio doubly curved frames, but as the aspect ratio is increased, out-of-plane displacements peak at approximately DR=11%, where the typical MAVs fall into DRs that are less than the 11% category (Figure 4-50). This means the amount of percent camber would have a significant effect on the overall deformations. Peak values are similar to open curved frame simulations, and curve paths are akin to closed curved frames. Simulations showed that after DR=40%, maximum w/c values do not vary significantly. For higher ARs (>0.1), maximum w/c locations start at the peak of the curve, move toward the

center of the overall frame, and hold at about 35% after DR=40% (where the center of the frame is at 50%; Figure 4-51).

For AR=0.1, the spanwise strain curve behaves very different than other AR values (Figure 4-52): the strains only keep increasing with higher depth ratios, where the magnitudes of even the closed curved cells are exceeded (Figure 4-52). The rest of the AR curves are similar to the ones shown in Figure 4-14. Chordwise strains for higher ARs rapidly drop up to 11% depth ratio and remain stagnant at -1.5% strain, while the AR=0.1 curve holds a relatively much higher strain throughout the entire spectrum of selected depth ratios (Figure 4-53). Spanwise stresses remain at a constant 21.5 kPa for all DRs when low AR is selected and the values drop as the span is increased with increasing slopes and an eventual stagnation after DR=11% (Figure 4-54). Chordwise stresses behave similar to spanwise stresses; however, the magnitude drop is much higher with increasing DRs (Figure 4-55).

Effect of Asymmetry for Double Curved Frames

All simulations performed for the double curved frames above were described with equal chord lengths for both curves. This section complicates the situation further by breaking the symmetry with a steadily moving “inflection point” toward the trailing edge, but without changing the depth ratio of either curve (Figure 4-56). Curve #1 seen on the figure represents the camber on a MAV wing while Curve #2 represents the reflex that is used to control pitch stability. Since the effects of DR and AR on double curved frames were discussed thoroughly, the simulations are executed for only ARs of 0.1 and 0.5 and DRs of 2% and 8%, as most MAV wings’ percent camber fall into this category. The inflection point axis on each plot is calculated by dividing the larger chord length with the entire chord length. For example, inflection point values for the dots shown in

the figure would be 50.0%, 62.5%, 75.0%, and 87.5% from the black dot in the middle to the red dot at the trailing edge.

Each curve can be treated as an open curved model except with additional forces at the local trailing edge, since the two trailing edges are shared with opposite forces resulted by each curve's geometry. The AR values shown on the plot are for the entire structure: as the inflection point is moved toward the trailing edge, the aspect ratios constantly change for the individual curves as demonstrated in Figure 4-57. Local AR decreases at the convex curve (Curve #1: span is constant as the chord length increases) while the local AR increases on the concave curve (Curve #2: span is constant as the chord length decreases), which is numerically expressed in Table 4-1.

Table 4-1. Local aspect ratios with respect to initial and final inflection points.

<i>Asymmetric Loc.</i>	$AR_{global}=0.1$		$AR_{global}=0.5$	
	AR_{local} (Curve #1)	AR_{local} (Curve #2)	AR_{local} (Curve #1)	AR_{local} (Curve #2)
0.5	0.2	0.2	1.0	1.0
0.9	0.1	1.0	0.5	10.0

Two out-of-plane displacement extremes reported in Figure 4-58 and Figure 4-59 are results from each curve, where the maximum w/c occurs at the convex curve, and the minimum w/c occurs at the concave curve as explained in Figure 4-37. Maximum out-of-plane displacements follow a linear trend with a negative slope throughout the entire spectrum of inflection points (from 50% to 90%), which may be partly caused by the decreasing local aspect ratio. The curves behave differently depending on AR for minimum out-of-plane displacements that occur on the second curve: minimum w/c values start with the same values as the maximums at the inflection point of 0.5 actually

represents symmetry, and as the location is moved further, minimum displacements deviate further from the maximum w/c values. Increasing the DR from 2% to 8% at an AR of 0.5 causes a greater difference in out-of-plane displacements than an increase at AR=0.1. Locations of both minimum and maximum displacements increase linearly with respect to the leading edge (Figure 4-60 and Figure 4-61). At AR=0.5, w/c_{max} follows the same path regardless of depth ratio whereas for AR=0.1 depth ratio has a considerable effect on displacement locations. When AR=0.1, curve #1 shows a relatively linear behavior in comparison to curve #2, where the spanwise strains increase at a very high rate (further elaborated on in the next section, Displacement, Stress, and Strain Gradients of Selected Cases), as the inflection point is moved further to the trailing edge; however, for an AR of 0.5 the effect is reversed and spanwise strains decrease (Figure 4-62 and Figure 4-63). The slope increases even further for the higher depth ratio at the minimum out-of-plane displacement location. In the chordwise direction, strain magnitudes for the convex part of the membrane decrease while slopes increase as the AR and/or DR is increased (Figure 4-64). Once again the concave curve behaves differently and responds by decreasing for AR=0.1 and increasing for AR=0.5 (Figure 4-65). This response is the reverse version of the spanwise strains for the concave curve, which is likely caused by the Poisson's effect. Spanwise stresses at the w/c_{max} location for AR=0.1 follow a relatively flat and linear path throughout the entire inflection point spectrum regardless of depth ratio (Figure 4-66). At the w/c_{min} location the behavior is very similar, except, when the inflection point is moved further away to the trailing edge, stresses start to decrease (Figure 4-67). At the maximum displacement location, where AR=0.5 and DR=2% stresses slowly increase, but when

the DR is raised to 8%, spanwise stresses lower in magnitude with an increased slope in comparison to DR=2%. This behavior is mirrored at the minimum displacement location with decreasing slopes and slightly lower magnitudes. All chordwise stresses at the w/c_{\max} location for AR=0.1 are very similar to those seen in the spanwise direction both in terms of magnitude and trend lines, which in this respect Curve #1 behaves very similar to a 2-D closed cell (Figure 4-68). When the aspect ratio is increased to 0.5, the trend lines are very similar for both depth ratios, but the magnitudes are much lower, most likely due to the tremendously decreasing local aspect ratio of Curve #1. The analysis of chordwise stresses at the w/c_{\min} location for AR=0.1 shows the stress values decrease at a much greater rate as the inflection point is moved toward the trailing edge. For AR=0.5, stress magnitudes start changing at a lower rate until the inflection point is moved to 80% of the entire chord length, and the rate rapidly increases thereafter this point depending on the depth ratio (Figure 4-69).

Displacement, Stress, and Strain Gradients of Selected Cases

Four double curved cases are investigated in more detail to gain in depth understanding in the rapid changes that occur in some of the plots shown in the previous sections. Three of the aforementioned cases are discussed together to be compared; another case with full depth ratio is analyzed only for out-of-plane displacements to demonstrate values that cannot be depicted from the plots discussed.

Comparison of Double Curved Symmetrical and Unsymmetrical Cases

To better visualize the effect of inflection point gradients, three cases are compared by keeping the AR, DR, and membrane strain at attachment constants. As discussed previously, maximum normalized displacements shift toward the trailing edge and decrease in magnitude at the Curve #1 region (Figure 4-70). Curve #2 region also

experiences a decrease for the given inflection point spectrum; however, since the change is minute, as demonstrated in Figure 4-59, this difference is not obvious to the naked eye.

Spanwise strain gradients are identical for both curves when the geometry is symmetric; however, as the Curve #1 chord length is increased, the maximum strain at the center of the Curve #2 region starts to polarize toward the left and right and intensifies with higher inflection point values (Figure 4-71), which explains the rapid decrease of spanwise strains in Figure 4-67. This effect is entirely muted for very low aspect ratios, such as 0.1, but the local strain keeps increasing at the center of Curve #2 region. In the Curve #1 region, magnitude of strains in x-direction do not change significantly although the gradient continuously redistribute for greater dimensions when compared to the neighboring Curve #2 region. Chordwise strains at the w/c_{max} location decrease while it increases at the w/c_{min} point with increasing inflection point values (Figure 4-72). The peak strains are observed at the longitudinal edges indicating the adhesive used to attach the membrane should be able to resist high stresses experienced at the constrained margins. Spanwise stresses decrease at the trailing edge and at the mid-section of Curve #2 region with increasing inflection point values; however, the tension intensifies on either side of the area (Figure 4-73). The opposite effect is observed in the Curve #1 region, the spanwise tension increases at the mid-section (where the w/c_{max} is present) and leading edge while the tension is relieved from the left and right edges. Spanwise stresses remain stagnant at the inflection point line for every case. Chordwise stress gradients behave very similar to the corresponding strains with values ranging from 8 kPa to 20 kPa (Figure 4-74).

Displacement Gradients on a Double Curved Frame with 100% Depth Ratio

A depth ratio of 100% for a membrane attached to a closed double curved frame is unique because additional out-of-plane displacements occur close to the leading and trailing edges. These normalized displacement values are in the order of ± 0.005 for Figure 4-75, and start to form for depth ratios greater than 65% for the silicone rubber membrane described in Table 2-1. Strain and stress gradients are not reported since these simulation results look very similar to the data shown for the membrane attached to symmetrical double curved frame in Figure 4-71-Figure 4-74, except with different magnitudes.

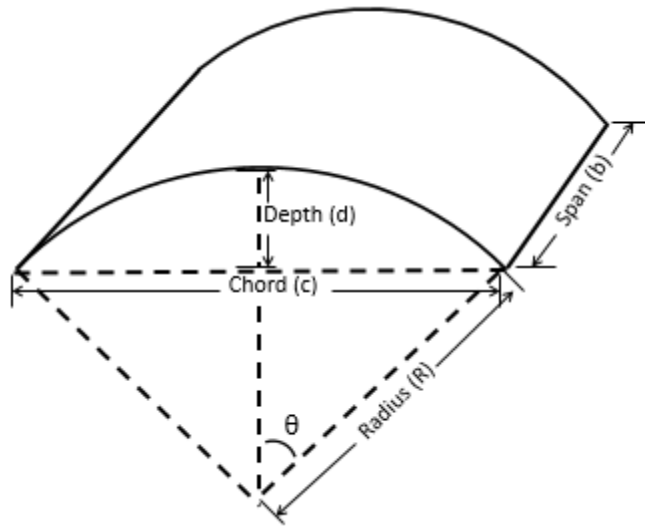


Figure 4-1. Curved membrane nomenclature.

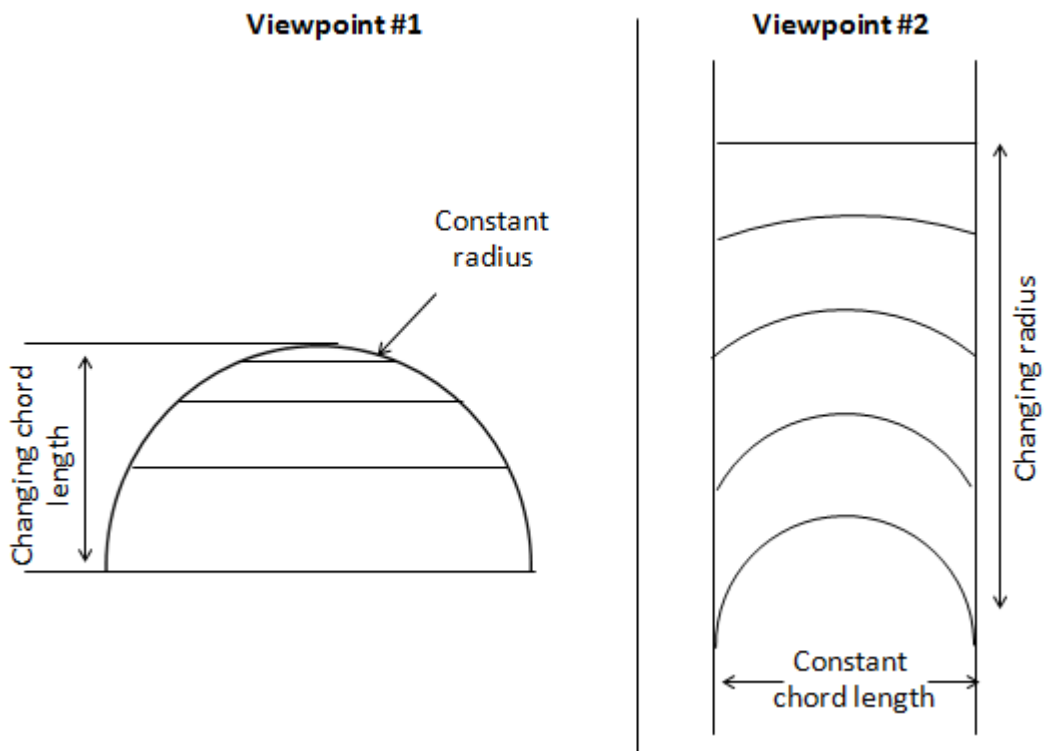


Figure 4-2. Two alternate perspectives to approach the varying depth ratio problem.

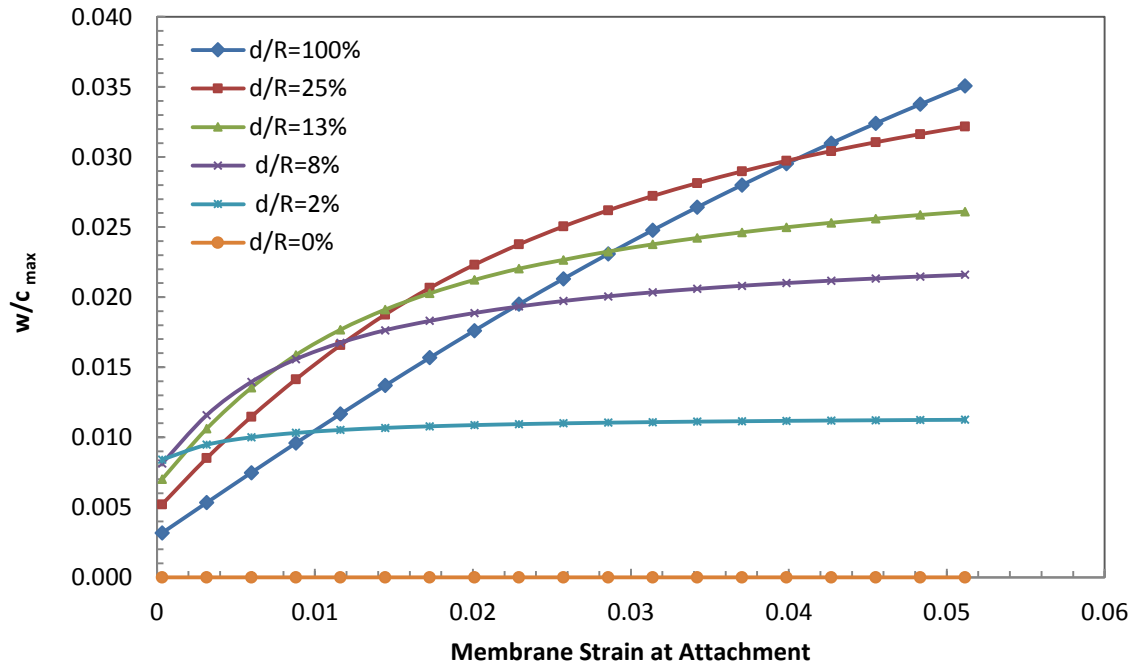


Figure 4-3. Normalized maximum out-of-plane displacements versus temperature for various depth ratios when a silicone membrane is attached on a closed curved frame with an AR of 0.5.

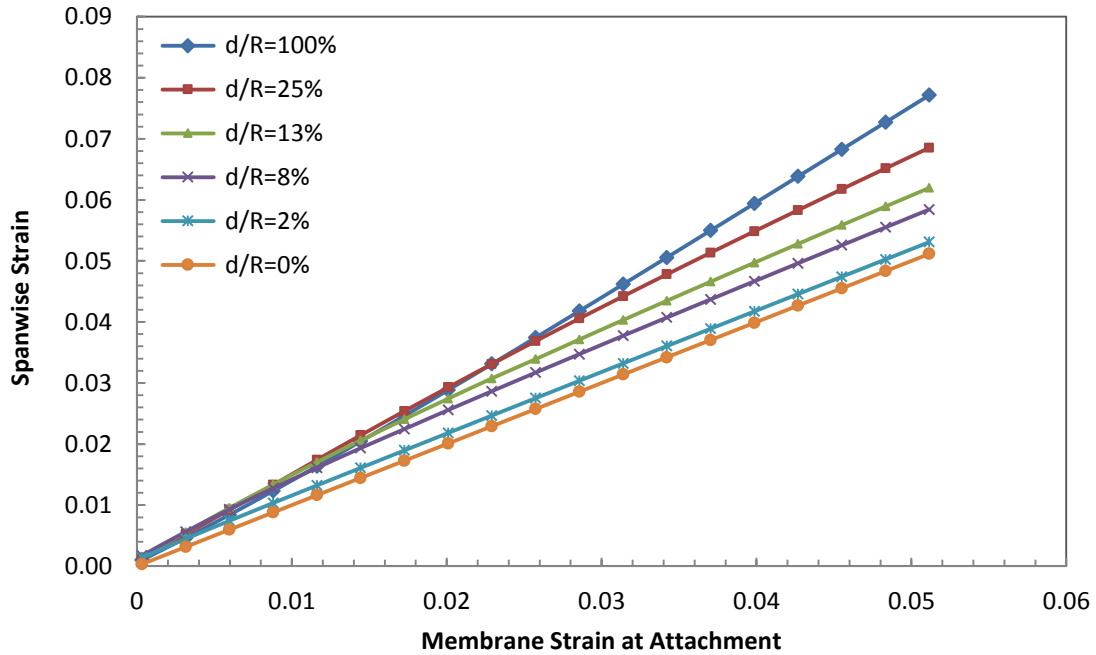


Figure 4-4. Spanwise strains at the maximum out-of-plane displacement locations versus membrane strain at attachment for various depth ratios when a silicone membrane is attached on a closed curved frame with an AR of 0.5.

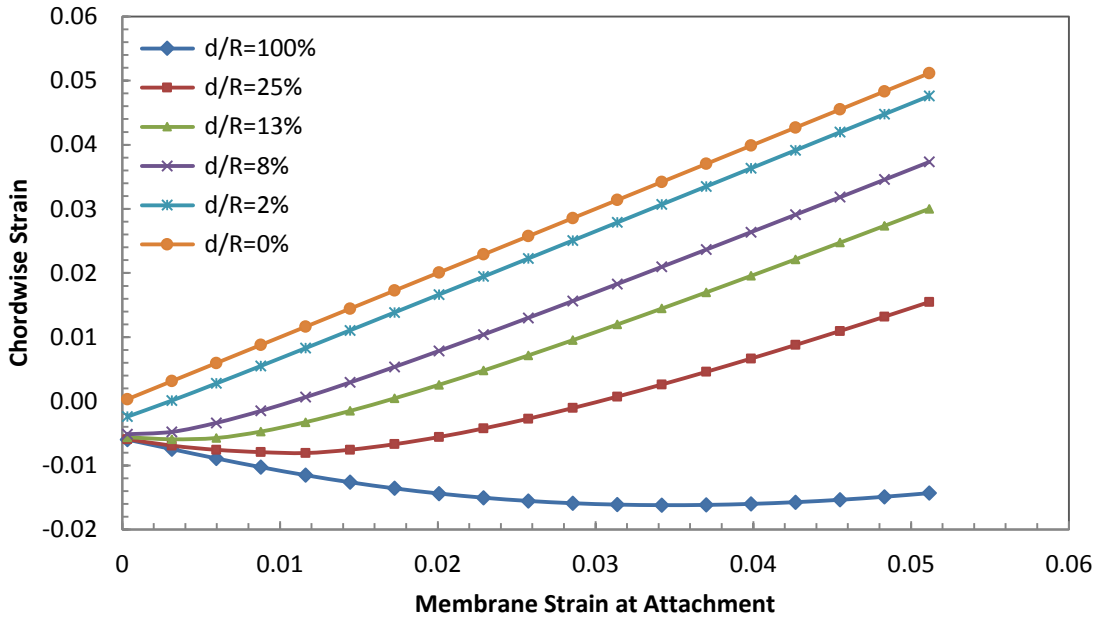


Figure 4-5. Chordwise strains at the maximum out-of-plane displacement locations versus membrane strain at attachment for various depth ratios when a silicone membrane is attached on a closed curved frame with an AR of 0.5.

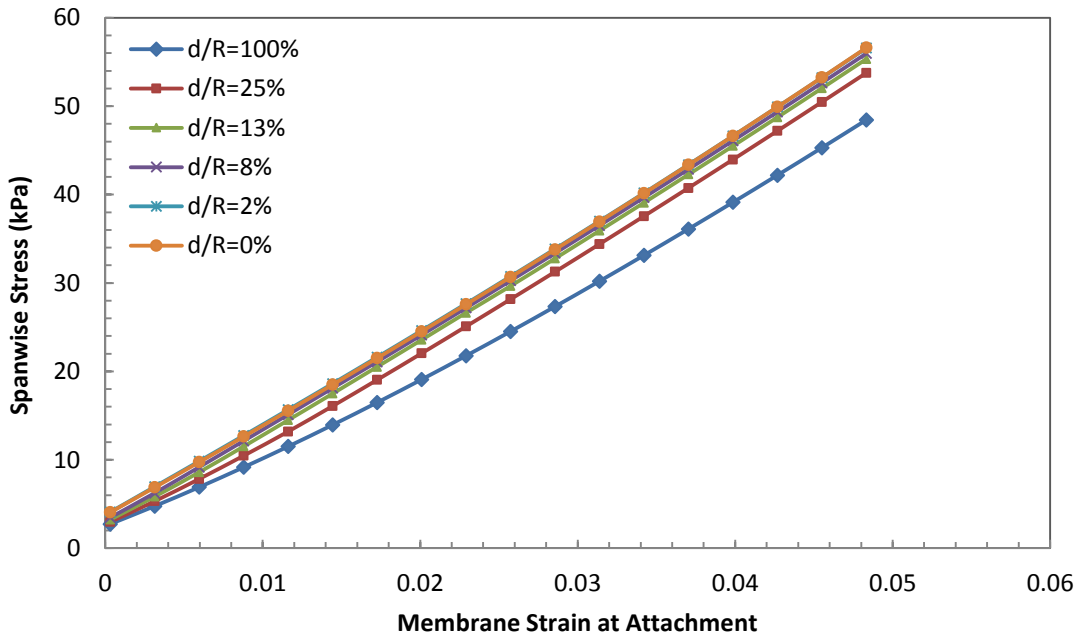


Figure 4-6. Spanwise stresses (kPa) at the maximum out-of-plane displacement locations versus membrane strain at attachment for various depth ratios when a silicone membrane is attached on a closed curved frame with an AR of 0.5.

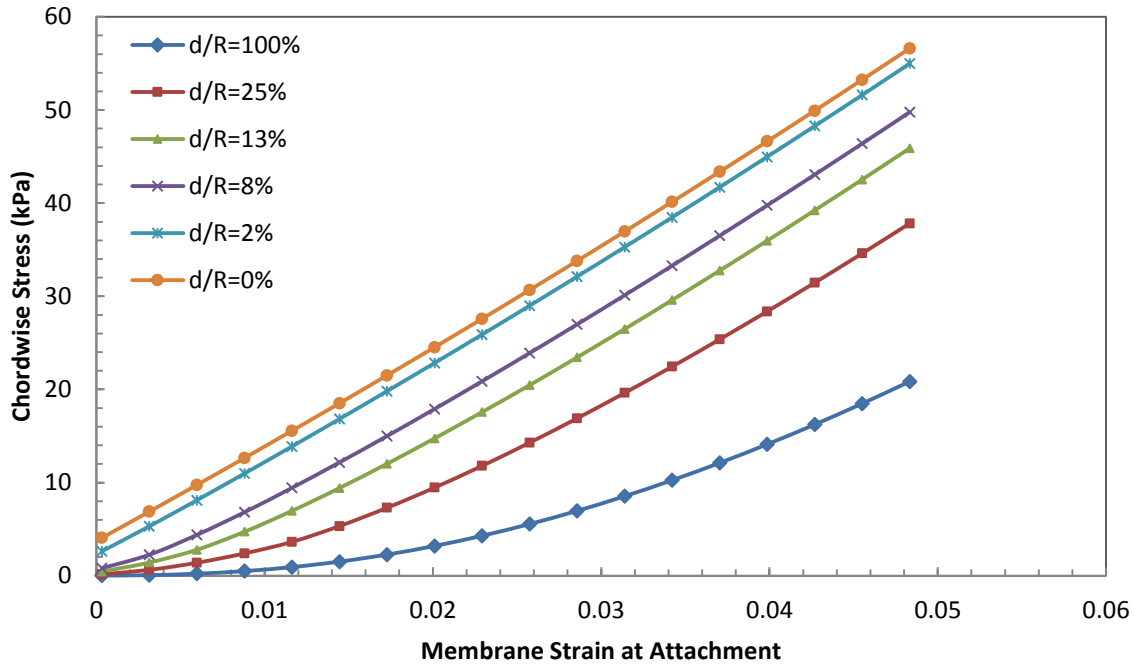


Figure 4-7. Chordwise stresses (kPa) at the maximum out-of-plane displacement locations versus membrane strain at attachment for various depth ratios when a silicone membrane is attached on a closed curved frame with an AR of 0.5.

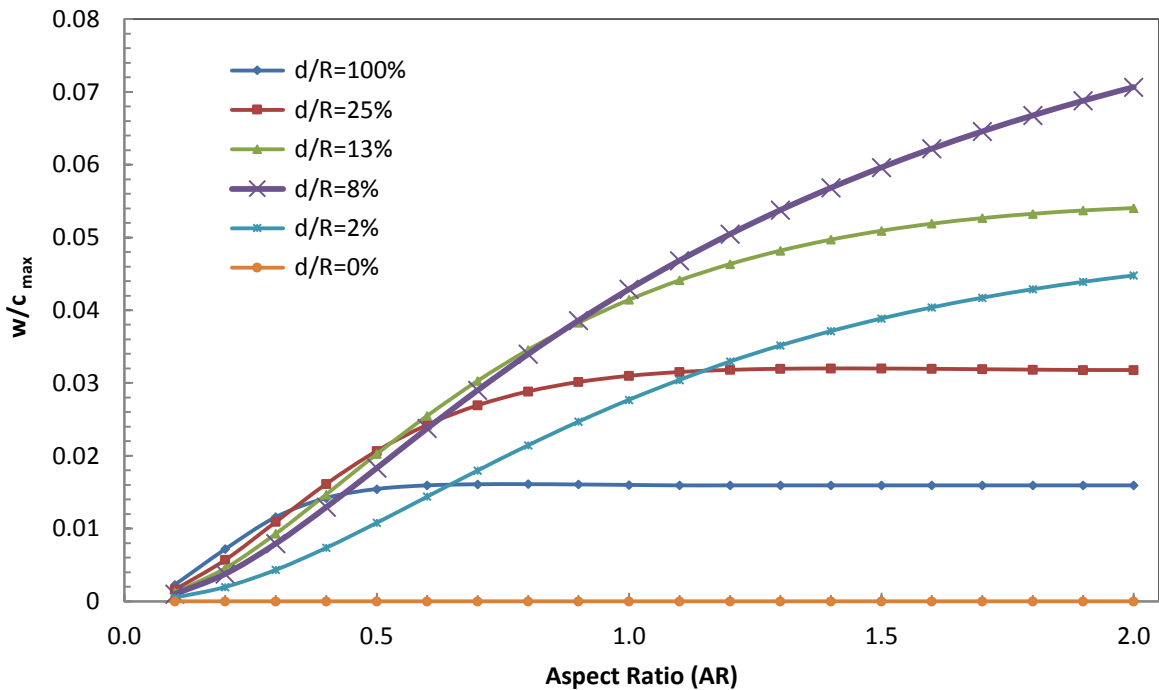


Figure 4-8. Normalized maximum out-of-plane displacements for various aspect ratios and depth ratios for a silicone membrane attached on a closed curved frame at 100°C (1.7% membrane strain).

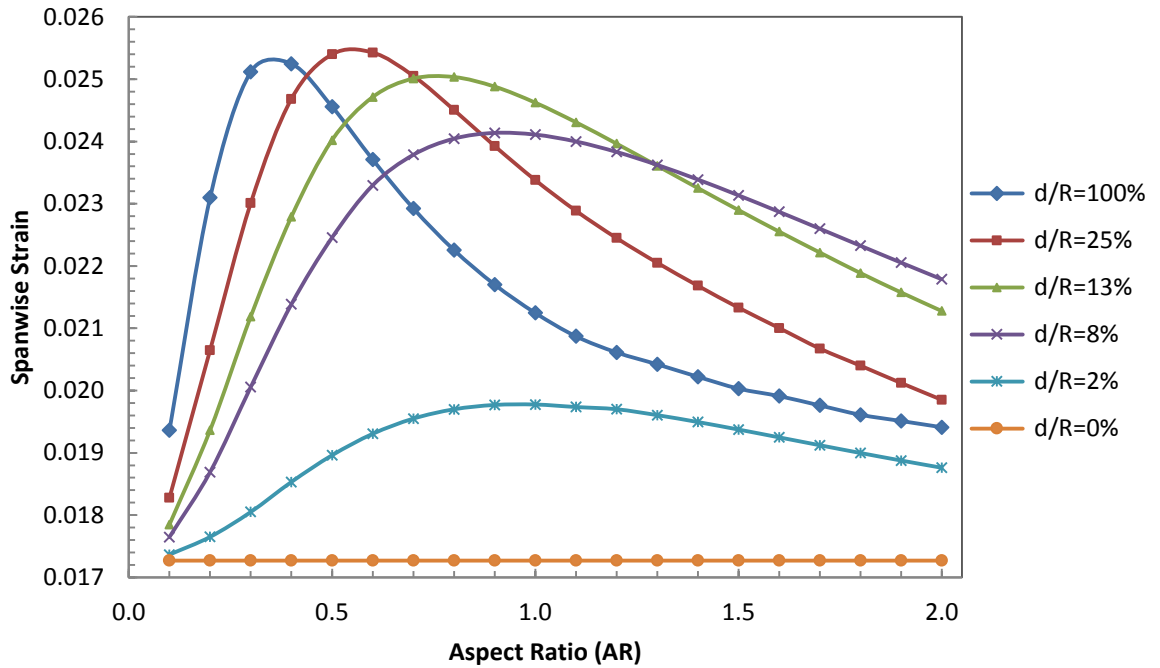


Figure 4-9. Spanwise strains at the maximum out-of-plane displacement locations versus aspect ratio for various depth ratios when a silicone membrane is attached on a closed curved frame at 100°C (1.7% membrane strain).

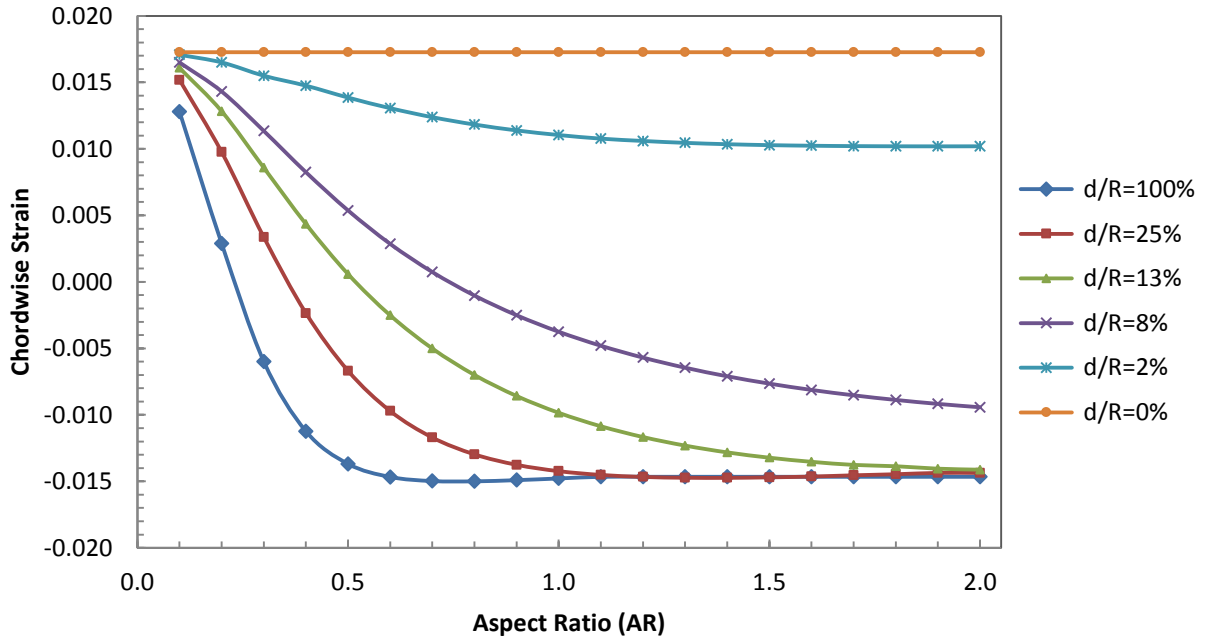


Figure 4-10. Chordwise strains at the maximum out-of-plane displacement locations versus aspect ratio for various depth ratios when a silicone membrane is attached on a closed curved frame at 100°C (1.7% membrane strain).

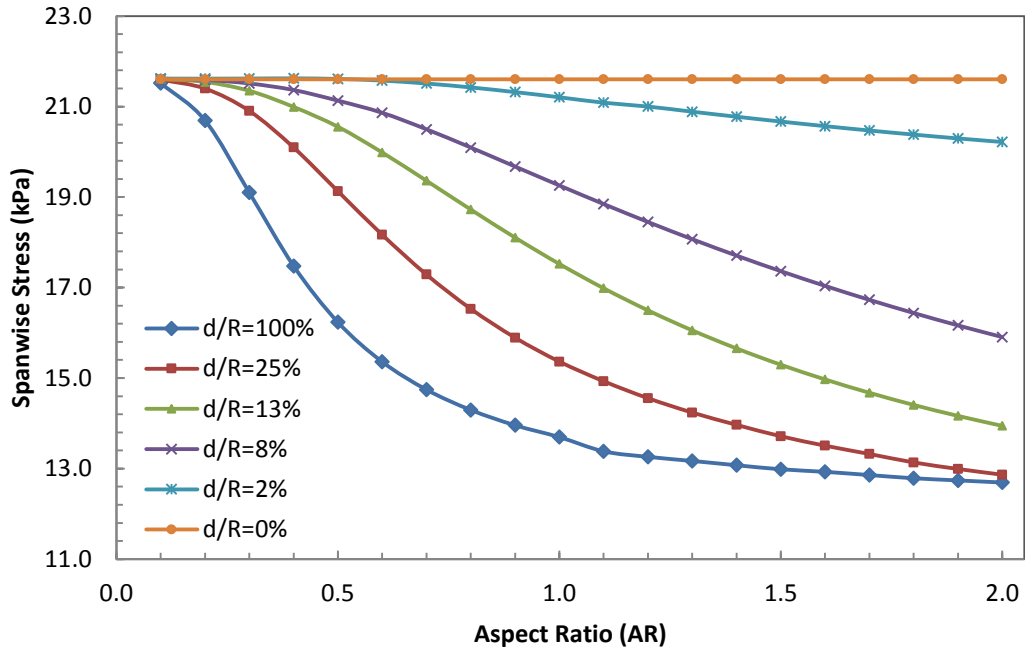


Figure 4-11. Spanwise stresses (kPa) at the maximum out-of-plane displacement locations versus aspect ratio for various depth ratios when a silicone membrane is attached on a closed curved frame at 100°C (1.7% membrane strain).

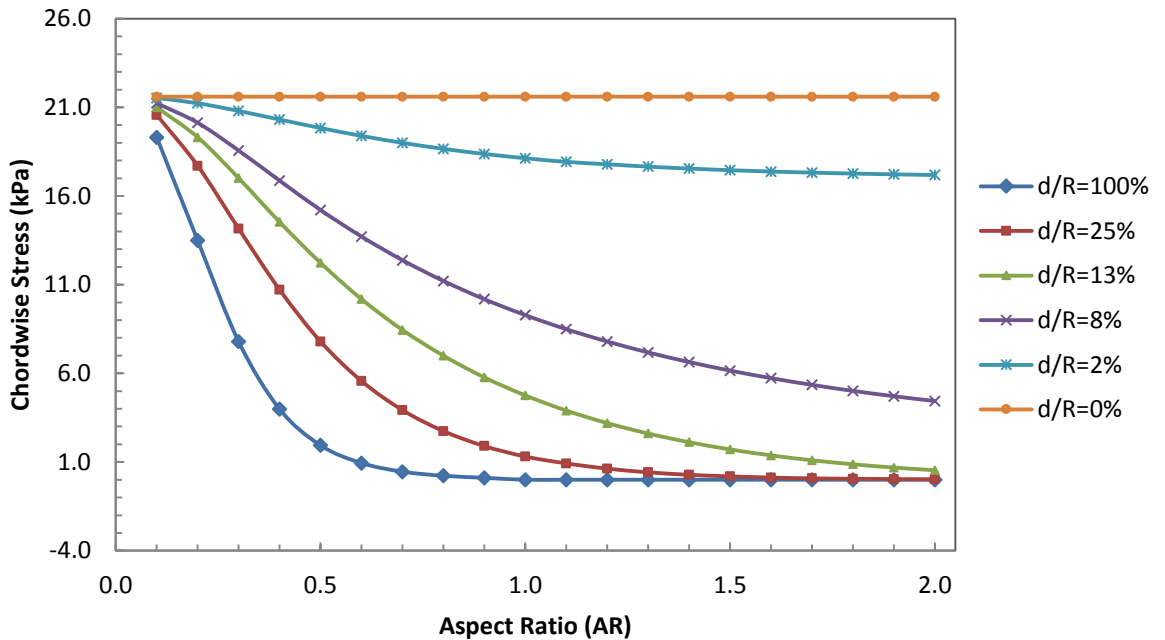


Figure 4-12. Chordwise stresses (kPa) at the maximum out-of-plane displacement locations versus aspect ratio for various depth ratios when a silicone membrane is attached on a closed curved frame at 100°C (1.7% membrane strain).

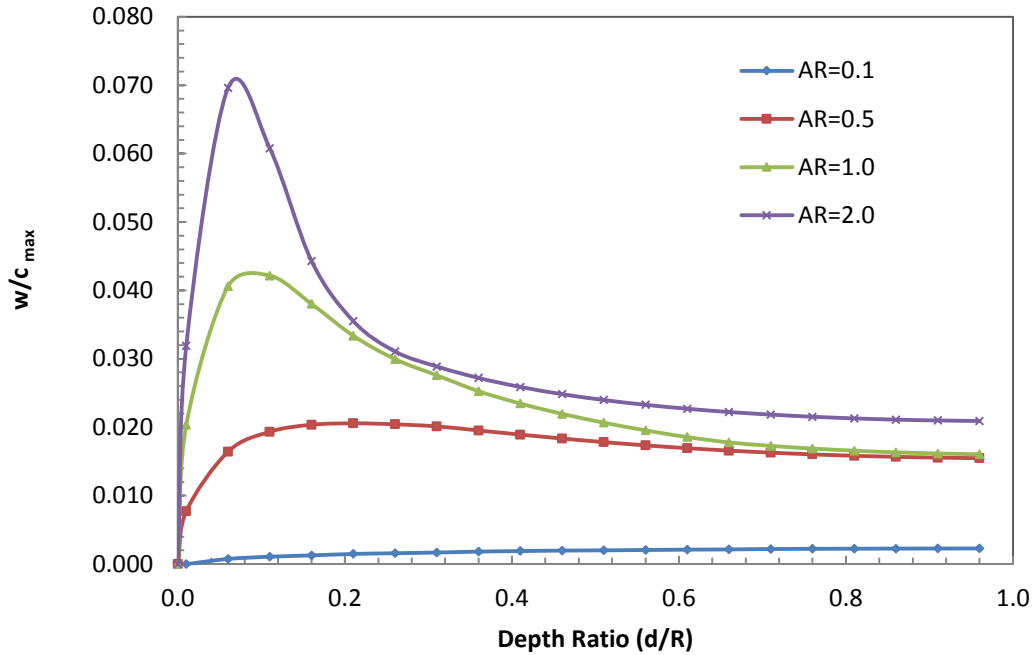


Figure 4-13. Normalized maximum out-of-plane displacements versus depth ratio for various aspect ratios when a silicone membrane is attached on a closed curved frame at 100°C (1.7% membrane strain).

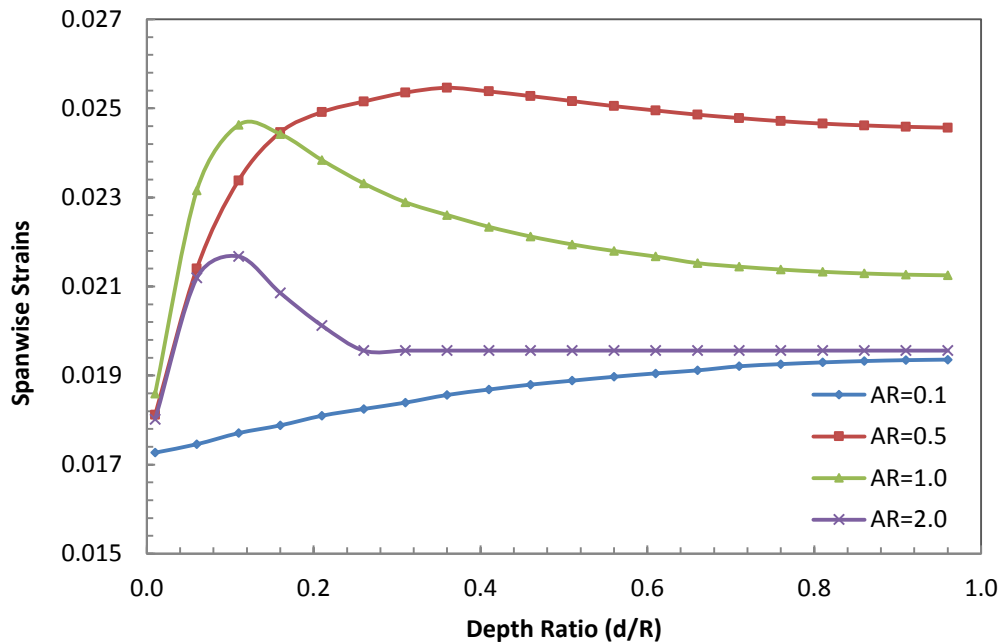


Figure 4-14. Spanwise strains at the maximum out-of-plane displacement locations versus depth ratio for various aspect ratios when a silicone membrane is attached on a closed curved frame at 100°C (1.7% membrane strain).

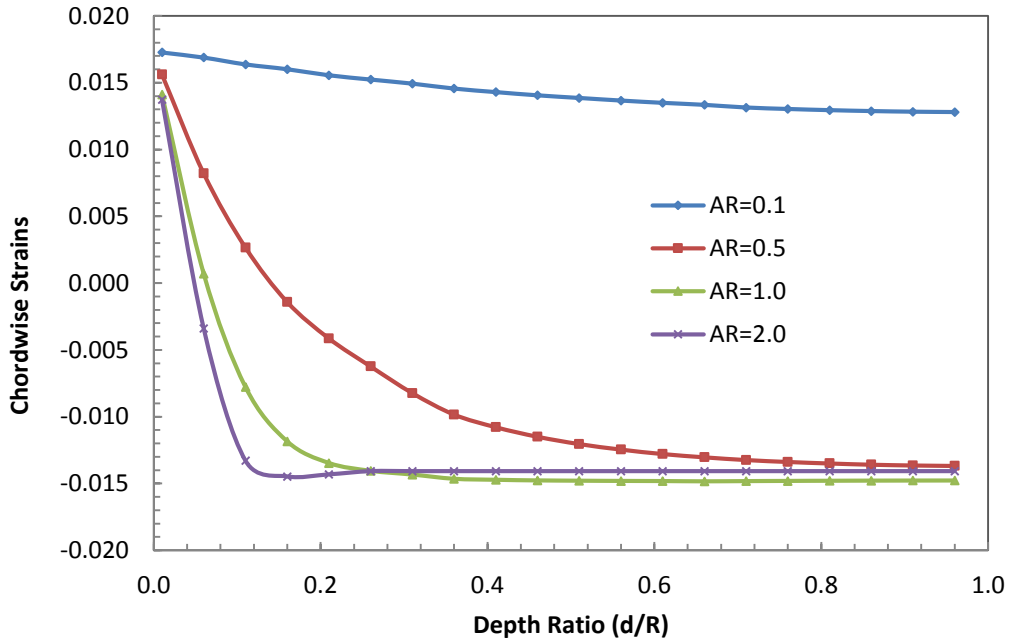


Figure 4-15. Chordwise strains at the maximum out-of-plane displacement locations versus depth ratio for various aspect ratios when a silicone membrane is attached on a closed curved frame at 100°C (1.7% membrane strain).

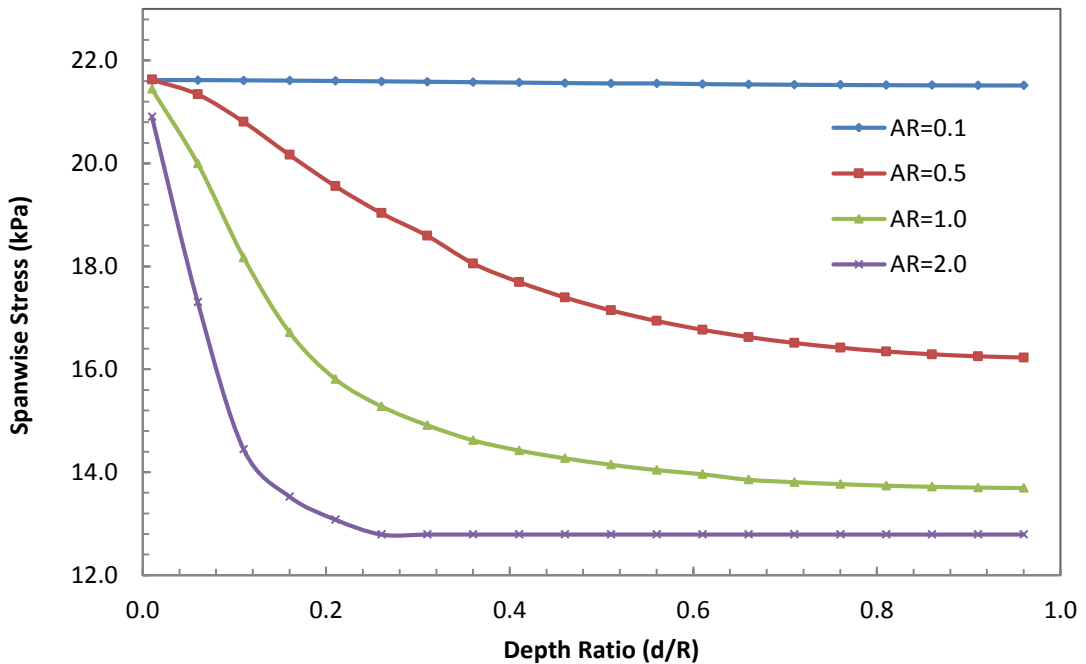


Figure 4-16. Spanwise stresses (kPa) at the maximum out-of-plane displacement locations versus depth ratio for various aspect ratios when a silicone membrane attached on a closed curved frame at 100°C (1.7% membrane strain).

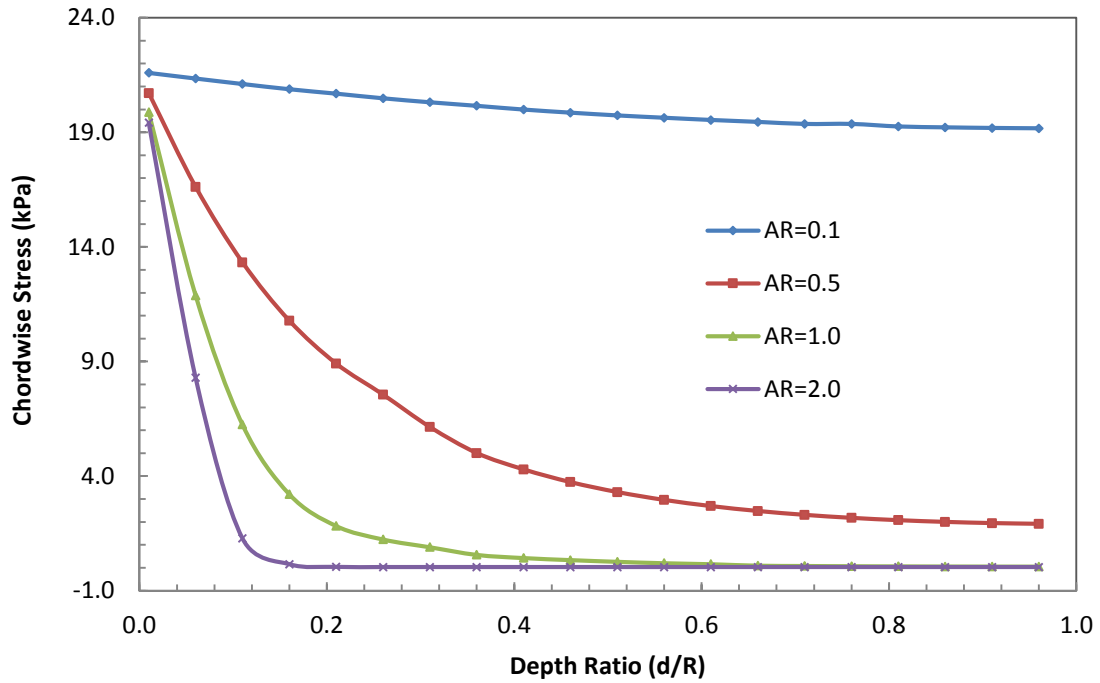


Figure 4-17. Chordwise stresses (kPa) at the maximum out-of-plane displacement locations versus depth ratio for various aspect ratios when a silicone membrane attached on a closed curved frame at 100°C (1.7% membrane strain).

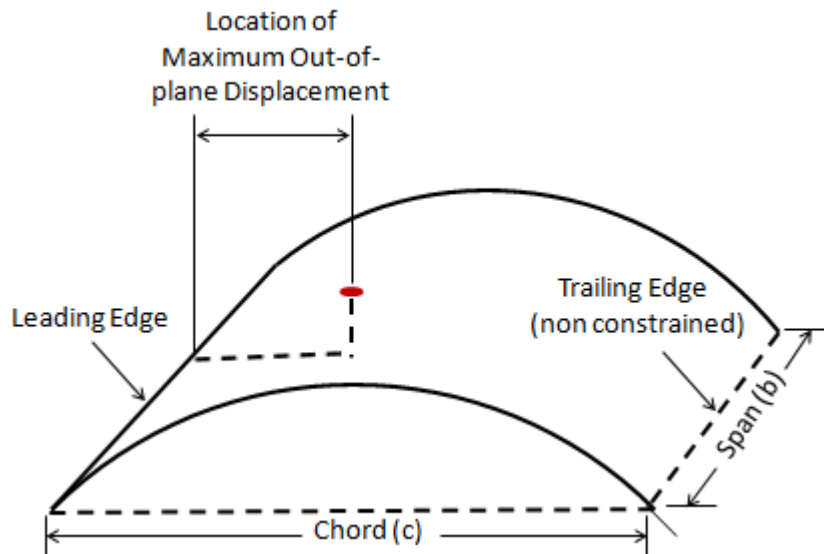


Figure 4-18. Determining the location of maximum out-of-plane displacement.

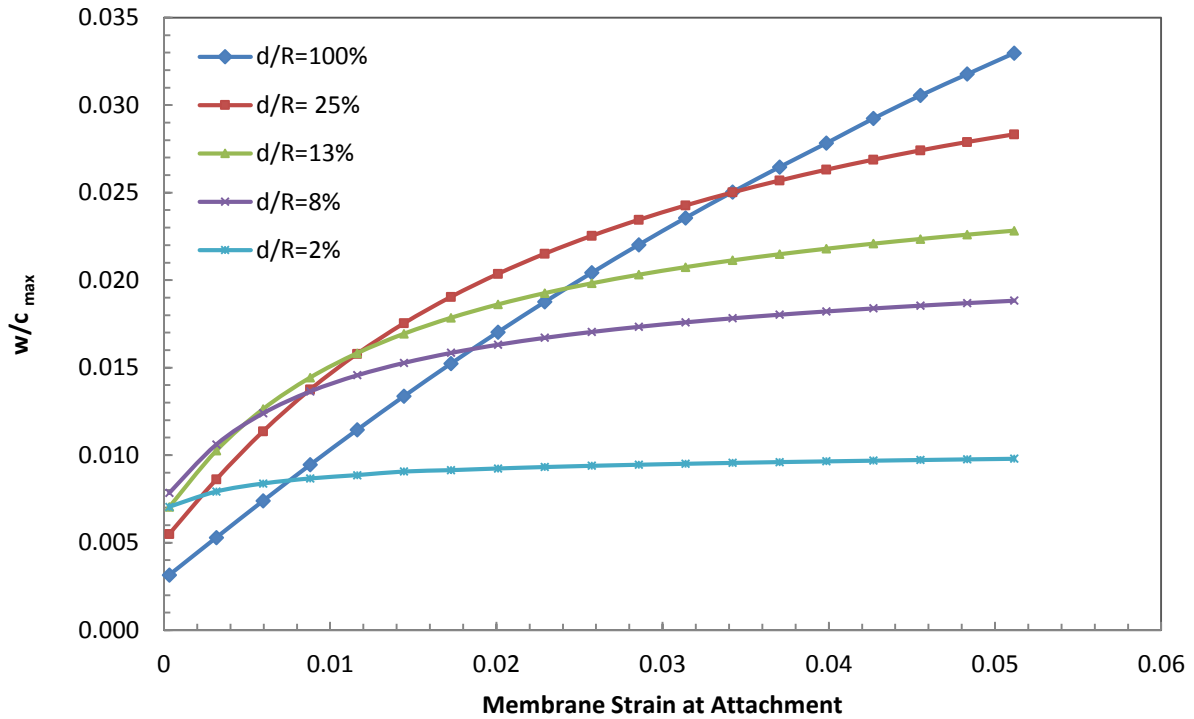


Figure 4-19. Normalized maximum out-of-plane displacements versus temperature for various depth ratios when a silicone membrane is attached on an open curved frame with an AR of 0.5.

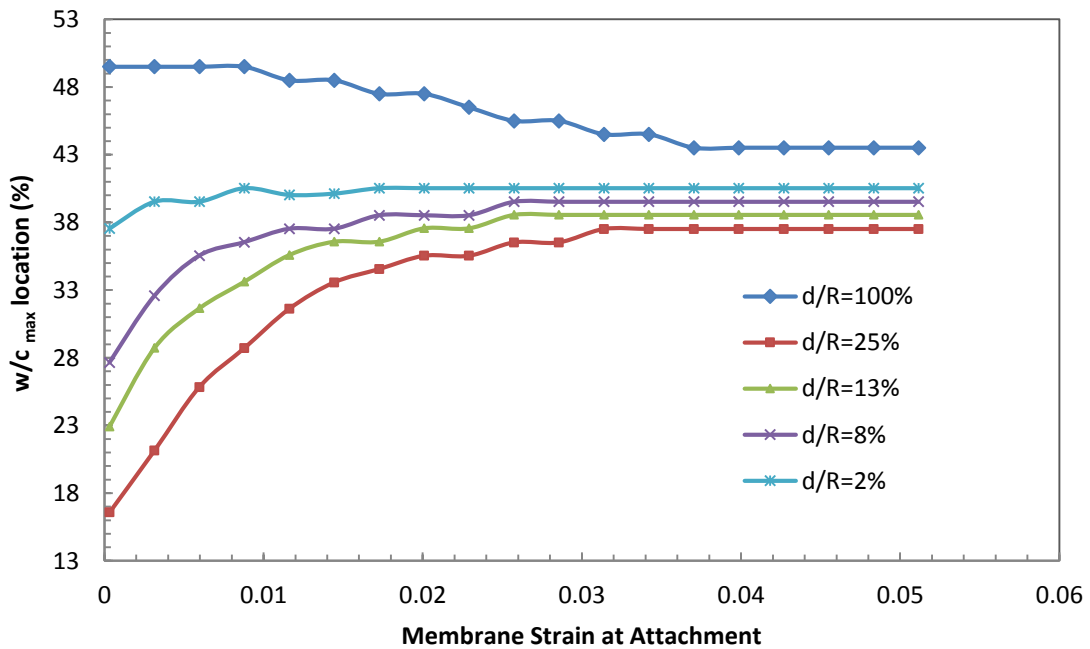


Figure 4-20. Location of the maximum out-of-plane displacements versus membrane strain at attachment for various depth ratios when a silicone membrane is attached on an open curved frame with an AR of 0.5.

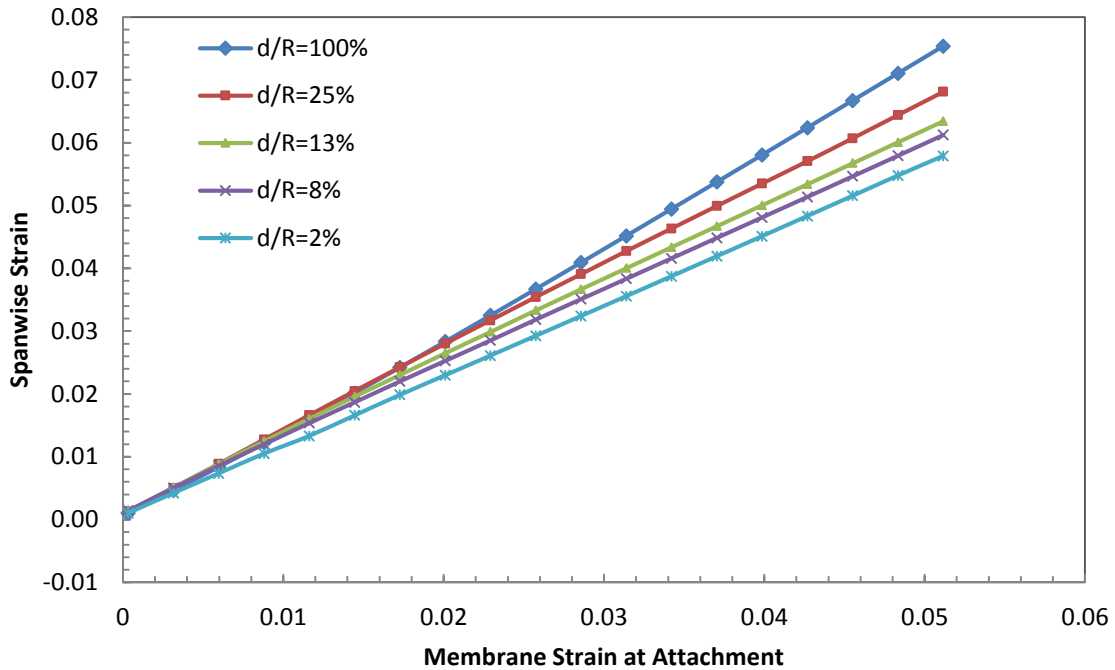


Figure 4-21. Spanwise strains at the maximum out-of-plane displacement locations versus membrane strain at attachment for various depth ratios when a silicone membrane is attached on an open curved frame with an AR of 0.5.

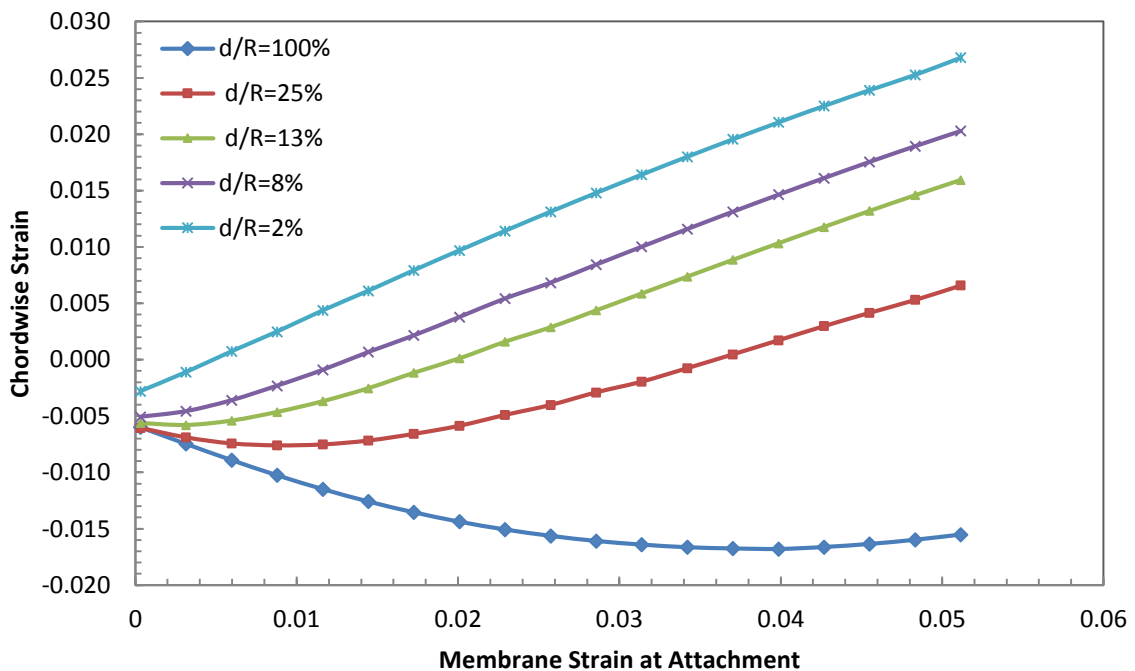


Figure 4-22. Chordwise strains at the maximum out-of-plane displacement locations versus membrane strain at attachment for various depth ratios when a silicone membrane is attached on an open curved frame with an AR of 0.5.

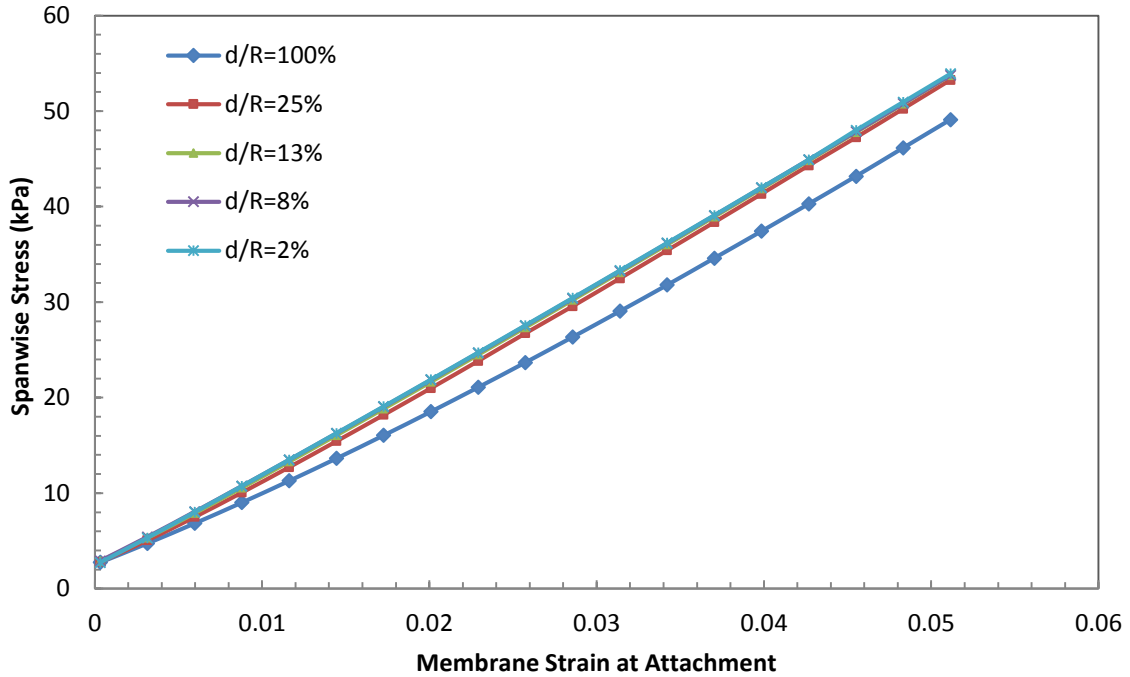


Figure 4-23. Spanwise stresses (kPa) at the maximum out-of-plane displacement locations versus membrane strain at attachment for various depth ratios when a silicone membrane is attached on an open curved frame with an AR of 0.5.

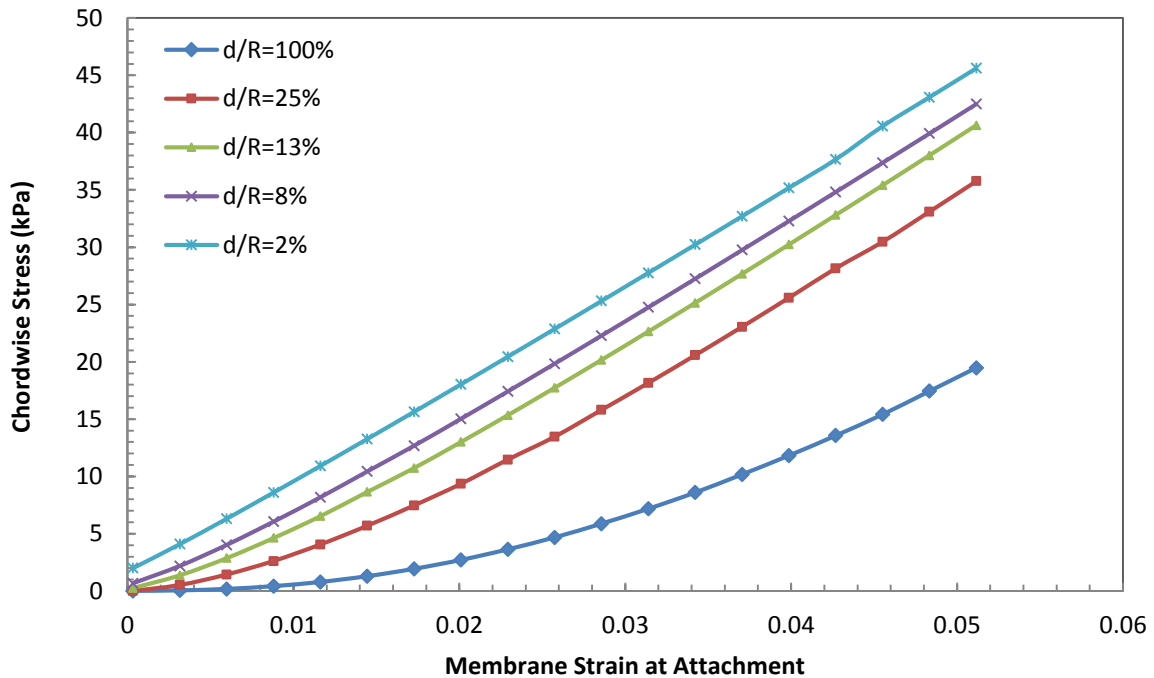


Figure 4-24. Chordwise stresses (kPa) at the maximum out-of-plane displacement locations versus membrane strain at attachment for various depth ratios when a silicone membrane is attached on an open curved frame with an AR of 0.5.

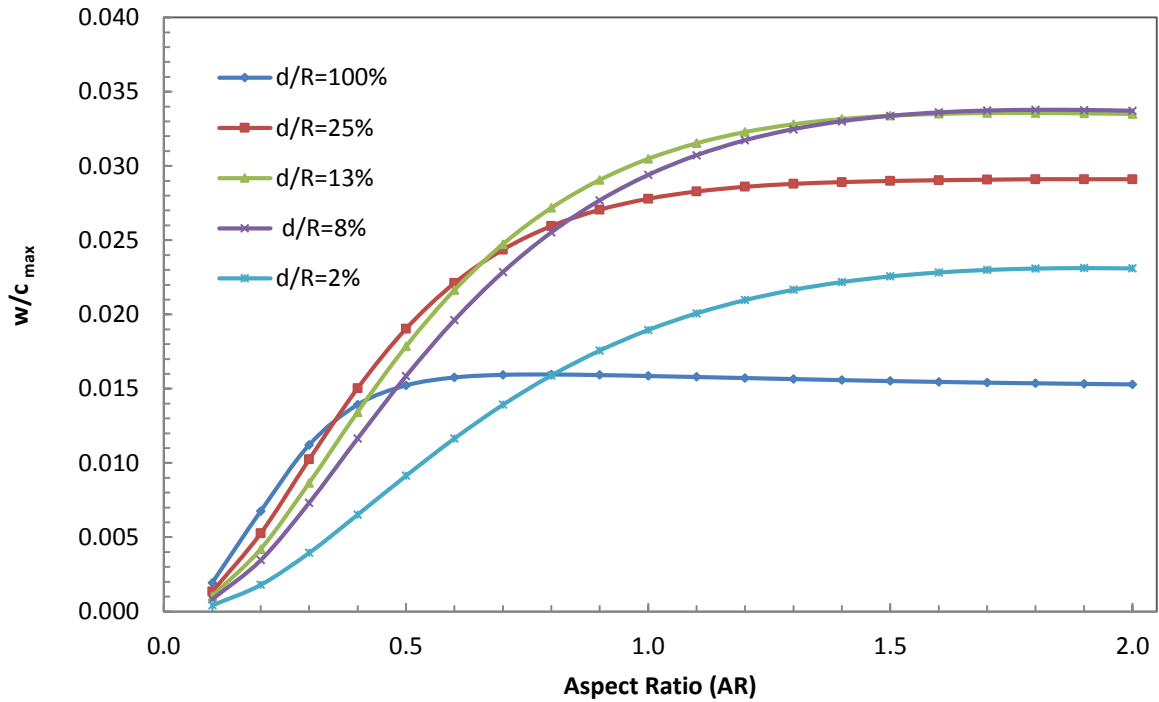


Figure 4-25. Normalized maximum out-of-plane displacements versus aspect ratio for various depth ratios when a silicone membrane is attached on an open curved frame at 100°C (1.7% membrane strain).

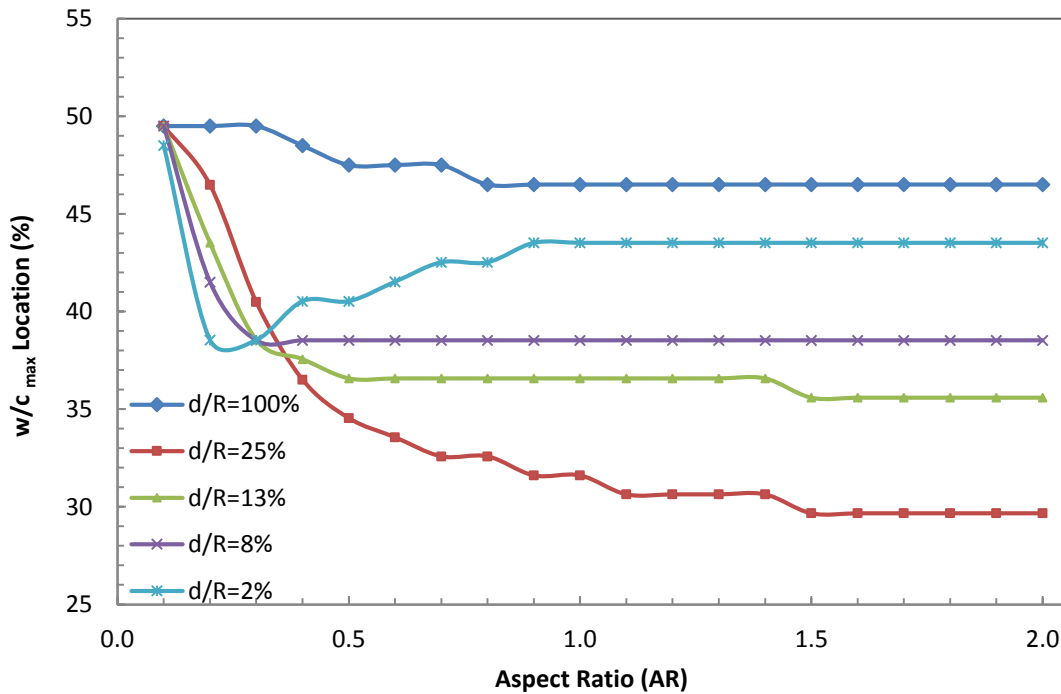


Figure 4-26. Location of the maximum out-of-plane displacements versus AR for various depth ratios when a silicone membrane is attached on an open curved frame at 100°C (1.7% membrane strain).

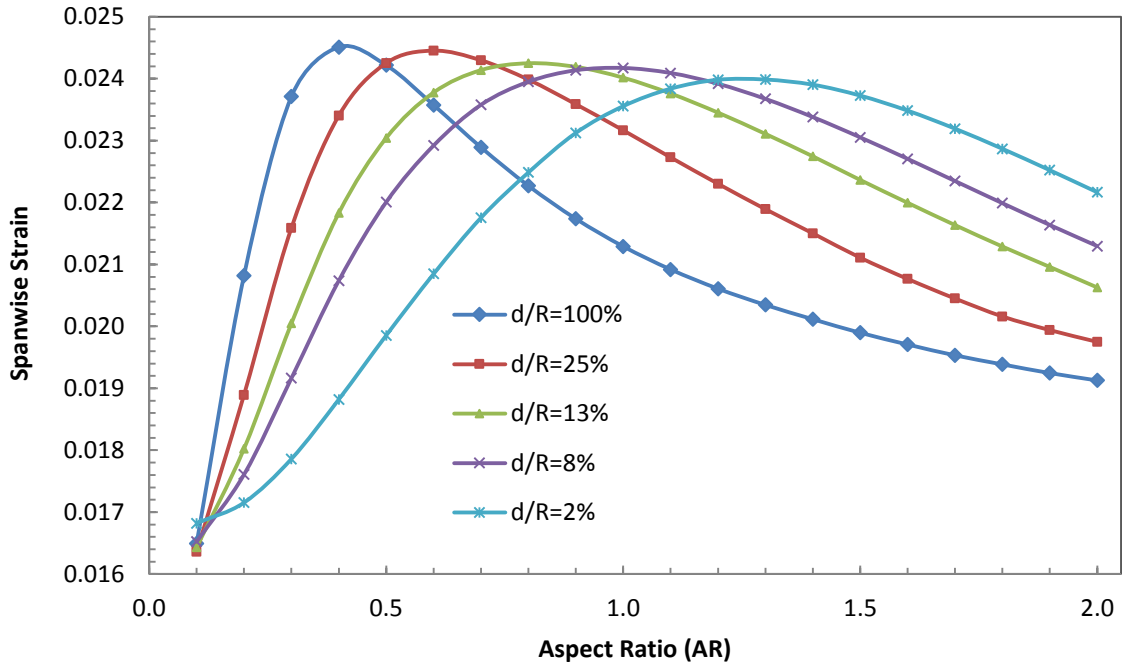


Figure 4-27. Spanwise strains at the maximum out-of-plane displacement locations versus AR for various depth ratios when a silicone membrane is attached on an open curved frame at 100°C (1.7% membrane strain).

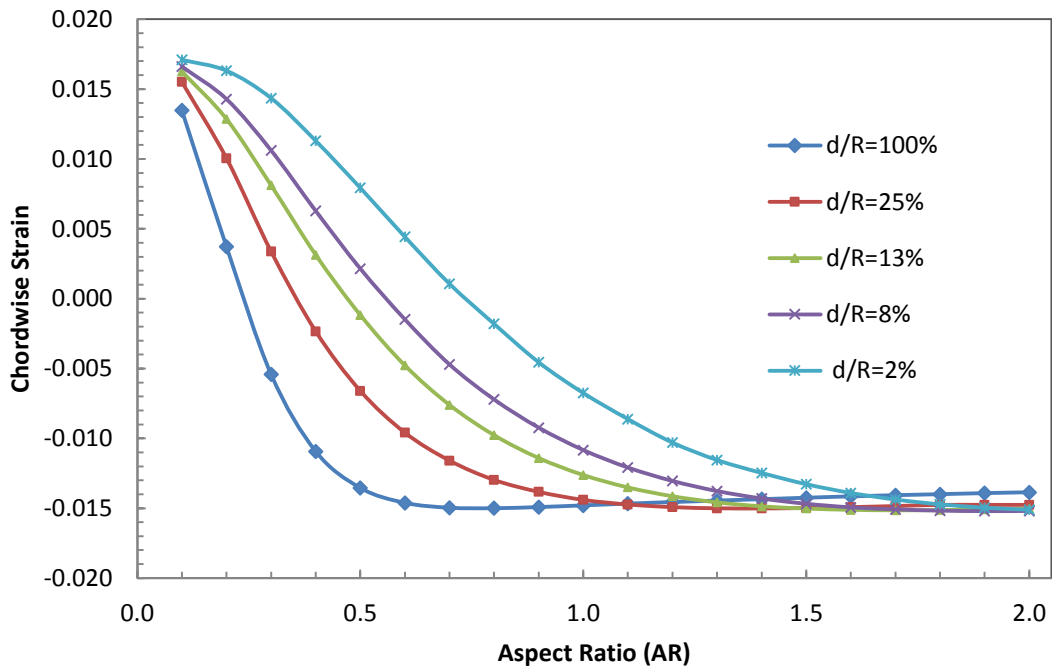


Figure 4-28. Chordwise strains at the maximum out-of-plane displacement locations versus AR for various depth ratios when a silicone membrane is attached on an open curved frame at 100°C (1.7% membrane strain).

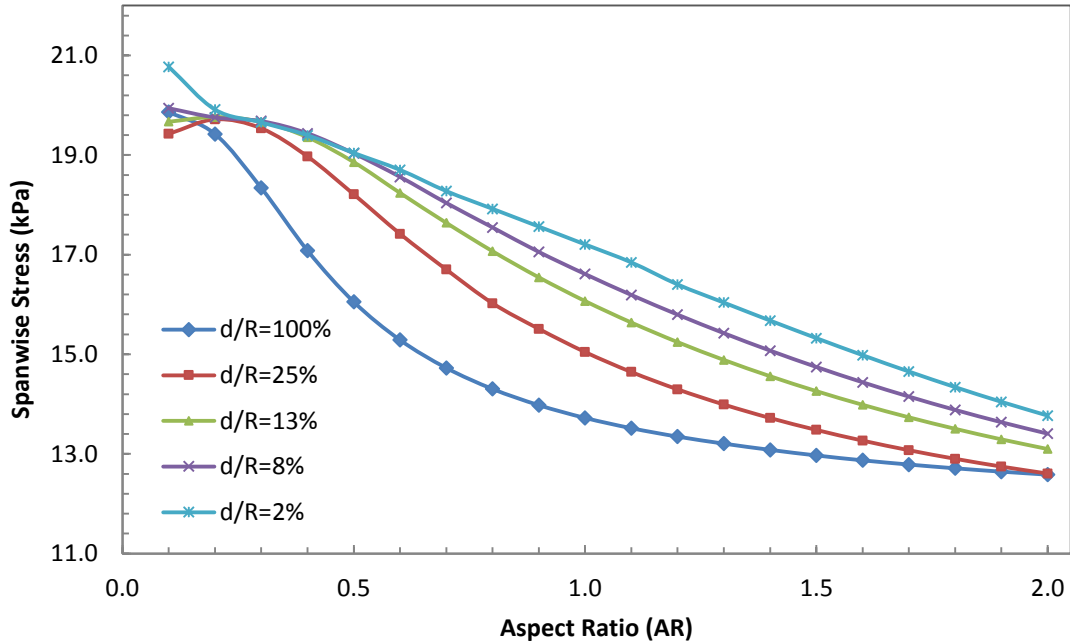


Figure 4-29. Spanwise stresses (kPa) at the maximum out-of-plane displacement locations versus AR for various depth ratios when a silicone membrane is attached on an open curved frame at 100°C (1.7% membrane strain).

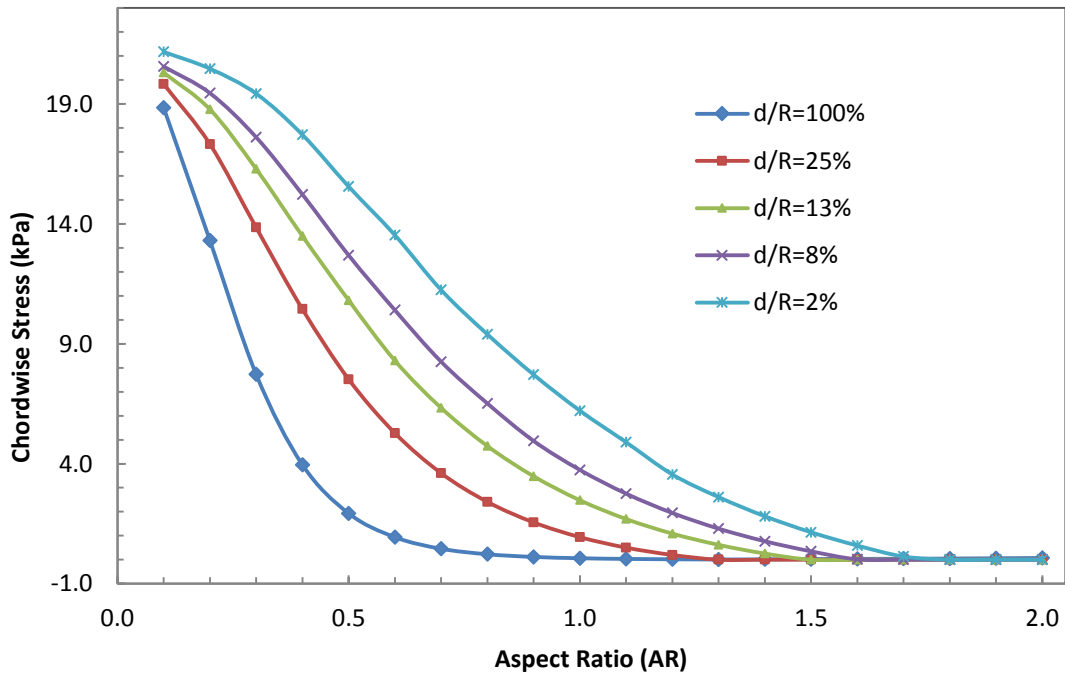


Figure 4-30. Chordwise stresses (kPa) at the maximum out-of-plane displacement locations versus AR for various depth ratios when a silicone membrane is attached on an open curved frame at 100°C (1.7% membrane strain).

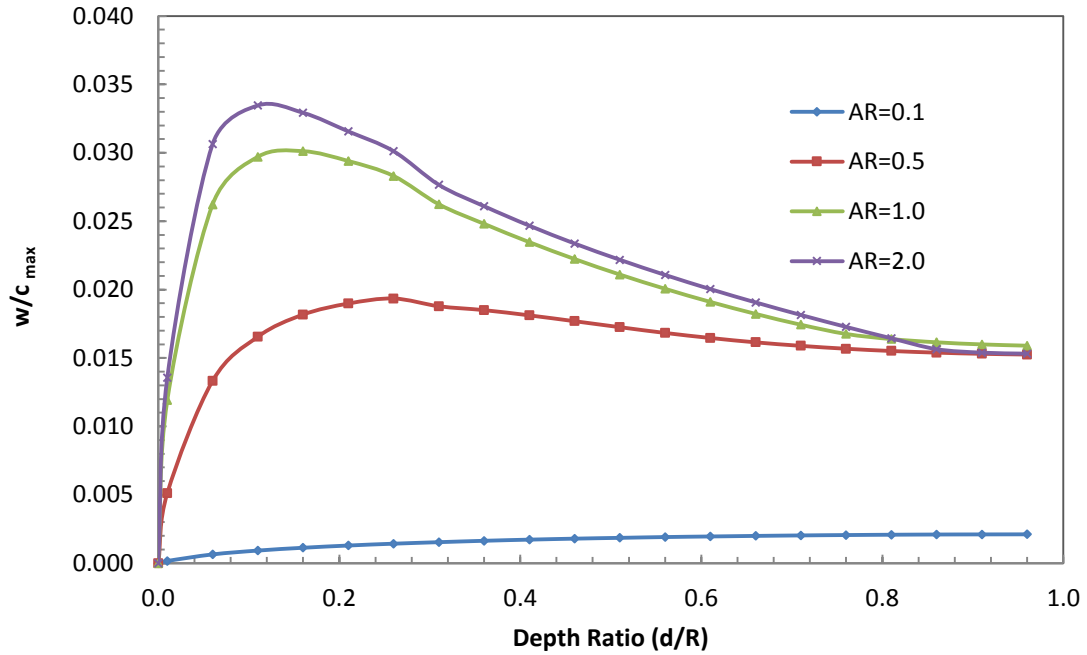


Figure 4-31. Normalized maximum out-of-plane displacements versus depth ratio for various aspect ratios when a silicone membrane is attached on an open curved frame at 100°C (1.7% membrane strain).

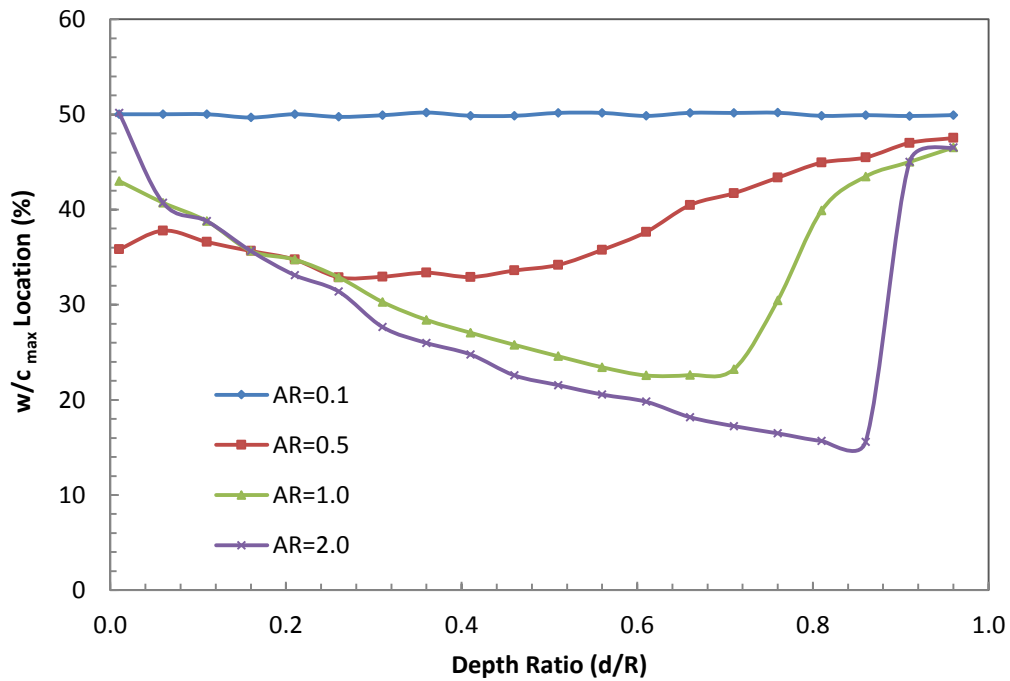


Figure 4-32. Location of the maximum out-of-plane displacements versus DR for various aspect ratios when a silicone membrane is attached on an open curved frame at 100°C (1.7% membrane strain).

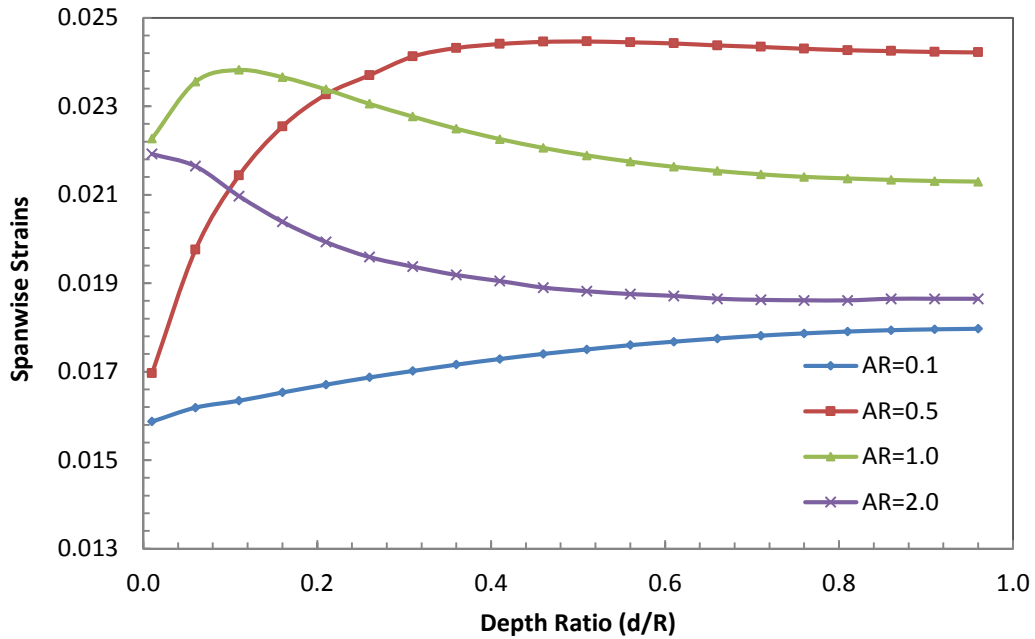


Figure 4-33. Spanwise strains at the maximum out-of-plane displacement locations versus depth ratio for various aspect ratios when a silicone membrane is attached on an open curved frame at 100°C (1.7% membrane strain).

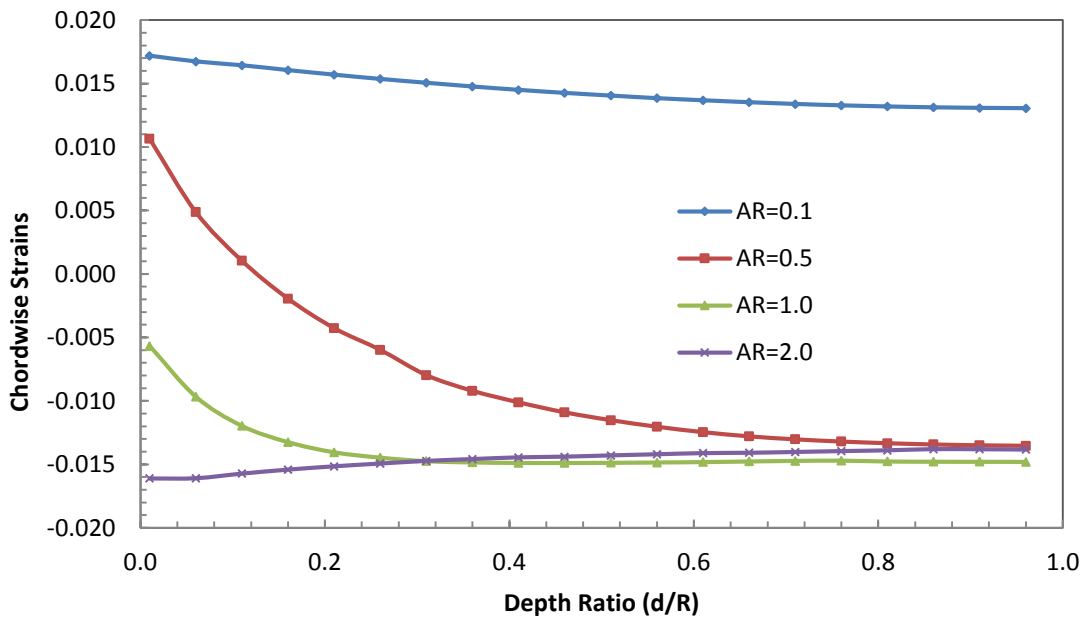


Figure 4-34. Chordwise strains at the maximum out-of-plane displacement locations versus depth ratio for various aspect ratios when a silicone membrane is attached on an open curved frame at 100°C (1.7% membrane strain).

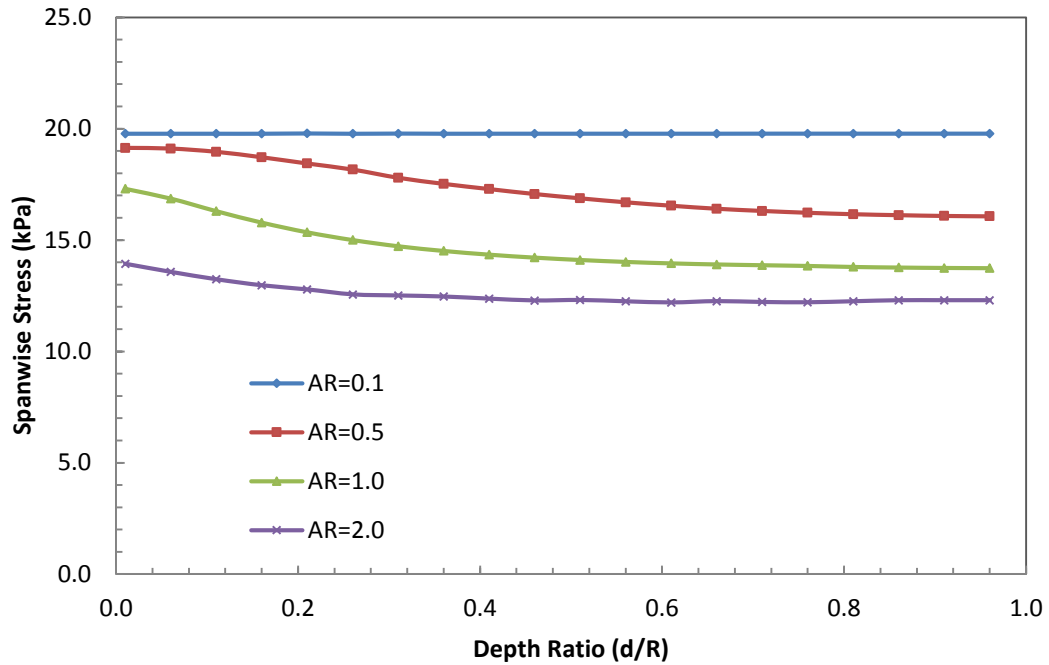


Figure 4-35. Spanwise stresses (kPa) at the maximum out-of-plane displacement locations versus depth ratio for various aspect ratios when a silicone membrane is attached on an open curved frame at 100°C (1.7% membrane strain).

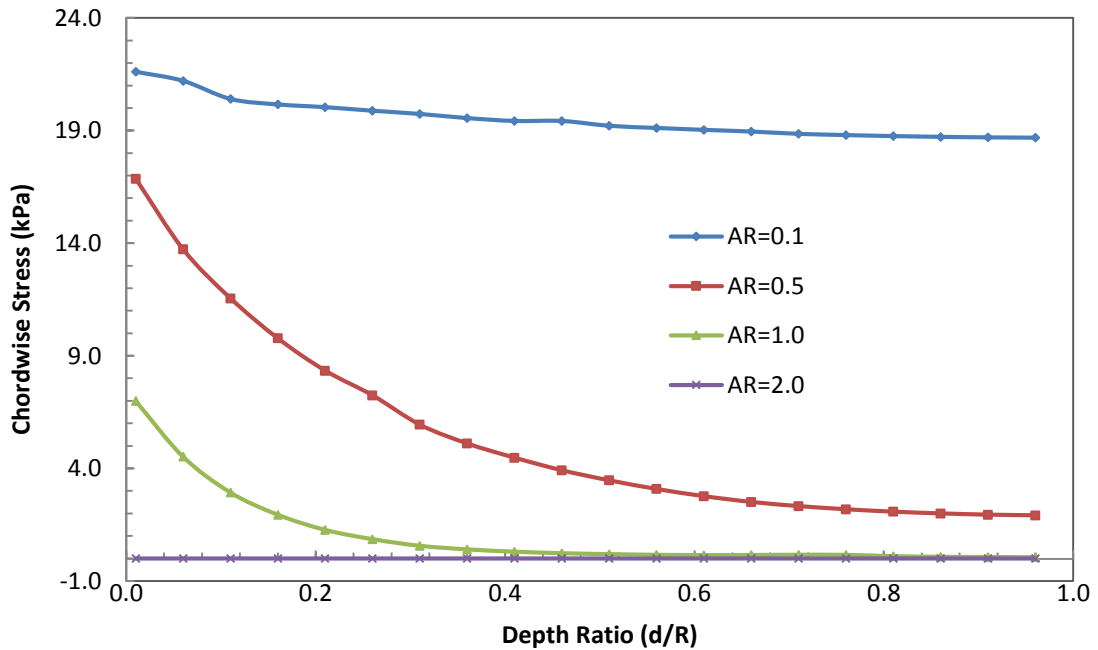


Figure 4-36. Chordwise stresses (kPa) at the maximum out-of-plane displacement locations versus depth ratio for various aspect ratios when a silicone

membrane is attached on an open curved frame at 100°C (1.7% membrane strain).

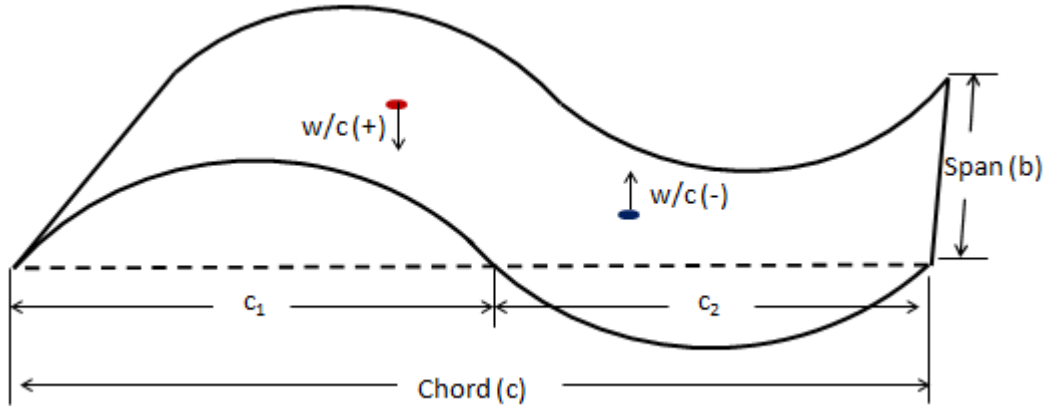


Figure 4-37. The two extreme displacement locations of a membrane on a doubly curved frame.

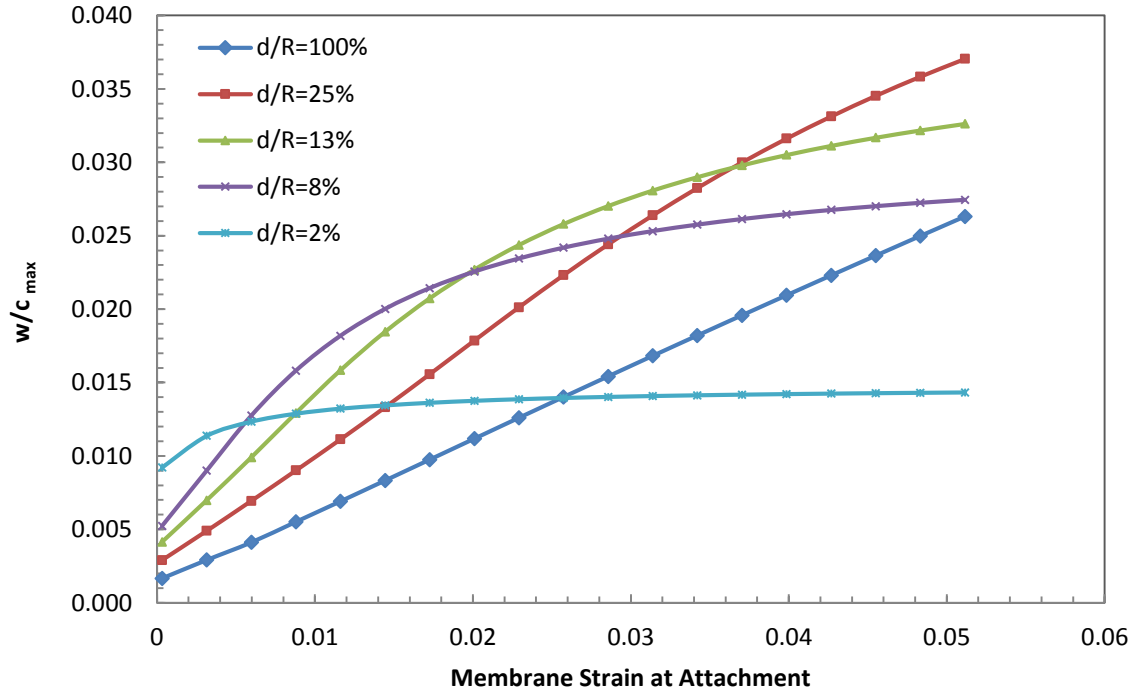


Figure 4-38. Normalized maximum out-of-plane displacements versus membrane strain at attachment for various depth ratios when a silicone membrane is attached on a closed double curved frame with an AR of 0.5.

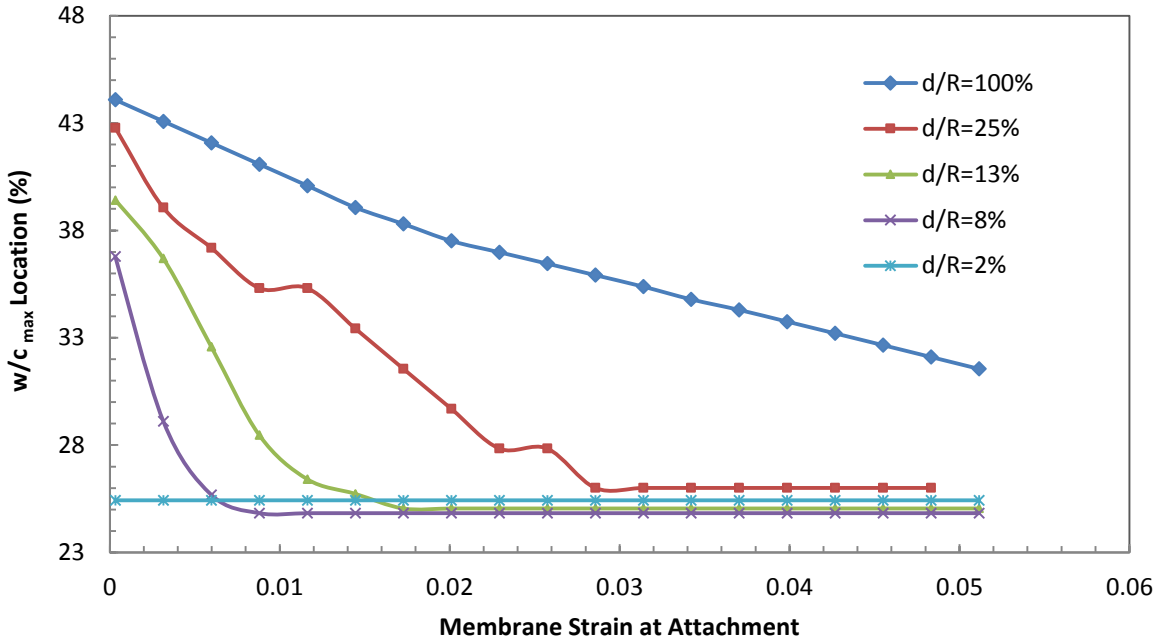


Figure 4-39. Location of the maximum out-of-plane displacements versus membrane strain at attachment for various depth ratios when a silicone membrane is attached on a closed double curved frame with an AR of 0.5.

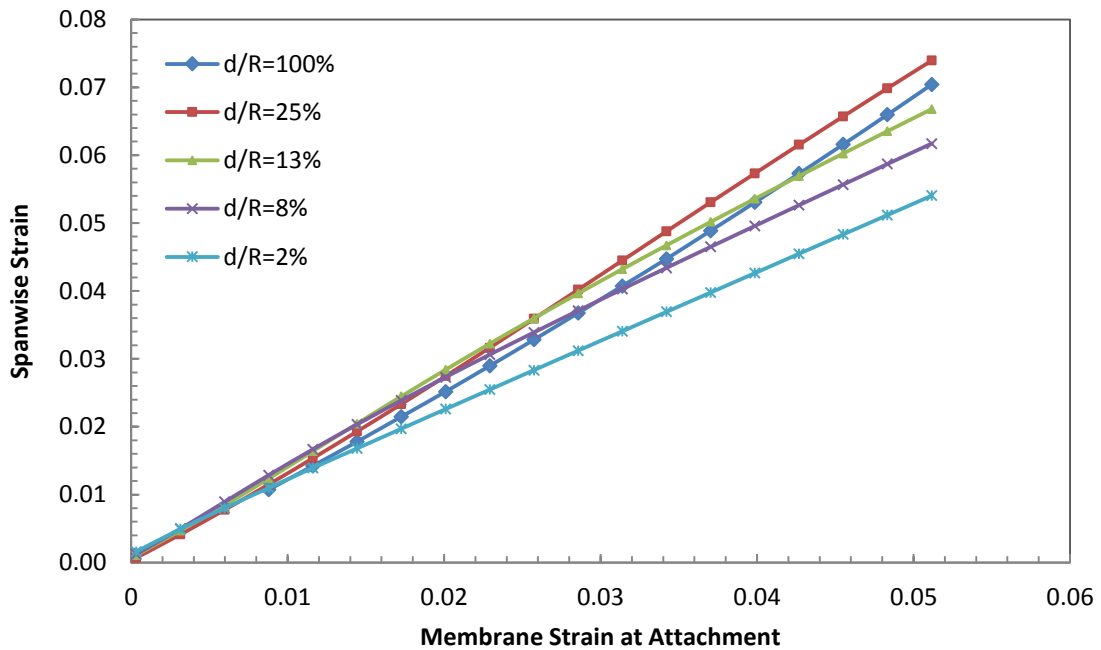


Figure 4-40. Spanwise strains at the maximum out-of-plane displacement locations versus membrane strain at attachment for various depth ratios when a silicone membrane is attached on a closed double curved frame with an AR of 0.5.

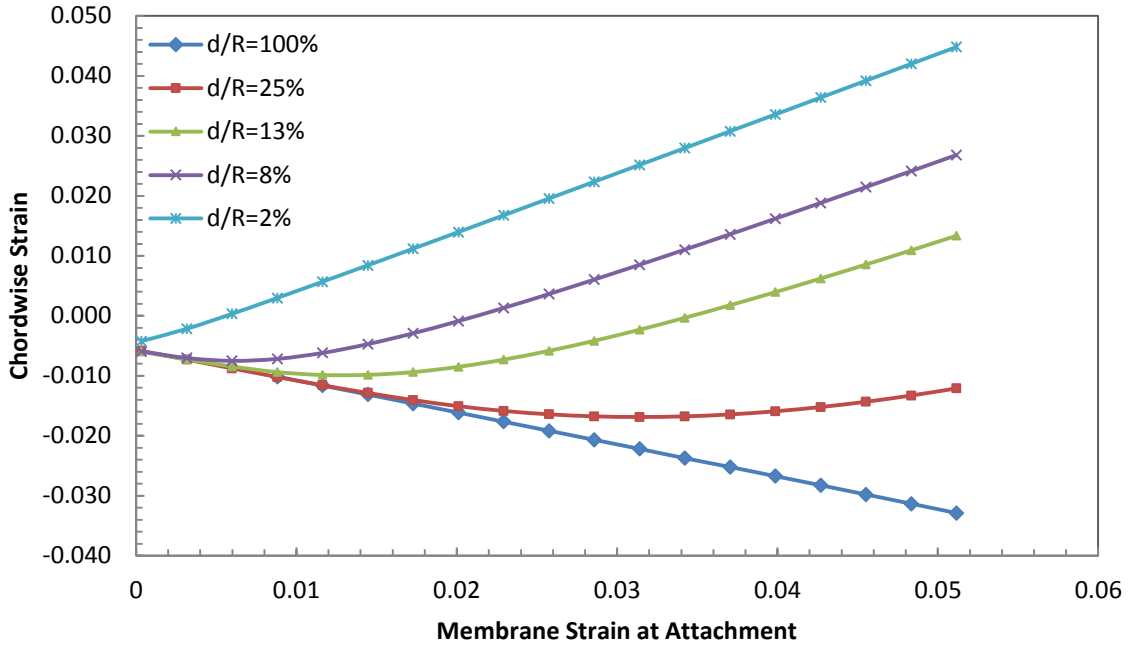


Figure 4-41. Chordwise strains at the maximum out-of-plane displacement locations versus membrane strain at attachment for various depth ratios when a silicone membrane is attached on a closed double curved frame with an AR of 0.5.

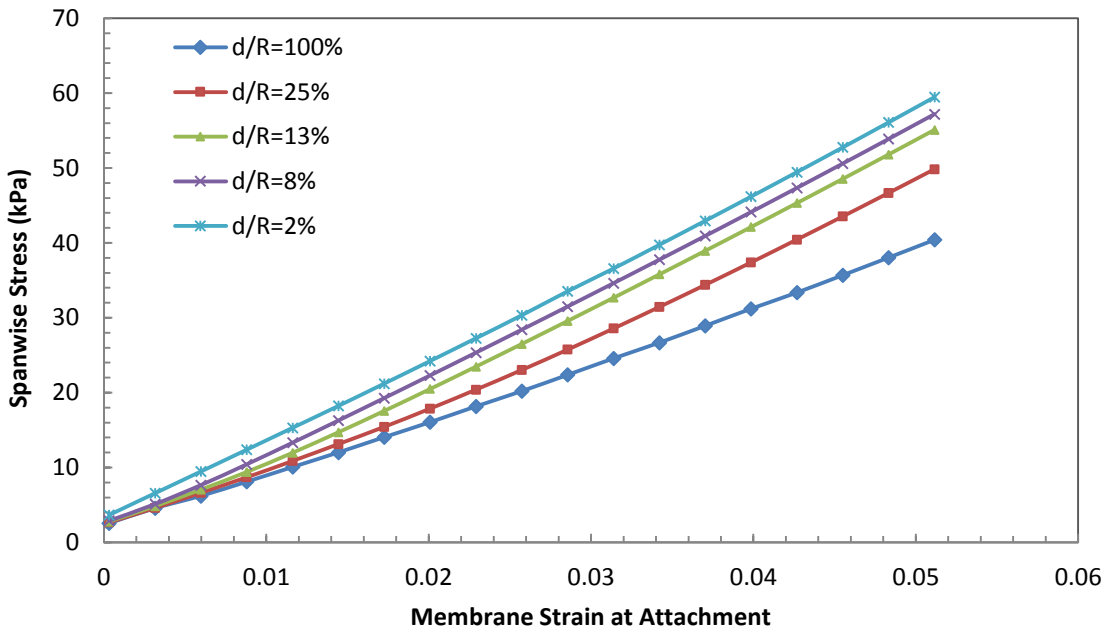


Figure 4-42. Spanwise stresses (kPa) at the maximum out-of-plane displacement locations versus membrane strain at attachment for various depth ratios when a silicone membrane is attached on a closed double curved frame with an AR of 0.5.

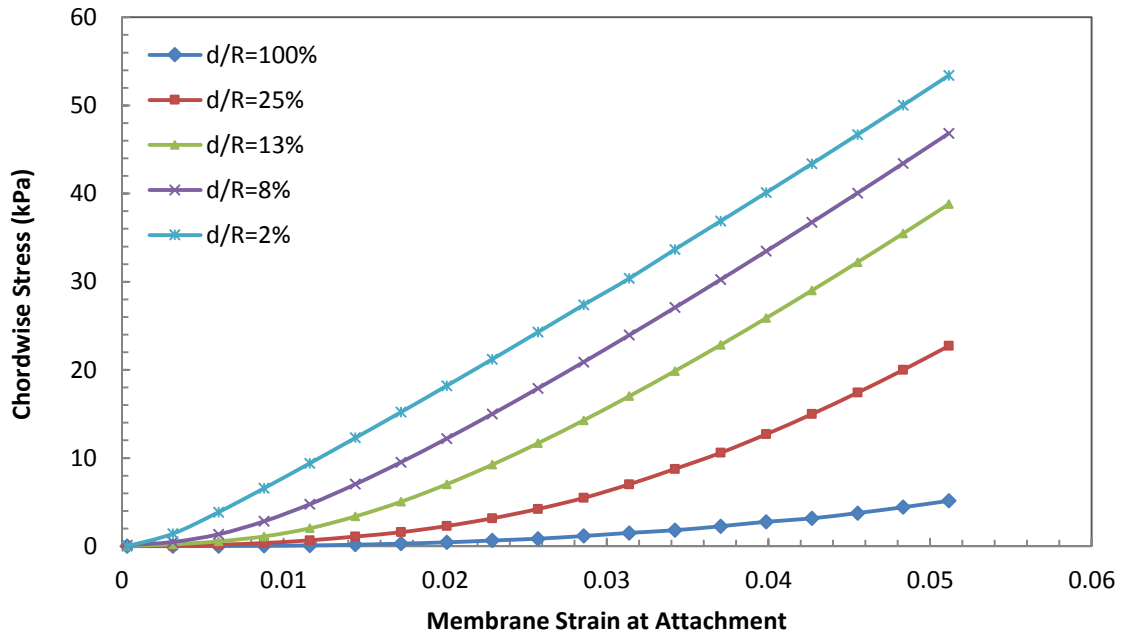


Figure 4-43. Chordwise stresses (kPa) at the maximum out-of-plane displacement locations versus membrane strain at attachment for various depth ratios when a silicone membrane is attached on a closed double curved frame with an AR of 0.5.

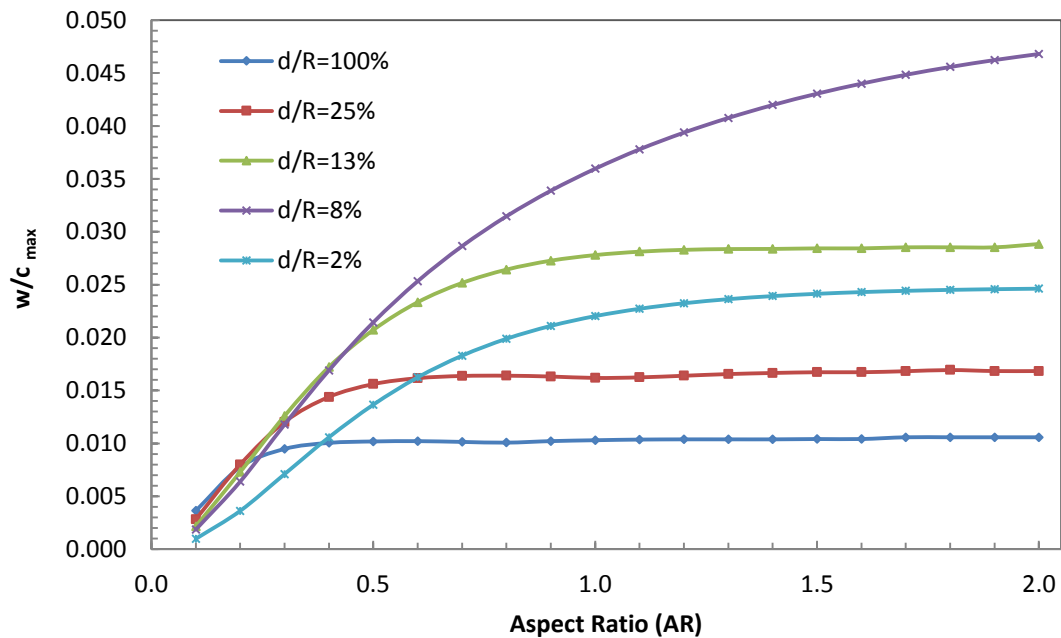


Figure 4-44. Normalized maximum out-of-plane displacements for various aspect ratios and depth ratios for a silicone membrane attached on a double curved frame at 100°C (1.7% membrane strain).

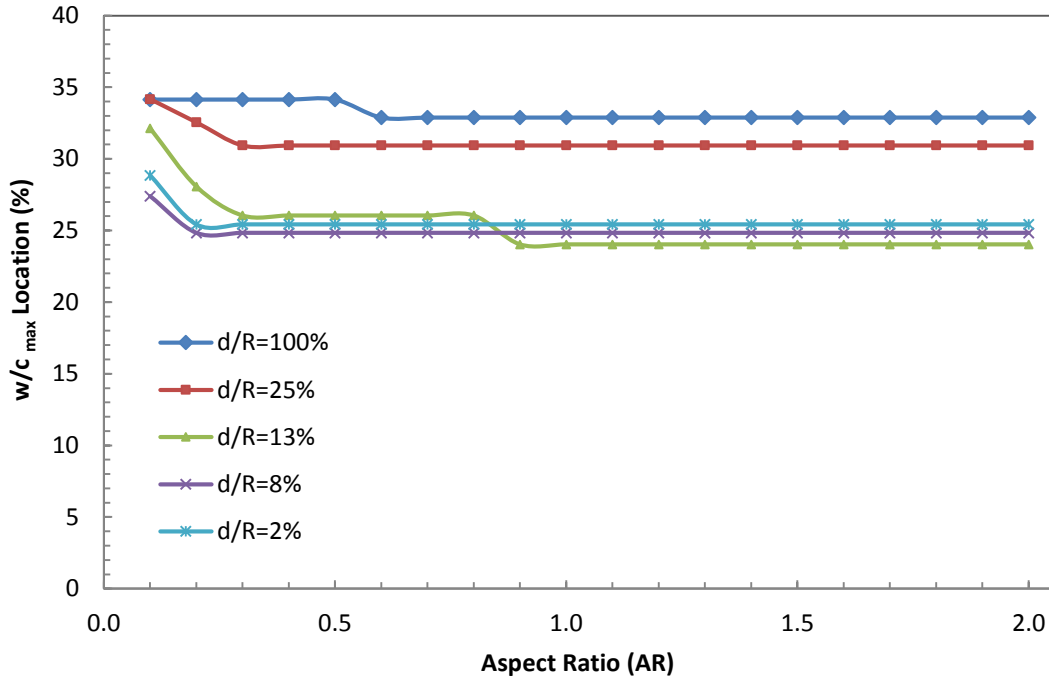


Figure 4-45. Location of the maximum out-of-plane displacements versus AR for various depth ratios when a silicone membrane is attached on a doubly curved frame at 100°C (1.7% membrane strain).

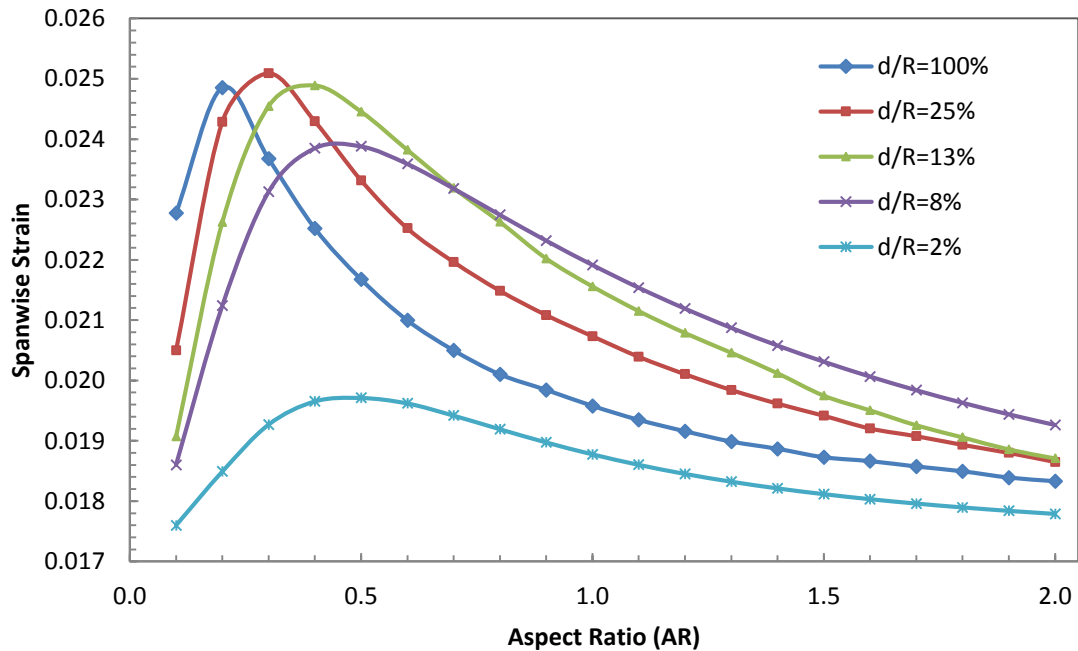


Figure 4-46. Figure 4-27. Spanwise strains at the maximum out-of-plane displacement locations versus AR for various depth ratios when a silicone membrane is attached on an open curved frame at 100°C (1.7% membrane strain).

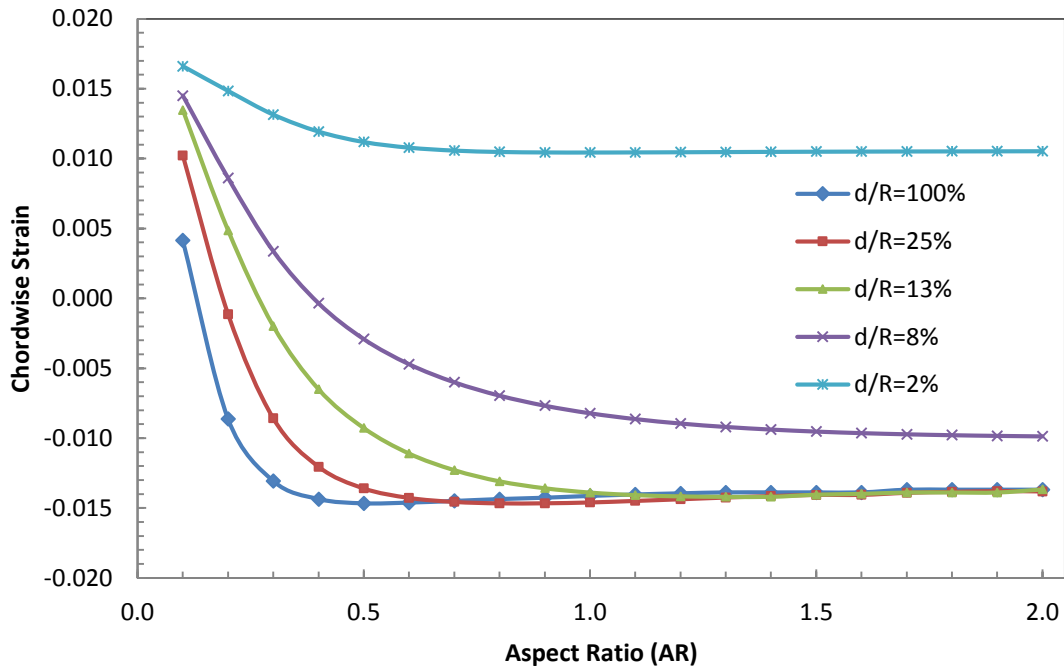


Figure 4-47. Figure 4-27. Spanwise strains at the maximum out-of-plane displacement locations versus AR for various depth ratios when a silicone membrane is attached on an open curved frame at 100°C (1.7% membrane strain).

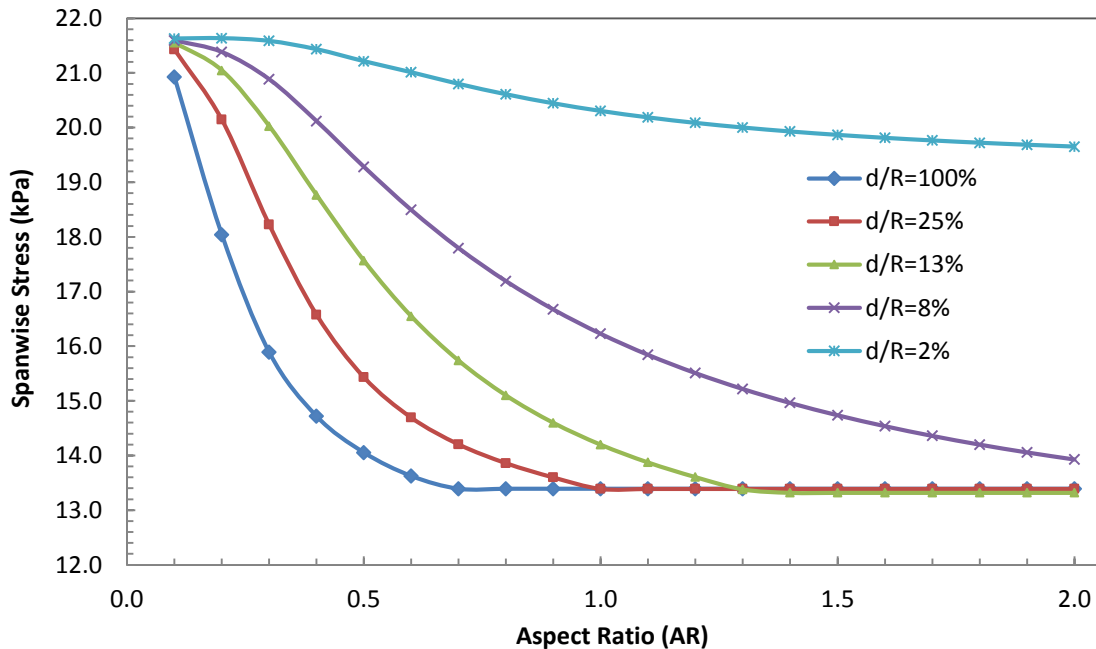


Figure 4-48. Figure 4-27. Spanwise strains at the maximum out-of-plane displacement locations versus AR for various depth ratios when a silicone membrane is attached on an open curved frame at 100°C (1.7% membrane strain).

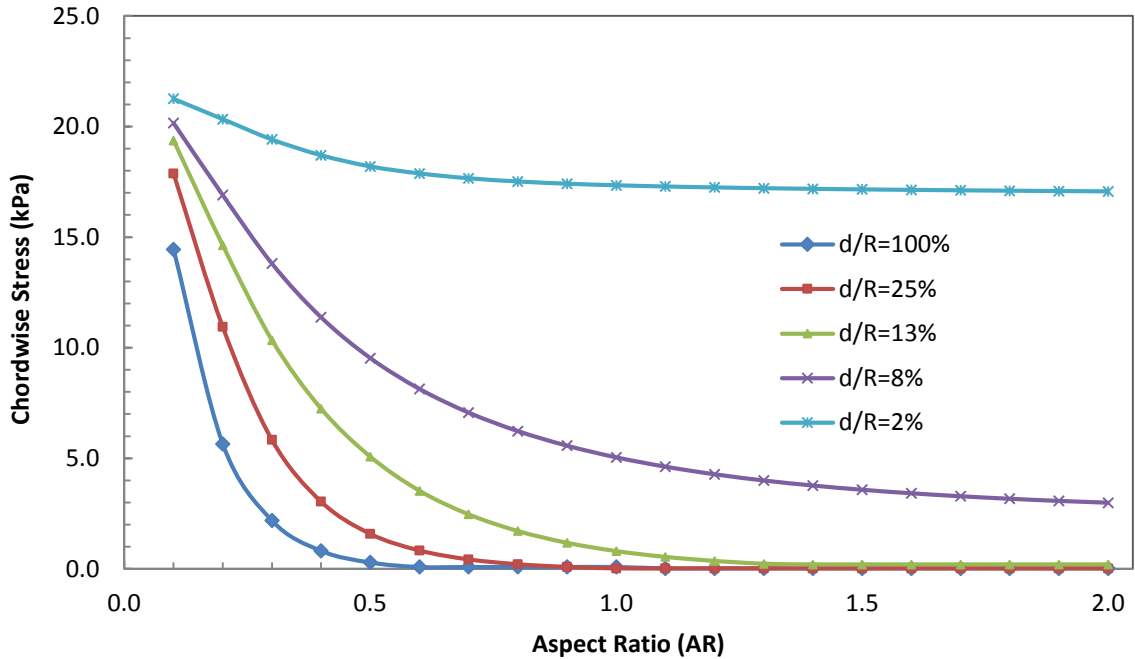


Figure 4-49. Figure 4-27. Spanwise strains at the maximum out-of-plane displacement locations versus AR for various depth ratios when a silicone membrane is attached on an open curved frame at 100°C (1.7% membrane strain).

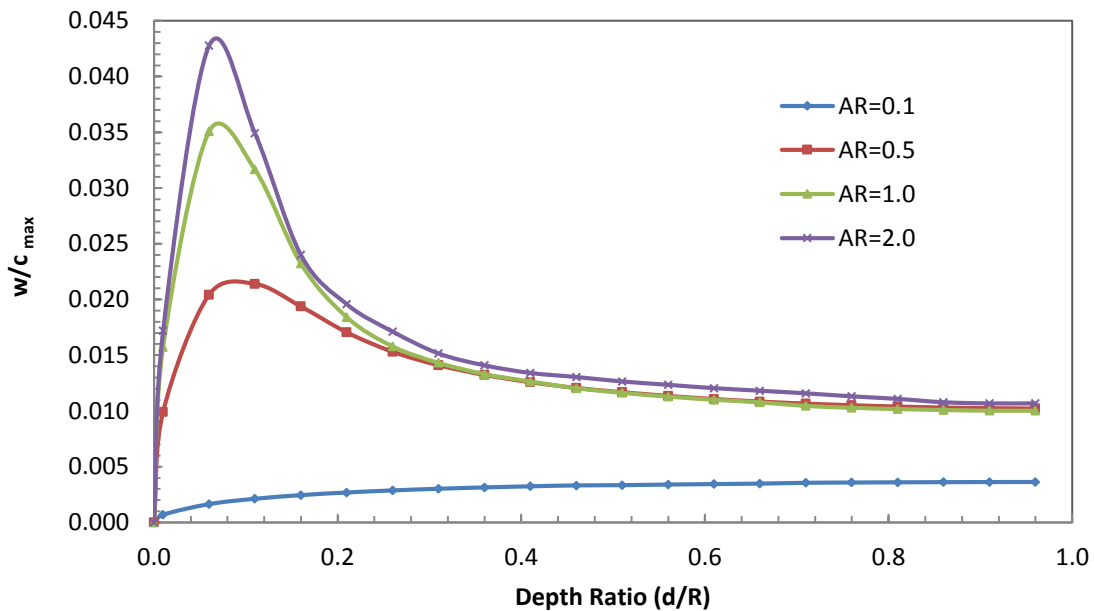


Figure 4-50. Normalized maximum out-of-plane displacements versus depth ratio for various aspect ratios when a silicone membrane is attached on a closed doubly curved frame at 100°C (1.7% membrane strain).

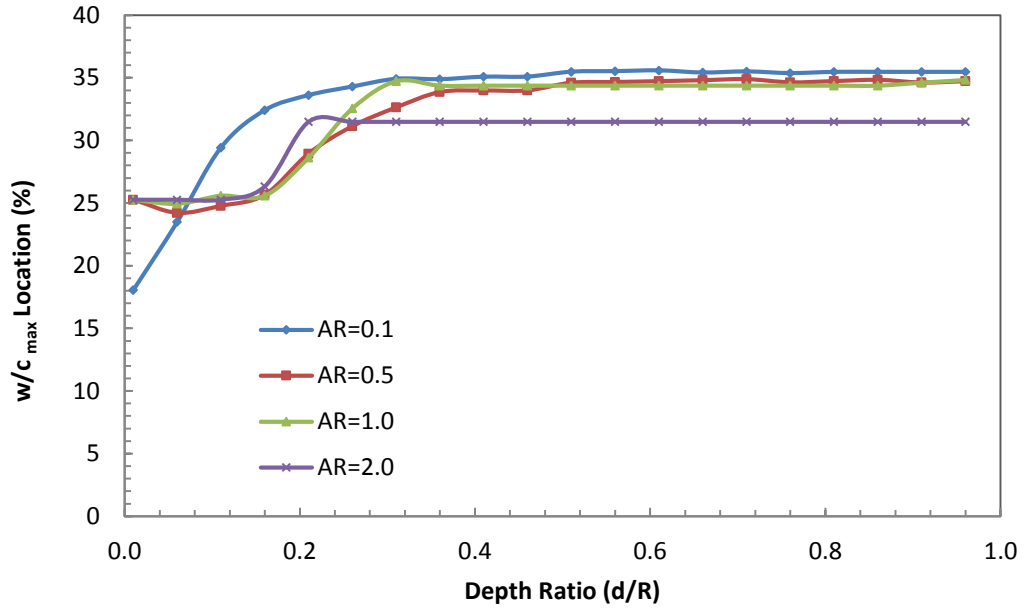


Figure 4-51. Location of the maximum out-of-plane displacements versus DR for various aspect ratios when a silicone membrane is attached on a closed doubly curved frame at 100°C (1.7% membrane strain).

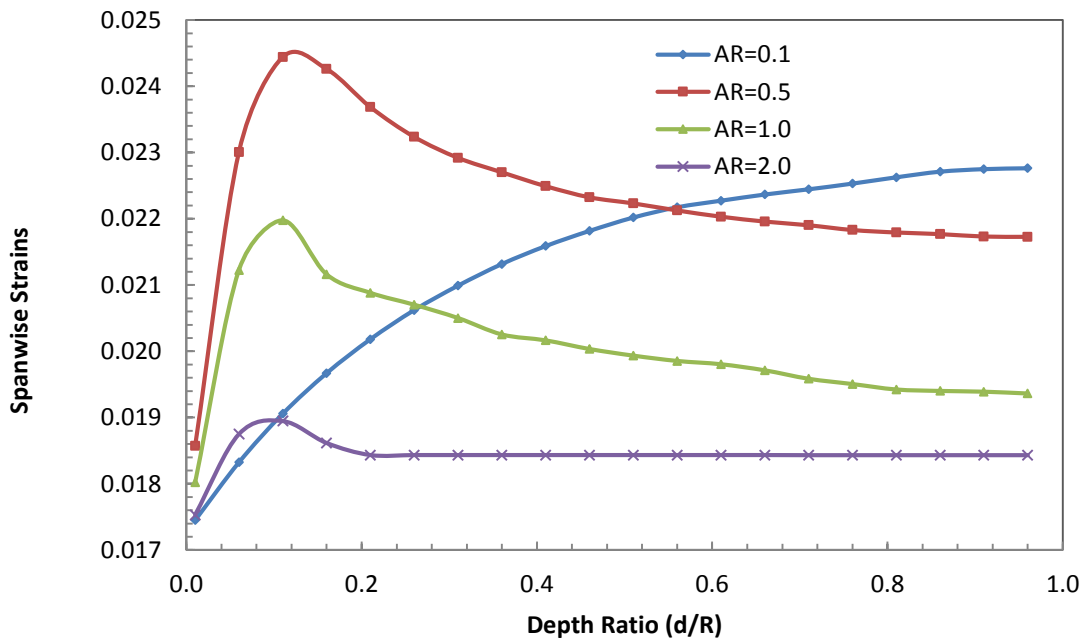


Figure 4-52. Spanwise strains at the maximum out-of-plane displacement locations versus depth ratio for various aspect ratios when a silicone membrane is attached on a closed doubly curved frame at 100°C (1.7% membrane strain).

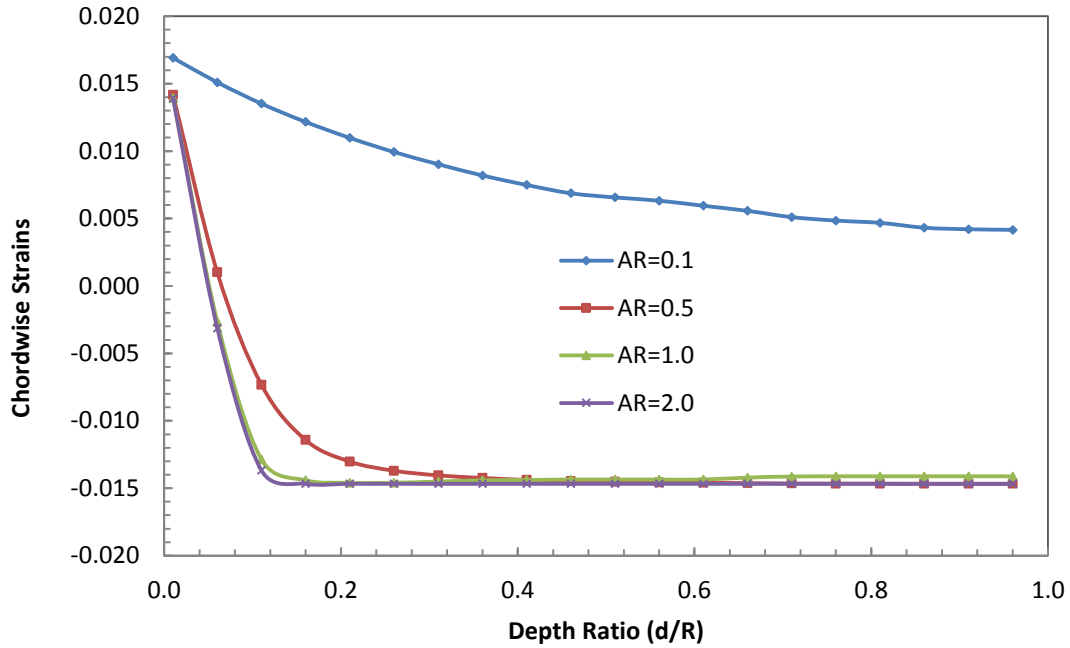


Figure 4-53. Chordwise strains at the maximum out-of-plane displacement locations versus depth ratio for various aspect ratios when a silicone membrane is attached on a closed doubly curved frame at 100°C (1.7% membrane strain).

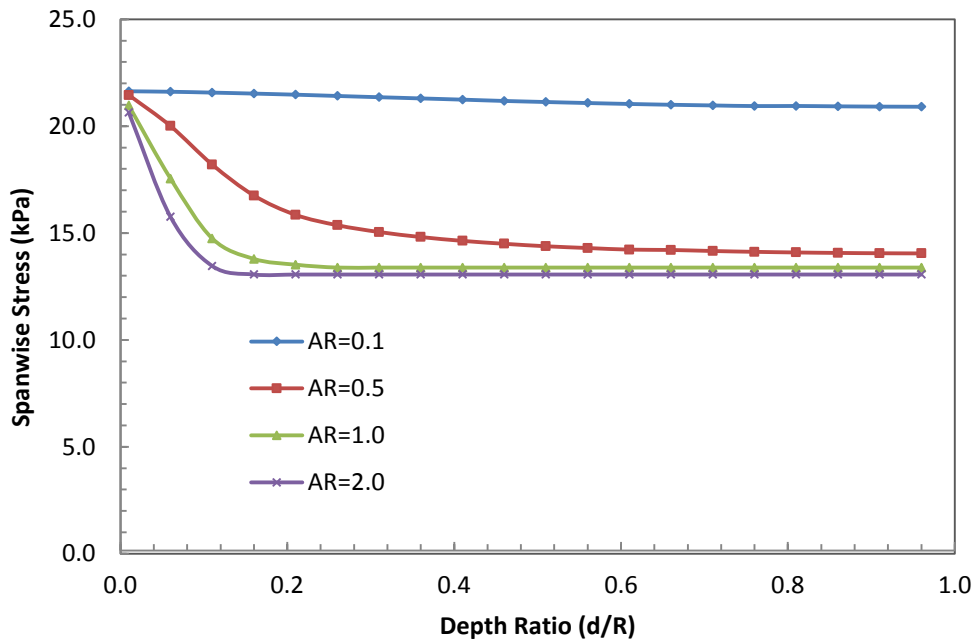


Figure 4-54. Spanwise stresses (kPa) at the maximum out-of-plane displacement locations versus depth ratio for various aspect ratios when a silicone membrane is attached on a closed doubly curved frame at 100°C (1.7% membrane strain).

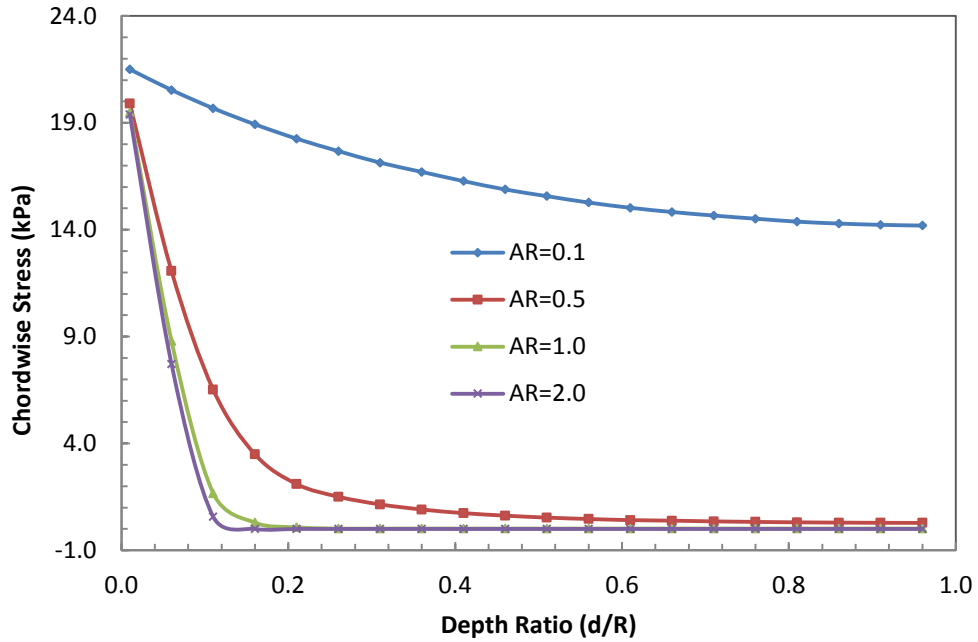


Figure 4-55. Chordwise stresses (kPa) at the maximum out-of-plane displacement locations versus depth ratio for various aspect ratios when a silicone membrane is attached on a closed doubly curved frame at 100°C (1.7% membrane strain).

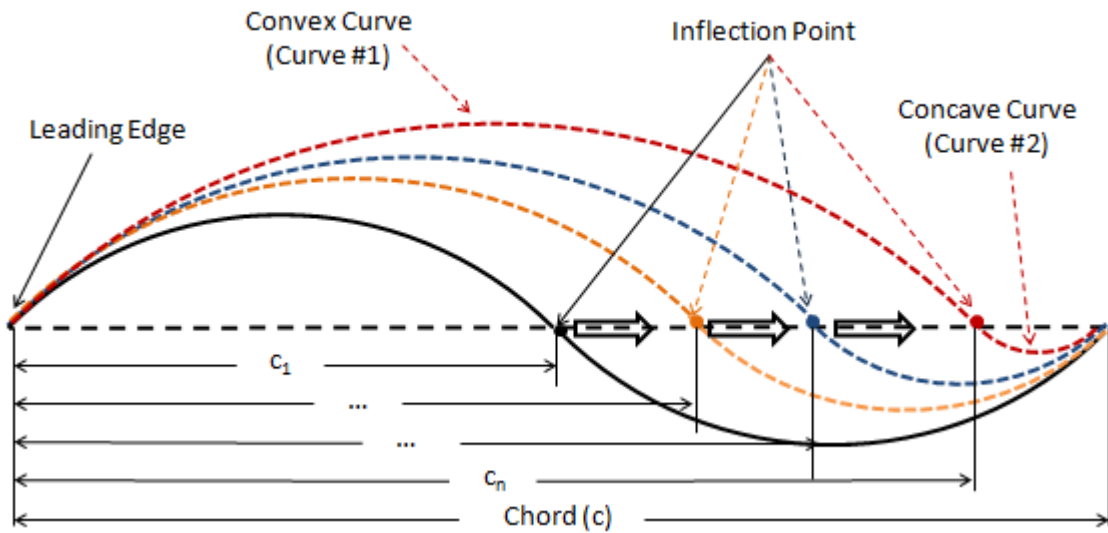


Figure 4-56. Schematic for the locations of asymmetry (side view).

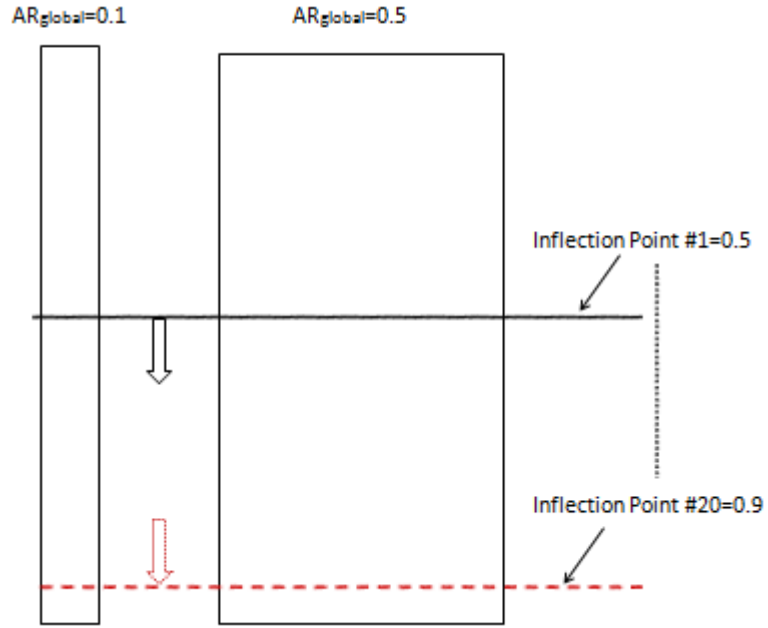


Figure 4-57. Effect of inflection point on AR_{local} of each curve.

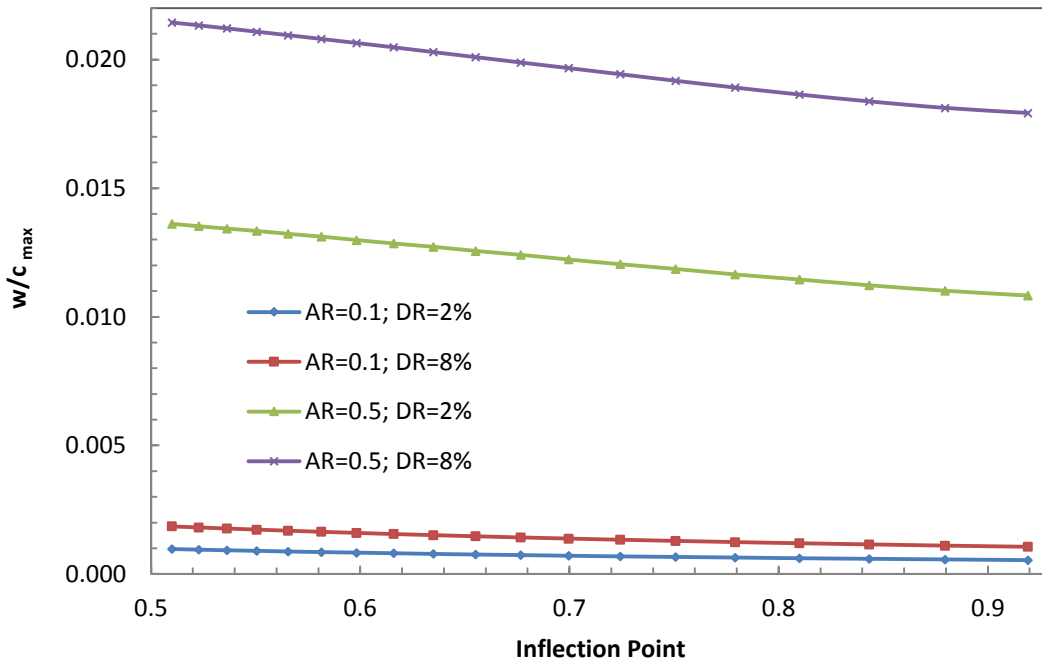


Figure 4-58. Normalized maximum out-of-plane displacements versus inflection point for a combination of ARs and DRs when a silicone membrane is attached on a doubly curved frame at 100°C (1.7% membrane strain).

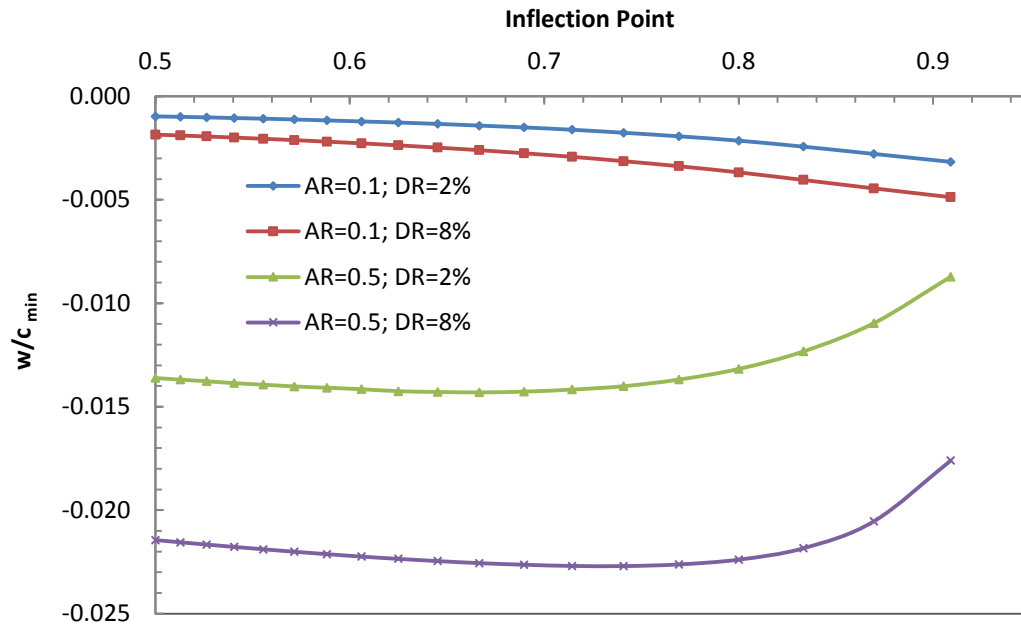


Figure 4-59. Normalized minimum out-of-plane displacements versus inflection point for a combination of ARs and DRs when a silicone membrane is attached on a doubly curved frame at 100°C (1.7% membrane strain).

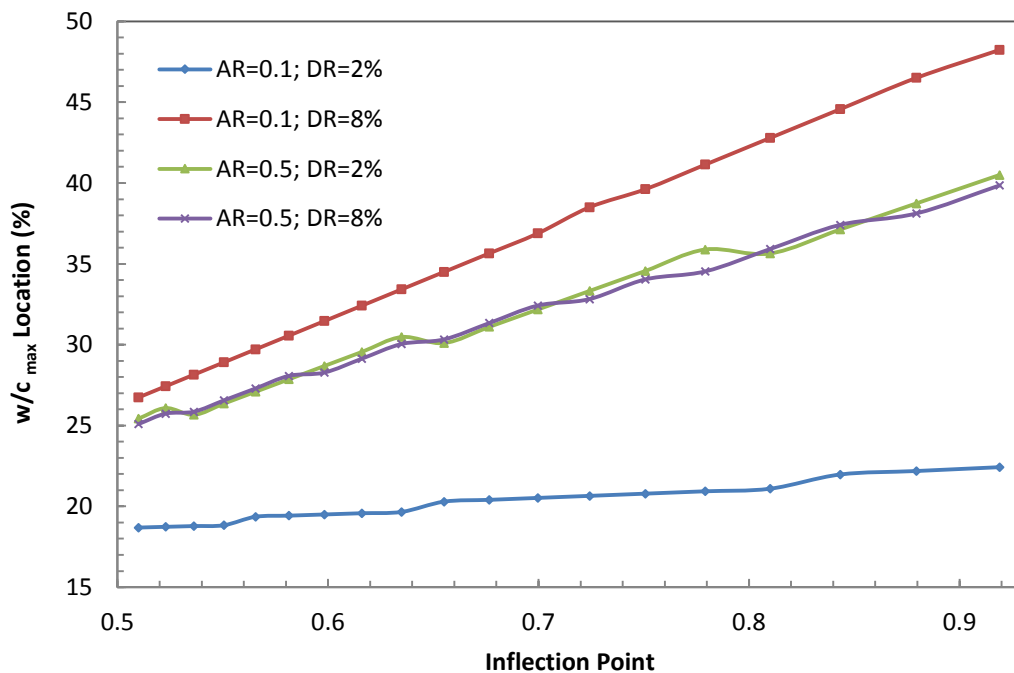


Figure 4-60. Location of the maximum out-of-plane displacements along the chord length versus inflection point for a combination of ARs and DRs when a silicone membrane is attached on a doubly curved frame at 100°C (1.7% membrane strain).

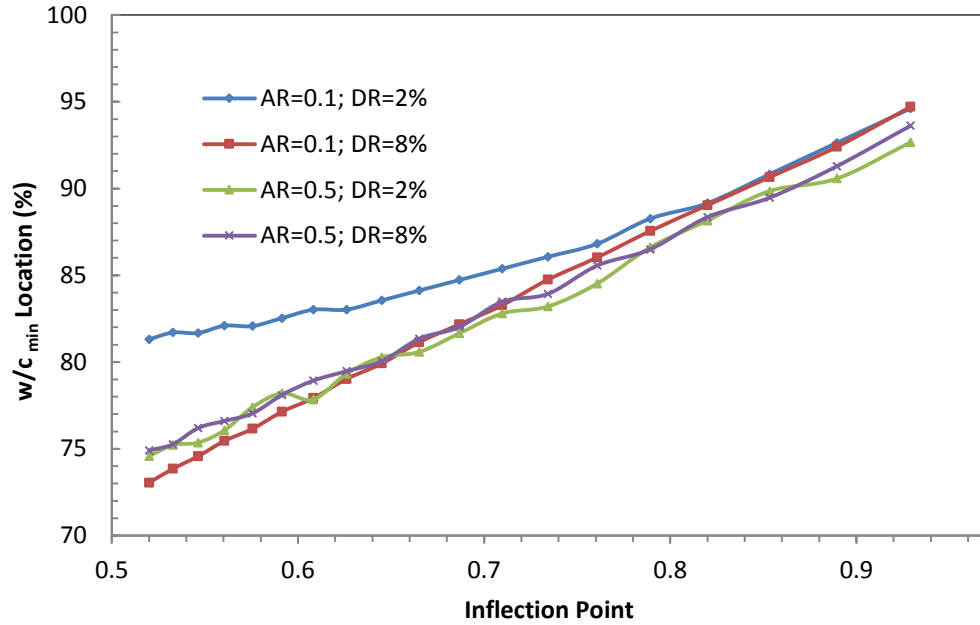


Figure 4-61. Location of the minimum out-of-plane displacements along the chord length versus inflection point for a combination of ARs and DRs when a silicone membrane is attached on a doubly curved frame at 100°C (1.7% membrane strain).

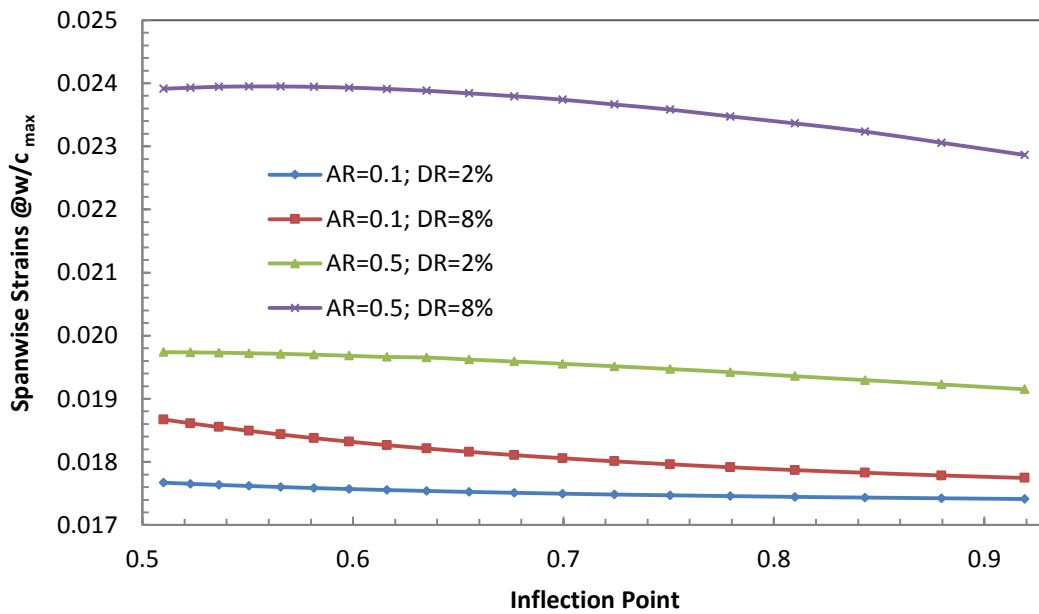


Figure 4-62. Spanwise strains at the maximum out-of-plane displacement locations versus inflection point for a combination of ARs and DRs when a silicone membrane is attached on a doubly curved frame at 100°C (1.7% membrane strain).

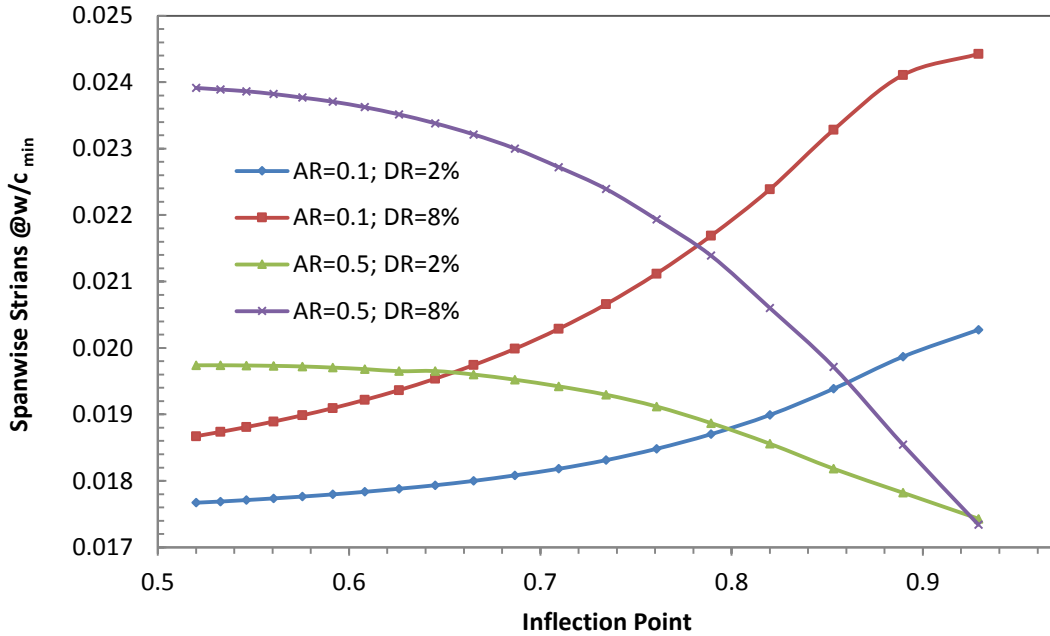


Figure 4-63. Spanwise strains at the minimum out-of-plane displacement locations versus inflection point for a combination of ARs and DRs when a silicone membrane is attached on a doubly curved frame at 100°C (1.7% membrane strain).

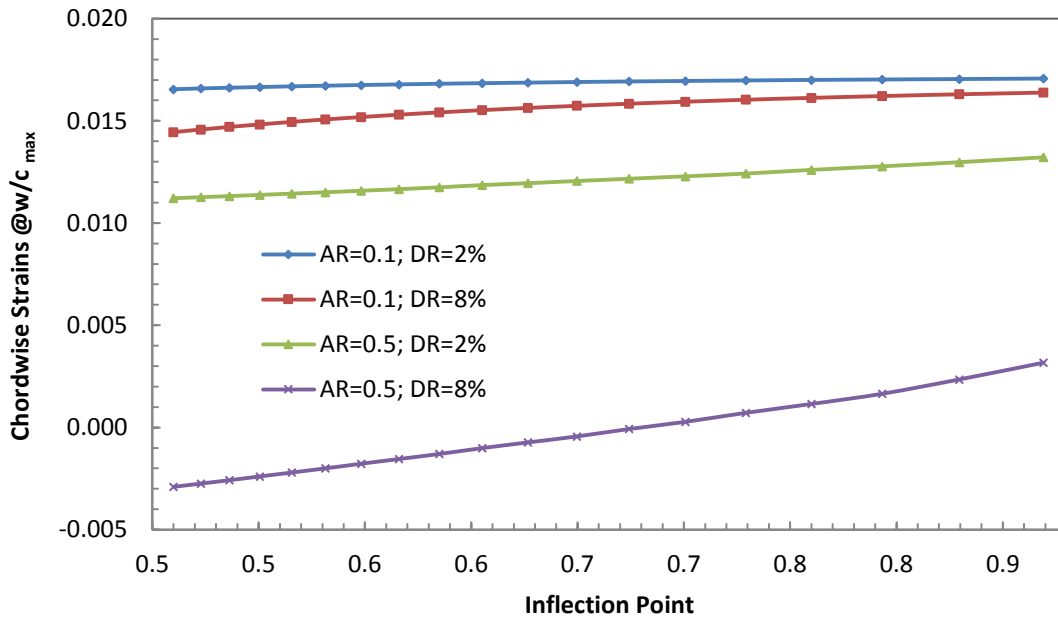


Figure 4-64. Chordwise strains at the maximum out-of-plane displacement locations versus inflection point for a combination of ARs and DRs when a silicone membrane is attached on a doubly curved frame at 100°C (1.7% membrane strain).

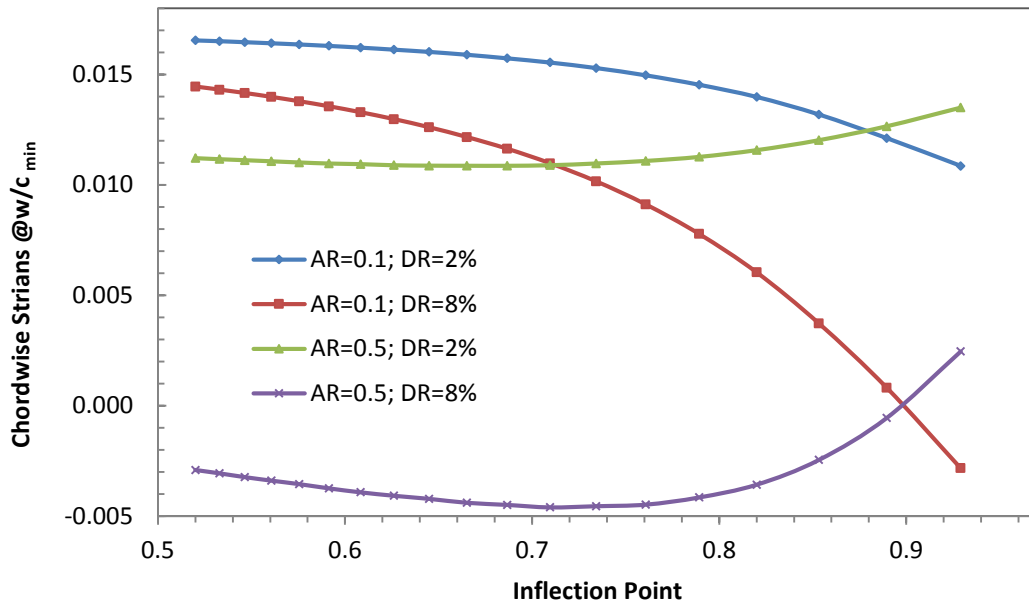


Figure 4-65. Chordwise strains at the minimum out-of-plane displacement locations versus inflection point for a combination of ARs and DRs when a silicone membrane is attached on a doubly curved frame at 100°C (1.7% membrane strain).

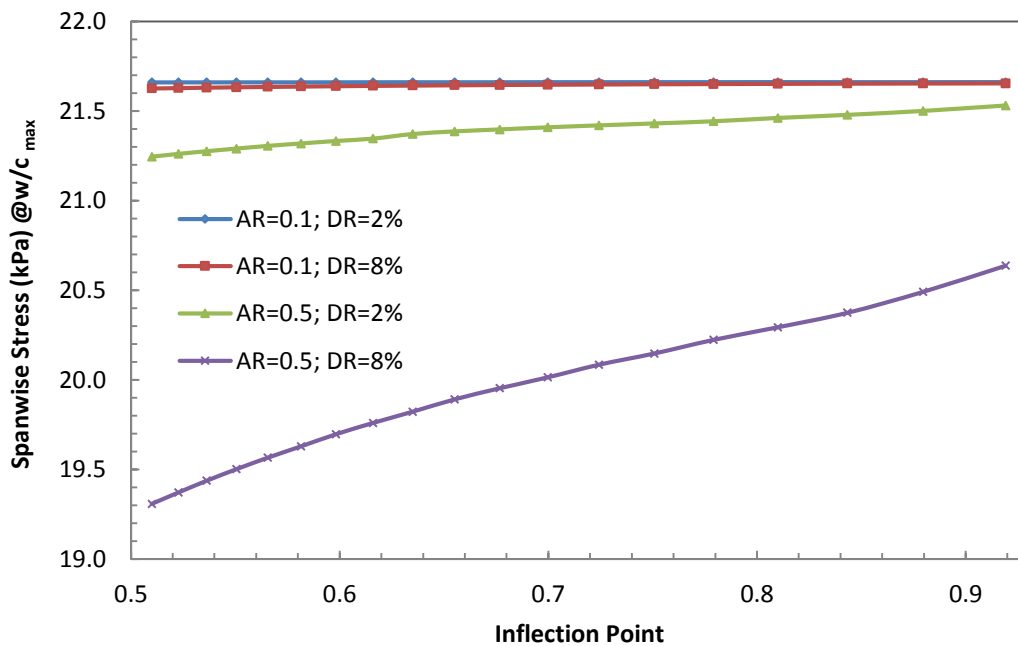


Figure 4-66. Spanwise stress (kPa) at the maximum out-of-plane displacement locations versus inflection point for a combination of ARs and DRs when a silicone membrane is attached on a doubly curved frame at 100°C (1.7% membrane strain).

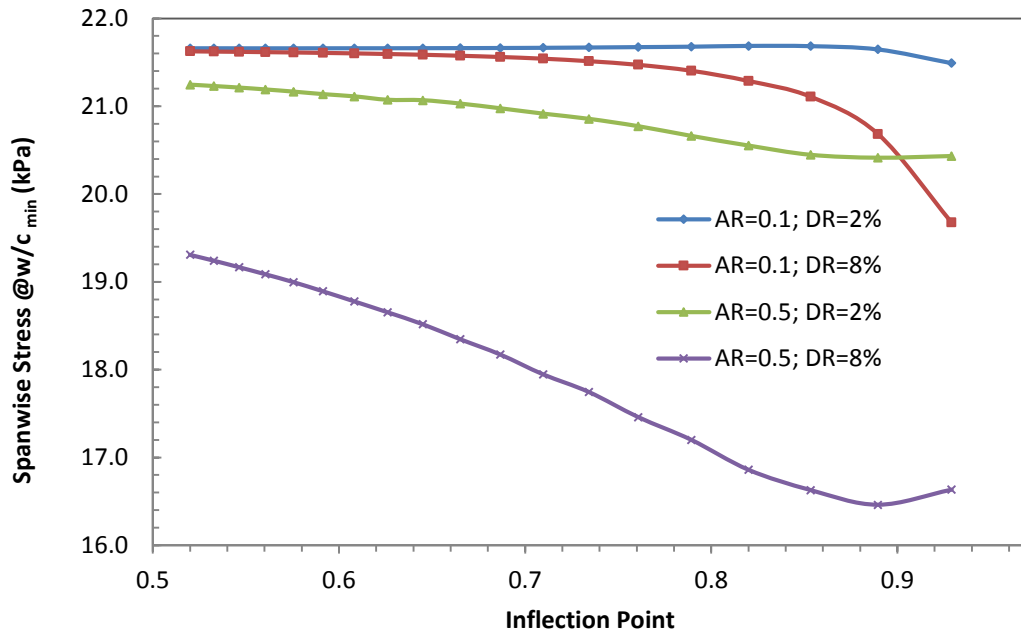


Figure 4-67. Spanwise stress (kPa) at the minimum out-of-plane displacement locations versus inflection point for a combination of ARs and DRs when a silicone membrane is attached on a doubly curved frame at 100°C (1.7% membrane strain).

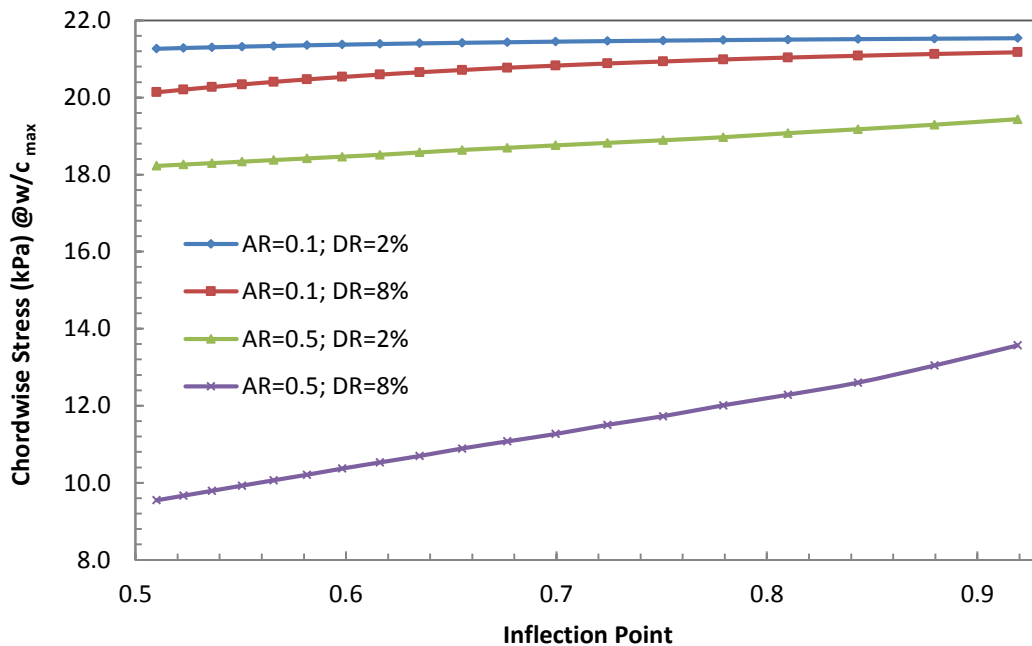


Figure 4-68. Chordwise stress (kPa) at the maximum out-of-plane displacement locations versus inflection point for a combination of ARs and DRs when a silicone membrane is attached on a doubly curved frame at 100°C (1.7% membrane strain).

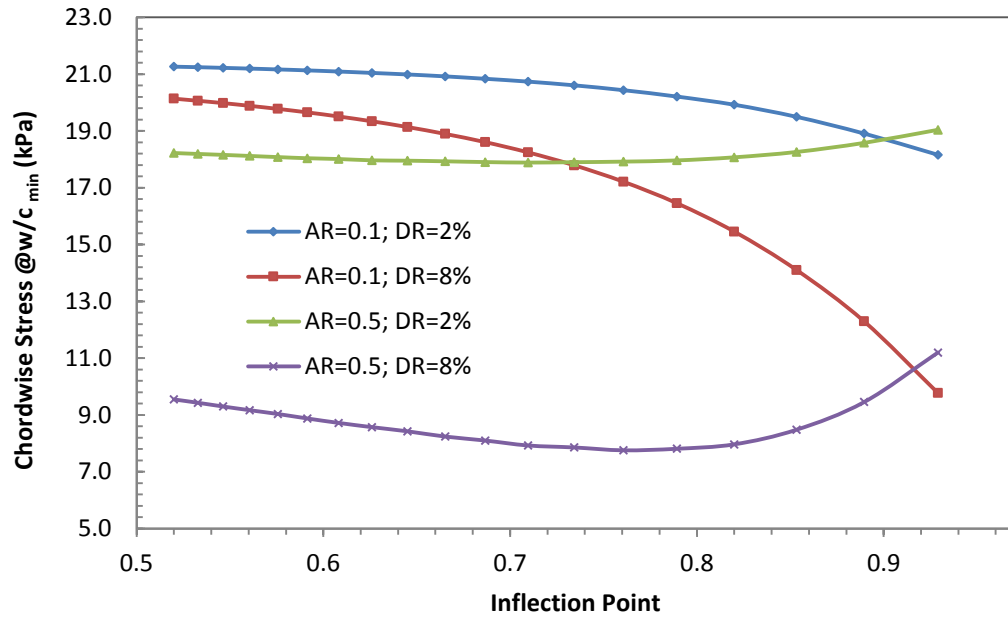


Figure 4-69. Chordwise stress (kPa) at the minimum out-of-plane displacement locations versus inflection point for a combination of ARs and DRs when a silicone membrane is attached on a doubly curved frame at 100°C (1.7% membrane strain).

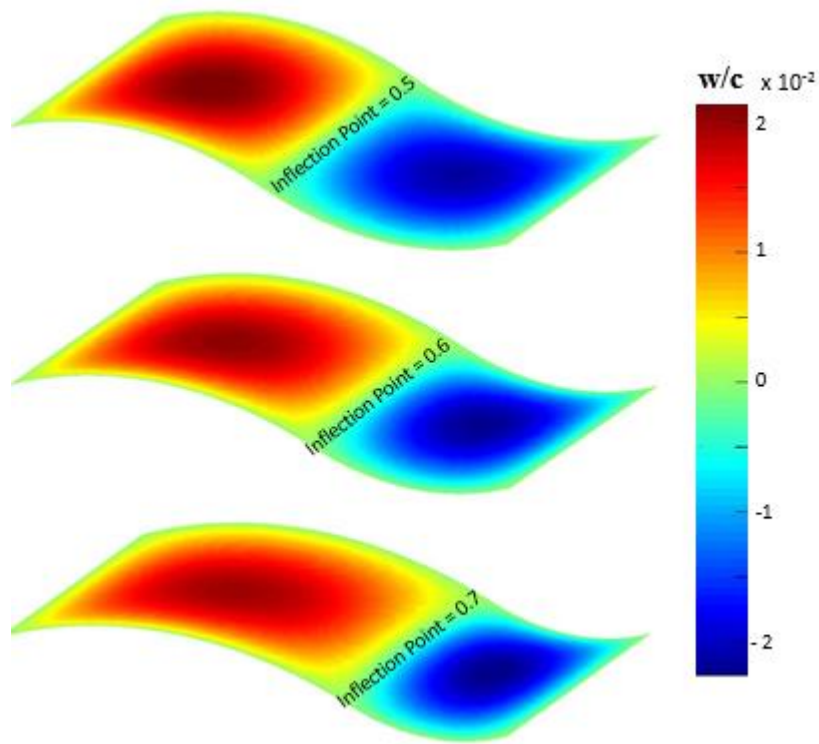


Figure 4-70. Normalized out-of-plane displacement gradients for three frames that have various inflection points with AR=0.5, DR=0.8, and attached at 100°C

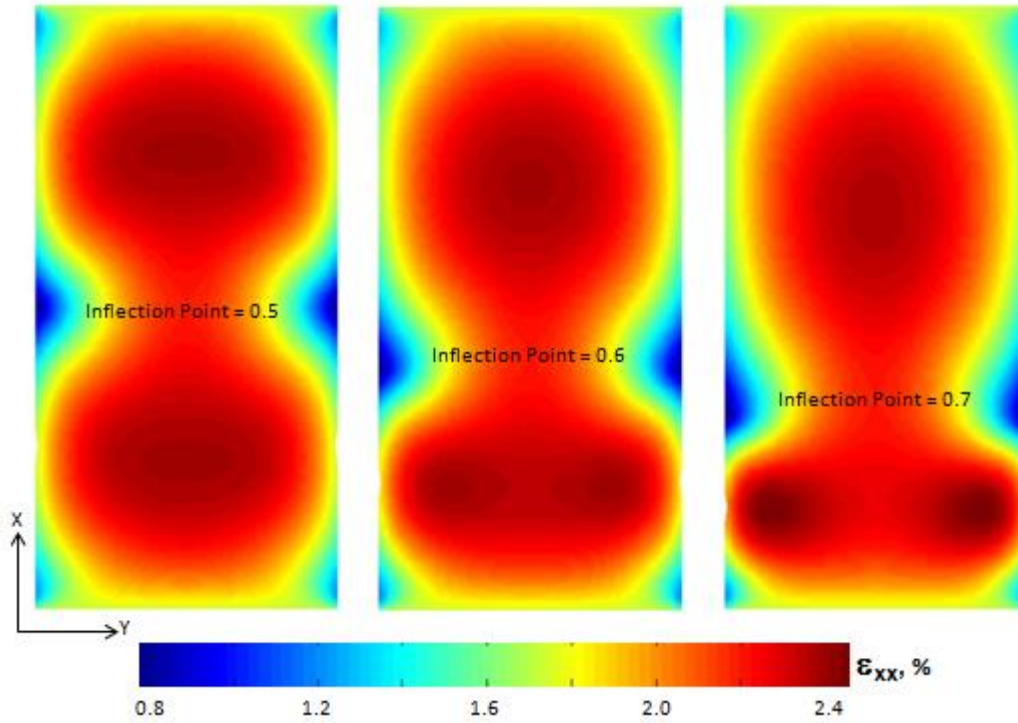


Figure 4-71. Spanwise strain gradients for three frames that have various inflection points with AR=0.5, DR=0.8, and attached at 100°C.

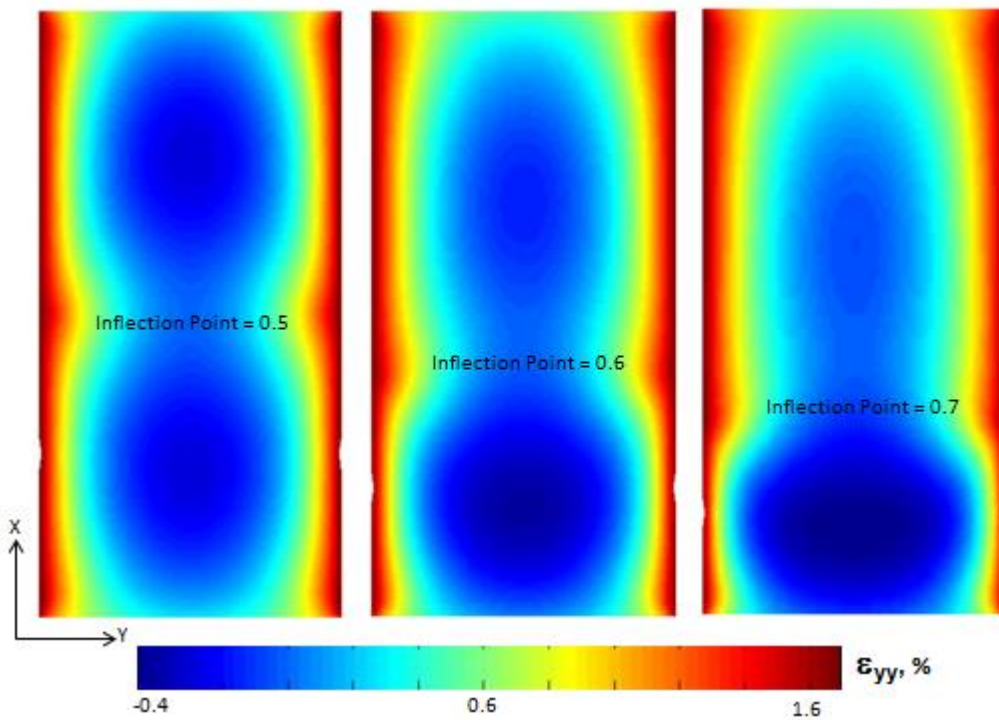


Figure 4-72. Chordwise strain gradients for three frames that have various inflection points with AR=0.5, DR=0.8, and attached at 100°C.

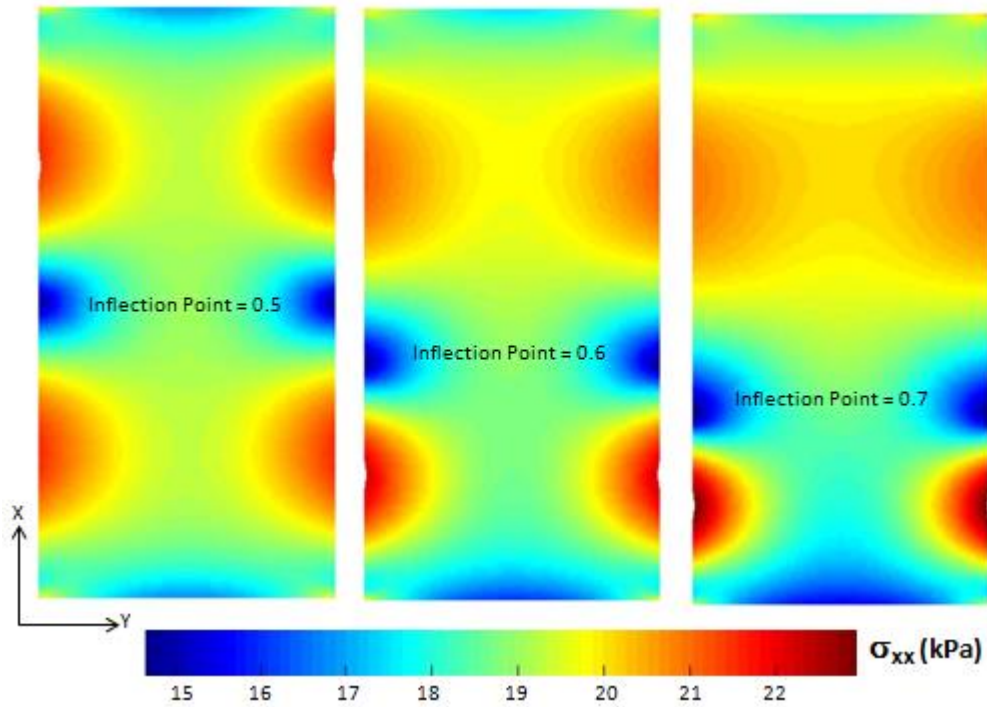


Figure 4-73. Spanwise stress gradients for three frames that have various inflection points with AR=0.5, DR=0.8, and attached at 100°C.

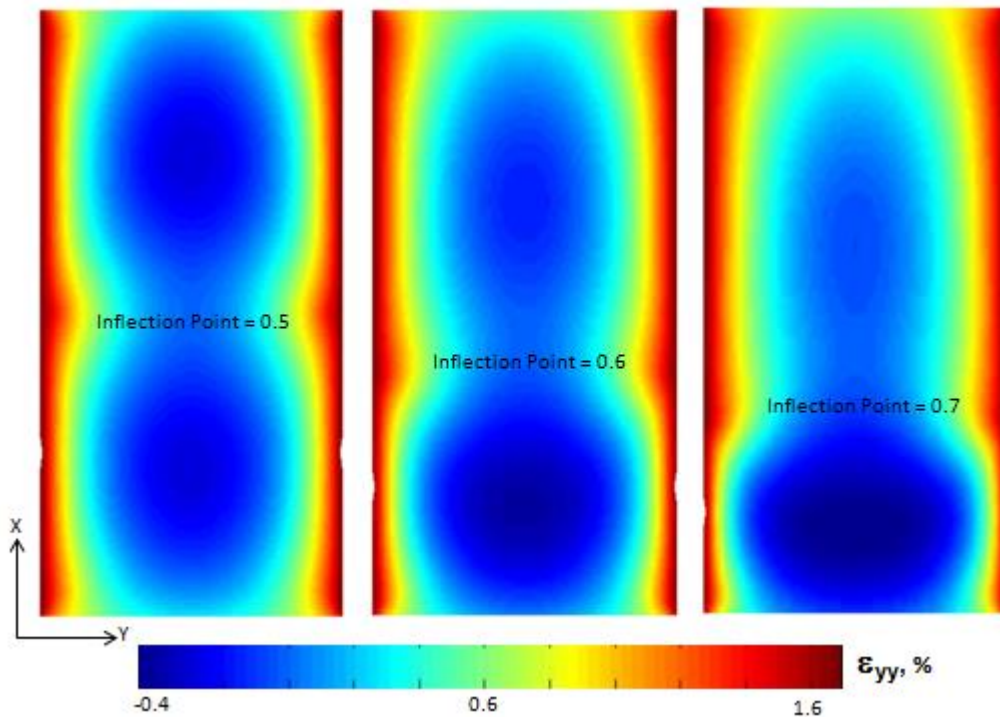


Figure 4-74. Chordwise stress gradients for three frames that have various inflection points with AR=0.5, DR=0.8, and attached at 100°C.

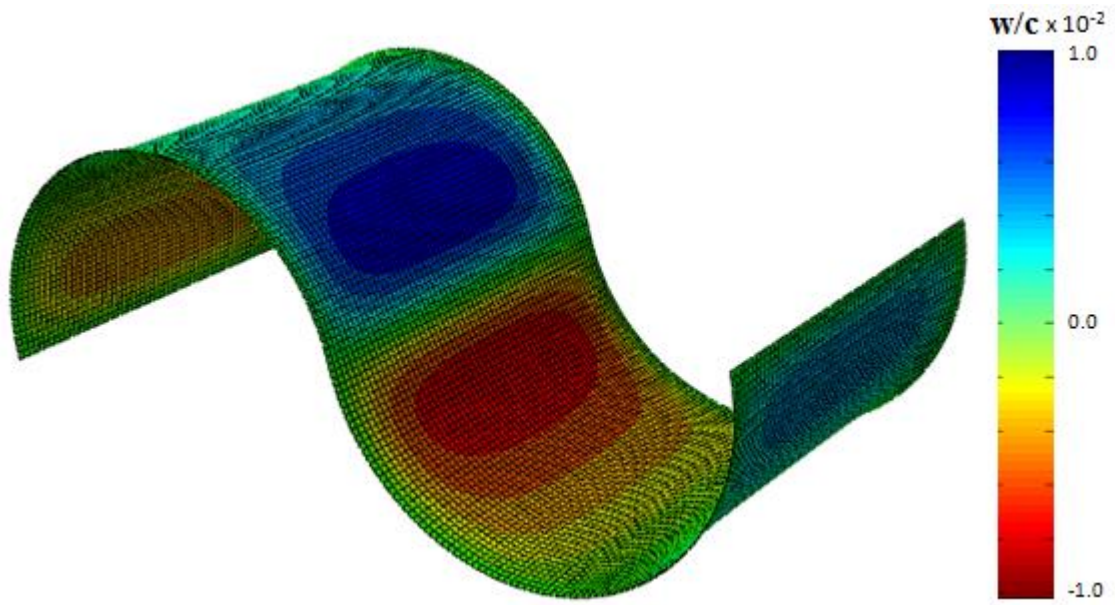


Figure 4-75. Normalized out-of-plane displacement gradient for a membrane attached on a double curved frame with AR=0.5, DR=1.0, and attached at 100°C.

CHAPTER 5 MANUFACTURING METHODS OF CO-CURING MEMBRANE AND WING SKELETONS

Many MAV wings have been manufactured at the University of Florida's composite lay-up laboratories under the supervision of Dr. Peter Ifju via a method of co-curing the silicone rubber membrane with the pre-preg composite skeleton, in which these wings have been successfully flight tested. From a practical standpoint, these MAVs perform extremely well under various environmental conditions (such as gust, wind, heat, etc.) in terms of controllability, lift, drag, and longitudinal stability. Additionally, the shelf lives of the silicone rubber wings are observed to be significantly higher than of the latex rubber MAV wings. Both pictures seen on Figure 5-1 are taken over a year after manufacturing, where the silicone rubber has not lost any observable tension or visible degradation (on left) while the latex rubber has completely disintegrated (on right). Experiments were performed to investigate the possibility of curing the pre-preg carbon skeleton and the silicone membrane together at the same time in the vacuum bag assembly. It was found that the pre-preg did not adhere to the silicone rubber. This was predictable since in general epoxy does not adhere to silicone rubber. In fact, most adhesives, except silicone rubber adhesives, do not adhere to solid silicone rubber. The application of primer does not work for co-curing due to its mixing with the epoxy and disappearing from the pre-preg carbon-fiber surface during the curing process. Therefore, to adhere the membrane to the carbon-fiber frame, a method called corona treatment technique was utilized.

This chapter will explain the manufacturing processes involved to quantify the amount of pre-strain and out-of-plane displacements developed on the silicone rubber membrane. The problem will be first reduced to a 2-D case for a simple understanding,

and then expanded to 3-D structures, such as the MAV wing shown in Figure 5-1. To evaluate the effectiveness of corona treatment, a double cantilever beam experiment was conducted to quantify the adhesion of carbon fiber to corona treated silicone rubber as well as non-treated silicone rubber.

Fabrication of 2-D Specimens via Co-cure Method

Five specimens of 6-layer, 0°-90° oriented, plain weave, pre-preg carbon fiber were prepared to be adhered on speckled silicone rubber membrane specimens to investigate the amount of pre-strain developed in 2-D co-cured samples (Figure 5-2). The window of the frame was cut as 2.5 cm by 2.5 cm while the outer dimension of the frame was measured to be 4.5 cm. After applying Teflon material on a flat surface, the appropriately cut uncured carbon fiber frame was placed on a flat tool. The white speckled black silicone rubber membrane (properties provided in Table 2-1) was then applied carefully on top of the carbon fiber frame such that the edges overlapped the surrounding frame by 5mm. The following images were acquired by the VIC system after the preparation:

- Image 1: Membrane was laid on raw pre-preg carbon fiber at 25°C as the initial field reference.
- Image 2: Membrane/carbon fiber assembly was vacuumed at 35 Hg in a transparent, air-tight, temperature resistant bag at 25°C.
- Image 3: The assembly reached to 75°C.
- Image 4: Another image was obtained at curing temperature (135°C) 10 minutes after the target temperature was reached.
- Image 5: The cured assembly was cooled to room temperature; however still remained in the vacuum bag at 35psi.
- Image 6: The frame was removed from the bag to acquire the final picture at 25°C.

Results are discussed in detail along with figures in Chapter 6, and additional results are provided in Appendix A.

Fabrication of Wings and Pre-tensioning via Co-cure Method

The general procedural steps to apply a pre-tensioned silicone rubber membrane to a wing frame are listed below and schematically shown in Figure 5-3.

- Step 1: A preexisting wing mold was used to construct the wing. A light coat of spray adhesive was applied.
- Step 2: Teflon film was laid on the mold for easy separation of the composite wing after the curing process was completed.
- Step 3: Two layers of 45⁰ oriented plain-weave pre-preg carbon fiber layers were cut out utilizing a template. Another layer of carbon fiber was cut out only for the leading edge for added strength.
- Step 4: A random speckling pattern was applied on one side of the silicone membrane while both sides are corona treated.
- Step 5: The perimeter of the silicone membrane was sandwiched between the layers of the composite. The procedures outlined by Albertani et al. [93] were used to facilitate visual image correlation testing.
- Step 6: The entire assembly was vacuumed to be cured in the oven at 130°C for four hours.
- Step 7: The final image was obtained utilizing the VIC cameras for analysis. Five perimeter reinforced wings were manufactured for analysis and to determine repeatability.

Corona Treatment

Despite being an integral part of the manufacture of polymers, corona treatment is rarely discussed. The name corona comes from the halo like appearance it gives off. Early tests confirmed its existence, but the potential for commercial application was not fully realized until the 1950's. Although this unique technique has been used for over 50 years, the principle behind how corona treatment improves adhesion is not entirely understood. Four generally accepted theories remain behind how the air plasma affects

the surface of the substrate. The formation of electrets, the removal of weak boundary layers, an increase in roughness caused by small pits, and the deposition of chemically charged hydroxide ions on the surface are the most common explanations [94]. Electrets are non-conducting substances, like polymers, which become partially charged when placed under an electric field. The air plasma is generated by creating a steep electrical gradient. The surface to be treated is placed near the air plasma so the electrets hypothesis is a possible explanation. The weak boundary layer theory asserts that failures of adhesives are primarily the cause of weak boundary layers, which can be the result of air pockets between the surfaces or impurities in the adhesive [95]. The third explanation for the improved adhesion of surfaces treated with air plasma is attributed to an increase in roughness. Common practice is to sand a surface before an adhesive is to be applied in order increase the strength of the bond. The theory behind this is that the surface area increases as the surface area increases. A change from a flat surface to a rough one increases the surface area of the material on the microscopic level. The fourth theory of how corona treatment improves adhesion to materials is that the air plasma results in a separation of electrons from their molecules, which creates an abundance of charged free radicals to be deposited on the nearest surface. In the case of these applications this surface is the substrate being altered. The deposited charged particles now exhibit a strong static attraction to foreign bodies. Since these theories are not mutually exclusive, the actual mechanism may in fact be a combination of all or part of the four of the aforementioned reasons.

Fabrication of Width Tapered Double Cantilever Beam

To analyze the effectiveness of corona treatment between silicone and prepreg carbon fiber layers a width tapered double cantilever beam test was utilized. Jyoti et al.

[96] pointed out the difficulty of measuring the crack length during dynamic fracture toughness testing on double cantilever (DCB) specimens. A practical solution was found by Daniel et al. [97] with the study of the quasi-static Mode I energy release rate of width tapered specimens, which allowed the energy release rate to be independent of the crack length. There also exists a similar technique of thickness tapered DCB; however, this type is cumbersome to manufacture.

The reasons for the choice of the width tapered double cantilever beam WTDCB specimen discussed in the corona treatment section. The WTDCB test is generally used to test the adhesive bonds between two adherents. In this work a sheet of silicone rubber between two layers of carbon fiber pre-preg were sandwiched in a co-cure process. The silicone rubber was either treated with corona on both sides or untreated for comparison purposes. Four groups of WTDCB are manufactured according to the illustration shown in Figure 5-4, each group containing six specimens: untreated silicone with plain-weave and unidirectional carbon fiber and corona treated silicone with plane weave and unidirectional carbon fiber. The silicone membrane was sandwiched between two six-layer carbon fiber composites. A thin film of Teflon was applied to initiate the crack at the starting point of the beam. Finally, the entire assembly was cured in the oven under vacuum pressure. After curing, the specimens were tested in an Instron universal testing machine (model 5567).

Complete Experimental Arrangements

The experimental setup for the testing of corona treatment consists of two hinges adhered on both sides of the double cantilever beam. The hinges were clamped in the two jaws of the Instron as seen on Figure 5-5. The Instron machine is capable of measuring loads up to 30 kN with maximum and minimum speeds of 500mm/min and

0.001mm/min respectively. The V-clamp design provides an increasing compression force on the hinges with an increasing vertical tensile force applied on the jaws to avoid slipping. The crack was initiated with a Teflon film while the required forces (N) were recorded as the cross-head moved.

Figure 5-6 shows the experimental arrangement to take an initial image of the uncured MAV wing assembly. After the curing process is completed another image was taken using the same setup; however, the wing was held from the frame allowing the membrane to deform in the free space. If the final image was taken with the wing in the mold, the out-of-plane deformations would have been identical to the reference image, and strain values would be inaccurate.

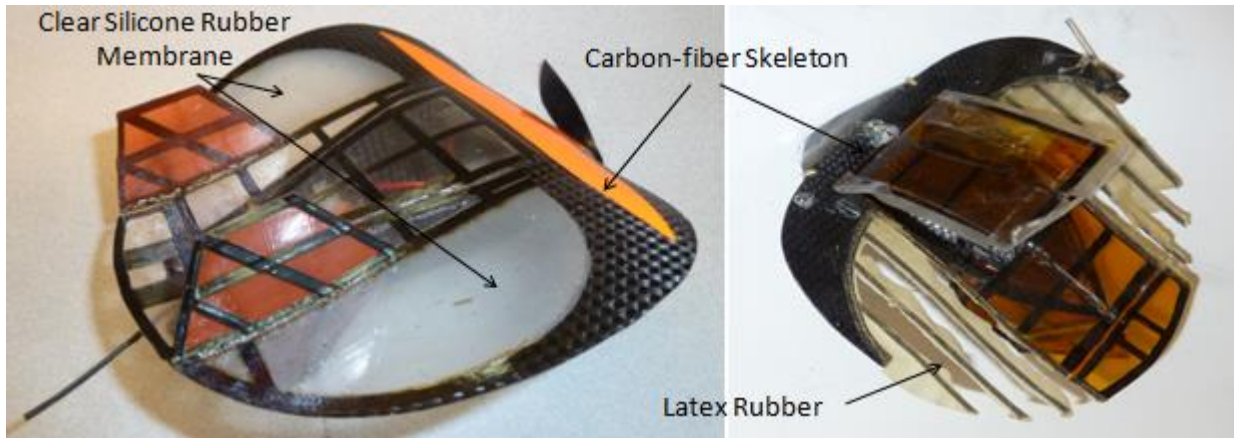


Figure 5-1. An actual perimeter reinforced MAV fabricated via co-cure method with a combination of clear silicone rubber membrane and carbon-fiber skeleton, and a batten reinforced latex rubber MAV one year after manufacturing.

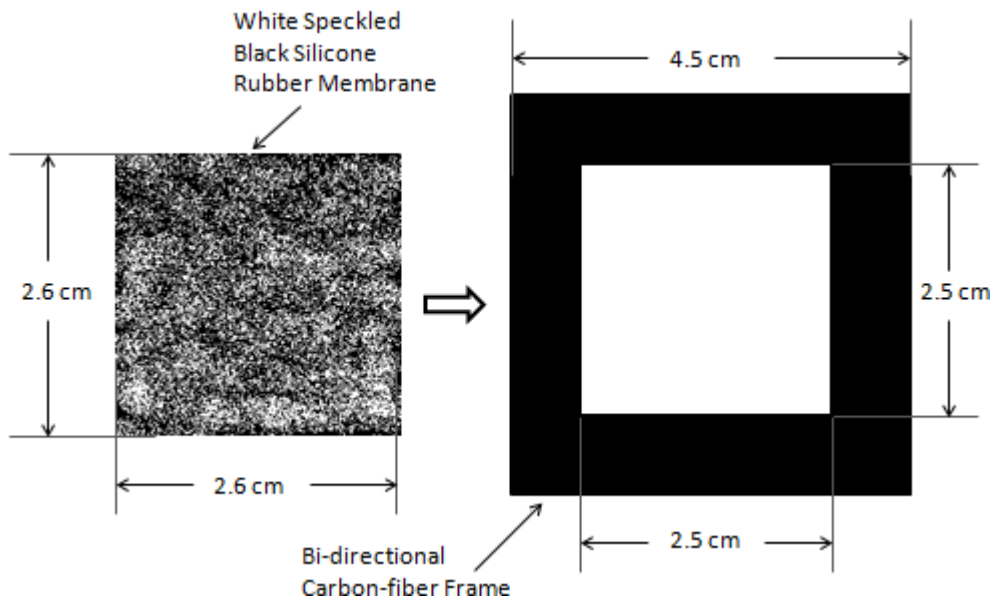


Figure 5-2. Specimen parts (silicone rubber film and carbon fiber frame) dimensions to be co-cured.

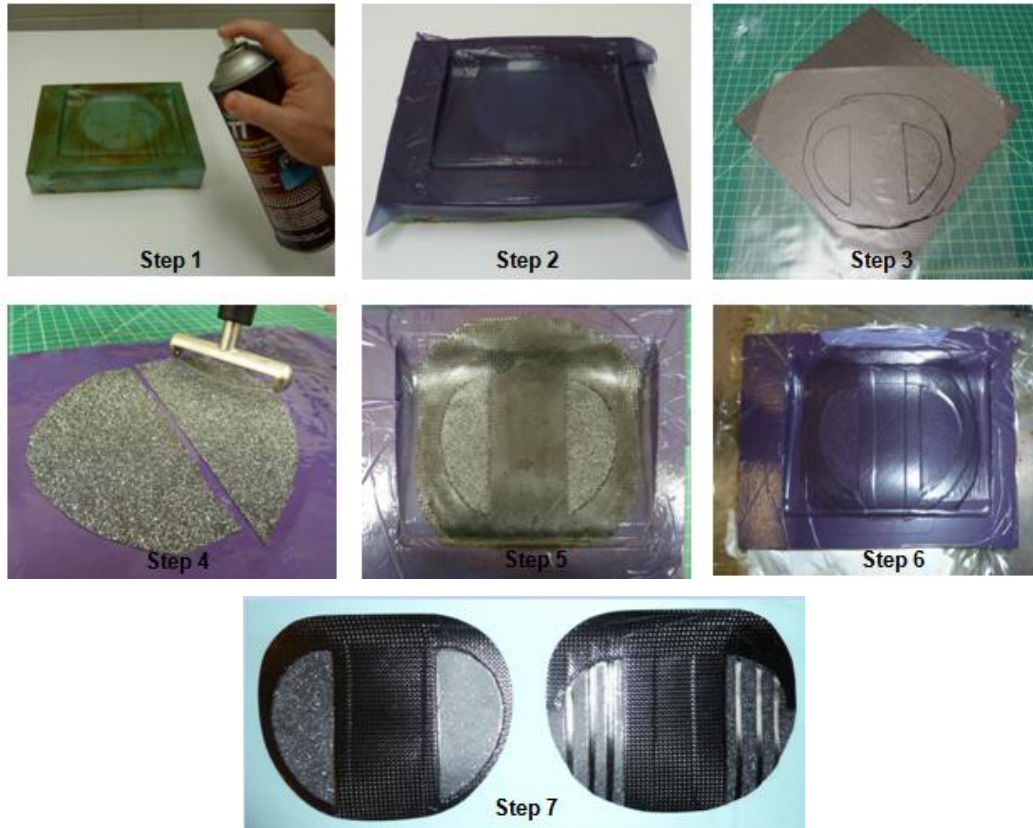


Figure 5-3. Experimental steps involved in the construction and analysis of the MAV wings.

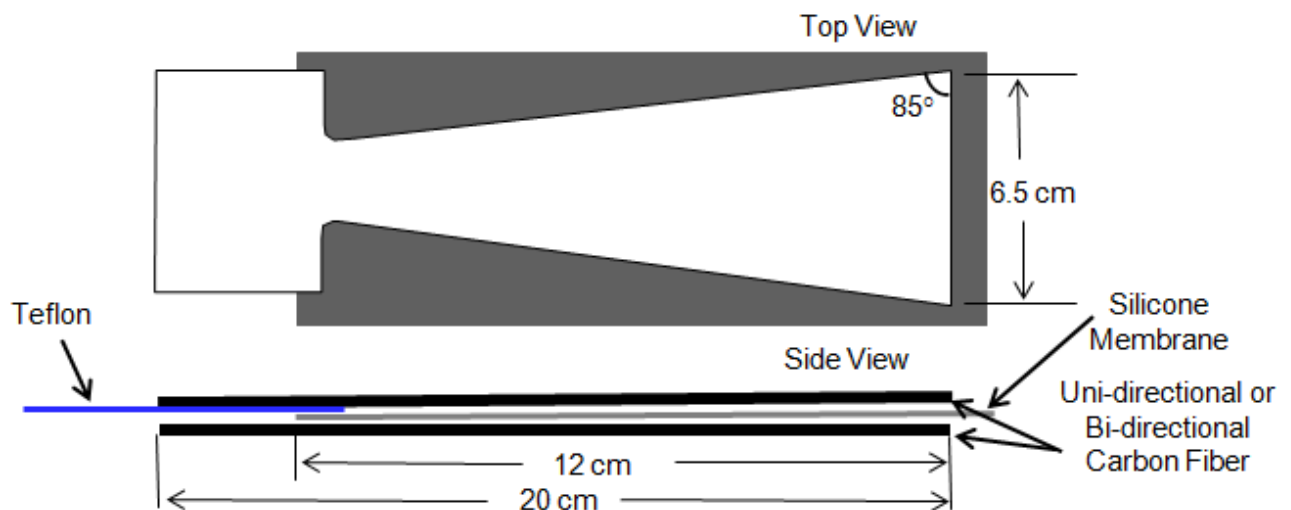


Figure 5-4. Preparation of tapered double cantilever beam.



Figure 5-5. Experimental setup for the analysis of the WTDCB specimens. B) Analysis of the deformed silicone membrane.



Figure 5-6. Experimental setup for the analysis of the deformed silicone membrane.

CHAPTER 6 RESULTS AND DISCUSSION OF CO-CURE METHOD

This chapter will make an effort to quantify the developed pre-strains and deformations of the membrane in the 2-D and 3-D configurations presented in Chapter 5. Strain and out-of-plane displacement gradients taken from various specimens will be compared and analyzed. Finally, to evaluate the effectiveness of corona treatment, results from width tapered double cantilevered beam specimens will be displayed via plots, tables, and photographs.

Membrane Pre-tensioning on 2-D Specimens via Co-cure Method

Initially, 3-D silicone rubber/carbon fiber perimeter reinforced wings were manufactured via co-curing method. To better understand the reasons behind the developed pre-tensions, the problem had to be simplified to a 2-D version. Experimental steps pertained to analyzing the 2-D specimens are thoroughly explained in Chapter 5.

Figure 6-1 shows that the developed pre-strains in x-direction at room temperature are uniform and approximately the same ranging anywhere between 0%-0.5%. Similar strain results are reported in y-direction (Figure 6-2). Samples show signs of negative strain gradients at the edges, which may be due to the membrane having been pressed into the frame through the thickness with the vacuum pressure and the membrane expansion during the curing cycle. This effect is better observed for some individual sample results in Appendix A with higher scale resolutions. Individual results for every step of the experiment are noteworthy for showing a slight increase in strains in all directions for all of the specimens as the temperature is increased from 25°C to 100°C and a slight strain decrease when the temperature reaches at 135°C. For example, in Figure A-4 negative strain gradients/magnitudes are present at the left and right edges

most likely due to the membrane pressed through the frame thickness by the vacuum pressure. In the next two steps as the temperature is elevated to 75°C and 100°C, the strains increase due to temperature and pressure. At this step, the membrane is either tensioned or compressed even further at the edges. When 135°C is reached, the absolute strain magnitudes slightly increase. This effect may be an indication of the vacuum bag shrinking at elevated temperatures. The membrane is then cooled down to room temperature under vacuum where the extreme strain magnitudes in either direction (positive or negative) are present at the edges, while the mid section of membrane is slightly compressed. Finally, when the sample is removed from the vacuum bag, the strain gradient is redistributed. For most of the samples, shear strains in the mid-section are zero while the corners experience the extreme ends of the spectrum (Figure 6-3). All specimens showed signs of shearing strain relief after reaching 135°C, curing temperature (Appendix A). Results show that the experiment is repeatable in two dimensions; however, the developed strains in both directions are not significant. Silicone rubber membrane adhered very well on the carbon-fiber frame proving the effectiveness on the corona treatment.

Membrane Pre-tensioning on MAV Wings via Co-cure Method

Before acquiring the final images, the wing samples were cooled down to room temperature and taken out of the mold allowing the membrane to deform freely in 3-D space to calculate the proper strains and displacements. Out-of-plane displacements are shown in Figure 6-4 while the normal strains in x-and y-directions along with shearing strains are reported in Figure 6-5 through Figure 6-7 for three of the typical wing results among five experiments. The VIC system is not expected to capture the strain information in the carbon fiber frame since a speckling pattern on pre-preg carbon

fiber material would degrade during the curing process. Therefore, only the membrane deformations and strains were taken into account for calculations.

The membrane expanded in-plane due to the vacuum pressure and the high temperature in the oven. When cooled down to room temperature, the wing is pre-tensioned. Peak out-of-plane displacements for all wings (Figure 6-4) vary between 1mm and 2mm, which are located toward the leading edge, and the gradients are different when compared to thermal expanding and adhering method, where two extreme values (positive and negative) are observed along the chord line (Figure 3-36). Similar out-of-plane displacement gradients are present on either side of the individual wings, but different gradients among the wings hint that manufacturing multiple wings in the same vacuum bag may lead to more repeatable results. This may be due to slight changes in vacuum pressure and vacuum bag properties from one experiment to another.

The non-uniformity of x-and y-strains is clearly evident from Figure 6-5 and Figure 6-6 as the wing has a camber and the frame geometry is not symmetrical. Note that all figures show the bottom of the wing. Average strains in x-direction are computed to be approximately 1.5% higher when compared to the strains in y-direction, which may be due to the camber and reflex on the wing. Though, the strain distributions over the membrane are entirely different when compared to thermally expanding and adhering method (Figure 3-37 and Figure 3-38). Shear strain gradients are not consistent; however, the magnitude window observed throughout the membrane area is similar among the three wing samples (Figure 6-7.)

Width Tapered Cantilever Beam (WTCB) Test for Corona Treatment

The cross-head displacement speed on the Instron machine was set to 10mm/s and the applied forces from crack initiation until the complete crack propagation are reported for all specimens in Table 6-1. Uniform application on each specimen during the fabrication plays a crucial role in the adhering process. The experimental scatter for all samples may have been caused by one or a combination of multiple factors in the process of corona treatment: the amount of application time, plasma application distance, and plasma application speed. The high deviation on untreated unidirectional specimens is probably due to the uneven thicknesses of the composite layers.

Table 6-1. Average forces (N) recorded on all specimens.

	Untreated Unidirectional (N)	Treated Unidirectional (N)	Untreated Bidirectional (N)	Treated Bidirectional (N)
Specimen #1	29.7	30.3	19.8	32.9
Specimen #2	21.1	33.9	18.8	22.0
Specimen #3	21.9	30.6	20.6	24.4
Specimen #4	30.5	29.7	20.0	NA*
Specimen #5	21.2	37.2	21.2	20.0
Specimen #6	32.2	30.7	18.9	21.9
Average	26.1	32.1	19.9	24.2
Standard Dev.	5.22	2.91	0.94	5.09

* Results for treated unidirectional specimen #4 are not reported on this table due to a manufacturing error.

The data indicates that more energy is required to separate corona treated specimens, although the difference was less than anticipated since the technique worked so well for MAV wings. Corona treated and untreated specimens with maximum averages are reported on Figure 6-8 and Figure 6-9 along with pictures after separation for further discussion. Untreated samples were separated in a much smoother fashion in comparison to corona treated samples. The dynamics involved in the detachment of corona treated samples are extremely complex due to adhesive and cohesive effects.

By careful viewing the failure surfaces of the samples, it was observed that for all untreated samples the silicone rubber remained only one side of the specimens. The failure was an adhesive failure of the bond between the silicone rubber and the adherent. The failure for the treated samples was markedly different in that silicone rubber remained on both portions.

Although a high standard deviation is observed for most of the specimens shown in Table 6-1, silicone rubber is observed to be adhering much better on MAV wings via Corona treatment method. Membrane never separates from the wing skeleton during flight tests and even after several crashes during these tests. Therefore, the effectiveness of the Corona treatment can be better judged from a practical point of view.

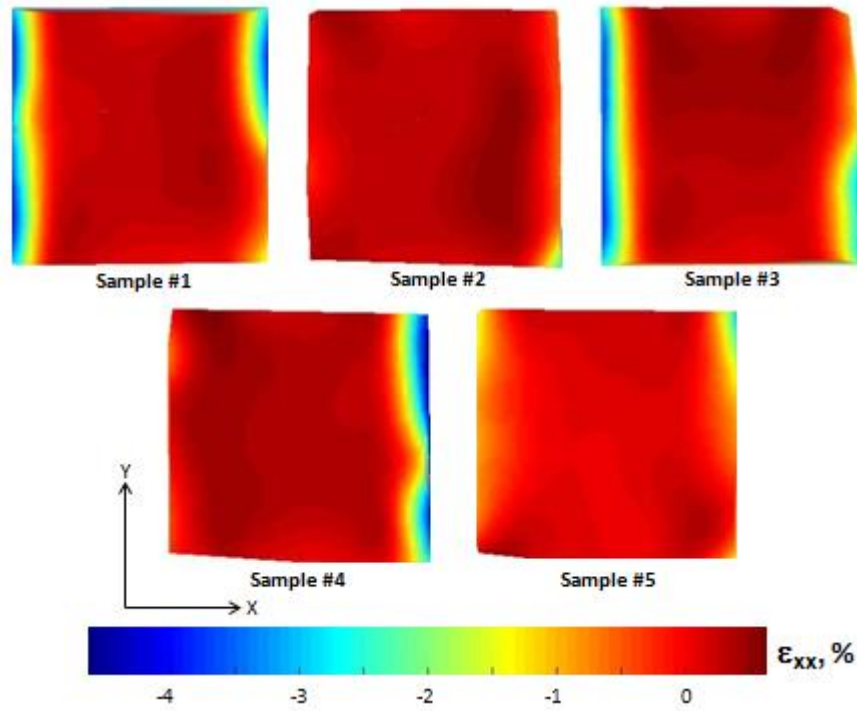


Figure 6-1. Developed pre-strains on 2-D specimens in x-direction with co-cure method.

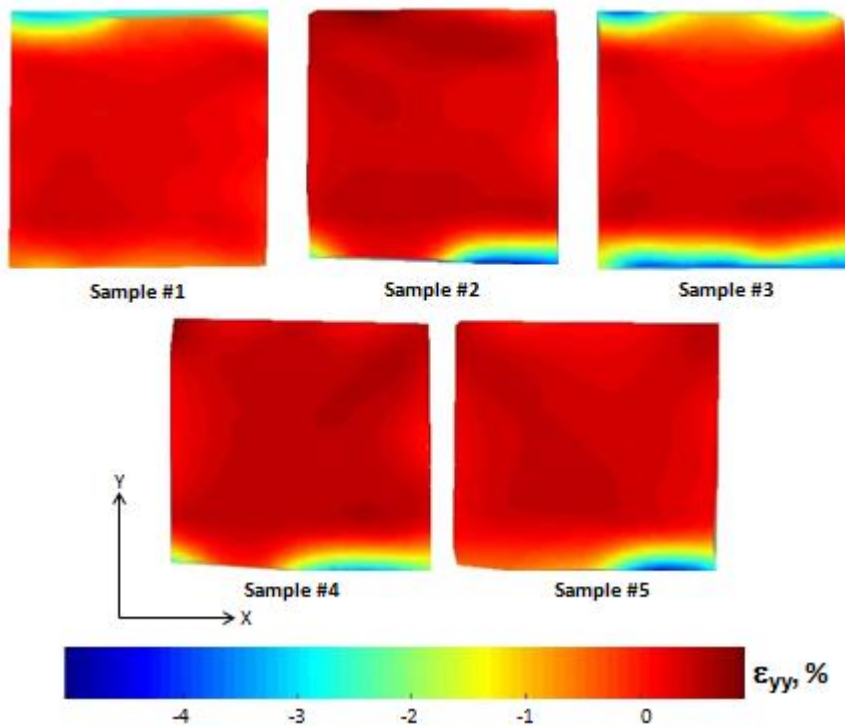


Figure 6-2. Developed pre-strains on 2-D specimens in y-direction with co-cure method.

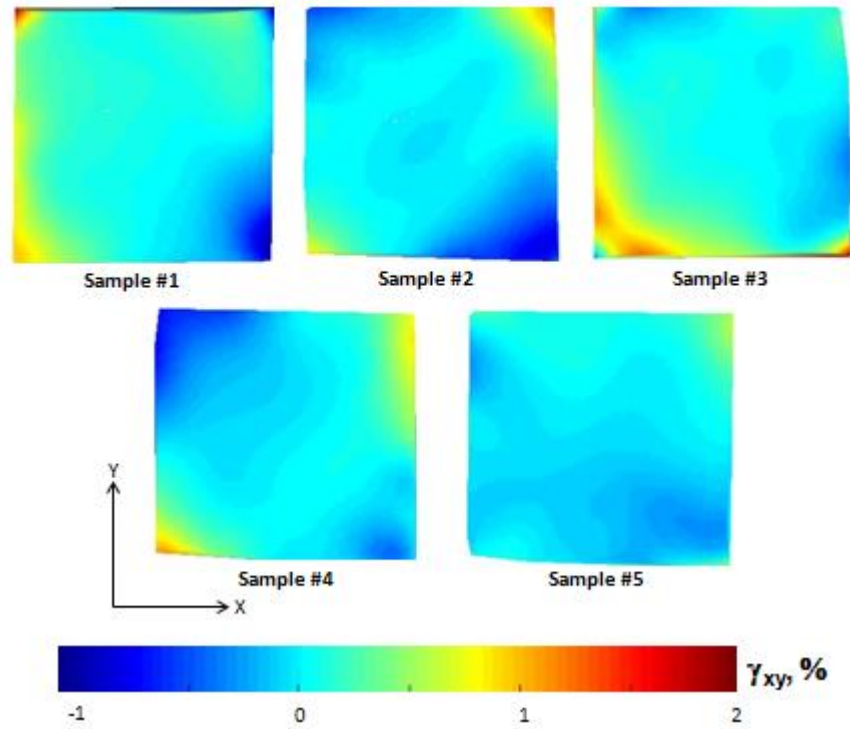


Figure 6-3. Developed shear pre-strains on 2-D specimens with co-cure method.

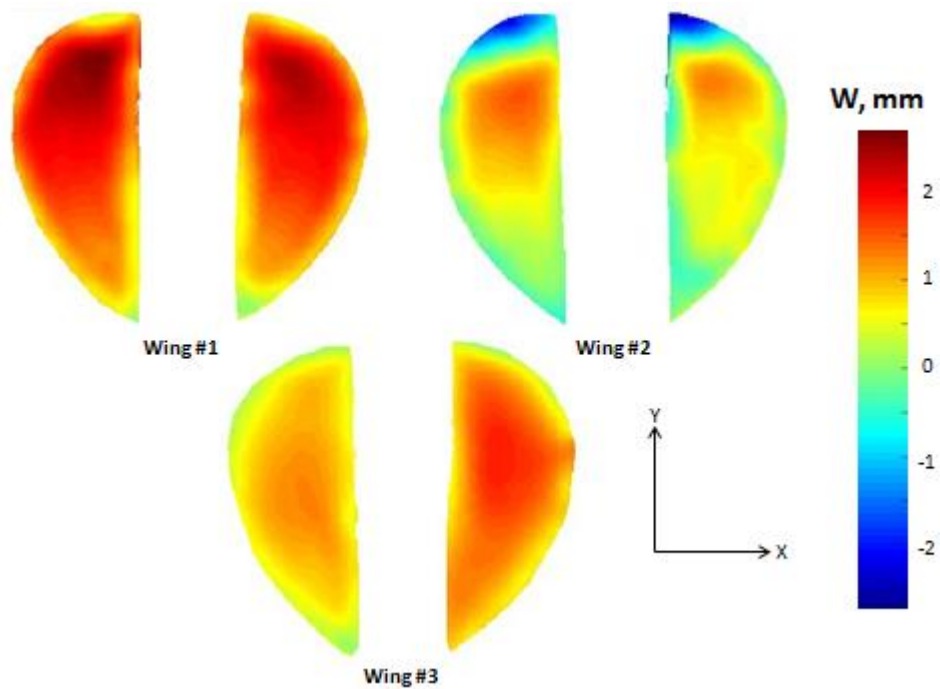


Figure 6-4. Out-of-plane displacements on the membrane for the three samples of perimeter reinforced wings.

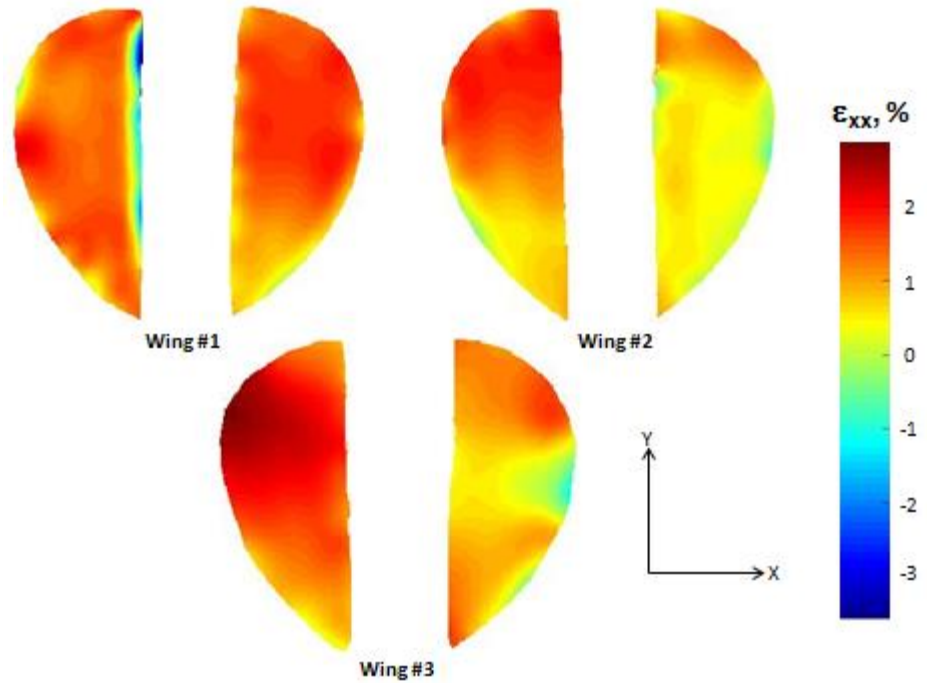


Figure 6-5. Pre-strain gradients in x-direction shown for the three samples of perimeter reinforced wings.

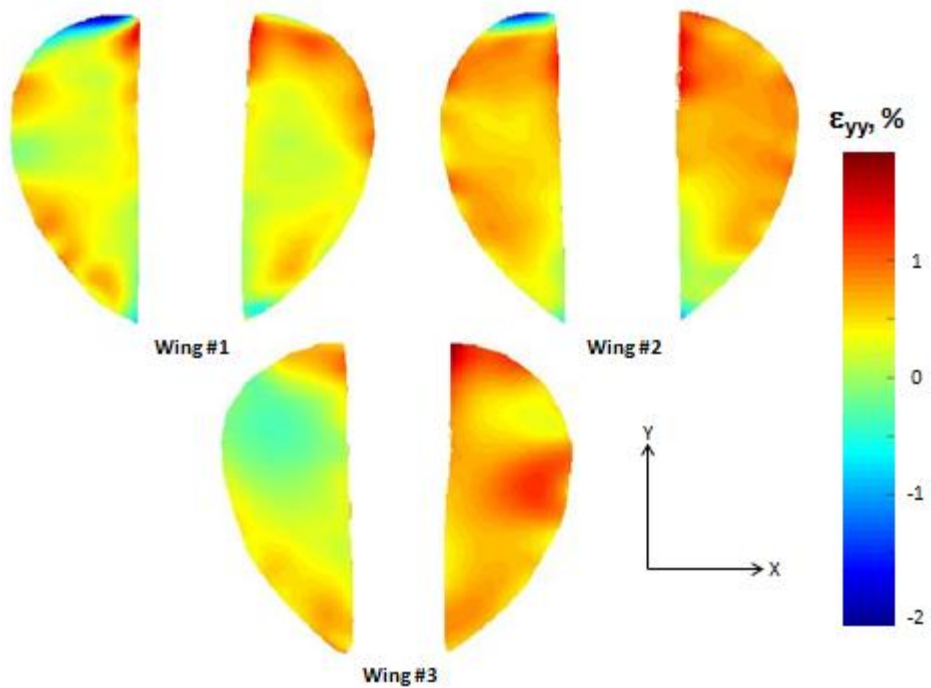


Figure 6-6. Pre-strain gradients in y-direction shown for the three samples of perimeter reinforced wings.

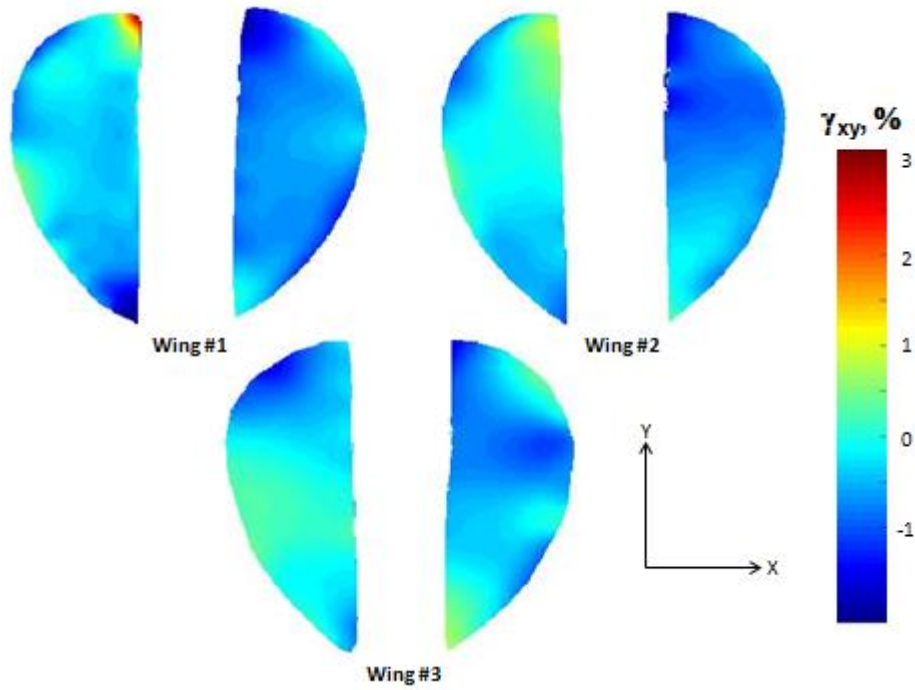


Figure 6-7. Shearing strain gradients for the three samples of perimeter reinforced wings.

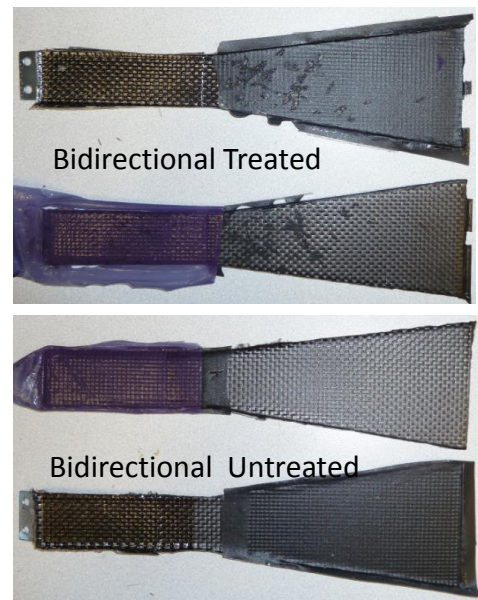
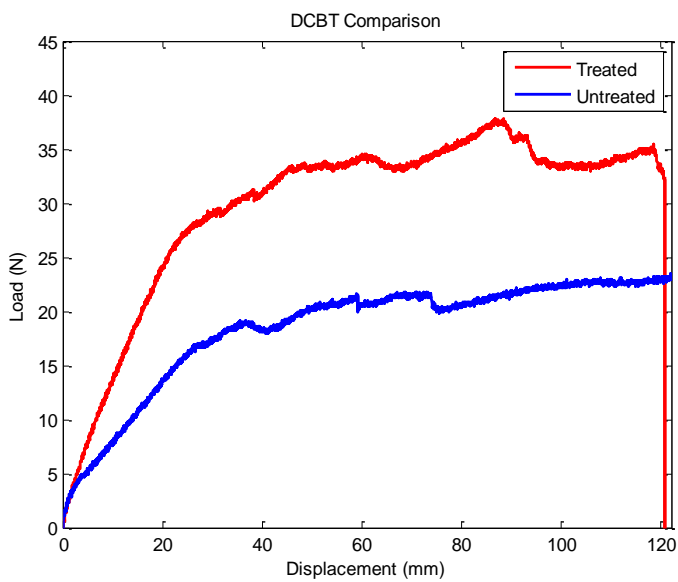


Figure 6-8. WTDCB tests for corona treated and untreated silicone on bidirectional carbon fiber.

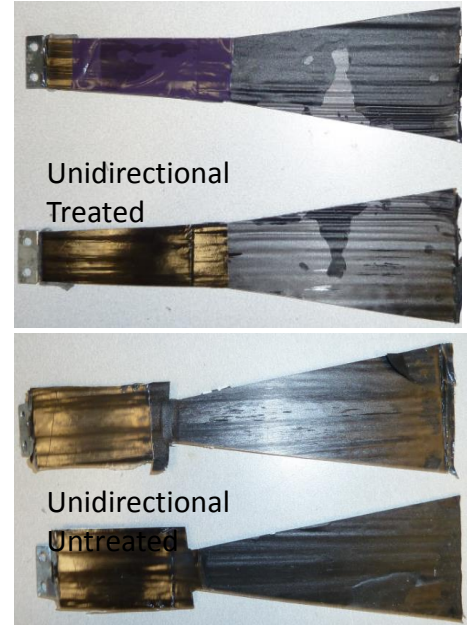
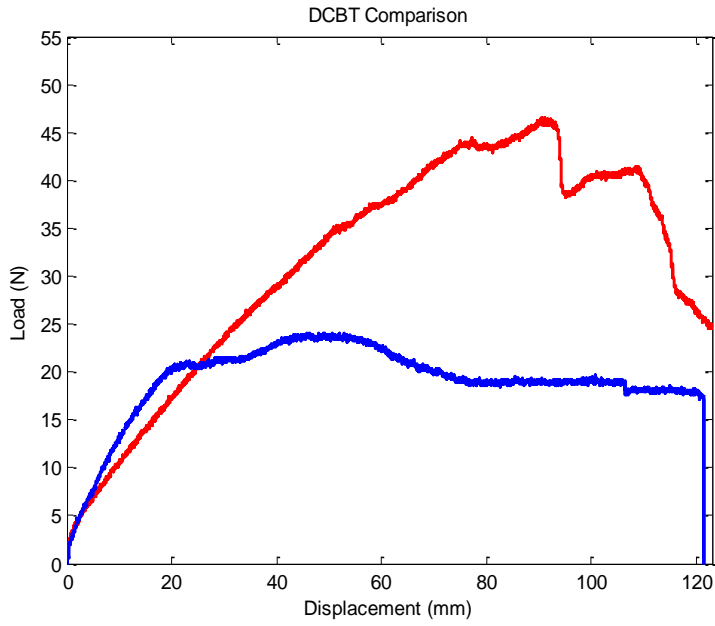


Figure 6-9. WTDCB tests for corona treated and untreated silicone on unidirectional carbon fiber.

CHAPTER 7 CONCLUSIONS AND FUTURE WORK

Conclusions

A new experimental technique regarding two dimensional framework was developed repeatedly adhere pre-strained thin silicone rubber membranes on various carbon fiber frame geometries mimicking fixed-flexible wings. The new procedure was developed to apply known pretension to MAVs and test articles with silicone rubber membranes. The technique showed a relationship between varied applied temperatures, which resulted in membrane stress and strain spatial fields. Repeatability was within $\pm 0.1\%$ strain error margin. The method is unique because it allows one to quantify the pre-tension on a full-field basis and to predict the average strain on a given frame. The displacements and strains on thin silicone rubber membranes attached to 3-D frames were simulated via numerical analysis. Analysis was further elaborated by analyzing more complex and realistic membrane wings with geometries that include dihedral, camber, and reflex. Experimental peak out-of-plane displacement for the wing deviated only 3.5% from the actual value with the Abaqus prediction while the highest strain deviated was approximately 0.3%. After proving the validity of the predictions, over a thousand simulations were performed to understand the relationship between stress, strain, and out-of-plane displacements of the membrane when attached to various 3-D frame geometries. Various configurations included closed single curved, open single curved, and multiple configurations of closed double curved platforms to mimic an array of MAV wings. Simulations showed that all parameters, including percent camber, aspect ratio, amount of reflex, and reflex location affected the membrane form, stresses, and strains.

The co-cure method to pre-strain the wings was also introduced: 2-D specimens and 3-D raw carbon fiber frames were cured with silicone rubber in a vacuum bag. Developed pre-strains for 2-D frames were not significant (approximately 0.5%); however, the strain gradients for the perimeter reinforced wings in x-and y-directions varied for each sample within -3.5% to 2.5%. Displacement magnitudes/gradients of individual samples were similar in both directions but significant changes were recorded among the wings; therefore, the effect of vacuum bag and the magnitude of negative pressure should be investigated for future work. Vacuum bag shrinkage may also have an effect on the developed pre-tension within the membrane. Numerical analysis may be overly complicated. The reasons behind variation in deformations and strains can be better understood with further experiments.

Future Work

The wings discussed in this paper can also be analyzed for aerodynamic loads by attaching the membranes on the wing frames at appropriate temperatures to explore the effect of pre-tension on lift, drag, and pitching moment data. The idea can be transferred to the batten reinforced wings with camber for the analysis of trailing edge vibration. The latter concept is currently studied by several research groups, but only for 2-D cases. The techniques discussed in this dissertation coupled with wind tunnel experiments may optimize the scalloping depth of membrane wings at the free trailing edges for various aspect ratios in 2-D and 3-D.

Stressed membrane structures are very commonly used in daily life, such as umbrellas, tents, and architecture. These constructions can fail under increased loads; for example, the membrane in an umbrella subjected to high winds may tear from its rib. Fabricating the entire structure out of high strength materials can be costly. As seen in

this research, stress and strain gradients were not uniform over a membrane stretched in 3-D space; therefore, high stress areas can be numerically analyzed and membrane thickness can be increased at critical surfaces. An alternative and potentially more aesthetically pleasing solution would be to construct the structure in a hybrid fashion involving the adhering/stitching of higher strength and more cost-effective membrane materials.

Another application of membrane materials is in canvas paintings, where the semi-extensible membrane (cotton or linen, where linen is preferred due to its ability to keep the tension better) is stretched over a 2-D wooden frame. Many different attachment methods exist in the industry to uniformly stretch the canvas on a given frame; however, the effectiveness of these techniques are not quantified or thoroughly proven. Uniform tensioning of a canvas oil painting is important because the material loses some of the tension with time, and non-uniform tensioning would result in a non-uniform relaxation, which in turn would yield a distorted image. A series of VIC experiments involving the speckling of linen canvases and comparing the images at each step for various manufacturing methods may resolve a popular debate in the art industry. In fact, this experimental method can be utilized to certify the proper uniform canvas tensioning for oil painting manufacturers.

APPENDIX
RESULTS FROM FIVE 2-D CO-CURED SPECIMENS

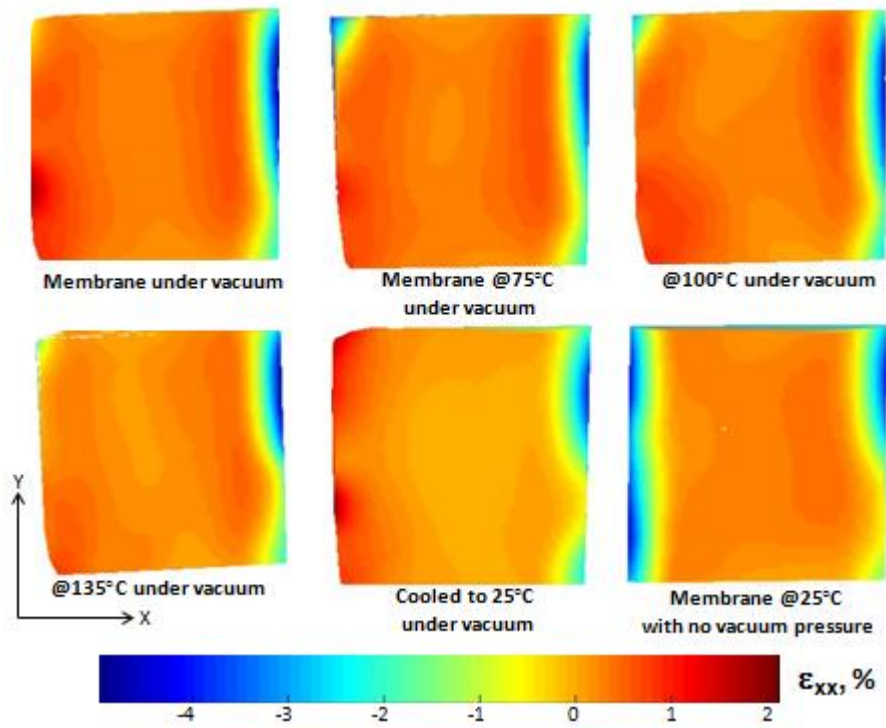


Figure A-1. Normal strains in x-direction for specimen 1 at each step.

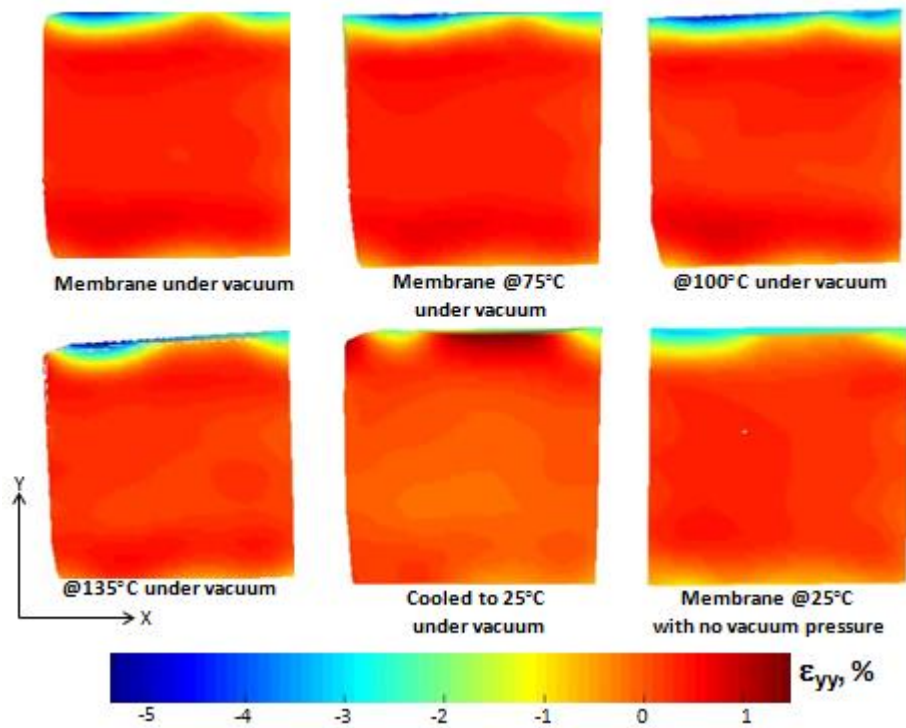


Figure A-2. Normal strains in y-direction for specimen 1 at each step.

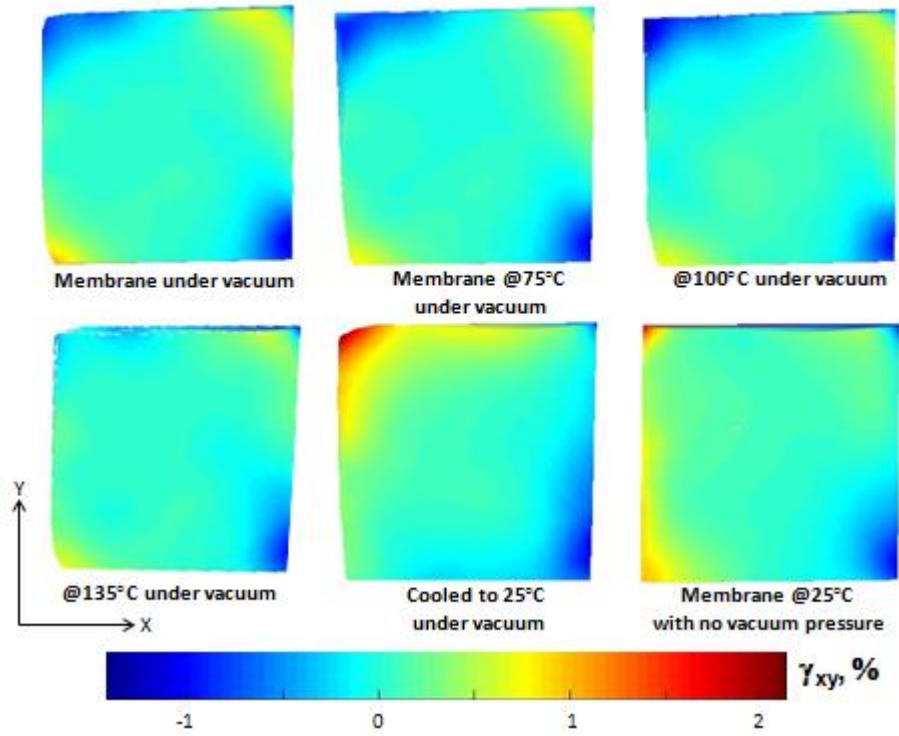


Figure A-3. Shearing strains for specimen 1 at each step.

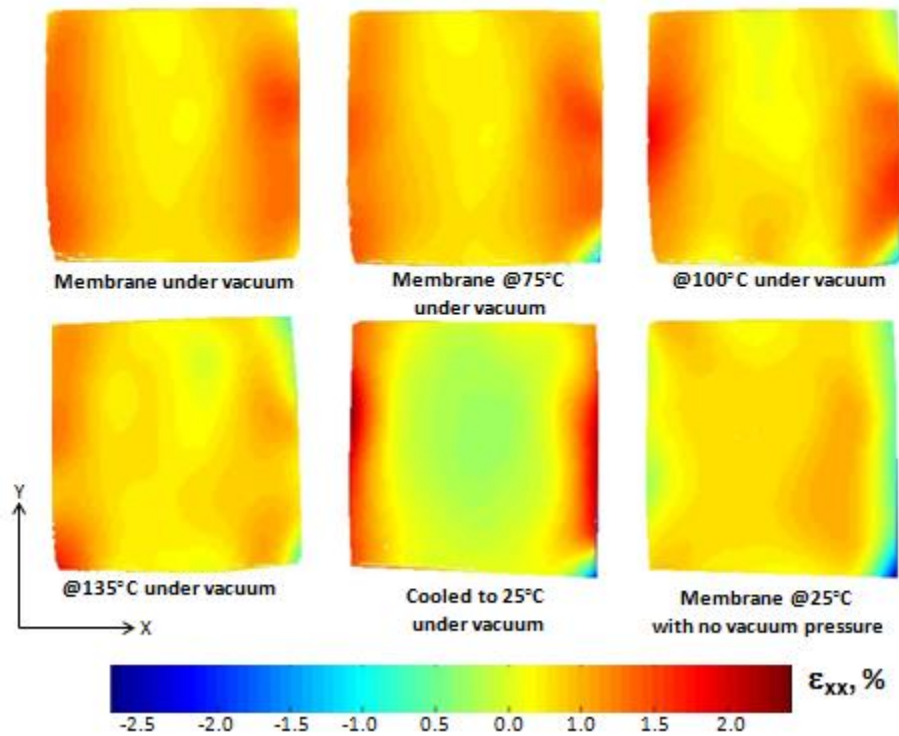


Figure A-4. Normal strains in x-direction for specimen 2 at each step.

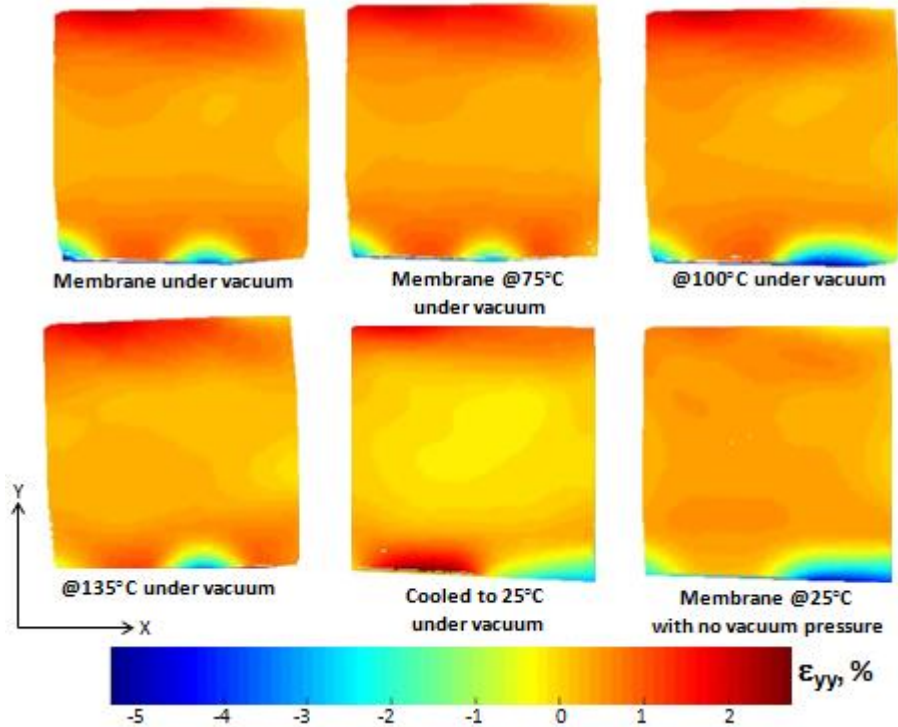


Figure A-5. Normal strains in y-direction for specimen 2 at each step.

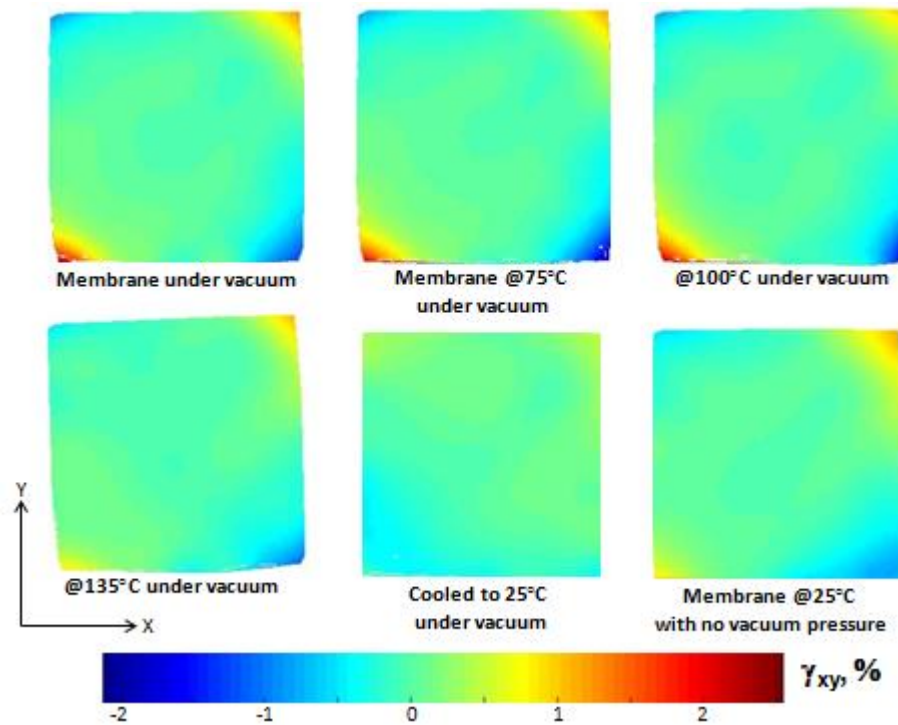


Figure A-6. Shearing strains for specimen 2 at each step.

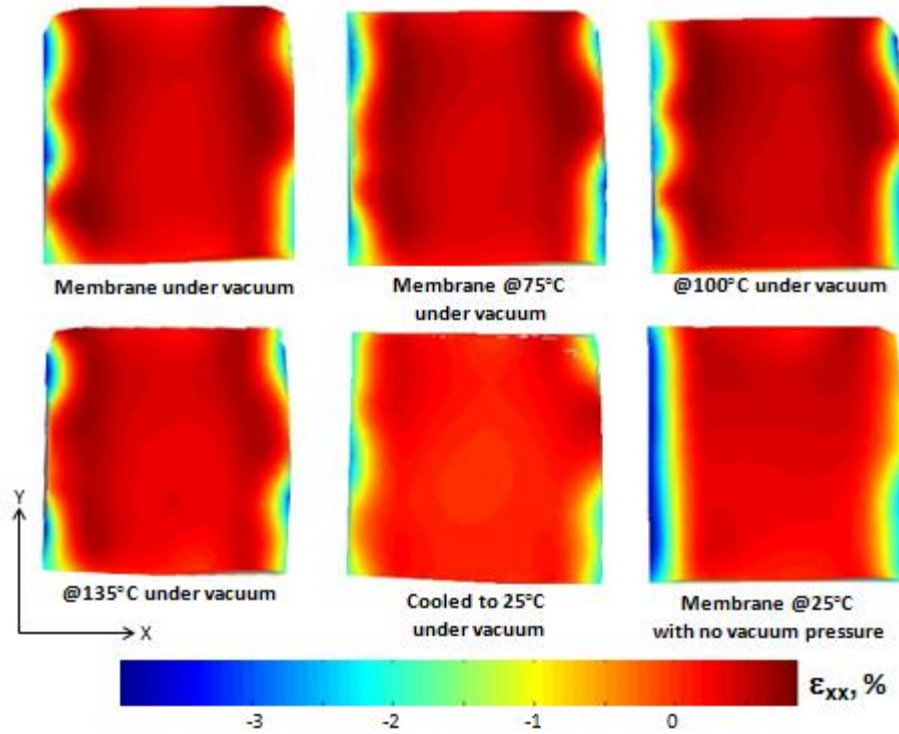


Figure A-7. Normal strains in x-direction for specimen 3 at each step.

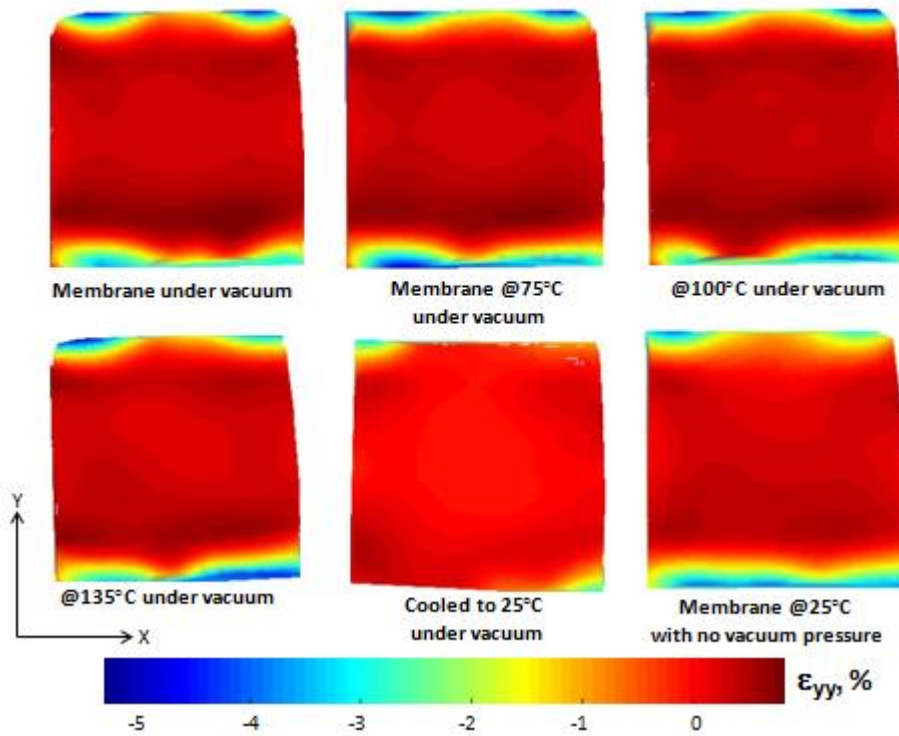


Figure A-8. Normal strains in y-direction for specimen 3 at each step.

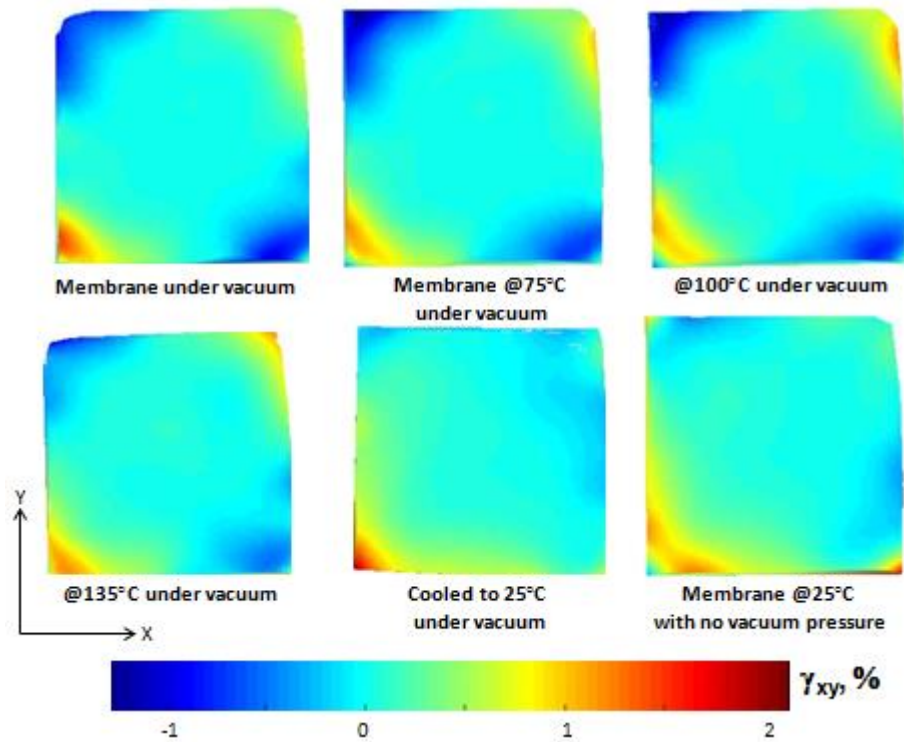


Figure A-9. Shearing strains for specimen 3 at each step.

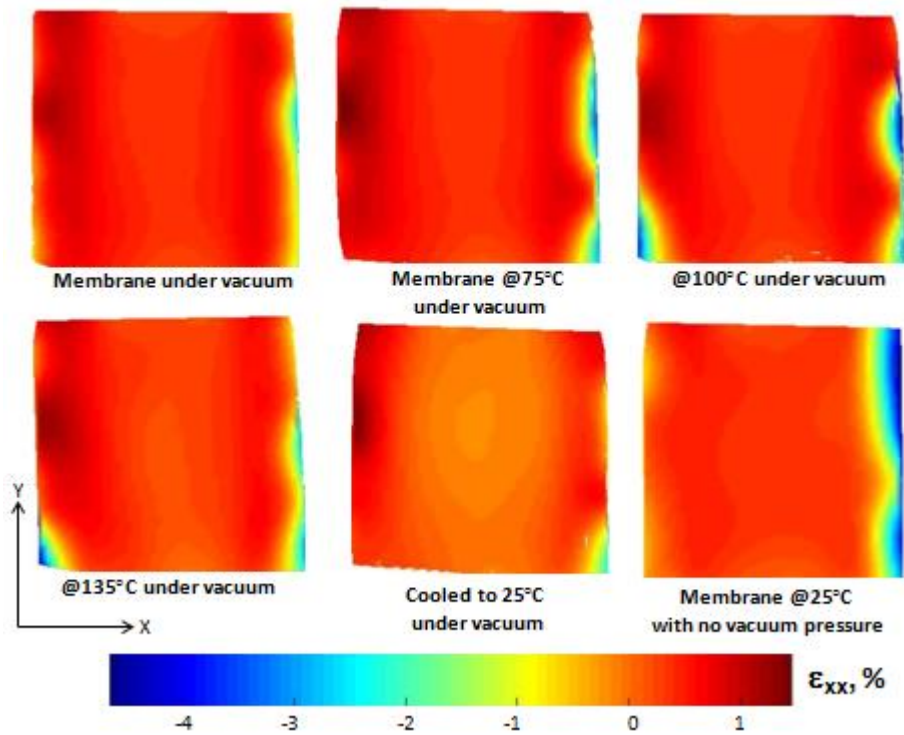


Figure A-10. Normal strains in x-direction for specimen 4 at each step.

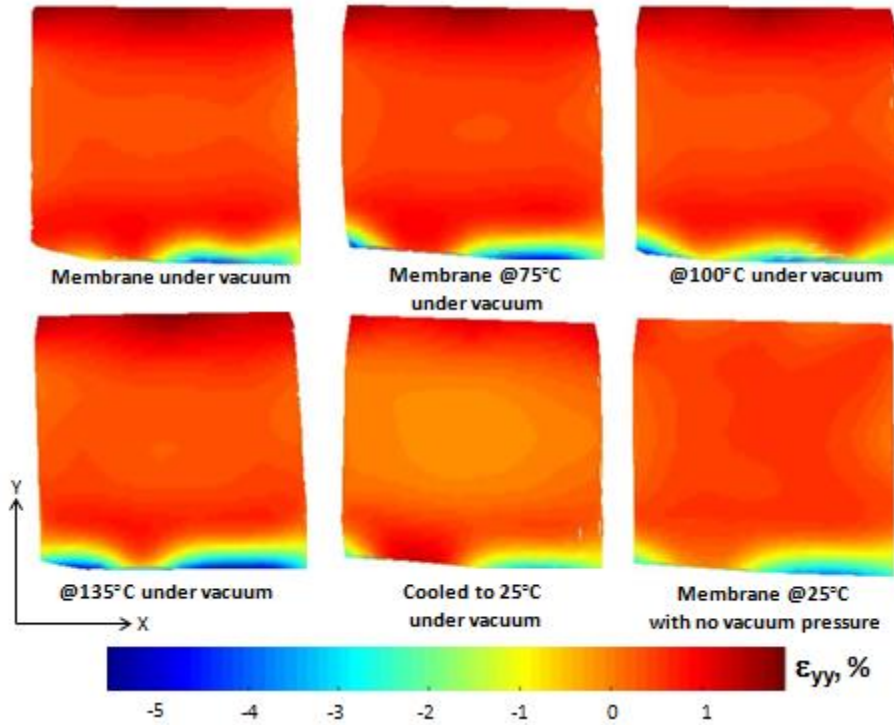


Figure A-11. Normal strains in y-direction for specimen 4 at each step.

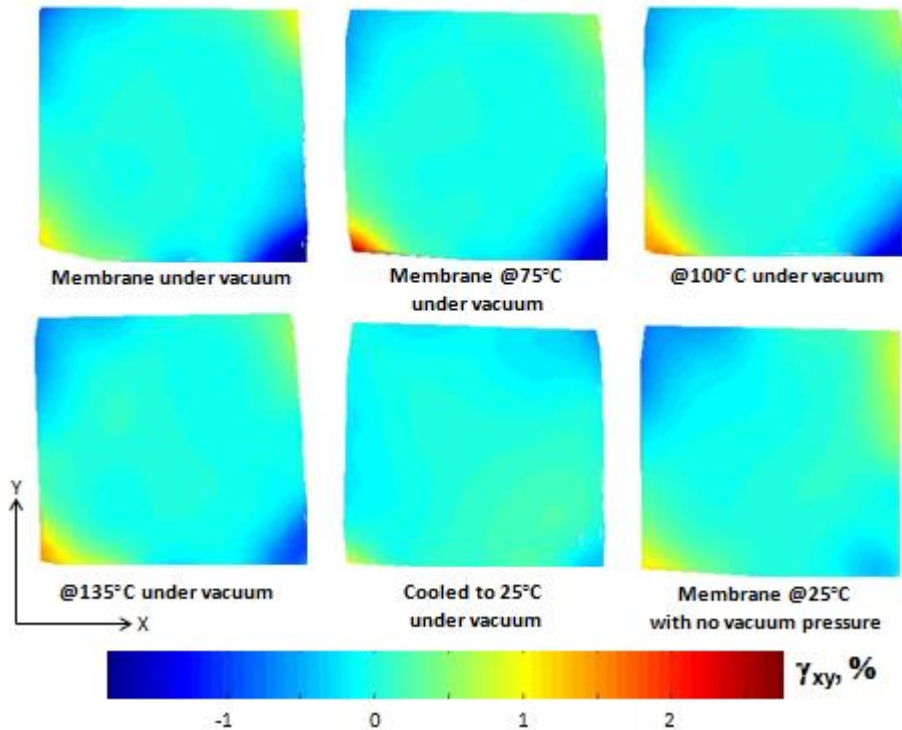


Figure A-12. Shearing strains for specimen 4 at each step.

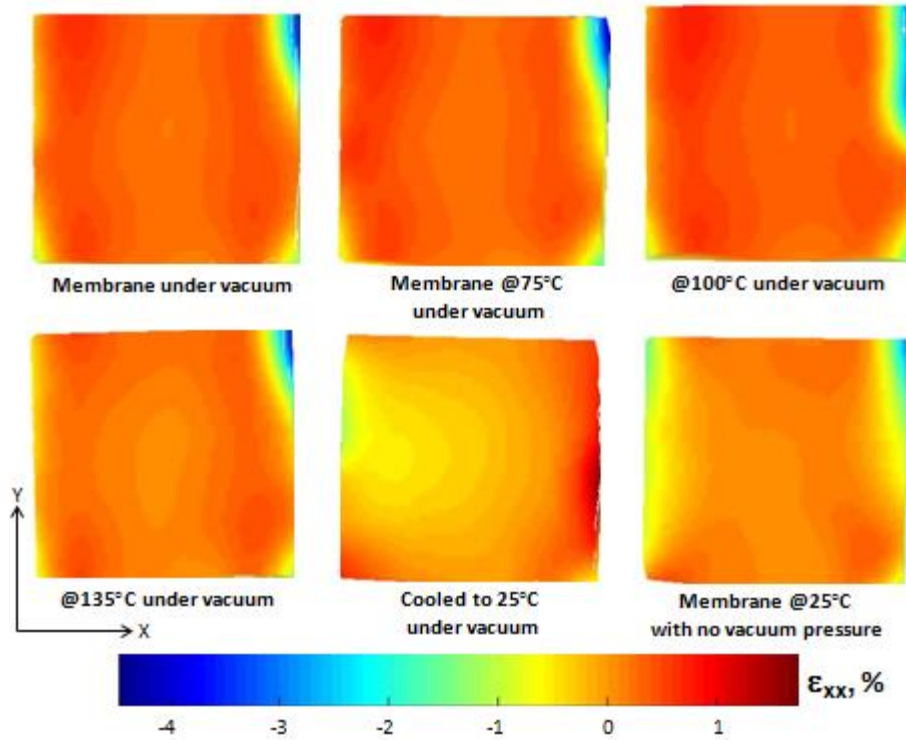


Figure A-13. Normal strains in x-direction for specimen 5 at each step.

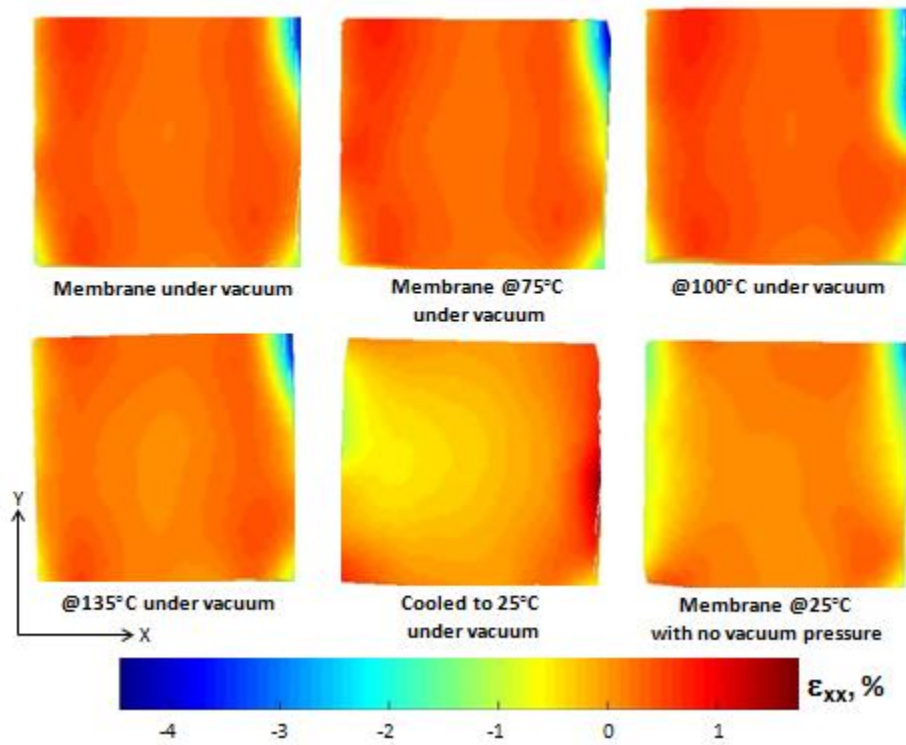


Figure A-14. Normal strains in y-direction for specimen 5 at each step.

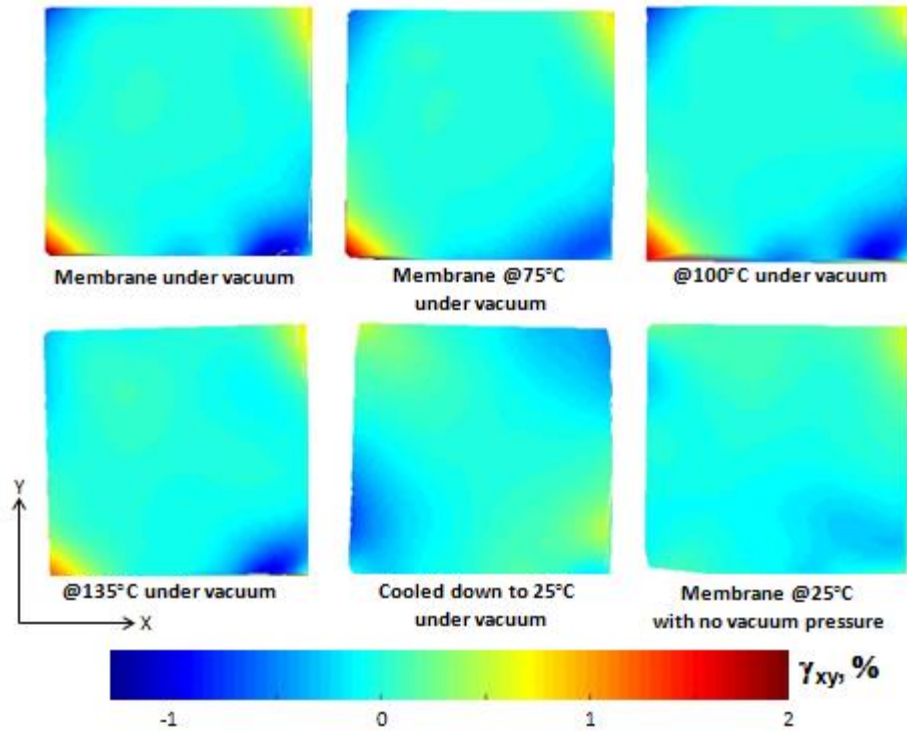


Figure A-15. Shearing strains in for specimen 5 at each step.

LIST OF REFERENCES

- [1] T. J. Mueller, Proceedings of the Conference on Fixed Flapping and Rotary Wing Vehicles at Very Low Reynolds Numbers, Indiana: Notre Dame University, June 5-7, 2000.
- [2] J. M. McMichael and C. M. S. Francis, "Micro Air Vehicles – Toward a New Dimension in Flight," 8 July 1997. [Online]. Available: http://www.fas.org/irp/program/collect/docs/mav_auvsi.htm.
- [3] P. G. Ifju, S. Ettinger, D. Jenkins and L. Martinez, "Composite Materials for Micro Air Vehicles (MAV's)," *SAMPE Journal*, vol. 37, no. 4, pp. 7-12, July/August 2001.
- [4] B. Stanford, P. Ifju, R. Albertani and W. Shyy, "Fixed Membrane Wings for Micro Air Vehicles: Experimental Characterization, Numerical Modeling, and Tailoring," *Progress in Aerospace Sciences*, vol. 44, pp. 258-294, 2008.
- [5] P. Ifju, D. Jenkins, S. Ettinger, Y. Lian, W. Shyy and M. Waszak, "Flexible-Wing Based Micro Air Vehicles," in *Confederation of European Aerospace Societies Aerodynamics Conference*, London, UK, June 10-12, 2003.
- [6] D. A. Lawrence and K. Mohseni, "Efficiency Analysis for Long Duration Electric MAVs," in *AIAA*, Arlington, VA, September 26-29, 2005.
- [7] K. Ailinger, "U.S. Navy Micro Air Vehicle Development," in *14th International UAV Conference*, Bristol, UK, April 12-14, 1999.
- [8] H. Wu, D. Sun and Z. Zhou, "Micro Air Vehicle: Configuration, Analysis, Fabrication, and Test," *IEEE/ASME Transaction on Mechatronics*, vol. 9, pp. 108-117, 2004.
- [9] J. Grasmeyer and M. Keenon, "Development of the Black Widow Micro Air Vehicle," in *39th Aerospace Sciences Meeting and Exhibit*, Reno, NV, January 8-11, 2001.
- [10] G. M. Massaro, "Multi-Disciplinary Design of High Aspect Ratio, Gravity Control Hang Glider with Aero Elastically Enhanced Manoeuvrability," in *ICAS*, 2000.
- [11] P. Dees, "Hang Glider Design and Performance," in *AIAA Aviation Technology, Integration, and Operations Conference*, 2010.
- [12] A. Hedenström, L. C. Johansson, M. Wolf, R. Von Busse, Y. Winter and G. R. Spedding, "Bat Flight Generates Complex Aerodynamic Tracks," *Science (New York, N.Y.)*, vol. 316, no. 5826, pp. 894-897, 2007.

- [13] X. Tian, "Direct measurements of the kinematics and dynamics of bat flight," *Bioinspiration & biomimetics*, vol. 1, no. 4, pp. 510-518, 2006.
- [14] F. T. Muijres, G. R. Spedding, Y. Winter and A. Hedenström, "Actuator disk model and span efficiency of flapping flight in bats based on time-resolved PIV measurements," *Experiments in Fluids*, 2011.
- [15] M. S. Genc, "Unsteady Aerodynamics and Flow-Induced Vibration of a Low Aspect Ratio Rectangular Membrane Wing with Excess Length," *Experimental Thermal and Fluid Science*, 2012, doi: <http://dx.doi.org/10.1016/j.expthermflusci.2012.09.018>.
- [16] N. Mastramico and P. Hubner, "A Study of Wake Characteristics for Membrane Flat and Cambered Plates," in *AIAA Aerodynamic Measurement Technology and Ground Testing Conference*, Seattle, WA, June 23-26, 2008.
- [17] J. P. Hubner and T. Hicks, "Trailing-edge Scalloping Effect on Flat-plate Membrane Wing Performance," *Aerospace Science and Technology*, vol. 15, pp. 670-680, 2011.
- [18] W. Shyy, D. A. Jenkins and R. W. Smith, "Study of Adaptive Shape Airfoils at Low Reynolds Number in Oscillatory Flow," *AIAA Journal*, vol. 35, pp. 1545-8, 1997.
- [19] W. Shyy, M. Berg and D. Ljungqvist, "Flapping and Flexible Wings for Biological and Micro Air Vehicles," *Progress in Aerospace Sciences*, vol. 35, pp. 455-505, 1999.
- [20] A. Song and K. Breuer, "Dynamics of a Compliant Membrane as Related to Mammalian Flight," *AIAA*, 2007.
- [21] Y. Lian, W. Shyy, D. Viieru and B. Zhang, "Membrane Wing Aerodynamics for Micro Air Vehicles," *Progress in Aerospace Sciences*, vol. 39, no. 6-7, pp. 425-465, Oct. 2003.
- [22] W. Pisano and D. Lawrence, "Autonomous Gust Insensitive Aircraft," in *AIAA Guidance, Navigation, and Control Conference*, Honolulu, HI, August 18-21, 2008.
- [23] I. Kajiwaru and R. Haftka, "Simultaneous Optimal Design of Shape and Control System for Micro Air Vehicles," in *AIAA Structures, Structural Dynamics, and Materials Conference*, St. Louis, MO, 1999.

- [24] B. Stanford and P. Ifju, "Aeroelastic Topology Optimization of Membrane Structures for Micro Air Vehicles," *Structural and Multidisciplinary Optimization*, vol. 38, no. 3, pp. 301-316, 2009.
- [25] Y. Abudaram, B. Stanford and P. Ifju, "Wind Tunnel Testing of Load-alleviating Membrane Wings at low Reynolds Numbers," in *47th AIAA Sciences Meeting Including The New Horizons Forum and Aerospace Exposition Conference*, Orlando, FL, 2009.
- [26] A. Fitt and M. Pope, "The Unsteady Motion of Two-dimensional Flags With Bending Stiffness," *Journal of Engineering Mechanics*, vol. 40, no. 3, pp. 227-248, 2001.
- [27] B. Carmichael, "Low Reynolds Number Airfoil Survey," NASA Contractor Report, CR 165803, 1981.
- [28] Y. Lian and W. Shyy, "Laminar-Turbulent Transition of a Low Reynolds Number Rigid or Flexible Airfoil," *AIAA Journal*, vol. 45, no. 7, pp. 1501-1513, 2007.
- [29] C. P. Haggmark, A. A. Bakchinov and P. H. Alfredsson, "Experiments on a Two-Dimensional Laminar Separation Bubble," *Philosophical Transactions: Mathematical, Physical and Engineering Sciences*, vol. 358, no. 1777, pp. 3193-3205, 2000.
- [30] A. Pelletier and T. J. Mueller, "Low Reynolds Number Aerodynamics of Low-Aspect-Ratio, Thin/Flat/Cambered-Plate Wings," *Journal of Aircraft*, vol. 37, no. 5, pp. 825-832, 2000.
- [31] I. Gursul, "Vortex Flows on UAVs: Issues and Challenges," *The Aeronautical Journal*, vol. 108, no. 1090, pp. 597-610, 2004.
- [32] M. Gad-el-Hak, "Micro-Air-Vehicles: Can They be Controlled Better?," *Journal of Aircraft*, vol. 38, no. 3, pp. 419-429, 2001.
- [33] A. Seifert, D. Greenblatt and I. J. Wygnanski, "Active Separation Control: an Overview of Reynolds and Mach Numbers," *Aerospace Science and Technology*, vol. 8, no. 7, pp. 569-582, 2004.
- [34] T. Mueller, "The Influence of Laminar Separation and Transition on Low Reynolds Number Airfoil Hysteresis," *Journal of Aircraft*, vol. 22, no. 9, pp. 763-770, 1985.
- [35] S. Ahuja and C. W. Rowley, "Low-Dimensional Models for Feedback Stabilization of Unstable Steady States," in *46th AIAA Aerospace Sciences Meeting and Exhibit*, Reno, Nevada, 7-10 Jan 2008.

- [36] J. Lin and L. Pauley, "Low-Reynolds-Number Separation on an Airfoil," *AIAA Journal*, vol. 34, no. 8, pp. 1570-1577, 1996.
- [37] J. Tang and K. Zhu, "Numerical and Experimental Study of Flow Structure of Low-Aspect Ratio Wing," *Journal of Aircraft*, vol. 41, no. 5, pp. 1196-120, 2004.
- [38] W. B. Roberts, "Calculation of Laminar Separation Bubbles and Their Effect on Airfoil Performance," *AIAA Journal*, vol. 18, no. 1, pp. 25-31, 1980.
- [39] R. L. Davis, J. E. Carter and E. Reshotko, "Analysis of Transitional Separation Bubbles on Infinite Swept Wings," *AIAA Journal*, vol. 25, no. 3, p. 421-428, 1987.
- [40] R. J. Volino and D. G. Bohl, "Separated Flow Transition Mechanism and Prediction with High and Low Freestream Turbulence under Low Pressure Turbine Conditions," *American Society of Mechanical Engineers Paper*, Paper No. GT2004-53360, 2004.
- [41] R. E. Mayle, "The Role of Laminar-Turbulent Transition in Gas Turbine Engine," *Journal of Turbomachinery*, vol. 113, pp. 509-537, 1991.
- [42] S. K. Roberts and M. I. Yaras, "Effects of Surface Roughness Geometry on Separation Bubble Transition," *American Society of Mechanical Engineers*, Paper No. GT2005-68664, 2005.
- [43] T. J. Praisner and J. P. Clark, "Predicting Transition in Turbomachinery," *American Society of Mechanical Engineers*, Paper No. GT2004-54108, 2004.
- [44] A. Young and H. Horton, "Some Results of Investigation of Separation Bubbles," in *AGARD Conference Proceedings*, No. 4, pp. 779-811, 1966.
- [45] A. Song, X. Tian, E. Israeli, R. Galvao, K. Bishop, S. Swartz and K. Breuer, "Aeromechanics of Membrane Wings with Implications for Animal Flight," *AIAA Journal*, vol. 46, no. 8, pp. 2096-2106, 2008.
- [46] G. Fleming, S. Bartram, M. Waszak and L. Jenkins, "Projection Moiré Interferometry Measurements of Micro Air Vehicle Wings," *SPIE Paper*, pp. 4448-16.
- [47] P. Wu, B. Stanford and P. Ifju, "Structural Deformation Measurements of Anisotropic Flexible Flapping Wings for Micro Air Vehicles," in *AIAA Structures, Structural Dynamics, and Materials Conference*, Schaumburg, IL, April 7-10, 2008.

- [48] H. Hu, M. Tamai and J. Murphy, "Flexible-Membrane Airfoils at Low Reynolds Numbers," *Journal of Aircraft*, vol. 45, no. 5, pp. 1767-1778, 2008.
- [49] P. Rojratsirikul, Z. Wang and I. Gursul, "Unsteady Aerodynamics of Membrane Airfoils," in *AIAA Aerospace Sciences Meeting and Exhibit*, Reno, NV, January 7-10, 2008.
- [50] A. Timpe, L. Ukeiley, Z. Zhang, J. Hubner and P. Ifju, "Flow and Structures Measurements of a Passively Compliant Wing," in *AIAA*, 2012.
- [51] J. W. Johnston, W. Romberg, P. J. Attar and R. Parthasarathy, "Experimental Characterization of Limit Cycle Oscillations in Membrane Wing Micro Air Vehicles," *Journal of Aircraft*, vol. 47, no. 4, pp. 1300-1308, 2010.
- [52] P. Rojratsirikul, Z. Wang and I. Gursul, "Unsteady Fluid-Structure Interactions of Membrane Airfoils at Low Reynolds Numbers," *Experiments in Fluids*, vol. 46, no. 5, pp. 859-872, 2009.
- [53] P. Rojratsirikul, Z. Wang and I. Gursul, "Unsteady Aerodynamics of Low Aspect Ratio Membrane Wings," in *48th AIAA Aerospace Sciences Meeting*, Orlando, Florida, 4-7 January 2010.
- [54] P. Rojratsirikul, M. S. Genc, Z. Wang and I. Gursul, "Flow-Induced Vibrations of Low Aspect Ratio Rectangular Membrane Wings," *Journal of Fluids and Structures*, vol. 27, pp. 1296-1309, 2011.
- [55] P. Rojratsirikul, Z. Wang and I. Gursul, "Effect of Pre-strain and Excess Length on Unsteady Fluid-structure Interactions of Membrane Airfoils," *Journal of Fluids and Structures*, vol. 26, no. 3, pp. 359-376, 2010.
- [56] R. E. Gordnier, "High Fidelity Computational Simulation of a Membrane Wing Airfoil," *Journal of Fluids and Structures*, vol. 25, pp. 897-917, 2008.
- [57] A. Timpe, *Flow and Structure Interactions in Membrane Wings at Low Reynolds Number*, Masters Thesis, Department of Mechanical and Aerospace Engineering, University of Florida, 2012.
- [58] E. Onate and B. Kroplin, *Textile Composites and Inflatable Structures*, Dordrecht: Springer, 2005.
- [59] J. Lodder, "Curvature in the Calculus Curriculum," *The American Mathematical Monthly*, vol. 110, no. 7, p. 593-605, 2003.

- [60] W. J. Lewis, *Tension Structures. Form and Behaviour*, London: Thomas Telford, 2003.
- [61] D. Veenendaal and P. Block, "An Overview and Comparison of Structural Form Finding Methods for General Networks," *International Journal of Solids and Structures*, vol. 49, no. 26, pp. 3741-3753, 2012.
- [62] K. U. Bletzinger and E. Ramm, "A General Finite Element Approach to the Form Finding of Tensile Structures by the Updated Reference Strategy," *International Journal of Space Structures*, vol. 14, pp. 131-145, 2011.
- [63] M. R. Barnes, "Form Finding and Analysis of Tension Structures by Dynamic Relaxation," *International Journal of Space Structures*, vol. 14, pp. 89-104, 1999.
- [64] H. Schek, "The Force Density Method for Form Finding and Computation of General Networks," *Computer Methods in Applied Mechanics and Engineering*, vol. 3, pp. 115-134, 1974.
- [65] A. Siev and J. Eidelman, "Stress Analysis of Prestressed Suspended Roofs," *Journal of the Structural Division*, pp. 103-121, 1964.
- [66] E. Haug and G. H. Powell, "Analytical Shape Finding for Cable Nets," in *Proceedings of the 1971 IASS Pacific Symposium Part II on Tension Structures and Space Frames*, Tokyo and Kyoto, Japan, 1972.
- [67] P. Basso and A. Del Grosso, "Form-finding Methods for Structural Frameworks: a Review," in *Proceedings of the International Association of Shells and Spatial Structures*, London, 2011.
- [68] L. Grundig, E. Moncrieff, P. Singer and D. Strobel, "A History of the Principal Developments and Application of the Force Density Method in Germany 1970-1999," in *Proceedings of IASS-IACM 2000 Fourth International Colloquium on Computation of Shell & Spatial Structures*, Chania-Crete, Greece, 2000.
- [69] R. M. O. Pauletti and P. M. Pimenta, "The Natural Force Density Method for the Shape Finding of Taut Structures," *Computer Methods in Applied Mechanics and Engineering*, vol. 197, pp. 4419-4428, 2008.
- [70] J. Y. Zhang and O. M., "Adaptive Force Density method for Form-finding Problem of Tensegrity Structures," *International Journal of Solids and Structures*, vol. 43, pp. 5658-5673, 2006.

- [71] T. Van Mele and P. Block, "Novel Form Finding method for Fabric Formwork for Concrete Shells," *Journal of the International Association of Shell and Spatial Structures*, vol. 52, pp. 217-224, 2011.
- [72] B. Maurin and R. Motro, "Investigation of Minimal Forms with Density Methods," *Journal of the International Association for Shell and Spatial Structures*, vol. 38, no. 3, pp. 143-154, 1997.
- [73] J. Sancez, M. A. Serna and M. Paz, "A multi-step Force-density Method and surface-fitting approach for the Preliminary Shape Design of Tensile Structures," *Engineering Structures*, vol. 29, pp. 1966-1976, 2007.
- [74] R. B. Haber and J. F. Abel, "Initial Equilibrium Solution Methods for Cable Reinforced Membranes," *Computer Methods in Applied Mechanics and Engineering*, vol. 30, pp. 263-284, 1982.
- [75] J. H. Argyris, T. Angelopoulos and B. Bichat, "A General Method for the Shape Finding of Lightweight Tension Structures," *Computer Methods in Applied Mechanics and Engineering*, vol. 3, pp. 135-149, 1974.
- [76] K. Linkwitz, "Formfinding by the "Direct Approach" and Pertinent Strategies for the Conceptual Design of Prestressed and Hanging Structures," *International Journal of of Space Structures*, vol. 14, pp. 73-87, 1999.
- [77] H. A. Buchholdt, M. Davies and M. J. L. Hussey, "The Analysis of Cable Nets," *Journal of the Institute of Mathematics and Applications*, vol. 4, pp. 339-358, 1968.
- [78] W. C. Knudson and A. C. Scordelis, "Cable Forces for Desired Shapes in Cable-net Structures," in *Proceeding of the 1971 IASS Pacific Symposium Part II on Tension Structures and Space Frames*, Tokyo and Kyoto, Japan, 1972.
- [79] H. Ohyama and S. Kawamata, "A Problem of Surface Design for Prestressed Cable Nets," in *Proceedings of the 1971 IASS Pacific Symposium Part II on Tension Structures and Space Frames*, Tokyo and Kyoto, Japan, 1972.
- [80] B. Maurin and R. Motro, "The Surface Stress Density method as a Form-finding Tool for Tensile Membranes," *Engineering Structures*, vol. 20, no. 8, pp. 712-719, 1998.
- [81] B. Maurin and R. Motro, "Investigation of Minimal Forms with Conjugate Gradient Method," *International Journal of Solids and Structures*, vol. 38, no. 14, pp. 2387-2399, 2001.

- [82] M. R. Barnes, "Form-finding and Analysis of Prestressed Nets and Membranes," *Computers & Structures*, vol. 30, no. 3, pp. 685-695, 1988.
- [83] K. Y. Tan, "The Computer Design of Tensile Membrane Structures," in *PhD thesis, University of Queensland*, Brisbane, Australia, 1989.
- [84] K.-U. Bletzinger, M. Firi, J. Linhard and R. Wuchner, "Computational Morphogenesis of Free Form Shells: Filter Methods to Create Alternative Solutions," in *Symposium of the International Association for Shell and Spatial Structures*, Valencia, 2009.
- [85] R. Wuchner and K. U. Bletzinger, "Stress-adapted Numerical Form Finding of Prestressed Surfaces by the Updated Reference Strategy," *International Journal of Numerical Methods in Engineering*, vol. 64, pp. 143-166, 2005.
- [86] W. J. Lewis, "The Efficiency of Numerical Methods for the Analysis of Prestressed Nets and Pin-jointed Frame Structures," *Computers and Structures*, vol. 33, no. 3, pp. 791-800, 1989.
- [87] W. J. Lewis, "Computational Form-finding Methods for Fabric Structures," *Proceedings of the ICE -Engineering and Computational Mechanics*, vol. 161, no. 3, pp. 139-149, 2008.
- [88] Y. W. Wong, S. Pellegrino and K. C. Park, "Prediction of Wrinkle Amplitudes in Square Solar Sails," in *Proceedings of 44th AIAA/ASME/ASCE/AHS/ASC Structures, Structural Dynamics, and Materials Conference and Exhibit*, Norfolk, VA, 2003.
- [89] M. Sutton, M. Cheng, W. Peters, Y. Chao and S. McNeill, "Application of an Optimized Digital Correlation Method to Planar Analysis," *Image and Vision Computing*, vol. 4, no. 3, pp. 143-151, 1986.
- [90] H. Schreier, J. Braasch and M. Sutton, "Systematic Errors in Digital Image Correlation Caused by Intensity Interpolation," *Optical Engineering*, vol. 39, no. 11, pp. 2915-2921, 2000.
- [91] B. Stanford, M. Sytsma, R. Albertani, D. Viieru, W. Shyy and P. Ifju, "Static Aeroelastic Model Validation of Membrane Micro Air Vehicle Wings," *AIAA Journal*, vol. 45, no. 12, pp. 2828-2837, December 2007.
- [92] Z. Zhang, J. P. Hubner, Y. Abudaram, L. Ukeiley, P. Ifju, N. Martin and A. Wrist, "Force and Deformation Measurement on Low Aspect Ratio Membrane Airfoils," in *51st AIAA Sciences Meeting*, Grapevine, TX, January 7-10, 2013.

- [93] R. Albertani, B. Stanford, J. Hubner and P. Ifju, "Aerodynamic Coefficients and Deformation Measurements on Flexible Micro Air Vehicle Wings," *Experimental Mechanics*, vol. 47, no. 5, pp. 625-635, 2007.
- [94] D. Zhang, Q. Sun and L. C. Wadsworth, "Mechanism of Corona Treatment on Polyolefin Films," *Polymer Engineering & Science*, vol. 38, no. 6, pp. 965-970, 1998.
- [95] J. Bikerman, "Causes of Poor Adhesion: Weak Boundary Layers," *Ind. Eng. Chem.*, vol. 59, no. 9, pp. 40-44, 1967.
- [96] J. Aurodhya, R. Gibson and G. Newaz, "Experimental Studies of Mode I Energy Release Rate in Adhesively Bonded Width Tapered Composite DCB Specimens," *Composites Science and Technology*, vol. 65, pp. 9-18, 2005.
- [97] I. M. Daniel, I. Shareef and A. A. Aliyu, "Rate Effect On Delamination Fracture Toughness Of A Toughened Graphite/Epoxy," *American Society for Testing and Materials*, pp. 260-274, 1987.
- [98] W. Shyy and Y. Lian, "Laminar-Turbulent Transition of a Low Reynolds Number," *AIAA*, vol. 45, no. 7, pp. 1501-1513, 2007.
- [99] Y. Abudaram, P. Ifju, J. P. Hubner and L. Ukeiley, "Controlling Pre-tension of Silicone Membranes on Micro Air Vehicle Flexible Wings," in *50th AIAA Sciences Meeting*, Nashville, TN, January 9-12, 2012.
- [100] Z. Zhang, H. J. P, A. Timpe, L. Ukeiley, Y. Abudaram and P. Ifju, "Effect of Aspect Ratio on Flat-Plate Membrane Airfoils," in *50th AIAA Sciences Meeting*, Nashville, TN, January 9-12, 2012.
- [101] Y. Abudaram, S. Rohde, J. P. Hubner and P. Ifju, "A Novel Method to Attach Membranes Uniformly on MAV wings," in *Society of Experimental Mechanics*, Costa Mesa, CA, June 11-14, 2012.
- [102] Polytec, Polytec Scanning Vibrometer Theory Manual, As of Software 8.4.

BIOGRAPHICAL SKETCH

Yaakov Jack Abudaram was born in Istanbul, Turkey. Having been under the influence of his father, he had always wanted to become a medical doctor; though, during the last year of high school, he realized he loved numbers more than dissecting humans, so he chose to study a major that would fulfill his desire: he studied physics for two years at the University of Kocaeli in Izmit, Turkey. Afterward, he took the opportunity to come to the United States, learn English, and continue his education at Edison College aiming to study aerospace engineering. He earned his dual Bachelor of Science Degree in mechanical and aerospace engineering in December 2006 from the University of Florida. During the last two semesters of his college years, his enthusiasm toward airplanes pushed him to the doors of Dr. Ifju's Micro Air Vehicle Laboratory. After working there for a few weeks, he felt that this laboratory was where he belonged. He spent extensive hours at the lab building wings and fuselages, installing servos, linkages, motors, cameras, and talking to his supervisor, Kyuho Lee, about airplanes and life. Finally, he found himself studying under Dr. Peter Ifju as a graduate student, and earned his Master of Science Degree in mechanical engineering in December 2009. He pursued his dream of getting a PhD degree under the same professor starting in August 2010, and graduated in December 2013.